Magnetic fields in Astrophysics

Thesis submitted for the degree of
Doctor of Philosophy

by

Daniel James Price
B.Sc. (Hons)

Institute of Astronomy
&
Churchill College

University of Cambridge
August 2004

CONTENTS

For Catherine

DECLARATION

I hereby declare that my thesis entitled *Magnetic fields in Astrophysics* is not substantially the same as any that I have submitted for a degree or diploma or other qualification at any other University. I further state that no part of my thesis has already been or is being concurrently submitted for any such degree, diploma or other qualification. This dissertation is the result of my own work and includes nothing which is the outcome of work done in collaboration except where specifically indicated in the text. Those parts of this thesis which have been published or accepted for publication are as follows:

- Much of the work contained in Chapter 2 was published as:
  Price, D.J., Pringle, J.E., King, A. (2003) 'A comparison of the jet acceleration mechanisms in young stellar objects and active galactic nuclei.', *Monthly Notices of the Royal Astronomical Society* **339**, 1223-1236 and was completed in collaboration with these authors.

- Much of the work presented in Chapter 4 has been completed in collaboration with Joe Monaghan, published as: Price, D.J., Monaghan, J.J. (2004) 'Smoothed Particle Magnetohydrodynamics I. Algorithm and tests in one dimension.', *Monthly Notices of the Royal Astronomical Society*, **348**, 123-138, together with:
  Price, D.J., Monaghan, J.J. (2004) 'Smoothed Particle Magnetohydrodynamics II. Variational principles and variable smoothing length terms.', *Monthly Notices of the Royal Astronomical Society*, **348**, 139-152

- Work on 'Toy Stars' in Chapters 3 and 4 has also resulted from a collaboration with Joe Monaghan and has been published as:
  Monaghan, J.J., Price, D.J. (2004) 'Toy stars in one dimension', *Monthly Notices of the Royal Astronomical Society*, **350**, 1449-1456

This thesis contains fewer than 60,000 words.

D. J. Price
Cambridge, August 2004

ACKNOWLEDGEMENTS

Firstly I would like to thank my supervisor, Jim Pringle, for all of the encouragement, support and insights over the past 3 years and for helping me to 'think physics'. I am also deeply indebted to Joe Monaghan for innumerable discussions, the many kind and thoughtful responses to my steady stream of emails, a wonderful trip back home, for productive collaborations and for the continued hospitality which Joe and Jen have shown towards my family. I would also like to thank Matthew Bate for providing much encouragement and motivation and for many useful discussions and Diego Molteni for a great trip to Sicily and for the many encouragements given during that visit and since. I would like to acknowledge other useful work-related discussions with, amongst others, Enrico Ramirez-Ruiz, Melvyn Davies, James Murray, Jim Stone, Ian Bonnell and Gordon Ogilvie which have helped to clarify my own thoughts and understandings of much of the work in this thesis.

To those who shared the joy, the pain and the IoA coffee: Adrian, Ali, Lisa, Elizabeth, John, Will, Adam, Elena & Davide, Antonio, Suzanne and Jo. Thanks in particular to Adrian for plenty of interesting coffee-time discussions about life, the universe and everything.

To my parents for all of the love and support they have shown throughout. Also to the rest of my family: Bec & Andrew, Matt & Kathy and JARS for all of their prayers and support. Thanks to the English relatives: Grandma, Uncle Rog & Aunty Helen, Ben, Sarah and Joe, Uncle Frank & Aunty Jan and especially Aunty Andrea & Uncle John for looking after us in this strange and bewildering country.

To friends new and old: John & Elizabeth, Rob & Katriona, Paul & Louisa, Miles & Ali, Mike & Bec, Paul & Jill, Mick & Sally, Adrian & Anna, Daniella & Peter, Enrico & Kristen and Maria & Brett. Also thanks to the everyone in the Minaar's home group and in Catherine's bible study group at St. Andrew the Great for all of their interest, prayers and support.

To everyone who came to visit us in Cambridge.

To my office mates: Phil, Jim, Enrico, James, George, Alan, Leda, Glenda, Sam, Clemens and Lola. Thanks especially to Phil for answering pretty much every computer-related query I could muster. Practical thanks also go to Glenn Morris for supplying the LaTeXstyle used to typeset this thesis.

This research has been funded by the Commonwealth Scholarship Commission and the Cambridge Commonwealth Trust, to whom I am extremely grateful. Particular thanks go to Teresa Anderson of the Association of Commonwealth Universities and Jennifer Yap of the British Council for their administration of the scholarship.

Most of all, I would like to express my gratitude to my wife Catherine for her great patience, continual encouragement and endless love and support through all the ups and downs of the last 3 years; to our daughter Gabriella for making life so much fun and to God for making it all worth studying in the first place.

DJP
Cambridge, August 2004

SUMMARY

In this thesis we develop approaches to studying two of the most longstanding theoretical problems in astrophysics, namely the nature and origin of astrophysical jets and the role of magnetic fields in star formation. The results are, however, more widely applicable to a range of problems in which magnetic fields are important.

For the former problem we employ a very simplified physical model of the jet acceleration process. We use time-dependent, spherically symmetric wind models in Newtonian and relativistic gravitational fields to ask whether the energy input rates required to produce the jet velocities observed in Young Stellar Objects (of about $2 \times$ the escape velocity from the central object) can also produce Active Galactic Nuclei jet velocities (Lorentz factors of $\gamma \sim 10$). Such a scaling would be expected if there is a common production mechanism for such jets. We demonstrate that such a scaling does exist, provided that the energy input process takes place sufficiently deep in the gravitational potential well, enabling physical use to be made of the speed of light as a limiting velocity, and provided that the energy released in the accretion process is imparted to a small fraction of the available accreting material.

For the latter problem we focus on developing accurate numerical methods for solving the equations of magnetohydrodynamics (MHD) using the Smoothed Particle Hydrodynamics (SPH) method. The implementation of a 'Smoothed Particle Magnetohydrodynamics' algorithm has previously been accompanied by numerous technical difficulties all of which are addressed at some level in this thesis in order to develop a robust and accurate method which can be applied to a wide range of problems of current theoretical interest. In the process we have undertaken a thorough review of the SPH method itself, from which several new results are derived. Amongst the technical issues addressed in the development of the SPMHD algorithm are the treatment of terms proportional to the divergence of the magnetic field in the MHD equations, the self-consistent formulation of the discrete equations from a variational principle, numerical stability of the algorithm and the self-consistent treatment of terms relating to the use of a spatially varying smoothing length. Considerable attention is paid to the ability of the algorithm to capture shocks for which artificial dissipation terms are formulated. Several methods are also examined for maintaining the divergence-free constraint in an SPMHD context. Perhaps most importantly the algorithm is benchmarked against a wide range of standard problems used to test recent high resolution shock-capturing grid-based MHD codes.

‘There is not a single effect in Nature, not even the least that exists, such that the most ingenious theorists can ever arrive at a complete understanding of it. This vain presumption of understanding everything can have no other basis than never understanding anything.’

GALILEO GALILEI

‘..we do not ask for what useful purpose birds do sing, for song is their pleasure since they were created for singing. Similarly we ought not to ask why the human mind troubles to fathom the secrets of the heavens. Our Creator has added mind to the senses not simply so that man might earn his daily keep - many kinds of creatures possessing unreasoning souls can do this much more skilfully - but also so that from the existence of the things which we behold with our eyes, we might delve into the causes of their being and becoming, even if this might serve no further useful purpose’

Mysterium Cosmographicum
JOHANNES KEPLER

‘One of the great things about books is sometimes there are some fantastic pictures.’

GEORGE W. BUSH

"The Americans, they always depend on a method what I call ... stupid, silly. All I ask is check yourself. Do not in fact repeat their lies"

MUHAMMED SAEED AL-SAHAF
Former Iraqi Information Minister

1 Introduction

Magnetic fields play an important, in some cases crucial, role in many areas of astrophysics: in the production of jets and outflows from a wide range of sources; in Star and Planet formation; in Accretion Discs; in compact star mergers, Supernovae and Gamma Ray Bursts (GRBs); in the Sun and other stars; the Interstellar Medium; in galaxy collisions and in galaxy clusters, to name just a few. In fact it is difficult to name an area of astrophysics in which magnetic fields are *not* important at some level. However, despite the relative simplicity and well-studied nature of the equations which describe them, their effects are complicated and both analytic and numerical studies present severe technical challenges. It is for this reason that despite a large theoretical effort over the past few decades profound questions remain over the role, configuration, effects and origin of magnetic fields in many astrophysical contexts.

In no field is this more relevant than that of star formation. For many years magnetic fields were thought to play the decisive role in the star formation process, leading to the so-called 'standard model' of star formation as a quasi-static process mediated by slow diffusion of the gas through a supporting magnetic field (Shu et al., 1987). In recent years, however, with a substantial increase in spatial resolution in the observations of star forming regions and the development of sophisticated codes for magnetohydrodynamics (MHD), the standard model of star formation has become extremely difficult to reconcile with both observational fact and numerical investigation. In its place a new 'standard model' has taken hold, where the crucial ingredient in the star formation recipe is not the magnetic field, but rather the details of the supersonic turbulence in the parental molecular cloud (Mac Low and Klessen, 2004).

This new picture of the star formation process has come through the dramatic increase in computational power over the last decade or so and with it the ability to study the properties of compressible MHD turbulence in detail. A series of grid-based MHD simulations (e.g. Stone et al. 1998; Klessen et al. 2000) have demonstrated that magnetic fields in realistic turbulent configurations cannot provide the support required to prevent molecular clouds from collapsing. However, the role of magnetic fields in other parts of the star formation process remains unknown. Importantly, magnetic fields may control

the overall star formation efficiency in molecular clouds either by preventing material from collapsing or by inducing feedback via jets and outflows. Magnetic fields are also thought to play a crucial role in angular momentum transport both in the infalling gas and by the magnetic braking of cores. The effect of magnetic fields on fragmentation is also unclear and represents an issue of key importance. Magnetic fields are also thought to play a crucial role in the accretion discs which are observed to form around newborn stars.

More generally, the formation of an accretion disc is thought to be the primary means by which gas is accreted onto astrophysical objects, since it is in a disc that the substantial angular momentum of the infalling material can be dissipated. The means by which this might be achieved remained for many years a subject of much speculation since the seminal work of Shakura and Sunyaev (1973) in which the source of the angular momentum dissipation was parametrised into a viscosity-like term, although the physical source of such a viscosity remained unknown. This so-called 'α-disc model' provided a standard model for describing the accretion process in thin discs (Pringle, 1981) which could be used to explain many astrophysical phenomena (such as the outbursts observed in Dwarf Novae[1]). However a physical source of the viscosity term remained elusive until Balbus and Hawley (1991) rediscovered[2] a powerful instability present in shear flows with a weak magnetic field, dubbed the Magneto-Rotational Instability (MRI) (see the review by Balbus and Hawley, 1998). The effect of the MRI is to drive magnetic turbulence in the disc, leading to significant dissipation of energy and hence angular momentum transport. These theoretical expectations have been confirmed by direct numerical simulations (e.g. Hawley et al., 1995). Since the requirements for the MRI to operate are quite general, it is the leading candidate for driving angular momentum transport in most (but not all) classes of accretion discs, such as those found in Active Galactic Nuclei (AGN), in stellar and compact binary systems and around young stars.

An alternative, though still magnetic, mechanism for removing angular momentum in accretion discs is via the outflows and powerful, collimated jets which are observed in nearly all of the classes of object in which accretion discs are found (Livio, 1999). Although jets were first observed in the centres of active galaxies, they are now routinely observed in Young Stellar Objects (YSOs), stellar and compact binary systems, and even in planetary nebulae. Despite the wide variety of jets observed the ultimate source of their acceleration and high degree of collimation over substantial length scales remains uncertain. What is known is that the acceleration and most likely also the collimation mechanism are almost certainly magnetic in origin, from both observational constraints and theoretical ideas. Various such mechanisms have been proposed invoking either large or small scale magnetic fields present in the accretion disc (e.g. Blandford and Payne, 1982; Heinz and Begelman, 2000), however the quest to understand the origin of jet production remains one of the most longstanding problems in theoretical astrophysics.

Magnetic fields are also thought to be the main driving mechanism behind the most powerful and luminous objects ever observed in the universe, the mysterious Gamma Ray Bursts (GRBs). Much progress has been made in this area recently, with GRBs now observed in two general classes – those of long ($\sim 10s$) and short ($\sim 0.1s$) duration. In the former case rapid-response observations have been able to capture the fading afterglows of such bursts through longer wavelengths, in many cases clearly

[1] for this and other examples see Frank et al. (2002).

[2] although the instability was known previously (e.g. Chandrasekhar, 1961), Balbus and Hawley were the first to recognise the importance of this instability in accretion discs.

identifying their origin in the host galaxy. The standard 'fireball' model for such bursts (e.g. Mészáros, 2002) suggests that the long duration bursts are caused by extremely powerful supernovae explosions in which an ultrarelativistic (Lorentz factor $\gtrsim 100$) jet penetrates the surrounding material blown off in the explosion. Such events would be viewed as GRBs when the jet is directed towards the observer. The mechanism by which such a jet is produced is widely believed to be magnetic in origin. The origin of the short duration bursts remains somewhat less certain, primarily because of the difficulty of making follow-up observations on such short timescales. However a leading suggestion is that the burst is produced following the merger of two neutron stars. The mechanism by which it might do so is highly speculative, although a prime candidate is that the energy extraction is due to a magnetic field which is wound up by differential rotation in the merger remnant (Rosswog et al., 2003).

Thus there are a wide range of astrophysical problems which require a detailed understanding of the role of the magnetic field in many different physical regimes and in highly dynamical environments. In order to tackle these problems two general approaches may be taken. The first is to attempt to simplify the physics to the point where simple solutions are possible which focus on a few narrow aspects of the problem. The second approach is to undertake full numerical simulations, which in general involves solving the equations of magnetohydrodynamics (MHD) numerically.

In the first part of this thesis (Chapter 2) we take the first approach, that of simplification, to one specific astrophysical problem in which the magnetic field is thought to play a dominant role, namely in the production of jets from accretion discs. Numerical simulations incorporating both the accretion disc and the jet formation process are extremely difficult in this case due to the large range in length scales and the extreme timestepping constraints caused by the disc corona. We focus on the jet acceleration process, making simple physical assumptions in order to compare the acceleration of jets in both relativistic and non-relativistic environments in a fairly generic manner. The aim of the investigation is to examine the hypothesis of a common acceleration mechanism (ascribed to the magnetic field) for jets born in such different environments by reconciling the observed jet velocities in each class of object to a common energy input rate. The results of this investigation are presented at the end of Chapter 2 and summarised in Chapter 6.

In the second part of the thesis (Chapters 3, 4 and 5) we focus on developing new methods for solving the MHD equations numerically in an astrophysical context. The MHD equations represent a one-fluid approximation to the equations of plasma physics (a combination of gas dynamics with Maxwell's equations for the electromagnetic field). Traditionally MHD studies have been the domain of solar physicists, due to the clear and unmistakable presence of magnetic phenomena in the Sun. However in the last decade or so the importance of magnetic phenomena in many other areas of astrophysics has become clear (mostly in connection with accretion phenomena) and therefore a substantial research effort has been devoted to the development of accurate numerical methods for solving the compressible MHD equations, albeit on fixed spatial grids. This has also been fuelled by a dramatic increase in computational power which has made previously inaccessible problems open to study. The development of such algorithms has enabled significant new insights to be made into a wide range of problems, many of which have been described above. However, the primary disadvantage of such methods is that adaptivity is a crucial requirement for astrophysical problems, since problems are frequently highly asymmetric with important dynamical effects occurring over length and time scales of many orders of magnitude. This has been redressed somewhat in recent years with the development of (somewhat complicated) proce-

dures for adaptive mesh refinement (AMR), although there remains significant scope for other adaptive methodologies since there are also many disadvantages (such as high numerical transport of angular momentum) in performing simulations involving highly asymmetric flow geometries (ie. non-Cartesian) on (fixed or adaptive) Cartesian grids. Furthermore the complexity of such algorithms means that introducing even moderate amounts of new physics is a lengthy and time-consuming process.

Smoothed Particle Hydrodynamics (SPH) is a unique numerical method widely used for astrophysical problems since it involves no spatial grid. Rather, fluid quantities are carried by a set of Lagrangian 'particles' which move with the flow, meaning that complicated dynamics and asymmetric phenomena are treated with ease. Since adaptivity is a built-in feature of the method there is no need to resort to complicated additional mesh refinement procedures. The implementation of MHD into SPH has been studied in detail by several authors. However a substantial number of issues remain to be addressed, particularly with respect to the recent rapid progress in MHD algorithms developed for grid-based codes. The remainder of this thesis (Chapters 3, 4 and 5) is dedicated to addressing many of these issues in order to provide a sufficiently robust and accurate numerical method for the simulation of magnetic phenomena in many of the problems considered above. Doing so involves a comprehensive review of the SPH method itself (Chapter 3) before discussing the implementation of MHD (Chapter 4) and the many further issues involved in multidimensional MHD related to the divergence-free (no monopoles) constraint for the magnetic field (Chapter 5). A discussion of the main results is presented at the end of each chapter and summarised in Chapter 6, along with a brief discussion of problems to which the algorithm can be applied.

"If I had only known, I would have been a locksmith."

ALBERT EINSTEIN

2

A comparison of the jet acceleration mechanisms in young stellar objects and active galactic nuclei

2.1 Introduction

Astrophysical jets were first discovered when Curtis (1918) observed a 'curious straight ray' emanating from the nucleus of the M87 nebula. Such jets are now commonly observed in a wide variety of astrophysical environments, including Active Galactic Nuclei (AGN), Young Stellar Objects (YSOs), stellar and compact binary systems and their presence is even inferred in the violent supernovae which manifest as Gamma-Ray Bursts. Despite an ever-growing mountain of observations[1], many of the fundamental questions regarding the basic processes which govern their acceleration and high degree of collimation over substantial length scales remain a mystery.

Since the relativistic AGN jets were discovered first, presumably powered by accretion onto the central black hole (Rees, 1984), it was natural that early models for jet formation were inherently relativistic (Ferrari, 1998). For example, the oft-cited mechanism of Blandford and Znajek (1977) involves tapping the rotational energy of a spinning black hole. The mere existence of jets in classes of object where black holes are not present clearly indicates that such processes cannot provide a universal explanation of jet origins. Similarly, mechanisms invoking a star rotating at near break-up speed (Shu et al., 1988) or accretion disc boundary layers (Pringle, 1989) must also be excluded (although in the latter case there may be some analogy in black hole accretion discs), unless we argue that different processes operate in each separate class of object, despite the ubiquity of jet production. Since it was clear from the lack of substantial thermal emission that the jet acceleration process was not purely hydrodynamic in nature (see e.g. Blandford and Rees, 1974; Konigl, 1982), nearly all jet production mechansisms invoke some kind of magnetic field, whether large- (Blandford and Payne, 1982; Pudritz and Norman, 1986) or small-

[1] for example a search of the NASA ADS for papers with 'jet' in the title produces 390 hits for 2003 alone.

(Heinz and Begelman, 2000) scale. Of these the most popular and by far the most successful mechanism for explaining both the acceleration and collimation of jets is the magneto-centrifugal model of Blandford and Payne (1982) which has been demonstrated in a number of numerical simulations (Ouyed and Pudritz 1997, 1999; Ouyed et al. 1997; Kudoh et al. 1998; Koide et al. 2000).

In this model a large scale vertical field threading the accretion disc causes material to be centrifugally accelerated along the magnetic field lines, analogous to 'beads on wires'. Blandford and Payne (1982) demonstrated that such acceleration could take place if the angle of inclination between the field lines and the disk was $> 30^{\circ}$. Although it might be claimed that some form of consensus has been reached on magnetocentrifugal acceleration forming the the heart of the jet production process, these models suffer from several problems. The first of these is the origin of the large-scale field which must be invoked for the model to work, in particular whether such fields can be either advected inwards from the environment from which the disc formed (see Lubow et al., 1994) or produced spontaneously from a dynamo operating in the disc itself (Tout and Pringle, 1992, 1996). The second problem is that large-scale magnetic fields dominated by toroidal components are found to be unstable (Spruit et al., 1997; Lucek and Bell, 1996; Begelman, 1998) (where the instabilities are similar to those observed in a wound-up rubber band, which begins to bend and kink as it becomes dominated by toroidal stresses). For this reason the role of collimation is now generally assigned to a dominant poloidal component of the field (e.g. Lucek and Bell 1997).

A further problem, and the issue we focus on in the present work, is that the Blandford and Payne (1982) model is scale-free (ie. self-similar). The problem with this is the fairly general observation that jet velocities appear to be very close to the escape velocity from the central gravitating object (Livio, 1999), suggesting that jets are somehow aware of the strength of the gravitational potential close to the central object itself. This would seem to indicate that the jet originates from the inner part of the accretion disc (ie. close to the central object) and is supported by observations such as those of HH30 showing a jet clearly emanating from the centre of the accretion disc (Burrows et al., 1996) and variability in the $\mu-$quasar system GRS1915+105, where dips in the X-ray flux are observed immediately prior to the observation of a blob of plasma being ejected into the jet, interpreted as the inner edge of the accretion disc dropping away prior to the ejection event (Mirabel et al., 1998; Mirabel and Rodríguez, 1999). Similar observations have been made over longer timescales in the active galaxy 3C120 by Marscher et al. (2002). Intrinsic jet velocities in both relativistic and non-relativistic jets are somewhat difficult to measure because in order to be visible the jet material must be interacting with the surrounding medium in some way (and therefore decelerating). In the YSO case, jet velocities are typically inferred from measurements of the proper motions of features travelling along the jet (such as the Herbig-Haro objects which are interpreted as shocks within the jet due to material travelling at different speeds) or by mapping the velocity structure around such features (Reipurth and Bally, 2001). Typical jet velocities thus measured lie in the range $v_{jet} \sim 300-500$ km/s (Eislöffel and Mundt 1998; Micono et al. 1998; Bally et al. 2001; Hartigan et al. 2001; Reipurth et al. 2002; Bally et al. 2002; Pyo et al. 2002) which may be compared to the escape velocity from a typical young star (mass 1 $M_{\odot}$, radius 5 $R_{\odot}$; Tout et al. 1999) of $v_{esc} \sim 270$ km/s. In the AGN case, jet velocities are observed to be very close to the speed of light, in keeping with the escape velocity from the central black hole. Although estimates vary, observationally typical Lorentz factors for AGN jets lie in the range $\gamma_{jet} \sim 5-10$ (Urry and Padovani 1995; Biretta et al. 1999), although arguments for higher values ($\gamma_{jet} \sim 10-20$) have been made on theoretical grounds

(Ghisellini and Celotti, 2001).

In recent years it has been suggested that small scale, tangled magnetic fields could perhaps both accelerate (Heinz and Begelman, 2000) and collimate (Li, 2002) jets, without invoking any large-scale field. These ideas are attractive theoretically as they are in keeping with the turbulent magnetic fields known to drive accretion in discs via the magneto-rotational instability (Balbus and Hawley, 1991). Collimation via small scale fields does not suffer from the problem of instabilities and since acceleration via small scale fields is an inherently local process, the scale associated with the acceleration regions would be naturally reflected in the velocity of the resulting outflow.

In this chapter we take an extremely simplified approach to the problem of jet acceleration, paying particular attention to the observation that jet velocities are of order the escape velocity from the central object. We pose the question of whether or not a simple scaling exists between jets accelerated in non-relativistic environments and those accelerated in relativistic environments by considering a highly simplified model of the jet acceleration process. Since we are concerned only with acceleration, not collimation, we examine the driving of a spherically symmetric outflow by injecting energy into an initially hydrostatic gas reservoir at a fixed radius close to the central object. The gas is treated in a simple manner as having a purely thermal pressure, P, and internal energy, u, and a ratio of specific heats γ which we take to be $\gamma = 4/3$. The exact value of γ is not particularly critical to the arguments developed in this chapter, provided that $\gamma < 5/3$ so that the outflow becomes supersonic. Taking $\gamma = 4/3$, however, is in fact appropriate to the case of an optically thick radiation-pressure dominated flow, and to the case in which the dominant pressure within the gas is caused by a tangled magnetic field (Heinz and Begelman, 2000). It should therefore, despite the simplistic treatment, allow us to draw some quite general conclusions.

If the same acceleration process is at work in both relativistic and non-relativistic jets, then the same (appropriately scaled) energy input rate should account for the observed jet velocities in both classes of object. Specifically, the energy input rate required to give rise to a final jet velocity $v_{jet} \sim 2v_{esc}$ in the non-relativistic case should also be able to produce outflows with Lorentz factors of $\gamma_{jet} \sim 7$ in the relativistic case. We therefore undertake the following computations: In §2.2 we examine the non-relativistic case, appropriate to YSO jets. Energy is injected at a steady rate over a small volume into an initially hydrostatic gas reservoir, following the time evolution of the gas as it expands. Since we cannot follow the time evolution for an infinite time, once the gas has reached a large enough radius the time-dependent solution is matched to a steady state wind solution in order to determine the terminal velocity of the outflow. In §2.3 exactly the same computations are performed using relativistic fluid dynamics, appropriate to AGN (and $\mu-$quasar) jets. The final jet velocity is then plotted as a function of the (dimensionless) energy input rate (heating rate) in both the relativistic and non-relativistic cases. Results and conclusions are presented in §2.4.

2.2 Non-relativistic (YSO) jets

2.2.1 Fluid equations

For YSO jets we expect the gravitational field to be well approximated by a non-relativistic (Newtonian) description. In one (radial) dimension the equations describing such a fluid including the effects of

energy input are expressed by the conservation of mass,

$$\frac{\partial \rho}{\partial t} + \mathrm{v}^r \frac{\partial \rho}{\partial r} + \frac{\rho}{r^2}\frac{\partial}{\partial r}(r^2 \mathrm{v}^r) = 0, \tag{2.1}$$

momentum,

$$\frac{\partial \mathrm{v}^r}{\partial t} + \mathrm{v}^r \frac{\partial \mathrm{v}^r}{\partial r} + \frac{1}{\rho}\frac{\partial P}{\partial r} + \frac{GM}{r^2} = 0, \tag{2.2}$$

and energy,

$$\frac{\partial (\rho u)}{\partial t} + \mathrm{v}^r \frac{\partial (\rho u)}{\partial r} + \left[\frac{P+\rho u}{r^2}\right]\frac{\partial}{\partial r}(r^2 \mathrm{v}^r) = \rho \Lambda, \tag{2.3}$$

where ρ, v^r, P and u are the fluid density, radial velocity, pressure and internal energy per unit mass respectively, M is the mass of the gravitating object (in this case the central star), and

$$\Lambda = \frac{dQ}{dt} = T\frac{ds}{dt} \tag{2.4}$$

is the heat energy input per unit mass per unit time (where T and s are the temperature and specific entropy respectively). The equation set is closed by the equation of state for a perfect gas in the form

$$P = (\gamma - 1)\rho u. \tag{2.5}$$

Scaling

To solve (2.1)-(2.5) numerically we scale the variables in terms of a typical length, mass and timescale. These we choose to be the inner radius of the gas reservoir $[L] = R_*$, the mass of the gravitating body $[M] = M_*$ and the dynamical timescale at the the inner radius ($r = R_*$), $[\tau] = (GM_*/R_*^3)^{-1/2}$. In these units $GM = 1$ and the density, pressure, velocity and internal energy, respectively, have units of density, $[\rho] = M_*/R_*^3$, pressure, $[P] = M_*/(R_*\tau^2)$, circular velocity at R_*, $[\mathrm{v}] = \sqrt{GM_*/R_*}$ and gravitational potential energy at R_*, $[u] = GM_*/R_*$. Note that the net heating rate per unit mass Λ is therefore given in units of gravitational potential energy, GM_*/R_*, per dynamical timescale at R_*, $(GM_*/R_*^3)^{-1/2}$. We point out that this scaling is simply to ensure that the numerical solution is of order unity and that when comparing the results to the relativistic simulations we scale the solution in terms of dimensionless variables.

2.2.2 Numerical solution

We solve (2.1)-(2.5) in a physically intuitive way using a staggered grid where the fluid velocity is defined on the half grid points whereas the density, pressure, internal energy and heating rate are specified on the integer points. This allows for physically appropriate boundary conditions and allows us to treat the different terms in a physical way by applying upwind differencing to the advective terms but using centred differencing on the gradient terms. The scheme is summarised in Figure 2.1 with the discretized form of the equations given in appendix A. The staggered grid means that only three boundary conditions

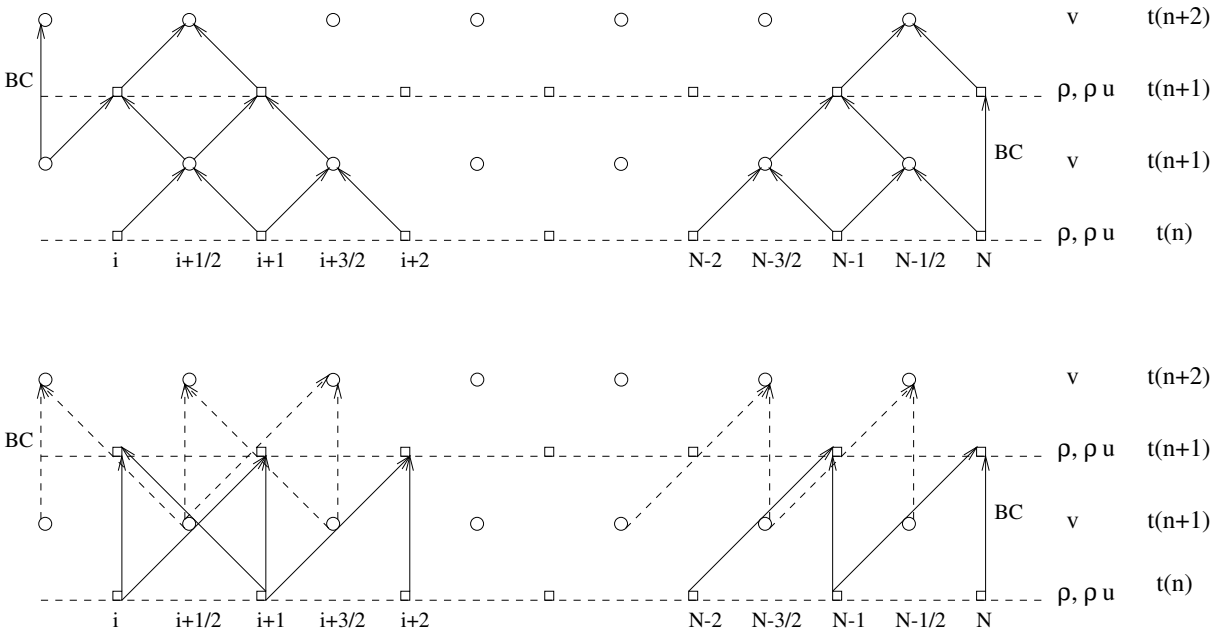

Figure 2.1: Schematic diagram of numerical method: density and internal energy are defined on the integer points while velocity is calculated on the half points. The solution requires one inner boundary condition on v and two outer boundary conditions for ρ and ρu. Updated velocities (v^{n+1}) are used to calculate ρ^{n+1} and ρu^{n+1}. The scheme allows centred differencing on terms involving staggered quantities (top panel) while upwind differencing is used on the advective terms (bottom panel).

are required, as shown in Figure 2.1. We set $v = 0$ at the inner boundary and the density and internal energy equal to their initial values (effectively zero) at the outer boundary.

2.2.3 Initial conditions

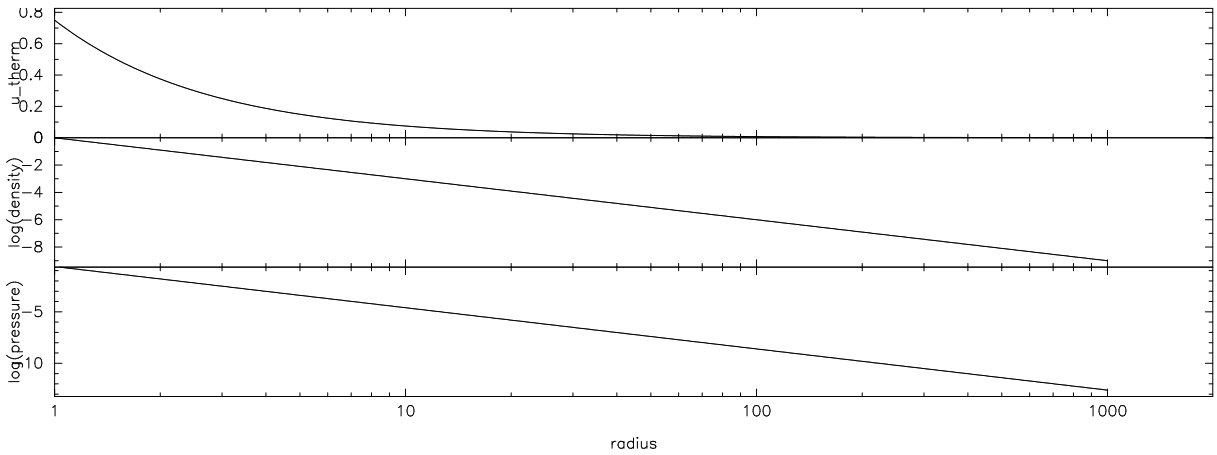

Figure 2.2: The initial conditions for the non-relativistic case, We plot profiles of density, pressure and internal energy per unit mass (or temperature) as functions of radius. The quantities here are dimensionless and the units are as described in §2.2.1.

The form of the initial conditions is not particularly crucial to the problem, as the wind eventually reaches a quasi-steady state that is independent of the initial setup. What the initial conditions do affect

is the time taken to reach this steady state (by determining how much mass must initially be heated in the wind). We proceed by setting up a body of gas (loosely 'an atmosphere') above the 'star' (or rather, an unspecified source of gravity) initially in hydrostatic equilibrium, such that v = 0 everywhere and

$$\frac{dP}{dr} = -\frac{GM\rho}{r^2}. \tag{2.6}$$

The pressure is related to the density by a polytropic equation of state

$$P = K\rho^{\gamma}, \tag{2.7}$$

where K is some constant. Combining these two conditions we obtain an equation for the density gradient as a function of radius

$$\frac{d\rho(r)}{dr} = -\frac{\rho(r)^{-(\gamma-2)}}{\gamma K}\frac{GM}{r^2}. \tag{2.8}$$

Integrating this equation from r to some upper bound R_∞ we obtain

$$\rho(r) = \left[\frac{\gamma-1}{\gamma K}\left(\frac{GM}{r} - \frac{GM}{R_\infty}\right)\right]^{1/(\gamma-1)}. \tag{2.9}$$

To ensure that pressure and density are finite everywhere (for numerical stability) we set $R_\infty = \infty$. The density is then given as a simple function of radius where it remains to specify the polytropic constant K. In scaled units we choose $K = (\gamma-1)/\gamma$ such that $\rho(R_*) = 1$ (*i.e.* the central density equals the mean density of the gravitating body – note that we neglect the self-gravity of the gas itself. Choosing K effectively determines the amount of mass present in the atmosphere and thus the strength of the shock front which propagates into the ambient medium (in terms of how much mass is swept up by this front).

We set the initial pressure distribution using (2.7). If we do this, however, the slight numerical imbalance of pressure and gravity results in a small spurious response in the initial conditions if we evolve the equations with zero heating. In the non-relativistic case the spurious velocity is kept to an acceptably small level by the use of a logarithmic radial grid (thus increasing the resolution in the inner regions). In the relativistic case however this slight departure from numerical hydrostatic equilibrium is more significant. This response is therefore eliminated by solving for the pressure gradient numerically using the same differencing that is contained in the evolution scheme. That is we solve from the outer boundary condition $P(r_{\rm max}) = K\rho(r_{\rm max})^{\gamma}$ according to

$$P_{i-1} = P_i - (r_i - r_{i-1})\frac{\rho_{i-1/2}}{r^2_{i-1/2}}. \tag{2.10}$$

Solving for the pressure in this manner reduces any spurious response in the initial conditions to below round–off error. The internal energy is then given from (2.5). The pressure calculated using (2.10) is essentially indistinguishable from that found using (2.7)($\Delta P/P \sim 10^{-5}$). The initial conditions calculated using equation (2.9), (2.10) and (2.5) are shown in Figure 2.2. We use a logarithmic grid with 1001 radial grid points, setting the outer boundary at $r/R_* = 10^3$. Using a higher spatial resolution does not affect the simulation results.

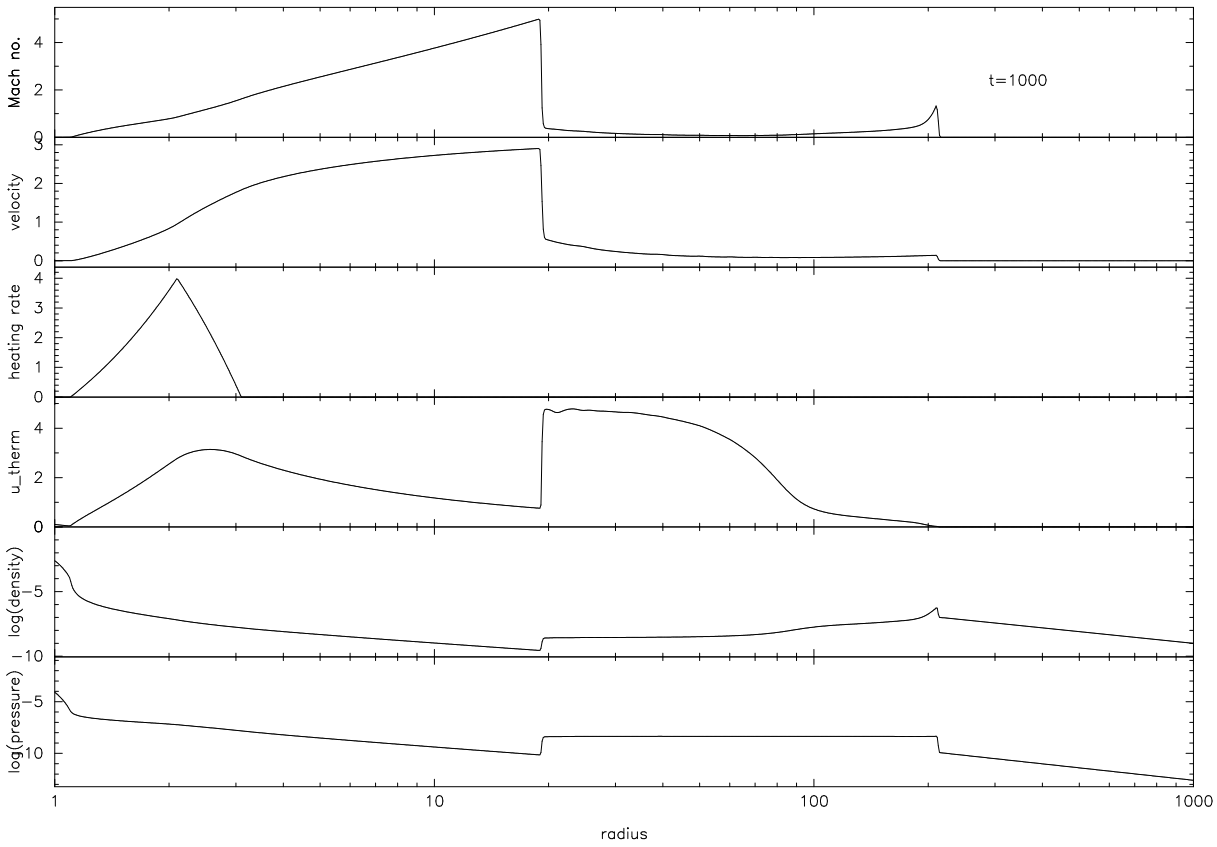

Figure 2.3: Results of a typical non-relativistic simulation at time $t = 1000$ (where units of time are the dynamical time at the innermost radius, $\sqrt{R_*^3/GM}$). Quantities shown are the Mach number (v/c_s), velocity, heating rate (Λ), internal energy per unit mass ($u \equiv u_{\rm therm}$), log(density) and log(pressure).

Heating profile

The choice of the shape of the heating profile $\Lambda(r)$ is fairly arbitrary since we wish simply to make a comparison between the non-relativistic and relativistic results. We choose to heat the wind in a spherical shell of a fixed width using a linearly increasing and then decreasing heating rate, symmetric about some heating radius $r_{\rm heat}$ which we place at $r = 2.1R_*$. The heating profile is spread over a radial zone of width $2R_*$ (that is the heating zone extends from $r = 1.1R_*$ to $3.1R_*$)(see Figure 2.3). We choose a heating profile of this form such that it is narrow enough to be associated with a particular radius of heating (necessary since we are looking for scaling laws) whilst being wide enough to avoid the need for high spatial resolution or complicated algorithms (necessary if the heat input zone is too narrow). The important parameter is thus the *location* of the heating with respect to the Schwarzschild radius, so long as the heating profiles are the same in both the relativistic and non-relativistic cases. Provided that the heating profile is narrow enough to be associated with a particular radius and wide enough to avoid numerical problems, the results do not depend on the actual shape of the profile used.

2.2.4 Results

The results of a typical non-relativistic simulation with a moderate heating rate are shown in Figure 2.3 at $t = 1000$ (where t has units of the dynamical time at the inner radius). We observe the effect of the heating propagating outwards in the atmosphere in the form of a shock front. After several hundred dynamical

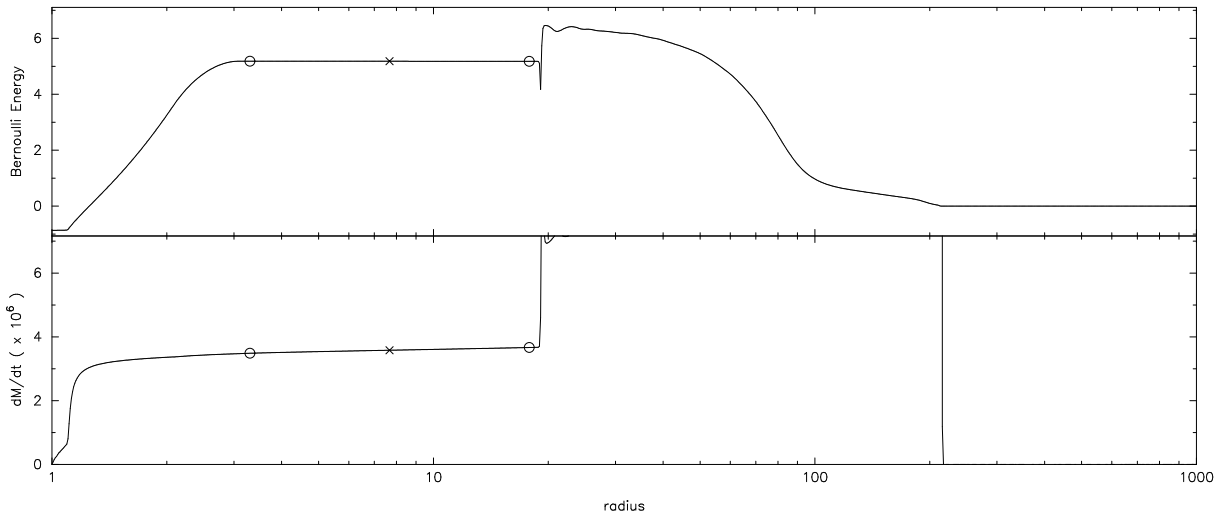

Figure 2.4: Bernoulli energy $E = \frac{1}{2}\mathrm{v}^2 + \rho u + P - GM/r$ (top) and mass outflow rate $\dot{M} = 4\pi r^2 \rho \mathrm{v}$ (bottom) in the time-dependent wind solution at $t = 1000$. The profiles are approximately constant over the region between the two circles. The sample point used to match this flow to the appropriate steady state solution is indicated by a cross.

times the wind structure approaches a steady state in that there is only a small change of the overall wind structure due to the shock continuing to propagate outwards into the surrounding medium. The small disturbance propagating well ahead of the main shock is a transient resulting from the response of the atmosphere to the instantaneous switch-on of the heating. The velocity of the gas begins to asymptote to a constant value as the shock propagates outwards. Plotting the mass outflow rate $\dot{M} = 4\pi r^2 \rho \mathrm{v}$ and the Bernoulli energy $E = \frac{1}{2}\mathrm{v}^2 + \rho u + P - GM/r$ as a function of radius (Figure 2.4), we see that indeed the wind structure is eventually close to that of a steady wind above the heating zone (ie. $\dot{M}$ and $E \sim$ constant). It is thus computationally inefficient and impractical to compute the time-dependent solution for long enough to determine an accurate velocity as $r \to \infty$ when the wind will continue to have a steady structure. Instead we find the steady wind solution for a given amount of energy input to the wind corresponding to the energy plotted in Figure 2.4 (top panel).

2.2.5 Steady wind solution

Non-relativistic, steady state ($\partial/\partial t = 0$) winds with energy input have been well studied by many authors, and the equations describing them can be found in Lamers and Cassinelli (1999), who credit the original work to Holzer and Axford (1970). The reader is thus referred to Lamers and Cassinelli (1999) for details of the derivation. As in the usual Bondi/Parker (Bondi 1952, Parker 1958) wind solution with no heat input, we set $\partial/\partial t = 0$ in (2.1)-(2.5) and combine these equations into one equation for the Mach number $M^2 = \mathrm{v}^2/c_s^2$ as a function of radius, given by

$$\frac{dM^2}{dr} = -\frac{M^2(2+(\gamma-1)M^2)}{2(M^2-1)\left[e(r)+GM/r\right]}\left[(1+M^2\gamma)\frac{dQ}{dr} + \frac{GM}{r^2}\frac{(5-3\gamma)}{(\gamma-1)} - \frac{4e(r)}{r}\right], \tag{2.11}$$

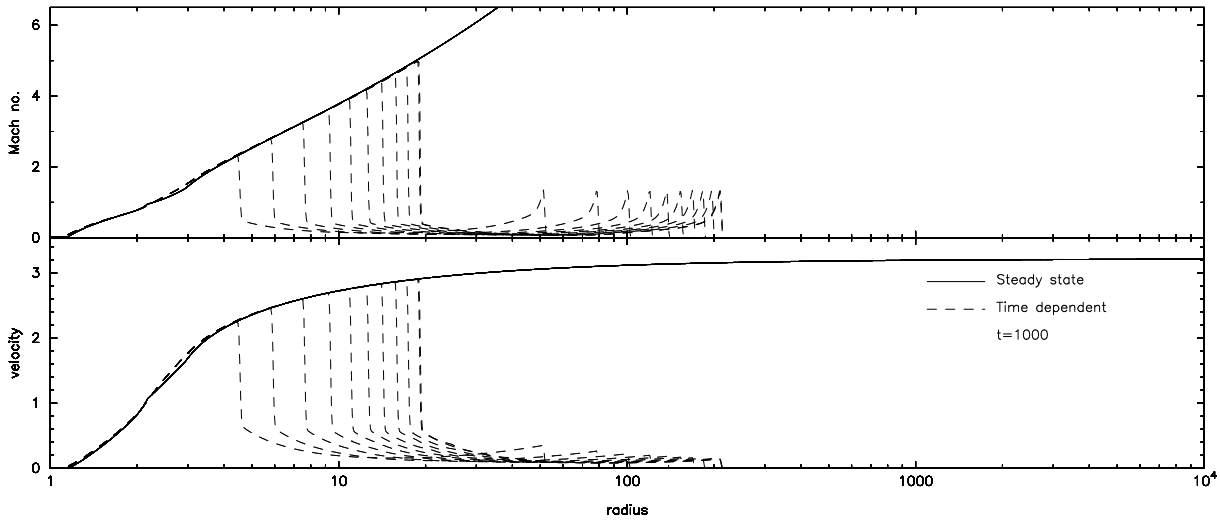

Figure 2.5: Steady wind Mach number (top panel) and velocity (centre panel) profiles are compared to the time-dependent solution (plotted every 100 dynamical times). There is a small discrepancy between the two solutions where we have taken the limit in approaching the singular point at $M = 1$, but an otherwise excellent agreement between the two solutions.

where dQ/dr is the local heating gradient and $e(r)$ is the Bernoulli energy which is specified by integrating the Bernoulli equation

$$\frac{de(r)}{dr} = \frac{d}{dr}\left[\frac{1}{2}\mathrm{v}^2 + \rho u + P - \frac{GM}{r}\right] = \frac{dQ}{dr}, \tag{2.12}$$

to give

$$\begin{aligned} e(r) &= e(r_\infty) - Q(r) \\ &= e(r_\infty) - \int_r^{r_\infty} \frac{dQ}{dr}, \end{aligned} \tag{2.13}$$

where $Q(r)$ is the total energy input to the wind. Since we are interested in the terminal velocity of the outflow we choose a point above the heating shell where the energy has reached its steady state value (*i.e.* where the energy is constant in Figure 2.4, top panel) and integrate outwards using the energy and Mach number at this point to solve (2.11) as an initial value problem. Note that in fact the terminal velocity is determined by the (constant) value of the Bernoulli energy above the heating zone since as $r \to \infty$, $e(r) \to \frac{1}{2}\mathrm{v}^2$. However we compute the steady wind profiles both inwards and outwards to show the consistency between the time-dependent solution and the steady state version.

In order to perform the inward integration, we must determine the energy at every point for our steady solution by subtracting the heat input from the steady state energy as we integrate inwards through the heating shell (2.13). To determine this however we must also determine the local (steady state) heating gradient dQ/dr, which is related to the (time dependent) heating rate Λ by setting $\partial/\partial t = 0$ in the time dependent version, ie.

$$\Lambda = \frac{dQ}{dt} = \frac{\partial Q}{\partial t} + \mathrm{v}\frac{dQ}{dr} = \mathrm{v}\frac{dQ}{dr}. \tag{2.14}$$

We therefore calculate dQ/dr from the time dependent solution using

$$\frac{dQ}{dr} = \frac{\Lambda(r)}{\mathrm{v}(r)}, \tag{2.15}$$

where $\mathrm{v}(r)$ is the wind velocity at each point in the heating shell from the time-dependent solution. The problem with this is that at the inner edge of the heating shell the heating rate is finite while the velocity is very close to zero, resulting in a slight overestimate of the total energy input near the inner edge of the shell in the steady wind solution. Care must also be taken in integrating through the singular point in equation (2.11) at $M^2 = 1$. Most authors (e.g. Lamers and Cassinelli 1999) solve the steady wind equations starting from this point but for our purposes it is better to start the integration outside of the heating shell where the energy is well determined. We integrate through the critical point by using a first order Taylor expansion and appropriate limit(s), although this introduces a small discrepancy between the steady state and time-dependent results in this region (Figure 2.5).

Having determined the energy and heating gradient at each point in the wind we integrate (2.11) both inwards and outwards from the chosen point above the heating shell using a fourth order Runge-Kutta integrator (scaling (2.11) to the units described in §2.2.1). The velocity profile is then given by $\mathrm{v}^2 = M^2 c_s^2$ where

$$c_s^2(r) = \frac{2(\gamma-1)}{2+M^2(r)(\gamma-1)}\left[e(r) + \frac{GM}{r}\right]. \tag{2.16}$$

The resulting steady wind solution is shown in Figure 2.5 along with the time-dependent solution. The two profiles are in excellent agreement, proving the validity of our time-dependent numerical solution and the assumption that the wind is in a steady state. The steady solution thus provides an accurate estimate of the velocity at arbitrarily large radii (although as pointed out previously this is set by the value of the steady state Bernoulli energy).

2.2.6 Terminal wind velocities as a function of heating rate

Using the steady wind extrapolation of the time-dependent solution, we can determine the relationship between the heating rate and the terminal wind velocities. In order to make a useful comparison between the heating rates used in both the Newtonian and the relativistic regimes, we need to define a local canonical heating rate $\Lambda_c(r)$ valid in both sets of regimes. In dimensional terms the heating rate $\Lambda(r)$ corresponds to an input energy per unit mass per unit time. Thus we need to define the local canonical heating rate as

$$\Lambda_c(r) = \frac{\Delta E}{\Delta t}, \tag{2.17}$$

for some relevant energy ΔE and some relevant timescale Δt.

Although there are many different ways in which we might define a canonical heating rate, we find that the results are not sensitive to the particular choice made. Ideally we wish to choose a heating rate which reflects the physical processes inherent in the jet acceleration process. Although these processes remain obscure, the fundamental source of the energy available for jet acceleration is the rotational

energy present in the accretion disc. For this reason we take the canonical energy per unit mass, ΔE, to be the energy released locally by bringing to rest a particle of unit mass which is orbiting in a circular orbit at radius r. In the Newtonian regime this is simply the kinetic energy of a circular orbit

$$\Delta E = \frac{1}{2}\mathrm{v}_\phi^2 = \frac{GM}{2r}. \tag{2.18}$$

(An alternative possibility, for example, would be to take ΔE to be the energy released by dropping a particle from infinity and bringing it to rest at radius r, which would correspond to the escape energy from that radius, GM/r.) By similar reasoning, we take the canonical timescale on which the energy is released to be the orbital timescale at radius r, that is $\Delta t = \Omega_o^{-1}$, where

$$\Omega_o = (GM/r^3)^{1/2}. \tag{2.19}$$

Using this, the local canonical heating rate is given by

$$\Lambda_c(r) = \Delta E \times \Omega_o = \frac{(GM)^{3/2}}{2r^{5/2}}. \tag{2.20}$$

This definition of a local canonical heating rate thus enables a direct comparison between the results of the Newtonian and relativistic calculations. In practice we must take an appropriate average heating rate $\langle\Lambda\rangle$ in each case since heat is added over a range of radii. We average across the volume of the heating shell, using

$$\langle\Lambda\rangle = \frac{\int_{r_1}^{r_2}\Lambda(r)r^2dr}{\Lambda_c(r_{\max})\int_{r_1}^{r_2}r^2dr}, \tag{2.21}$$

where $r_{\max}$ is the radius at which the heating rate $\Lambda(r)$ takes its maximum value and r_1 and r_2 are the lower and upper bounds of the heating shell respectively.

The relation between this average dimensionless heating rate $\langle\Lambda\rangle$ and the terminal wind velocity is shown in Figure 2.6. The wind velocities are plotted in units of the escape velocity $\mathrm{v}_{\mathrm{esc}}$ at R_* and solutions are computed for wind velocities of up to $\sim 3\mathrm{v}_{\mathrm{esc}}$. The important point in the present analysis is that the heating rate can be meaningfully compared to the relativistic results (see below).

2.3 Relativistic jets

Having determined the heating rates required to produce the observed velocities in YSO jets we wish to perform exactly the same calculation within a relativistic framework. We proceed in precisely the same manner as in the non-relativistic case. We adopt the usual convention that Greek indices run over the four dimensions 0,1,2,3 while Latin indices run over the three spatial dimensions 1,2,3. Repeated indices imply a summation and a semicolon refers to the covariant derivative. The density ρ refers to the rest mass density only, that is $\rho = nm_0$ where n is the number density of baryons and m_0 is the mass per baryon.

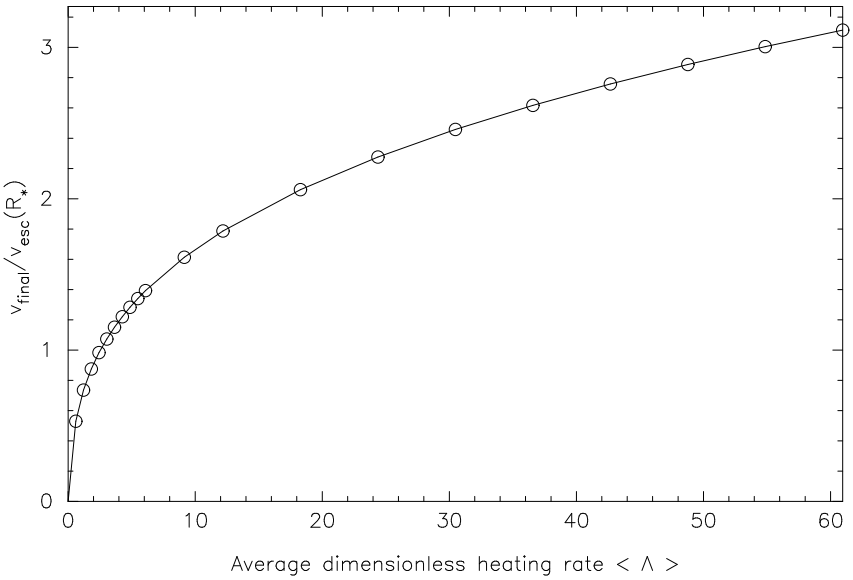

Figure 2.6: Terminal wind velocities plotted as a function of the average dimensionless heating rate $\langle\Lambda\rangle$. Wind velocities are plotted in units of the escape velocity at the inner radius (ie. $r = R_* = 1$), $v_{esc} = (2GM/R_*)^{1/2}$. We compute solutions corresponding to velocities typically observed in YSO jets (with a fairly generous upper limit of $v/v_{esc} \sim 3$).

2.3.1 Fluid equations

The equations describing a relativistic fluid are derived from the conservation of baryon number,

$$(\rho U^{\mu})_{;\mu} = 0, \tag{2.22}$$

the conservation of energy-momentum projected along a direction perpendicular to the four velocity U^{μ} (which gives the equation of motion),

$$h_{\mu\alpha}T^{\alpha\nu}{}_{;\nu} = (g_{\mu\alpha} + U_{\mu}U_{\alpha})T^{\alpha\nu}{}_{;\nu} = 0, \tag{2.23}$$

and projected in the direction of the four-velocity (which gives the energy equation),

$$U_{\alpha}T^{\alpha\nu}{}_{;\nu} = 0. \tag{2.24}$$

Here the quantity $T^{\mu\nu}$ is the energy momentum tensor, which for a perfect fluid is given by

$$c^2 T^{\mu\nu} = \rho h U^{\mu}U^{\nu} + P g^{\mu\nu}, \tag{2.25}$$

where h is the specific enthalpy,

$$h = c^2 + u + \frac{P}{\rho} = c^2 + \frac{\gamma P}{(\gamma - 1)\rho}. \tag{2.26}$$

As in the non-relativistic case u is the internal energy per unit mass, P is the gas pressure and we have used the equation of state given by equation (2.5). The energy equation may also be derived from the first law of thermodynamics using equation (2.22), which is a more convenient way of deriving an energy

equation in terms of the internal energy (rather than the total energy) and in this case ensures that the meaning of the heating term is clear. The metric tensor is given by the Schwarzschild (exterior) solution to Einstein's equations, that is

$$ds^2 = -c^2 d\tau^2 = -\left(1-\frac{2GM}{c^2 r}\right)c^2 dt^2 + \left(1-\frac{2GM}{c^2 r}\right)^{-1} dr^2 + r^2(d\theta^2 + \sin^2\theta d\phi^2). \tag{2.27}$$

We consider radial flow such that $U^\theta = U^\phi = 0$. The four velocity is normalised such that

$$U_\mu U^\mu = -c^2, \tag{2.28}$$

and we define

$$U^t \equiv \frac{dt}{d\tau} = \left(1-\frac{2GM}{c^2 r}\right)^{-1}\left[\left(1-\frac{2GM}{c^2 r}\right) + \frac{(U^r)^2}{c^2}\right]^{1/2}, \tag{2.29}$$

which we denote as

$$U^t = \frac{\Gamma}{\alpha^2} \tag{2.30}$$

where we set for convenience

$$\Gamma = \left[\left(1-\frac{2GM}{c^2 r}\right) + \frac{(U^r)^2}{c^2}\right]^{1/2}, \tag{2.31}$$

and

$$\alpha^2 = \left(1-\frac{2GM}{c^2 r}\right). \tag{2.32}$$

Note that while α corresponds to the lapse function in the $3+1$ formulation of general relativity, the quantity Γ is *not* the Lorentz factor of the gas (which we denote as W) as it is usually defined in numerical relativity (e.g. Banyuls et al. 1997) but is related to it by $W = \Gamma/\alpha$. From (2.29) we also have the relation

$$\frac{\partial U^t}{\partial t} = \frac{U^r}{\alpha^2 \Gamma c^2}\frac{\partial U^r}{\partial t} \tag{2.33}$$

From (2.22), (2.23) and (2.24) using (2.25), (2.27), (2.29) and (2.33) we thus derive the continuity equation,

$$\frac{\partial \rho}{\partial t} + \mathrm{v}^r \frac{\partial \rho}{\partial r} + \frac{\alpha^2 \rho}{\Gamma}\left[\frac{1}{r^2}\frac{\partial}{\partial r}(r^2 U^r) + \frac{U^r}{\alpha^2 \Gamma c^2}\frac{\partial U^r}{\partial t}\right] = 0, \tag{2.34}$$

the equation of motion,

$$\frac{\partial U^r}{\partial t} + \mathrm{v}^r \frac{\partial U^r}{\partial r} + \frac{\Gamma \alpha^2 c^2}{\rho h}\frac{\partial P}{\partial r} + \frac{U^r}{\rho h}\frac{\partial P}{\partial t} + \frac{\alpha^2}{\Gamma}\frac{GM}{r^2} = 0, \tag{2.35}$$

and the internal energy equation,

$$\frac{\partial(\rho u)}{\partial t}+\mathrm{v}^r\frac{\partial(\rho u)}{\partial r}+\frac{\alpha^2}{\Gamma}(P+\rho u)\left[\frac{1}{r^2}\frac{\partial}{\partial r}(r^2U^r)+\frac{U^r}{\alpha^2\Gamma c^2}\frac{\partial U^r}{\partial t}\right]=\frac{\alpha^2}{\Gamma}\rho\Lambda, \tag{2.36}$$

where

$$\mathrm{v}^r\equiv\frac{U^r}{U^t}\equiv\frac{dr}{dt} \tag{2.37}$$

is the velocity in the co-ordinate basis. We define the heating rate per unit mass as

$$\Lambda\equiv T\frac{ds}{d\tau}, \tag{2.38}$$

where T is the temperature, s is the specific entropy and $d\tau$ refers to the local proper time interval (Λ is therefore a local rate of energy input, caused by local physics). A comparison of (2.34), (2.35) and (2.36) with their non-relativistic counterparts (2.1), (2.2) and (2.3) shows that they reduce to the non-relativistic expressions in the limit as $c\to\infty$, and to special relativity as $M\to 0$.

The 'source terms' containing time derivatives of U^r and P are then eliminated between the three equations using the equation of state (2.5) to relate pressure and internal energy. Substituting for pressure in (2.36) and substituting this into (2.35) we obtain the equation of motion in terms of known variables,

$$\frac{\partial U^r}{\partial t}+\frac{\mathrm{v}^r}{X}\left(1-\frac{\gamma P}{\rho h}\right)\frac{\partial U^r}{\partial r}=-\frac{c^2\alpha^4}{\rho h\Gamma X}\frac{\partial P}{\partial r}-\frac{\alpha^2}{\Gamma X}\frac{GM}{r^2}+\frac{\mathrm{v}^r}{X}\frac{\gamma P}{\rho h}\frac{2U^r}{r}-\frac{\mathrm{v}^r}{hX}(\gamma-1)\Lambda, \tag{2.39}$$

where for convenience we define

$$X\equiv 1-\left(\frac{\gamma P}{\rho h}\right)\frac{U^rU^r}{\Gamma^2c^2}, \tag{2.40}$$

and we have expanded the $\frac{1}{r^2}\frac{\partial}{\partial r}(r^2U^r)$ terms in order to combine the spatial derivatives of U^r into one term. We then substitute (2.39) into (2.34) and (2.36) to obtain equations for the density

$$\frac{\partial\rho}{\partial t}+\mathrm{v}^r\frac{\partial\rho}{\partial r}=-\frac{\alpha^2}{\Gamma}\left[\rho A-\frac{\mathrm{v}^r}{h\Gamma X}\frac{\partial P}{\partial r}-\frac{U^rU^r}{\Gamma^2c^2X}\frac{(\gamma-1)}{h}\rho\Lambda\right], \tag{2.41}$$

and internal energy,

$$\frac{\partial(\rho u)}{\partial t}+\mathrm{v}^r\left(1-\frac{\gamma P}{\rho h}\frac{\alpha^2}{\Gamma^2X}\right)\frac{\partial(\rho u)}{\partial r}=-\frac{\alpha^2}{\Gamma}\left[(P+\rho u)A-\left(1+\frac{U^rU^r}{\Gamma^2c^2X}\frac{\gamma P}{\rho h}\right)\rho\Lambda\right]. \tag{2.42}$$

where for convenience we have defined

$$A\equiv\left[1-\frac{U^rU^r}{\Gamma^2c^2X}\left(1-\frac{\gamma P}{\rho h}\right)\right]\frac{\partial U^r}{\partial r}+\left[1+\frac{U^rU^r}{\Gamma^2c^2X}\left(\frac{\gamma P}{\rho h}\right)\right]\frac{2U^r}{r}-\frac{U^r}{\Gamma^2c^2X}\frac{GM}{r^2} \tag{2.43}$$

From the solution specifying U^r we calculate the velocity measured by an observer at rest with respect

to the time slice (referred to as *Eulerian* observers), which is given by

$$\overline{\mathrm{v}}^r = \frac{U^r}{\alpha U^t} = \frac{\mathrm{v}^r}{\alpha}, \tag{2.44}$$

since there are no off-diagonal terms (ie. zero shift vector) in the Schwarzschild solution. For these observers the Lorentz factor is given by

$$W = \left(1 - \frac{\overline{\mathrm{v}}^r \overline{\mathrm{v}}_r}{c^2}\right)^{-1/2}, \tag{2.45}$$

where $\overline{\mathrm{v}}^r \overline{\mathrm{v}}_r = g_{rr} \overline{\mathrm{v}}^r \overline{\mathrm{v}}^r$, such that $U^r = W \overline{\mathrm{v}}^r$.

2.3.2 Scaling

The usual practice in numerical relativity is to scale in so-called geometric units such that $G = M = c = 1$. In these units the length scale would be the geometric radius GM/c^2 and the velocity would have units of c. Instead for the current problem, we adopt a scaling analogous to that of the non-relativistic case, that is we choose the length scale to be the radius of the central object, R_*, where R_* is given as some multiple of the geometric radius, ie.

$$[L] = R_* = n\frac{GM_*}{c^2}, \tag{2.46}$$

with $n \geq 2.0$. The mass scale is again the central object mass $[M] = M_*$ and the timescale is given by

$$[\tau] = \left(\frac{GM_*}{R_*^3}\right)^{-1/2} = n^{3/2}\frac{GM_*}{c^3} \tag{2.47}$$

In these units, velocity is measured in units of $[\mathrm{v}] = n^{-1/2}c$ (or equivalently $c^2 = n$). The scaled equations are thus given simply by setting $G = M = 1$ and $c^2 = n$ everywhere.

This scaling ensures that the relativistic terms tend to zero when c (or n) is large and that the numerical values of ρ, ρu and U^r are of order unity. We thus specify the degree to which the gravity/gas dynamics is relativistic by specifying the value of n (*i.e.* the proximity of the innermost radius, and thus the heating, to the Schwarzschild radius, $R_{\mathrm{Sch}} = 2GM/c^2$). We compute solutions corresponding to gas very close to a black hole (highly relativistic, $n = 2.0$, or $R_* = R_{\mathrm{Sch}}$), neutron star (moderately relativistic, $n = 5$, or $R_* = R_{\mathrm{NS}} = 5GM/c^2$, which is equivalent to heating further out and over a wider region around a black hole) and white dwarf/non-relativistic star (essentially non-relativistic, $n = 5000$, or $R_* = 2500R_{\mathrm{Sch}}$). Note that in the highly relativistic case although we scale the solution to $n = 2.0$ such that the mass, length and time scales (and therefore the units of heating rate, energy etc.) correspond to those at $r = R_{\mathrm{Sch}}$, our numerical grid cannot begin at R_* as it does in the other cases. We therefore set the lower bound on the radial grid to slightly below the heating shell (typically $r = 1.01R_*$ where the heating begins at $1.1R_*$). Note that the above scaling is merely to ensure that the numerical solution is of order unity, since we scale in terms of dimensionless variables to compare with the non-relativistic solution.

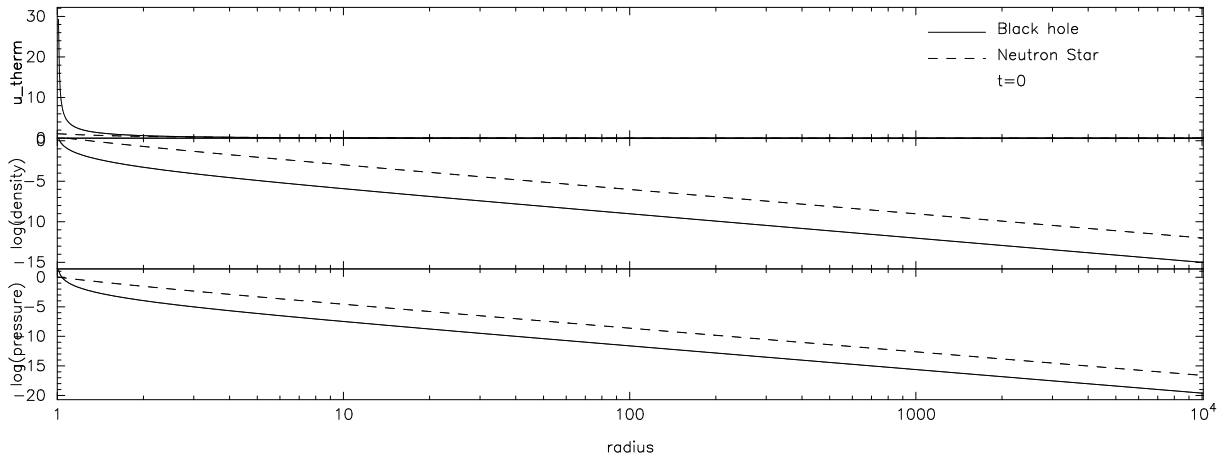

Figure 2.7: The initial conditions for the gas reservoir for the relativistic cases of a neutron star (dashed line) ($R_*/R_{\rm Sch} = 2.5$) and black hole (solid line)($R_*/R_{\rm Sch} = 1.0$). Note, however, that the innermost radius is at $r = 1.01R_*$ in the latter case. We plot profiles of internal energy per unit mass (or temperature), density and pressure, as functions of radius. These quantities are given in units of GM/R_*, M/R_*^3 and $M_*/(R_*t_*^2)$ respectively. Note that steeper gradients are required to hold the gas in hydrostatic equilibrium as the gravitational field becomes more relativistic. The black hole reservoir is of lower density than the neutron star version because of the choice of the polytropic constant (chosen such that the central density is of order unity).

2.3.3 Numerical Solution

In order to solve the relativistic fluid equations numerically we use a method analogous to that used in the non-relativistic case (Figure 2.1). That is, we first compute U^r on the staggered (half) grid and use this to solve for ρ and ρu on the integer grid points. Again the advective terms are discretized using upwind differences (where the 'upwindedness' is determined from the sign of the co-ordinate velocity $\mathbf{v}^r$) and other derivatives are calculated using centred differences. As in the non-relativistic case, where a centred difference is used, the quantities multiplying the derivative are interpolated onto the half grid points if necessary. In equation (2.41) we evaluate the $\partial P/\partial r$ term using upwind differences.

2.3.4 Initial Conditions

We determine initial conditions for the relativistic case by setting $U^r = 0$ and $\partial/\partial t = 0$ in (2.39), from which we have

$$\frac{dP}{dr} = -\frac{\rho h}{c^2}\frac{GM}{r^2}\left(1-\frac{2GM}{c^2 r}\right)^{-1}. \tag{2.48}$$

The pressure is thus calculated as a function of ρ, u and P (where $P = (\gamma-1)\rho u$). We solve (2.48) using the same assumptions as in the non-relativistic case (§2.2.3), that is an adiabatic atmosphere such that

$$P = K\rho^\gamma. \tag{2.49}$$

We therefore have

$$\frac{d\rho}{dr} = -\frac{1}{\gamma K\alpha^2}\left[\rho^{(2-\gamma)} + \frac{\gamma K\rho}{c^2(\gamma-1)}\right]\frac{GM}{r^2}, \tag{2.50}$$

which we solve using a first order (Euler) discretization to obtain a density profile. The pressure may then be calculated using (2.49), however to ensure that hydrostatic equilibrium is enforced numerically we solve (2.48) using the same discretization as in the fluid equations, integrating inwards from the outer boundary condition $P(r_{\rm max}) = K\rho(r_{\rm max})^\gamma$. However in this case the pressure gradient also depends on the pressure, so we use the pressure calculated from (2.49) to calculate the initial value of the specific enthalpy h and iterate the solution until converged ($[P^{n+1} - P^n]/P^n < 10^{-10}$). In the black hole case the resulting pressure differs from that found using (2.49) by $\Delta P/P \sim 10^{-2}$. We choose K such that the central density is of order unity – typically we use $K = 10\gamma/(\gamma-1)$ in the black hole case. Note that changing K simply changes the amount of matter present in the atmosphere but does not affect the temperature scaling and does not affect the final results (although it significantly affects the integration time since it determines the strength of the shock front and the amount of mass to be accelerated).

Initial conditions calculated in this manner for the black hole ($R_*/R_{\rm Sch} = n/2 = 1.0$) and neutron star ($R_*/R_{\rm Sch} = 2.5$) atmospheres are shown in Figure 2.7. The initial setup reduces to that of Figure 2.2 in the non-relativistic limit when the same value of K is used. We set the outer boundary at $r/R_* = 10^4$, using 1335 radial grid points (again on a logarithmic grid).

2.3.5 Results

The results of a typical (n=2.0) relativistic simulation are shown in Figure 2.8 at $t = 1000$. Again we observe that the wind structure reaches a quasi-steady state, with the velocity approaching a steady value at large radii. Note that because the steady state density is higher than that of the surrounding medium no wide shock front is observed.

Plotting the mass outflow rate $\dot{M} = 4\pi r^2 \rho U^r$ and the relativistic Bernoulli energy $E_{\rm rel} = \frac{1}{2}\Gamma^2 h^2/c^2 - \frac{1}{2}c^2$ (see e.g. Shapiro and Teukolsky 1983) as a function of radius (Figure 2.9), we see that indeed the structure approaches that of a steady (relativistic) wind (that is, the energy and $\dot{M}$ profiles are flat above the heating zone). We may thus apply a relativistic steady wind solution with this Bernoulli energy as an initial value to determine the final velocity and Lorentz factor as $r \to \infty$. Note that we cannot apply a non-relativistic steady wind solution because although the gravity is non-relativistic, the outflow velocities are not. As in the non-relativistic case the final wind velocity is determined by the steady Bernoulli energy, since in this case as $r \to \infty$, $E_{\rm rel} \to \frac{1}{2}[(U^r)^2 - c^2]$.

2.3.6 Steady wind solution

Relativistic, steady state ($\partial/\partial t = 0$) winds were first studied by Michel (1972) and extended to include energy deposition by Flammang (1982). The problem has recently received attention in the context of neutrino-driven winds in gamma-ray burst models by Pruet et al. (2001) and Thompson et al. (2001). We proceed in a manner analogous to that of the non-relativistic solution. Setting $\partial/\partial t = 0$ the continuity (2.22) and momentum (2.23) equations become

$$\frac{1}{\rho}\frac{\partial \rho}{\partial r} + \frac{1}{U^r}\frac{\partial U^r}{\partial r} + \frac{2}{r} = 0 \tag{2.51}$$

$$U^r \frac{\partial U^r}{\partial r} + \frac{\Gamma^2 c^2}{\rho h}\frac{\partial P}{\partial r} + \frac{GM}{r^2} = 0 \tag{2.52}$$

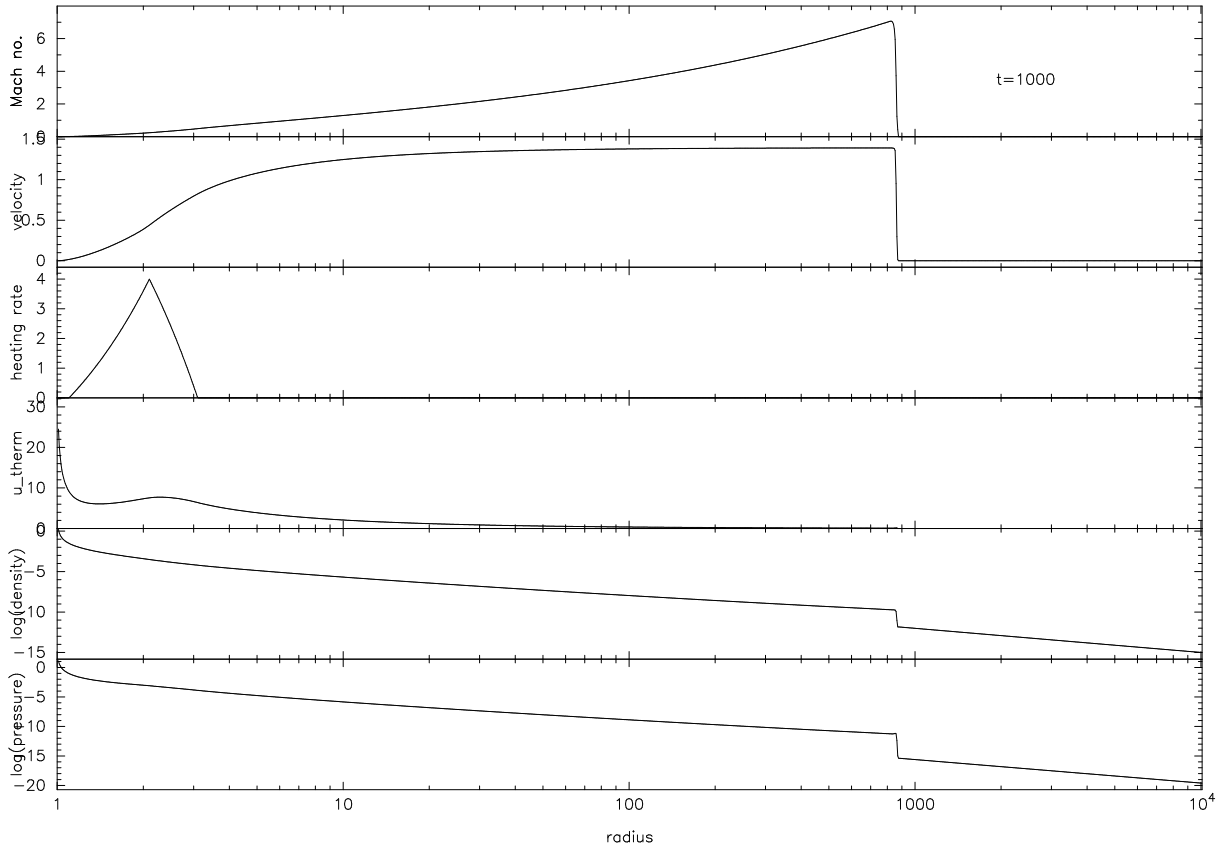

Figure 2.8: Results of a typical black hole relativistic simulation at t=1000 (where units of time are the dynamical time at the central object). Quantities shown are the Mach number (v/c_s), velocity for Eulerian observers ($\bar{v}$), heating rate (Λ), internal energy per unit mass ($u \equiv u_{\rm therm}$), log(density) and log(pressure). Units of velocity are such that $c = \sqrt{2}$ and as in the non-relativistic case energy has units of GM/R_*.

where (2.51) is equivalent to

$$r^2 \rho U^r = \text{const.} \tag{2.53}$$

Combining (2.52) and (2.51) we obtain

$$\frac{1}{U^r}\left[(U^r)^2 - \frac{c^2\Gamma^2 c_s^2}{h\gamma}\right]\frac{\partial U^r}{\partial r} = -\frac{c^2\Gamma^2}{h\gamma}\frac{dc_s^2}{dr} + \frac{c^2\Gamma^2}{h\gamma}\frac{2c_s^2}{r} - \frac{GM}{r^2}, \tag{2.54}$$

where $c_s^2 = \gamma P/\rho$ and $(U^r)^2 \equiv U^r U^r$. From the first law of thermodynamics and (2.52) we derive the relativistic Bernoulli equation in the form

$$\frac{d}{dr}\left(\frac{1}{2}\frac{\Gamma^2 h^2}{c^2}\right) = \frac{h\Gamma^2}{c^2}\frac{dQ}{dr}, \tag{2.55}$$

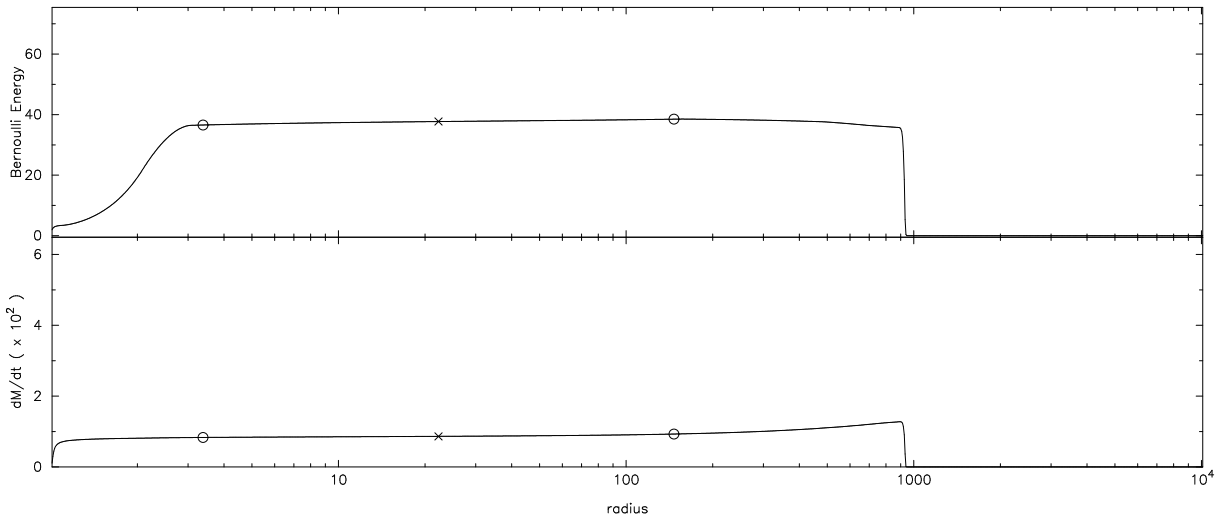

Figure 2.9: The relativistic Bernoulli energy $E_{\rm rel} = \frac{1}{2}\Gamma h/c^2 - \frac{1}{2}c^2$(top) and mass outflow rate $\dot{M} = 4\pi r^2 \rho U^r$ (bottom) in the time-dependent relativistic wind solution with a reasonably high heating rate are shown as functions of radius at time $t = 1000$. In order to match this solution to a steady outflow solution, the Bernoulli energy is assumed to be constant over the region indicated by the two circles, and the steady wind solution is computed using initial values at the point indicated by a cross.

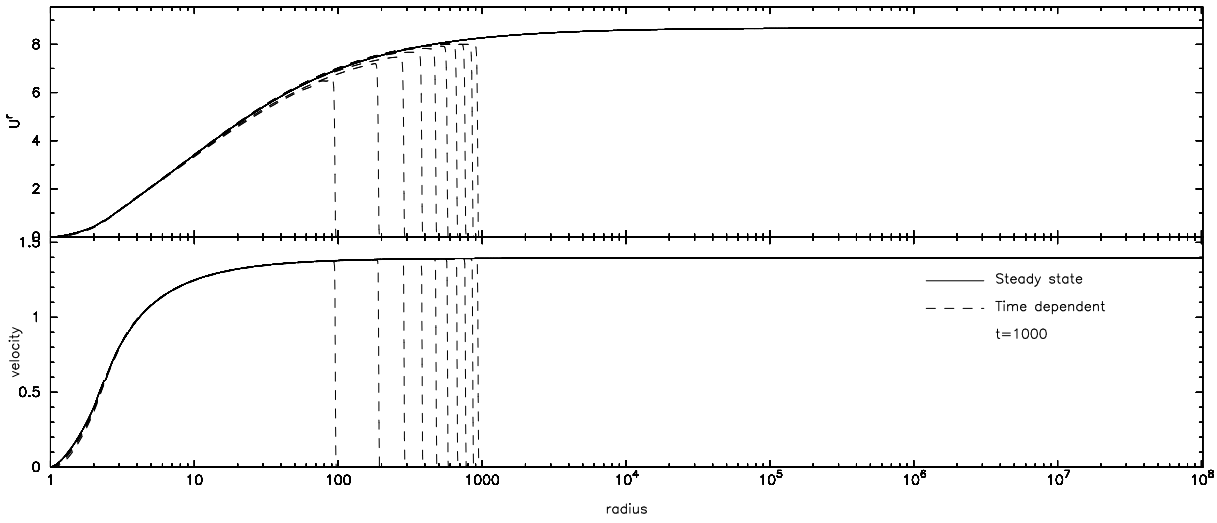

Figure 2.10: The radial profiles of the steady wind r-component of four velocity U^r (top panel) and of the velocity for Eulerian observers $\overline{v}$ (centre panel) are compared to the time-dependent solution (plotted every 100 dynamical times) for a typical relativistic calculation for the black hole (n=2.0) case. Units are such that $c = \sqrt{2}$ on the velocity plots. Note the excellent agreement between the two solutions.

such that both sides reduce to their non-relativistic expressions as $c \to \infty$. The quantity dQ/dr is the local heating gradient as in the non-relativistic case. Expanding this equation we find

$$\frac{dc_s^2}{dr} = (\gamma - 1)\left[\frac{dQ}{dr} - \frac{h}{c^2\Gamma^2}\frac{d}{dr}\left(\frac{1}{2}(U^r)^2\right) - \frac{h}{c^2\Gamma^2}\frac{GM}{r^2}\right]. \tag{2.56}$$

Combining (2.56) and (2.54) and manipulating terms, we obtain an equation for $(U^r)^2$,

$$\frac{d}{dr}(U^r)^2 = \frac{2(U^r)^2}{[(U^r)^2 - c^2\Gamma^2 c_s^2/h]}\left[\frac{c^2\Gamma^2}{h}\frac{2c_s^2}{r} - (\gamma-1)\frac{c^2\Gamma}{h}\left(\Gamma\frac{dQ}{dr}\right) - \frac{GM}{r^2}\right], \tag{2.57}$$

where c_s^2 and $h = c^2 + c_s^2/(\gamma-1)$ are given functions of known variables by integration of the Bernoulli equation (2.55), in the form

$$\frac{d}{dr}(\Gamma h) = \Gamma\frac{dQ}{dr}, \tag{2.58}$$

to ensure that h does not appear in the heating term on the right hand side. The integration is then

$$e(r) = \Gamma h = e(r_\infty) - \int_r^{r_\infty}\left\{\Gamma\frac{dQ}{dr}\right\}dr, \tag{2.59}$$

and hence

$$h = \frac{e(r)}{\Gamma}, \quad c_s^2 = (\gamma-1)(h-c^2). \tag{2.60}$$

The 'heating gradient', $\Gamma dQ/dr$, is calculated from the time-dependent solution using

$$\Gamma\frac{dQ}{dr}(r) = \frac{\alpha(r)\Lambda(r)}{\bar{v}(r)}, \tag{2.61}$$

since

$$\Lambda \equiv T\frac{ds}{d\tau} \equiv \frac{dQ}{d\tau} = U^t\left(\frac{\partial Q}{\partial t} + v^r\frac{dQ}{dr}\right), \tag{2.62}$$

where τ is the proper time and $U^t = \Gamma/\alpha^2$. The velocity profile for an Eulerian observer is then calculated using (2.44) and the final Lorentz factor W_∞ using equation (2.45). As in the non-relativistic case we choose a starting point for the integration above the heating shell and integrate outwards from this point using a fourth order Runge-Kutta integrator in order to determine the terminal Lorentz factor. The inward integration (and thus the determination of the steady state heating gradient $\Gamma dQ/dr$) is computed only for consistency. We integrate through the singular point in equation (2.57) by taking a low order integration with larger steps as this point is approached.

The solution calculated using (2.57) is shown in Figure 2.10 plotted against the evolving time-dependent solution. The profiles are in excellent agreement, verifying the accuracy of the relativistic calculation and showing that the wind may indeed be described by the steady state solution.

2.3.7 Terminal wind velocities and Lorentz factors as a function of heating rate

In order to compare the relativistic results to those in the Newtonian regime, we define the local canonical heating rate in a similar manner to the non-relativistic case, that is

$$\Lambda_c(r) = \frac{\Delta E}{\Delta t}, \tag{2.63}$$

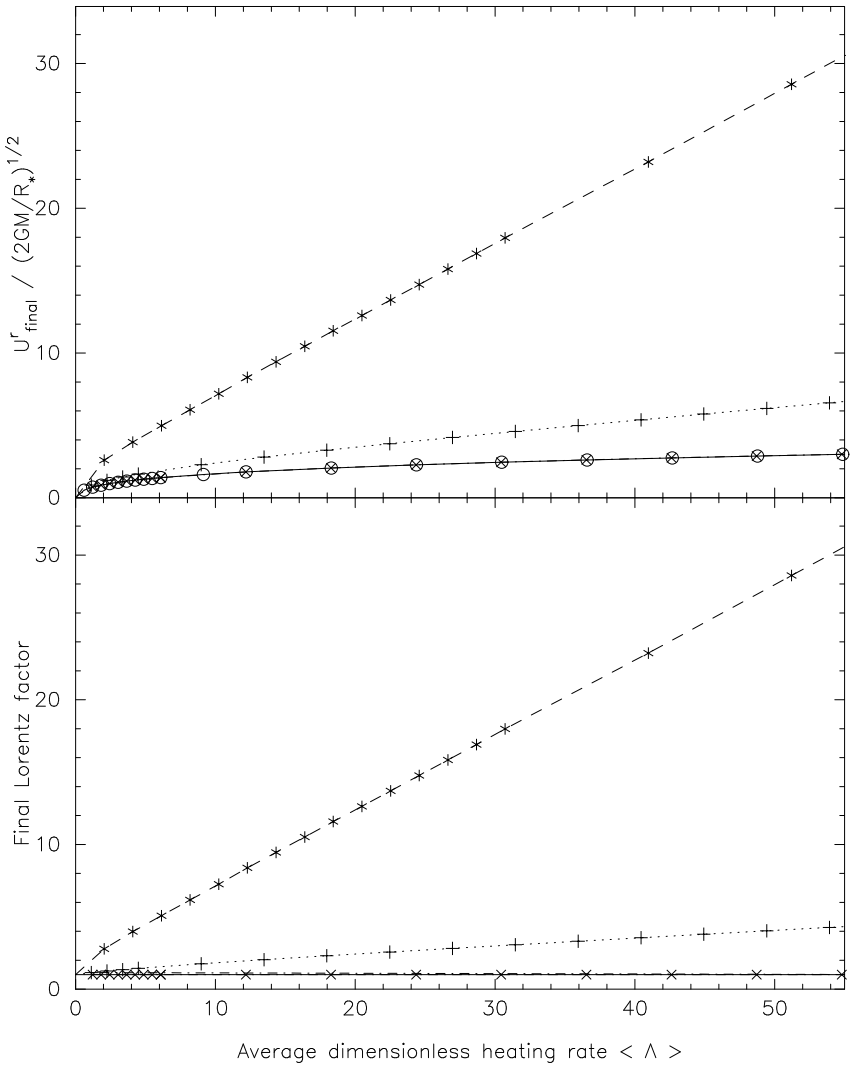

Figure 2.11: The terminal r-component of four velocity U^r (top panel) and Lorentz factor (bottom panel) of the wind in the non-relativistic ($\circ$, solid), white dwarf ($\times$, dot-dashed), neutron star ($+$, dotted) and black hole ($*$, dashed) cases, is plotted as a function of the dimensionless heating rate defined in §2.2.6. The top panel may be compared with Figure 2.6 in the non-relativistic case.

for some relevant energy ΔE and some relevant timescale Δt. As in Section 2.2.6 we take the canonical energy per unit mass, ΔE, to be the energy released locally by bringing to rest a particle of unit mass which is orbiting in a circular orbit at radius r. For a particle orbiting in the Schwarzschild metric this is the difference, ΔE, between the energy constants (defined by the timelike Killing vector) of a circular geodesic at radius r, and a radial geodesic with zero velocity at radius r. This implies (see, for example, Schutz 1985, Chapter 11)

$$\Delta E/c^2 = \frac{1-2GM/rc^2}{[1-3GM/rc^2]^{1/2}} - [1-2GM/rc^2]^{1/2}. \tag{2.64}$$

In the Newtonian limit, this reduces to the expected value $\Delta E = \frac{1}{2}v_\phi^2 = GM/2r$. We again take the canonical timescale on which the energy is released to be the orbital timescale at radius r as measured by a local stationary observer. For a circular geodesic in the Schwarzschild metric, the azimuthal velocity is

given in terms of coordinate time, t, by

$$d\phi/dt = \Omega = (GM/r^3)^{1/2}. \tag{2.65}$$

This is the same expression as for the angular velocity of an orbiting particle in the Newtonian limit. But in terms of the proper time, τ, of a local stationary observer we have, from the metric,

$$d\tau/dt = (1 - 2GM/rc^2)^{1/2}, \tag{2.66}$$

and thus $d\phi/d\tau = \Omega_o$, where

$$\Omega_o^2 = \frac{GM}{r^3}\left[1 - \frac{2GM}{rc^2}\right]^{-1}. \tag{2.67}$$

Using this, the local canonical heating rate is therefore given by

$$\Lambda_c = \Delta E \times \Omega_o. \tag{2.68}$$

In the Newtonian limit, $r \gg 2GM/c^2$, this becomes as expected $\Lambda_c \simeq (GM)^{3/2}/2r^{5/2}$. As in the non-relativistic case we use the canonical heating rate derived above to define a dimensionless heating rate $\langle\Lambda\rangle$ as an appropriate volume average using equation (2.21).

The final Lorentz factor of the wind plotted as a function of this dimensionless heating rate is given in the bottom panel of Figure 2.11 in the highly relativistic (black hole), moderately relativistic (neutron star, equivalent to a broader heating shell further away from a black hole) and non-relativistic (white dwarf) cases.

We would also like to make a meaningful comparison of the final wind velocities in units of the escape velocity from the star. Note that we cannot simply compare the scaled velocities since we are in effect introducing a 'speed limit' in the relativistic solution such that the (scaled) relativistic velocity will always be slower than in the equivalent non-relativistic solution. Rather, we compare the 'momentum per unit mass', which in the relativistic case is given by the four velocity $U^r = dr/d\tau$ (in special relativity this is given by $U^r = \gamma v^r$, where γ is the Lorentz factor). Scaling this in units of the (Newtonian) escape velocity from the central object $(2GM/R_*)^{1/2}$ we can make a useful comparison with the non-relativistic results in terms of the actual energy input. This velocity is plotted in the top panel of Figure 2.11 against the dimensionless heating rate and is clearly higher in the relativistic case. The non-relativistic results correspond to those shown in Figure 2.6.

2.4 Discussion and Conclusions

In this chapter we have considered the injection of energy at a fixed radius into an initially hydrostatic atmosphere as a simple model of the acceleration process in both non-relativistic and relativistic jets. The problem is inherently time-dependent since the velocity is zero at the base of the atmosphere. We have therefore used time-dependent gas dynamics. In order to determine the terminal velocity of the resulting outflow we have used the fact that if the mass in the outflow is small compared to the initial mass reservoir then the outflow will reach an approximate steady state. Once the gas in the time-dependent solution has

evolved to a sufficiently large radius we are therefore able to match the solution to a steady-state wind profile (with a heating term) in order to determine the solution at infinity. The resulting terminal velocities and corresponding Lorentz factors are shown in Figures 2.6 and 2.11.

The first point to note, from the top panel of Figure 2.11 is that the dimensionless energy (or momentum) imparted to the gas is clearly larger in the relativistic case. The resulting outflow velocities also scale linearly with heating rate in this case, whereas in the non-relativistic case the relative increase in the outflow velocity becomes smaller as the heating rate becomes larger. These effects can be understood by considering the effect of the relativity in imposing a speed-limit on the gas as it travels through the (fixed) heating shell. In the non-relativistic case, as the gas is accelerated to higher velocities the time spent in the heating zone also becomes smaller, resulting in the tail-off in the terminal velocity with increasing heating rate. In the relativistic case, once the gas has been accelerated to close to the speed of light, the time spent in the heating zone remains constant ($\sim c$) and consequently the total energy imparted to the outflow scales linearly with dimensionless heating rate $\langle\Lambda\rangle$.

From Figure 2.6 we see that a dimensionless heating rate of $\langle\Lambda\rangle \simeq 17$ gives rise to a terminal outflow velocity of $v_{jet} \simeq 2v_{esc}$ in a Newtonian potential. For the same heating rate, in Figure 2.11, we see that the 'neutron star' wind, for which the heating rate peaks at about 5.2 R_{Sch} becomes mildly relativistic ($\gamma_{jet} \sim 2$), whereas the 'black hole' wind, for which the heating rate peaks at about 2.1 R_{Sch}, leads to an outflow with $\gamma_{jet} \simeq 11$. Similarly a dimensionless heating rate of $\langle\Lambda\rangle \simeq 55$ gives rise to a terminal velocity of $v_{jet} \simeq 3v_{esc}$ in the Newtonian case, to an outflow with $\gamma_{jet} \sim 4$ in the mildly relativistic case, and to an outflow with $\gamma_{jet} \simeq 31$ in the strongly relativistic case. We have already noted (§2.2.6) that although the exact numerical values here do depend slightly on the exact definition of the dimensionless heating rate, the basic results remain unchanged. For example, using the Newtonian dimensionless heating rate (§2.2.6) in the strongly relativistic case gives a Lorentz factor of $\gamma_{jet} \simeq 5$ for the rate which corresponds to $v_{jet} \simeq 2v_{esc}$ in the non-relativistic case.

It must be cautioned that this analysis does not assume that all of the physical processes in the jet acceleration process have been properly represented (for example the process by which the energy is transferred from rotational energy in the disk into kinetic energy in the outflow is clearly magnetic in nature), nor that all of these physical processes should be identical between the various classes of jet. It is evident that more detailed physical models need to be developed before further conclusions can be drawn. Nevertheless, the generic nature of the analysis presented in this chapter suggests that some conclusions into the physical processes involved in the jet acceleration process can be drawn.

On the basis of the simple physical models constructed in this chapter, therefore, it seems not unreasonable to suggest that the relativistic jets observed in AGN are simply scaled-up versions of their non-relativistic (YSO) counterparts and that the intrinsic acceleration process is the same in both classes of object. For this to be the case, two further conditions must also hold. The first is that jet acceleration must occur close to the central gravitating object, in order to make use of the speed of light as a limiting velocity in the black hole case. The second is that, since the dimensionless heating rates required are much larger than unity, the energy released in the outflow must be imparted to only a small fraction of the available accreting material.

"I went on to test the program in every way I could devise. I strained it to expose its weaknesses. I ran it for high-mass stars and low-mass stars, for stars born exceedingly hot and those born relatively cold. I ran it assuming the superfluid currents beneath the crust to be absent – not because I wanted to know the answer, but because I had developed an intuitive feel for the answer in this particular case. Finally I got a run in which the computer showed the pulsar's temperature to be less than absolute zero. I had found an error. I chased down the error and fixed it. Now I had improved the program to the point where it would not run at all."

Frozen Star: Of Pulsars, Black Holes and the Fate of Stars
GEORGE GREENSTEIN

3

Smoothed Particle Hydrodynamics

3.1 Introduction

The standard approach to solving the equations of fluid dynamics numerically is to define fluid quantities on a regular spatial grid, computing derivatives using finite difference or finite volume schemes. This is an extremely well studied approach and most 'state of the art' methods for fluid dynamics have been developed in this manner. In astrophysical fluid dynamics problems frequently involve changes in spatial, temporal and density scales over many orders of magnitude. Thus, adaptivity is an essential ingredient which is absent from a fixed-grid approach. Progress in this area has been rapid in recent years with the development of procedures for adaptive mesh refinement (AMR). The implementation of such procedures is far from trivial, although the availability of libraries and toolkits for grid-based codes eases this burden somewhat. However, a further constraint is that astrophysical problems are frequently asymmetric which can result in substantial numerical diffusion when solving on (fixed or adaptive) Cartesian grids. Other approaches to this problem are to use unstructured grids (where typically the grid is reconstructed at each new timestep) or Lagrangian grid methods, where the grid shape deforms according to the flow pattern.

An alternative to all of these methods is to remove the spatial grid entirely, resulting in methods which are inherently adaptive. In this approach fluid quantities are carried by a set of moving interpolation points which follow the fluid motion. Since each point carries a fixed mass, the interpolation points are referred to as 'particles'. Derivatives are evaluated either by interpolation over neighbouring particles (referred to as particle methods), or via a hybrid approach by interpolation to an overlaid grid (referred to as particle-mesh methods, typified by the particle-in-cell (PIC) method used extensively in plasma physics.

Smoothed Particle Hydrodynamics (SPH) is a particle method introduced by Lucy (1977) and Gingold and Monaghan (1977). It has found widespread use in astrophysics due to its ability to tackle a

wide range of problems involving complex, asymmetric phenomena with relative ease. Since these features are highly desirable in many non-astrophysical applications, it is unsurprising that SPH is currently finding many applications in other fields such as geophysics and engineering (and even film-making[1]).

The advantages of SPH over standard grid based approaches can be summarised as follows: Firstly, SPH is conceptually both simple and beautiful. All of the equations can be derived self-consistently from physical principles with a few basic assumptions. As a result complex physics is relatively simple to incorporate. Its simplicity means that for the user it is a very intuitive numerical method which lends itself easily to problem-specific modifications. Secondly, adaptivity is a built-in feature. The Lagrangian nature of the method means that changes in density and flow morphology are automatically accounted for without the need for mesh refinement or other complicated procedures. As a result of its adaptivity, SPH is also very efficient in that resolution is concentrated on regions of high density, whilst computational effort is not wasted on empty regions of space. Thirdly, free boundaries, common in astrophysical problems, are simple and natural in SPH but often present difficulties for grid-based codes (such as spurious heating from the interaction with a low density surrounding medium). This means that no portions of fluid can be lost from the simulation, unlike in a grid based code where fluid which has left the grid cannot return (this has been dubbed the 'Columbus effect' by Melvyn Davies, since fluid can fall off the edge of the world). Fourthly, a significant advantage in an astrophysical context is that SPH couples naturally with widely used N-Body codes and techniques, for which there exists a vast amount of literature. Finally (although perhaps many more advantages could be given) visualisation and analysis is also somewhat easier with Lagrangian techniques, since it is a simple matter to track and visualise portions of the flow.

SPH also has a number of disadvantages when compared to finite difference codes. The first of these is that, unlike grid-based codes, SPH involves the additional computational cost of constructing the neighbour lists. This is offset somewhat in that N-Body techniques used to calculate the gravitational force (namely via tree-codes) can also be used in constructing the neighbour lists. Secondly, SPH suffers from a lack of algorithm development, since a vast amount of research effort is focussed on finite difference or finite volume techniques. This often means that such techniques, although often applicable in an SPH context, can be slow to filter into mainstream use. Thirdly, although not a disadvantage as such but a point which is often overlooked, is that the setup of initial conditions is often more complicated and requires much greater care. Since particles can be laid down in an infinite variety of ways, choosing an appropriate setup for a given problem requires some experience and usually some experimentation. Inappropriate particle setups can lead to poorer simulation results than might otherwise be expected (we give some examples of this in §3.7.5). Finally, in the case of magnetohydrodynamics and other problems involving anisotropic stresses (as we will discuss in chapter 4), numerical stability can become an issue which must be dealt with appropriately.

In this chapter we provide an overview of the SPH method, including several improvements to the basic method which have been made since the review article of Monaghan (1992) was published (such as improvements in shock-capturing techniques and the treatment of terms related to the use of a variable smoothing length). In particular we focus on those aspects of the algorithm that are relevant in an MHD context. The chapter is organised as follows: In section §3.2 we present the basic formalisms inherent to

[1] for example many of the graphics involving fluids in the film 'Tomb Raider' were computed using SPH

SPH; in §3.3 we derive the SPH equations for compressible hydrodynamics using a variational principle. Formulations of dissipative terms used to capture shocks are presented and discussed in §3.5. In §3.3.4 we discuss the incorporation of terms relating to the spatial variation of the smoothing length and in §3.4 alternative formulations of SPH are examined within the variational framework. Timestepping is discussed in §3.6. Finally, we present numerical tests in §3.7 in support of the previous sections and as preliminaries for the MHD tests described in Chapters 4 and 5.

3.2 Basic formalisms

3.2.1 Interpolant

The basis of the SPH approach is given as follows (Monaghan, 1992). We begin with the trivial identity[2]

$$A(\mathbf{r}) = \int A(\mathbf{r}')\delta(|\mathbf{r}-\mathbf{r}'|)d\mathbf{r}', \tag{3.1}$$

where A is any variable defined on the spatial co-ordinates $\mathbf{r}$ and δ refers to the Dirac delta function. This integral is then approximated by replacing the delta function with a smoothing kernel W with characteristic width h, such that

$$\lim_{h\to 0} W(\mathbf{r}-\mathbf{r}',h) = \delta(\mathbf{r}-\mathbf{r}'), \tag{3.2}$$

giving

$$A(\mathbf{r}) = \int A(\mathbf{r}')W(|\mathbf{r}-\mathbf{r}'|,h)d\mathbf{r}' + O(h^2). \tag{3.3}$$

The kernel function is normalised according to

$$\int W(\mathbf{r}-\mathbf{r}',h)\mathrm{d}\mathbf{r}' = 1. \tag{3.4}$$

Finally the integral (3.3) is discretised onto a finite set of interpolation points (the particles) by replacing the integral by a summation and the mass element ρdV with the particle mass m, ie.

$$\begin{aligned} A(\mathbf{r}) &= \int \frac{A(\mathbf{r}')}{\rho(\mathbf{r}')}W(|\mathbf{r}-\mathbf{r}'|,h)\rho(\mathbf{r}')d\mathbf{r}' + O(h^2), \\ &\approx \sum_{b=1}^{N} m_b \frac{A_b}{\rho_b} W(|\mathbf{r}-\mathbf{r}_b|,h), \end{aligned} \tag{3.5}$$

where the subscript b refers the quantity evaluated at the position of particle b. This 'summation interpolant' is the basis of all SPH formalisms. The errors introduced in this step are discussed in §3.2.2. Gradient terms may be calculated by taking the analytic derivative of (3.5), giving

$$\nabla A(\mathbf{r}) = \frac{\partial}{\partial \mathbf{r}} \int \frac{A(\mathbf{r}')}{\rho(\mathbf{r}')}W(|\mathbf{r}-\mathbf{r}'|,h)\rho(\mathbf{r}')d\mathbf{r}' + O(h^2), \tag{3.6}$$

[2] It is interesting to note that this equation, with $A=\rho$ is used to define the density of the fluid in terms of the Lagrangian co-ordinates in the Hamiltonian description of the ideal fluid (eq. (94) in Morrison, 1998). Similarly the SPH equivalent of this expression, (3.42), forms the basis for the Hamiltonian description of SPH (see §3.3.2).

$$\approx \sum_b m_b \frac{A_b}{\rho_b} \nabla_a W_{ab}, \tag{3.7}$$

where we have assumed that the gradient is evaluated at another particle a (ie. $\mathbf{r} = \mathbf{r}_a$), defining $\nabla_a \equiv \frac{\partial}{\partial \mathbf{r}_a}$ and $W_{ab} \equiv W(|\mathbf{r}_a - \mathbf{r}_b|, h)$.

3.2.2 Errors

The errors introduced by the approximation (3.3) can be estimated by expanding $A(\mathbf{r}')$ in a Taylor series about $\mathbf{r}$ (Benz, 1990; Monaghan, 1992), giving

$$\begin{aligned} A(\mathbf{r}) &= \int \left[A(\mathbf{r}) + (\mathbf{r}' - \mathbf{r})^\alpha \frac{\partial A}{\partial \mathbf{r}^\alpha} + \frac{1}{2}(\mathbf{r}' - \mathbf{r})^\beta (\mathbf{r}' - \mathbf{r})^\gamma \frac{\partial^2 A}{\partial \mathbf{r}^\beta \partial \mathbf{r}^\gamma} + \mathscr{O}((\mathbf{r} - \mathbf{r}')^3) \right] W(|\mathbf{r} - \mathbf{r}'|, h) \mathrm{d}\mathbf{r}', \\ &= A(\mathbf{r}) + \frac{\partial A}{\partial \mathbf{r}^\alpha} \int (\mathbf{r}' - \mathbf{r})^\alpha W(r) \mathrm{d}\mathbf{r}' + \frac{1}{2} \frac{\partial^2 A}{\partial \mathbf{r}^\beta \partial \mathbf{r}^\gamma} \int (\mathbf{r}' - \mathbf{r})^\beta (\mathbf{r}' - \mathbf{r})^\gamma W(r) \mathrm{d}\mathbf{r}' + \mathscr{O}[(\mathbf{r}' - \mathbf{r})^3], \end{aligned} \tag{3.8}$$

where $r \equiv |\mathbf{r}' - \mathbf{r}|$; α, β and γ are indices denoting co-ordinate directions (with repeated indices implying a summation) and we have used the normalisation condition (3.4). The odd error terms are zero if W is an even function of $(\mathbf{r} - \mathbf{r}')$ (ie. depending only on its magnitude), which, since $|\mathbf{r} - \mathbf{r}'|$ is always less than the smoothing radius ($2h$ in most cases), results in an approximation to $\mathscr{O}(h^2)$. In principle it is also possible to construct kernels such that the second moment is also zero, resulting in errors of $\mathscr{O}(h^4)$ (discussed further in §3.2.7). The disadvantage of such kernels is that the kernel function becomes negative in some part of the domain, resulting in a potentially negative density evaluation. The errors in the summation interpolant differ slightly since the approximation of integrals by summations over particles no longer guarantees that these terms integrate exactly. Starting from the summation interpolant evaluated on particle a, we expand A_b in a Taylor series around $\mathbf{r}_a$, giving

$$\sum_b m_b \frac{A_b}{\rho_b} W_{ab} = A_a \sum_b \frac{m_b}{\rho_b} W_{ab} + \nabla A_a \cdot \sum_b \frac{m_b}{\rho_b} (\mathbf{r}_b - \mathbf{r}_a) W_{ab} + \mathscr{O}[(\mathbf{r}_b - \mathbf{r}_a)^2]. \tag{3.9}$$

From this we see that the summation interpolation is exact for constant functions only when the interpolant is normalised by dividing by the interpolation of unity. In practical calculations the summation interpolant is only used in the density evaluation (§3.3.1), resulting in a slight error in the density value. More important are the errors resulting from the SPH evaluation of derivatives, since these are used throughout in the discretisation of the fluid equations (§3.3).

The errors resulting from the gradient evaluation (3.6) may be estimated in a similar manner by again expanding $A(\mathbf{r}')$ in a Taylor series about $\mathbf{r}$, giving

$$\begin{aligned} \nabla A(\mathbf{r}) &= \int \left[A(\mathbf{r}) + (\mathbf{r}' - \mathbf{r})^\alpha \frac{\partial A}{\partial \mathbf{r}^\alpha} + \frac{1}{2}(\mathbf{r}' - \mathbf{r})^\beta (\mathbf{r}' - \mathbf{r})^\gamma \frac{\partial^2 A}{\partial \mathbf{r}^\beta \partial \mathbf{r}^\gamma} + \mathscr{O}[(\mathbf{r} - \mathbf{r}')^3] \right] \nabla W(|\mathbf{r} - \mathbf{r}'|, h) d\mathbf{r}', \\ &= A(\mathbf{r}) \int \nabla W d\mathbf{r}' + \frac{\partial A}{\partial \mathbf{r}^\alpha} \int (\mathbf{r}' - \mathbf{r})^\alpha \nabla W \mathrm{d}\mathbf{r}' + \frac{1}{2} \frac{\partial^2 A}{\partial \mathbf{r}^\beta \partial \mathbf{r}^\gamma} \int (\mathbf{r}' - \mathbf{r})^\beta (\mathbf{r}' - \mathbf{r})^\gamma \nabla W \mathrm{d}\mathbf{r}' + \mathscr{O}[(\mathbf{r}' - \mathbf{r})^3], \\ &= \nabla A(\mathbf{r}) + \frac{1}{2} \frac{\partial^2 A}{\partial \mathbf{r}^\beta \partial \mathbf{r}^\gamma} \int (\mathbf{r}' - \mathbf{r})^\beta (\mathbf{r}' - \mathbf{r})^\gamma \nabla W(r) \mathrm{d}\mathbf{r}' + \mathscr{O}[(\mathbf{r}' - \mathbf{r})^3], \end{aligned} \tag{3.10}$$

where we have used the fact that $\int \nabla W d\mathbf{r}' = 0$ for even kernels, whilst the second term integrates to unity for even kernels satisfying the normalisation condition (3.4). The resulting errors in the integral

interpolant for the gradient are therefore also of $\mathscr{O}(h^2)$. The errors in the summation interpolant for the gradient (3.7) are given by expanding A_b in a Taylor series around $\mathbf{r}_a$, giving

$$\begin{aligned}\nabla A_a &= \sum_b m_b \frac{A_b}{\rho_b}\nabla_a W_{ab}, \\ &= A_a \sum_b \frac{m_b}{\rho_b}\nabla_a W_{ab} + \frac{\partial A_a}{\partial \mathbf{r}^\alpha}\sum_b \frac{m_b}{\rho_b}(\mathbf{r}_b-\mathbf{r}_a)^\alpha \nabla_a W_{ab} \\ &\qquad + \frac{1}{2}\frac{\partial^2 A_a}{\partial \mathbf{r}^\beta \partial \mathbf{r}^\gamma}\sum_b \frac{m_b}{\rho_b}(\mathbf{r}_b-\mathbf{r}_a)^\beta(\mathbf{r}_b-\mathbf{r}_a)^\gamma \nabla_a W_{ab} + \mathscr{O}[(\mathbf{r}_b-\mathbf{r}_a)^3]. \end{aligned} \tag{3.11}$$

where the summations represent SPH approximations to the integrals in the second line of (3.10).

3.2.3 First derivatives

From (3.11) we immediately see that a straightforward improvement to the gradient estimate (3.7) can be obtained by a simple subtraction of the first error term (i.e. the term in (3.11) that is present even in the case of a constant function), giving (Monaghan, 1992)

$$\nabla A_a = \sum_b m_b \frac{(A_b - A_a)}{\rho_b}\nabla_a W_{ab}, \tag{3.12}$$

which is an SPH estimate of

$$\nabla A(\mathbf{r}) = \nabla A - A(\nabla 1). \tag{3.13}$$

Since the first error term in (3.11) is removed, the interpolation is exact for constant functions and indeed this is obvious from the form of (3.12). The interpolation can be made exact for linear functions by dividing by the summation multiplying the first derivative term in (3.11), ie.

$$\frac{\partial A_a}{\partial \mathbf{r}^\alpha} = \chi_{\alpha\beta}\sum_b \frac{m_b}{\rho_b}(A_b - A_a)\nabla^\beta W_{ab}, \qquad \chi_{\alpha\beta} = \left[\sum_b \frac{m_b}{\rho_b}(\mathbf{r}_b-\mathbf{r}_a)^\alpha \nabla^\beta W_{ab}\right]^{-1}. \tag{3.14}$$

where $\nabla^\beta \equiv \partial/\partial \mathbf{r}^\beta$. This normalisation is somewhat cumbersome in practice, since χ is a matrix quantity, requiring considerable extra storage (in three dimensions this means storing $3\times 3 = 9$ extra quantities for each particle) and also since calculation of this term requires prior knowledge of the density. However, for some applications of SPH (e.g. solid mechanics) it is desirable to do so in order to retain angular momentum conservation in the presence of anisotropic forces (Bonet and Lok, 1999).

A similar interpolant for the gradient follows by using

$$\nabla A = \frac{1}{\rho}[A\nabla\rho - \nabla(\rho A)] \tag{3.15}$$

$$\approx \frac{1}{\rho_a}\sum_b m_b (A_b - A_a)\nabla_a W_{ab}, \tag{3.16}$$

which again is exact for a constant A. Expanding A_b in a Taylor series, we see that in this case the

interpolation of a linear function can be made exact using

$$\frac{\partial A_a}{\partial \mathbf{r}^\alpha} = \chi_{\alpha\beta} \sum_b m_b (A_b - A_a) \nabla^\beta W_{ab}, \qquad \chi_{\alpha\beta} = \left[\sum_b m_b (\mathbf{r}_b - \mathbf{r}_a)^\alpha \nabla^\beta W_{ab} \right]^{-1}. \tag{3.17}$$

which has some advantages over (3.14) in that it can be computed without prior knowledge of the density.

An alternative gradient interpolant is given by

$$\begin{aligned} \nabla A(\mathbf{r}) &= \rho \left[\frac{A}{\rho^2} \nabla \rho + \nabla \left(\frac{A}{\rho} \right) \right] \\ &\approx \rho_a \sum_b m_b \left(\frac{A_a}{\rho_a^2} + \frac{A_b}{\rho_b^2} \right) \nabla_a W_{ab} \end{aligned} \tag{3.18}$$

which is commonly used in the SPH evaluation of the pressure gradient since it guarantees conservation of momentum by the pairwise symmetry in the gradient term. It is also the formulation of the pressure gradient which follows naturally in the derivation of the SPH equations from a variational principle (§3.3.2). Expanding A_b in a Taylor series about $\mathbf{r}_a$ we have

$$\begin{aligned} \sum_b m_b \left(\frac{A_a}{\rho_a^2} + \frac{A_b}{\rho_b^2} \right) \nabla_a W_{ab} &= A_a \sum_b m_b \left(\frac{1}{\rho_a^2} + \frac{1}{\rho_b^2} \right) \nabla_a W_{ab} + \frac{\partial A_a}{\partial \mathbf{r}^\alpha} \sum_b \frac{m_b}{\rho_b^2} (\mathbf{r}_b - \mathbf{r}_a)^\alpha \nabla_a W_{ab} \\ &\quad + \frac{1}{2} \frac{\partial^2 A_a}{\partial \mathbf{r}^\beta \partial \mathbf{r}^\gamma} \sum_b \frac{m_b}{\rho_b^2} (\mathbf{r}_b - \mathbf{r}_a)^\beta (\mathbf{r}_b - \mathbf{r}_a)^\gamma \nabla_a W_{ab} + \mathscr{O}[(\mathbf{r}_b - \mathbf{r}_a)^3] \end{aligned} \tag{3.19}$$

from which we see that for a constant function the error is governed by the extent to which

$$\sum_b m_b \left(\frac{1}{\rho_a^2} + \frac{1}{\rho_b^2} \right) \nabla_a W_{ab} \approx 0. \tag{3.20}$$

Although a simple subtraction of the first term in (3.19) from (3.18) eliminates this error, the symmetry in the gradient necessary for the conservation of momentum is lost by doing so. Retaining the exact conservation of momentum therefore requires that such error terms are not eliminated. In applications of SPH employing anisotropic forces (such in the MHD case), these error terms can be sufficient to cause numerical instabilities (§4.4).

Derivatives of vector quantities follow in a similar manner. For example the divergence of a vector quantity $\mathbf{v}$ can be estimated using

$$(\nabla \cdot \mathbf{v})_a \approx -\frac{1}{\rho_a} \sum_b m_b (\mathbf{v}_a - \mathbf{v}_b) \cdot \nabla_a W_{ab}, \tag{3.21}$$

or

$$(\nabla \cdot \mathbf{v})_a \approx \rho_a \sum_b m_b \left(\frac{\mathbf{v}_a}{\rho_a^2} + \frac{\mathbf{v}_b}{\rho_b^2} \right) \cdot \nabla_a W_{ab}, \tag{3.22}$$

whilst the curl is given by (e.g.)

$$(\nabla \times \mathbf{v})_a \approx -\frac{1}{\rho_a} \sum_b m_b (\mathbf{v}_a - \mathbf{v}_b) \times \nabla_a W_{ab}. \tag{3.23}$$

3.2.4 Second derivatives

Second derivatives are slightly more complicated since for kernels with compact support a straightforward estimation using the second derivative of the kernel proves to be very noisy and sensitive to particle disorder. For this reason it is better to use approximations of the second derivative which utilise only the first derivative of the kernel (Brookshaw, 1985; Monaghan, 1992). For a scalar quantity the second derivative may be estimated using the integral approximation

$$\nabla^2 A(\mathbf{r}) \approx 2\int [A(\mathbf{r}) - A(\mathbf{r}')] \frac{(\mathbf{r}-\mathbf{r}')\cdot\nabla W(\mathbf{r})}{|\mathbf{r}-\mathbf{r}'|^2} \mathrm{d}\mathbf{r}', \tag{3.24}$$

giving the SPH Laplacian

$$(\nabla^2 A)_a \approx 2\sum_b m_b \frac{(A_a - A_b)}{\rho_b} \frac{\mathbf{r}_{ab}\cdot\nabla_a W_{ab}}{\mathbf{r}_{ab}^2}, \tag{3.25}$$

where $\mathbf{r}_{ab} \equiv \mathbf{r}_a - \mathbf{r}_b$. This formalism is commonly used for heat conduction in SPH (e.g. Brookshaw 1985; Cleary and Monaghan 1999 and more recently Jubelgas et al. 2004). The integral approximation (3.24) can be derived by expanding $A(\mathbf{r}')$ to second order in a Taylor series about $\mathbf{r}$, giving

$$A(\mathbf{r}) - A(\mathbf{r}') = (\mathbf{r}-\mathbf{r}')^\alpha \frac{\partial A}{\partial \mathbf{r}^\alpha} + \frac{1}{2}(\mathbf{r}-\mathbf{r}')^\alpha (\mathbf{r}-\mathbf{r}')^\beta \frac{\partial^2 A}{\partial \mathbf{r}^\alpha \partial \mathbf{r}^\beta} + \mathscr{O}[(\mathbf{r}-\mathbf{r}')^3]. \tag{3.26}$$

Expanding this expression into (3.24), the integral is given by

$$\frac{\partial A}{\partial \mathbf{r}^\alpha}\int (\mathbf{r}-\mathbf{r}')^\alpha \frac{(\mathbf{r}-\mathbf{r}')\cdot\nabla W(\mathbf{r})}{|\mathbf{r}-\mathbf{r}'|^2}\mathrm{d}\mathbf{r}' + \frac{1}{2}\frac{\partial^2 A}{\partial \mathbf{r}^\alpha \partial \mathbf{r}^\beta}\int (\mathbf{r}-\mathbf{r}')^\alpha (\mathbf{r}-\mathbf{r}')^\beta \frac{(\mathbf{r}-\mathbf{r}')\cdot\nabla W(\mathbf{r})}{|\mathbf{r}-\mathbf{r}'|^2}\mathrm{d}\mathbf{r}'. \tag{3.27}$$

The first integral is zero for spherically symmetric kernels, whilst the second term integrates to a delta function, giving $\nabla^2 A$. A generalisation of (3.25) is derived for vector quantities by Español and Revenga (2003). In three dimensions the integral approximation is given by

$$\frac{\partial^2 \mathbf{v}}{\partial \mathbf{r}^\alpha \partial \mathbf{r}^\beta} \approx \int [\mathbf{v}(\mathbf{r}) - \mathbf{v}(\mathbf{r}')] \left[5(\mathbf{r}-\mathbf{r}')^\alpha (\mathbf{r}-\mathbf{r}')^\beta - \delta^{\alpha\beta}\right] \frac{(\mathbf{r}-\mathbf{r}')\cdot\nabla W(\mathbf{r})}{|\mathbf{r}-\mathbf{r}'|^2}\mathrm{d}\mathbf{r}', \tag{3.28}$$

which in SPH form becomes

$$\left(\frac{\partial^2 \mathbf{v}}{\partial \mathbf{r}^\alpha \partial \mathbf{r}^\beta}\right)_a \approx \sum_b m_b \frac{(\mathbf{v}_a - \mathbf{v}_b)}{\rho_b} \left[5\mathbf{r}_{ab}^\alpha \mathbf{r}_{ab}^\beta - \delta^{\alpha\beta}\right] \frac{\mathbf{r}_{ab}\cdot\nabla_a W_{ab}}{\mathbf{r}_{ab}^2}. \tag{3.29}$$

3.2.5 Smoothing kernels

The smoothing kernel W must by definition satisfy the requirement that it tends to a delta function as the smoothing length h tends to zero (3.2) and the normalisation condition (3.4). In addition the kernel is usually chosen to be an even function of r to cancel the first error term in (3.8) and may therefore be written in the form

$$W(r,h) = \frac{\sigma}{h^\nu} f\left(\frac{r}{h}\right), \tag{3.30}$$

where $r \equiv |\mathbf{r} - \mathbf{r}'|$ and ν is the number of spatial dimensions. Written in this form the normalisation condition (3.4) becomes

$$\sigma \int f(q)\mathrm{dV} = 1, \tag{3.31}$$

where $q = r/h$ and the volume element $dV = dq, 2\pi q dq$ or $4\pi q^2 dq$ in one, two and three dimensions. The simplest kernel with this property is the Gaussian

$$W(r,h) = \frac{\sigma}{h^\nu} e^{-q^2}, \tag{3.32}$$

where $q = r/h$ and $\sigma = [1/\sqrt{\pi}, 1/\pi, 1/(\pi\sqrt{\pi})]$ in [1,2,3] dimensions. This has the advantage that the spatial derivative is infinitely smooth (differentiable) and therefore exhibits good stability properties (Figure 3.2). For practical applications, however, using a Gaussian kernel has the immediate disadvantage that the interpolation spans the entire spatial domain (with computational cost of $\mathscr{O}(N^2)$), despite the fact that the relative contribution from neighbouring particles quickly become negligible with increasing distance. For this reason it is far more efficient to use kernels with finite extent (ie. having compact support), reducing the calculation to a sum over closely neighbouring particles which dramatically reduces the cost to $\mathscr{O}(nN)$ where n is the number of contributing neighbours (although there is also the additional cost of finding the neighbouring particles). Kernels which are similar to the Gaussian in shape generally give the best performance (see, e.g. Fulk and Quinn, 1996). Of these the most commonly used kernel is that based on cubic splines (Monaghan and Lattanzio, 1985), given by

$$f(q) = \sigma \begin{cases} 1 - \frac{3}{2}q^2 + \frac{3}{4}q^3, & 0 \le q < 1; \\ \frac{1}{4}(2-q)^3, & 1 \le q < 2; \\ 0. & q \ge 2. \end{cases} \tag{3.33}$$

with normalisation $\sigma = [2/3, 10/(7\pi), 1/\pi]$. This kernel satisfies the basic requirements (3.2) and (3.4), is even, has continuous first derivatives and compact support of size $2h$. Smoother kernels can be introduced by increasing the size of the compact support region (which correspondingly increases the cost of evaluation by increasing the number of contributing neighbours) and by using higher order interpolating spline functions. To this end the quartic spline kernel

$$f(q) = \sigma \begin{cases} (2.5-q)^4 - 5(1.5-q)^4 + 10(0.5-q)^4, & 0 \le q < 0.5; \\ (2.5-q)^4 - 5(1.5-q)^4, & 0.5 \le q < 1.5; \\ (2.5-q)^4, & 1.5 \le q < 2.5; \\ 0. & q \ge 2.5. \end{cases} \tag{3.34}$$

with normalisation $\sigma = [1/24, 96/1199\pi, 1/20\pi]$ and quintic spline kernel

$$f(q) = \sigma \begin{cases} (3-q)^5 - 6(2-q)^5 + 15(1-q)^5, & 0 \le q < 1; \\ (3-q)^5 - 6(2-q)^5, & 1 \le q < 2; \\ (3-q)^5, & 2 \le q < 3; \\ 0. & q \ge 3. \end{cases} \tag{3.35}$$

with normalisation $\sigma = [1/120, 7/478\pi, 1/120\pi]$ can be used (e.g. Morris, 1996). The higher order polynomials have the advantage of smoother derivatives which, in combination with the increased size of compact support, decreases the sensitivity of the kernel to disorder in the particle distribution (§3.2.7).

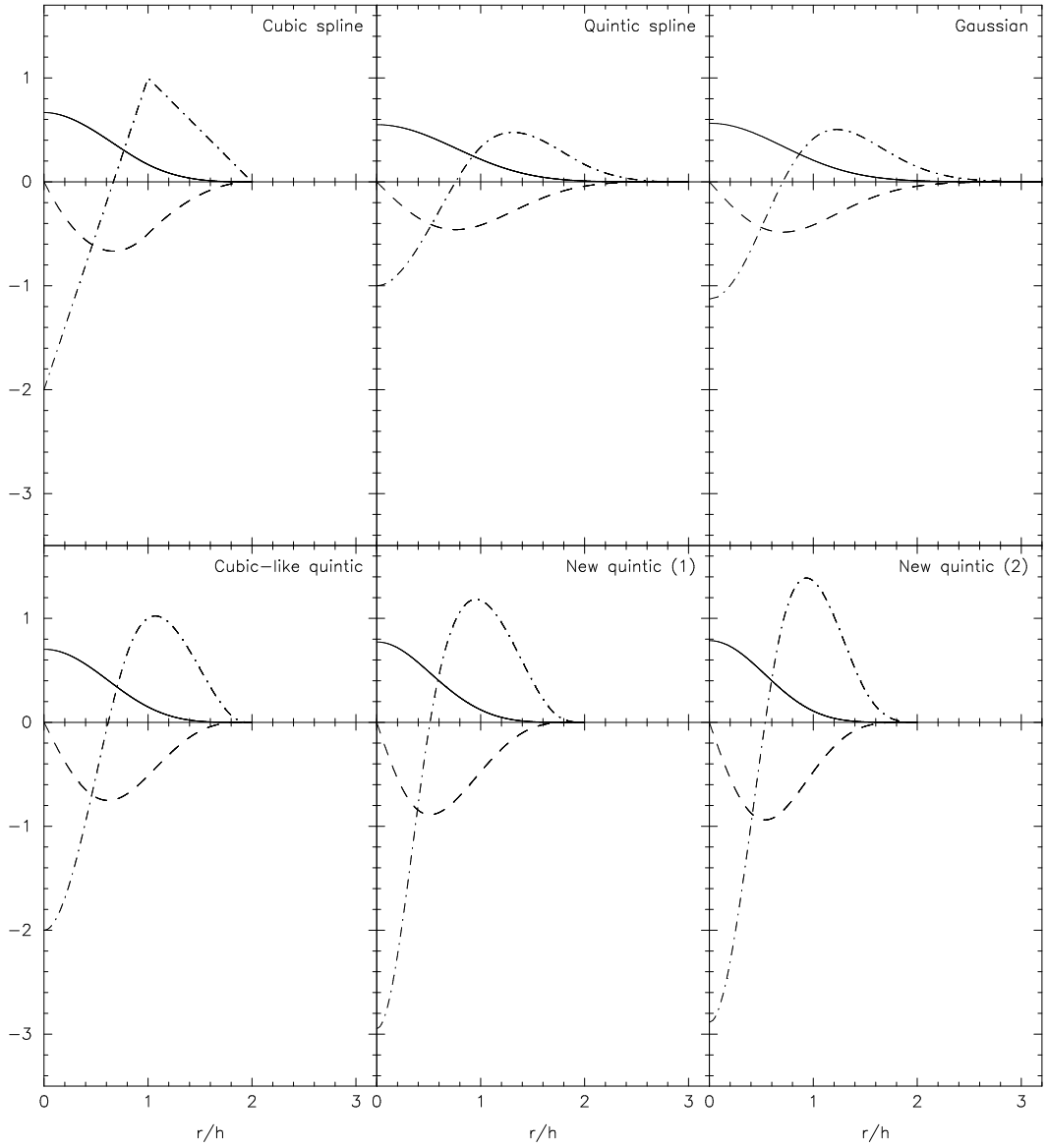

Figure 3.1: Examples of SPH smoothing kernels (solid line) together with their first (dashed) and second (dot-dashed) derivatives. Kernels correspond to those given in the text. The cubic spline (top left) is the usual choice, whilst the quintic (top, middle) represents a closer approximation to the Gaussian kernel (top right), at the cost of increased compact support. The bottom row correspond to various quintic kernels with compact support of $2h$ which we derive in §3.2.6. The stability properties of all these kernels are compared in Figure 3.2.

Note that it is entirely possible to construct kernels based on smoother splines but which retain compact support of size $2h$. We derive a class of such kernels and compare their stability properties with the kernels given in this section in §3.2.6. In principle it is also possible to construct higher order kernels where the second error term in (3.8) is also zero. Monaghan (1992) demonstrates that such higher order

kernels may be constructed from any lower order kernel such as (3.33) by the simple relation

$$W_{highorder} = B(1 - Aq^2)W(q) \tag{3.36}$$

where the parameters A and B are chosen to cancel the second moment and to satisfy the normalisation condition (3.4). The disadvantage of all such kernels is that the kernel becomes negative in part of the domain which could result in a negative density evaluation. Also it is not clear that such kernels actually lead to significant improvements in accuracy in practical situations (since the kernel is sampled at only a few points).

From time to time various alternatives have been proposed to the kernel interpolation at the heart of SPH, such as the use of Delaunay triangulations (Pelupessy et al., 2003) and normalisations of the kernel interpolant (involving matrix inversion) which guarantee exact interpolations to arbitrary polynomial orders (Maron and Howes, 2003; Bonet and Lok, 1999). It remains to be seen whether any such alternative proposals are viable in terms of the gain in accuracy versus the inevitable increase in computational expense and algorithmic complexity.

Finally we note that in most SPH codes, the kernel is evaluated by linear interpolation from a precomputed table of values, since kernel evaluations are computed frequently. The computational cost involved in calculating the kernel function is therefore the same whatever the functional form. In the calculations given in this thesis, the kernel is tabulated as $W(q)$ and $\partial W/\partial q$, where the table is evenly spaced in q^2 to give a better interpolation in the outer edges.

3.2.6 A general class of kernels

In this section we consider the possibility of constructing kernels based on smoother splines than the cubic but which retain compact support of size $2h$. A general class of such kernels may be derived by considering kernels of the form

$$f(q) = \sigma \begin{cases} (r-q)^n + A(\alpha - q)^n + B(\beta - q)^n, & 0 \le q < \beta; \\ (r-q)^n + A(\alpha - q)^n, & \beta \le q < \alpha; \\ (r-q)^n, & \alpha \le q < r; \\ 0. & q \ge r \end{cases} \tag{3.37}$$

where n is the order, r is the compact support size (in this case $r = 2$), A and B are parameters to be determined and α and β are the two matching points (with $0 < \beta < \alpha < r$), although an arbitrary number of matching points could be added. The formulation given above guarantees that the kernel and its derivatives are continuous at the matching points and zero at the compact support radius $W(r) = dW/dq(r) = 0$. To determine the parameters A and B we require two further constraints on the form of the kernel. For the kernels to resemble the Gaussian, we constrain the kernel gradient to be zero at the origin and also that the second derivative be minimum at the origin (this also constrains $n \ge 3$), ie.

$$W'(0) = 0, \qquad W'''(0) = 0. \tag{3.38}$$

For the moment we leave the matching points as free parameters. From the conditions (3.38), the parameters A and B are given in terms of the matching points by

$$A = \frac{r^{n-3}(r^2-\beta^2)}{\alpha^{n-3}(\alpha^2-\beta^2)}, \qquad B = -\frac{r^{n-1}+A\alpha^{n-1}}{\beta^{n-1}}. \tag{3.39}$$

In one dimension the normalisation constant is given by

$$\sigma = \frac{n+1}{2(A\alpha^{n+1}+B\beta^{n+1}+r^{n+1})}. \tag{3.40}$$

As an example we can construct a quintic ($n = 5$) kernel that closely resembles the cubic spline kernel (3.33) in all but the continuity of the second derivative. An example of such a kernel is given by the choice $\beta = 0.85$, $\alpha = 1.87$. This was chosen by constraining the second derivative to be equal to that of the cubic spline at the origin (ie. $W''(0) = -2$) and the turning point in the second derivative to be located as close as possible to the that of the cubic spline ($W'''(q \approx 1) = 0$; note that an exact match is not possible under the constraints given). This kernel is shown in Figure 3.1 ('cubic-like quintic'). The stability properties are discussed in §3.2.7.

However, it would be more interesting to investigate whether other kernels with even better stability properties can be constructed. To this end we have performed a survey of parameter space for quintic ($n = 5$) kernels, from which we find that the most stable kernels are those with matching points in the range $\beta \approx 0.5$ with $\alpha \approx 1.7$ or $\beta \approx 0.7$ with $\alpha \approx 1.5$. These two kernels ('New Quintic(1)' and 'New Quintic (2)') are shown in Figure 3.1. The stability properties are discussed below.

3.2.7 Kernel stability properties

The accuracy of the kernels given in §3.2.5 and §3.2.6 may be compared via a stability analysis of the SPH equations. Detailed investigations of the stability properties of SPH have been given elsewhere (e.g. Morris 1996) and for this reason we refer the details of the stability analysis to appendix B (although as for the fluid equations, the linearised form of the SPH equations are derived from a variational principle). The result for one-dimensional SPH (for any equation of state) is the dispersion relation

$$\begin{aligned}\omega_a^2 &= \frac{2mP_0}{\rho_0^2}\sum_b [1-\cos k(x_a-x_b)]\frac{\partial^2 W}{\partial x^2}(x_a-x_b,h) \\ &\quad + \frac{m^2}{\rho_0^2}\left(c_s^2 - \frac{2P_0}{\rho_0}\right)\left[\sum_b \sin k(x_a-x_b)\frac{\partial W}{\partial x}(x_a-x_b,h)\right]^2,\end{aligned} \tag{3.41}$$

where $c_s = \partial P/\partial\rho$ is the sound speed. Figure 3.2 shows contours of the (normalised) square of the numerical sound speed $C_{num}^2 = \omega^2/k^2$ as a function of wavenumber and smoothing length (both in units of the average particle spacing). The sums in (3.41) are calculated numerically assuming an (isothermal) sound speed and particle spacing of unity (both wavelength and smoothing length are calculated in units of the particle spacing). The quintic spline (top, centre) and the Gaussian (top right) show increasingly better stability properties over the standard cubic spline (top left) although at increased computational expense.

The stability properties of the 'cubic-like' quintic kernel derived in §3.2.6 (bottom left) are very

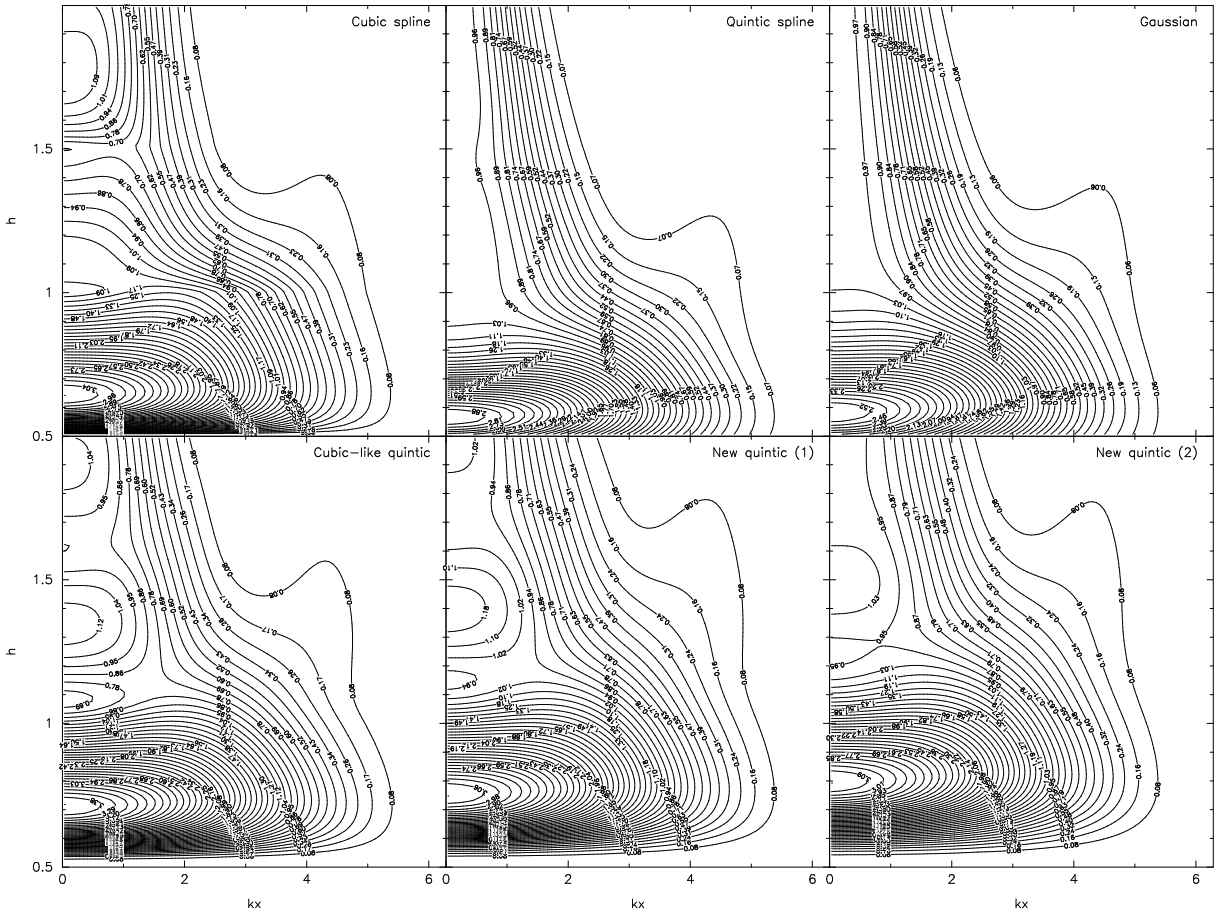

Figure 3.2: One dimensional stability properties of the kernels shown in Figure 3.1 for isothermal SPH. The y-axis gives the smoothing length in units of the particle spacing Δx, whilst the x-axis corresponds to wavenumber in units of $1/\Delta x$ (such that $kx \rightarrow 0$ represents the limit of an infinite number of particles per wavelength and $h \rightarrow \infty$ represents the limit of an infinite number of neighbours). Contours show the (normalised) square of the numerical sound speed from the dispersion relation (3.41). The quintic spline (top, centre) and Gaussian kernels show improved accuracy over the standard cubic spline kernel although at a higher computational cost. The kernels derived in §3.2.6 (bottom row) appear to give an improvement in accuracy for $h \gtrsim 1.1$ although degrade rapidly for $h \lesssim 1.1$ where the cubic spline retains a reasonable accuracy

similar to that of the cubic spline, except that the 'trough' in the contours of C^2_{num} observed at $h = 1.5\Delta p$ (where the closest neighbour crosses the discontinuity in the second derivative) is much smoother. However, the accuracy of this kernel appears to degrade for small smoothing lengths ($h \lesssim 1.1\Delta p$) where the cubic spline retains a reasonable accuracy. Of the remaining two kernels derived in §3.2.6 (bottom centre and bottom right), the second example ('New Quintic (2)') in particular appears to give slightly better accuracy than the cubic spline over the range $h \gtrsim 1.1\Delta p$ although both kernels show the rapid decline in accuracy for small smoothing lengths ($h \lesssim 1.1\Delta p$) observed in the cubic-like quintic. It is worth noting that most multidimensional calculations use smoothing lengths in the range $h = 1.1 - 1.2\Delta p$.

In summary the new kernels appear to give a small gain in accuracy over the cubic spline kernel, provided $h \gtrsim 1.1\Delta p$. However, the gain in accuracy from the use of these alternative kernels is very minor compared to the substantial improvements in accuracy gained by the incorporation of the variable smoothing length terms (§3.3.4), which effectively act as a normalisation of the kernel gradient.

3.3 Fluid Equations

3.3.1 Continuity equation

The summation interpolant (3.5) takes a particularly simple form for the evaluation of density, ie.

$$\rho_a = \sum_b m_b W_{ab}. \tag{3.42}$$

Taking the (Lagrangian) time derivative, we obtain

$$\frac{d\rho_a}{dt} = \sum_b m_b (\mathbf{v}_a - \mathbf{v}_b) \cdot \nabla_a W_{ab}, \tag{3.43}$$

which may be translated back to continuum form via the summation interpolant (3.5) to give

$$\begin{aligned} \frac{d\rho}{dt} &= \mathbf{v} \cdot \nabla\rho - \nabla \cdot (\rho \mathbf{v}), \\ &= -\rho(\nabla \cdot \mathbf{v}). \end{aligned} \tag{3.44}$$

This reveals that (3.43) and therefore (3.42) are SPH expressions for the continuity equation. It is a remarkable fact that the entire SPH formalism can be self-consistently derived using only (3.42) in conjunction with the first law of thermodynamics via a Lagrangian variational principle. Such a derivation demonstrates that SPH has a robust Hamiltonian structure and ensures that the discrete equations reflect the symmetries inherent in the Lagrangian, leading to the exact conservation of momentum, angular momentum and energy.

3.3.2 Equations of motion

The Lagrangian for Hydrodynamics is given by (Eckart, 1960; Salmon, 1988; Morrison, 1998)

$$L = \int \left(\frac{1}{2}\rho \mathrm{v}^2 - \rho u \right) \mathrm{dV}, \tag{3.45}$$

where u is the internal energy per unit mass. In SPH form this becomes

$$L = \sum_b m_b \left[\frac{1}{2}\mathrm{v}_b^2 - u_b(\rho_b, s_b) \right], \tag{3.46}$$

where as previously we have replaced the volume element ρdV with the mass per SPH particle m. We regard the particle co-ordinates as the canonical variables. Being able to specify all of the terms in the Lagrangian directly in terms of these variables means that the conservation laws will be automatically satisfied, since the equations of motion then result from the Euler-Lagrange equations

$$\frac{d}{dt}\left(\frac{\partial L}{\partial \mathbf{v}_a} \right) - \frac{\partial L}{\partial \mathbf{r}_a} = 0. \tag{3.47}$$

The internal energy is regarded as a function of the particle's density, which in turn is specified as a function of the co-ordinates by (3.42). The terms in (3.47) are therefore given by

$$\frac{\partial L}{\partial \mathbf{v}_a} = m_a \mathbf{v}_a, \tag{3.48}$$

$$\frac{\partial L}{\partial \mathbf{r}_a} = \sum_b m_b \left.\frac{\partial u_b}{\partial \rho_b}\right|_s \frac{\partial \rho_b}{\partial \mathbf{r}_a}. \tag{3.49}$$

From the first law of thermodynamics in the absence of dissipation we have

$$\left.\frac{\partial u_b}{\partial \rho_b}\right|_s = \frac{P_b}{\rho_b^2}, \tag{3.50}$$

and using (3.42) we have

$$\frac{\partial \rho_b}{\partial \mathbf{r}_a} = \sum_c m_c \nabla_a W_{bc} \left(\delta_{ba} - \delta_{ca}\right), \tag{3.51}$$

such that

$$\frac{\partial L}{\partial \mathbf{r}_a} = \sum_b m_b \frac{P_b}{\rho_b^2} \sum_c m_c \nabla_a W_{bc} \left(\delta_{ba} - \delta_{ca}\right), \tag{3.52}$$

$$= m_a \sum_b m_b \left(\frac{P_a}{\rho_a^2} + \frac{P_b}{\rho_b^2}\right) \nabla_a W_{ab}, \tag{3.53}$$

where we have used the fact that the gradient of the kernel is anti-symmetric (ie. $\nabla_a W_{ac} = -\nabla_a W_{ca}$). The SPH equation of motion in the absence of dissipation is therefore given by

$$\frac{d\mathbf{v}_a}{dt} = -\sum_b m_b \left(\frac{P_a}{\rho_a^2} + \frac{P_b}{\rho_b^2}\right) \nabla_a W_{ab}, \tag{3.54}$$

which can be seen to explicitly conserve momentum since the contribution of the summation to the momentum of particle a is equal and opposite to that given to particle b (given the antisymmetry of the kernel gradient). Taking the time derivative of the total angular momentum, we have

$$\frac{d}{dt}\sum_a \mathbf{r}_a \times m_a \mathbf{v}_a = \sum_a m_a \left(\mathbf{r}_a \times \frac{d\mathbf{v}_a}{dt}\right), \tag{3.55}$$

$$= \sum_a \sum_b m_a m_b \left(\frac{P_a}{\rho_a^2} + \frac{P_b}{\rho_b^2}\right) \mathbf{r}_a \times (\mathbf{r}_a - \mathbf{r}_b) F_{ab},$$

$$= -\sum_a \sum_b m_a m_b \left(\frac{P_a}{\rho_a^2} + \frac{P_b}{\rho_b^2}\right) \mathbf{r}_a \times \mathbf{r}_b F_{ab}. \tag{3.56}$$

where the kernel gradient has been written as $\nabla_a W_{ab} = \mathbf{r}_{ab} F_{ab}$ This last expression is zero since the double summation is antisymmetric in a and b (this can be seen by swapping the summation indices a and b in the double sum and adding half of this expression to half of the original expression, giving zero). Angular momentum is therefore also explicitly conserved.

3.3.3 Energy equation

The energy equation also follows naturally from the variational approach, where we may choose to integrate either the particle's internal energy u, its specific energy e or even its specific entropy s. Integrating the specific energy guarantees that the total energy is exactly conserved and it is common practice to use this quantity in finite difference schemes. However the usual argument against this (which applies equally to finite difference schemes) is that in some circumstances (where the kinetic energy is much greater than the thermal energy) the thermal energy can become negative by round-off error. Integration of the specific entropy has some advantages and has been argued for in both SPH (Springel and Hernquist, 2002) and finite difference schemes (e.g. Balsara and Spicer 1999).

Internal energy

The internal energy equation in the absence of dissipation follows from the use of the first law of thermodynamics (3.50), giving

$$\frac{du_a}{dt} = \frac{P_a}{\rho_a^2}\frac{d\rho_a}{dt}. \tag{3.57}$$

Using (3.43) therefore gives

$$\frac{du_a}{dt} = \frac{P_a}{\rho_a^2}\sum_b m_b \mathbf{v}_{ab}\cdot\nabla_a W_{ab}. \tag{3.58}$$

Total energy

The conserved (total) energy is found from the Lagrangian via the Hamiltonian

$$H = \sum_a \mathbf{v}_a \cdot \frac{\partial L}{\partial \mathbf{v}_a} - L, \tag{3.59}$$

where using (3.48) and (3.46) we have

$$H = \sum_a m_a \left(\frac{1}{2}\mathrm{v}_a^2 + u_a\right), \tag{3.60}$$

which is simply the total energy of the SPH particles E since the Lagrangian does not explicitly depend on the time. Taking the (Lagrangian) time derivative of (3.60), we have

$$\frac{dE}{dt} = \sum_a m_a \left(\mathbf{v}_a \cdot \frac{d\mathbf{v}_a}{dt} + \frac{du_a}{dt}\right). \tag{3.61}$$

Substituting (3.54) and (3.58) and rearranging we find

$$\frac{dE}{dt} = \sum_a m_a \frac{de_a}{dt} = \sum_a \sum_b m_a m_b \left(\frac{P_a}{\rho_a^2}\mathbf{v}_b + \frac{P_b}{\rho_b^2}\mathbf{v}_a\right)\cdot\nabla_a W_{ab}, \tag{3.62}$$

and thus the specific energy equation (in the absence of dissipation) is given by

$$\frac{de_a}{dt} = \sum_b m_b \left(\frac{P_a}{\rho_a^2} \mathbf{v}_b + \frac{P_b}{\rho_b^2} \mathbf{v}_a \right) \cdot \nabla_a W_{ab}. \tag{3.63}$$

Dissipative terms are discussed in §3.5.

Entropy

In the case of an ideal gas equation of state where

$$P = A(s)\rho^\gamma, \tag{3.64}$$

the function $A(s)$ evolves according to

$$\begin{aligned} \frac{dA}{dt} &= \frac{\gamma-1}{\rho^{\gamma-1}} \left(\frac{du}{dt} - \frac{P}{\rho^2} \frac{d\rho}{dt} \right), \\ &= \frac{\gamma-1}{\rho^{\gamma-1}} \left(\frac{du}{dt} \right)_{diss}. \end{aligned} \tag{3.65}$$

This has the advantage of placing strict controls on sources of entropy, since A is constant in the absence of dissipative terms. The thermal energy is evaluated using

$$u = \frac{A}{\gamma-1} \rho^{\gamma-1}. \tag{3.66}$$

This formulation of the energy equation has been advocated in an SPH context by Springel and Hernquist (2002).

3.3.4 Variable smoothing length terms

The smoothing length h determines the radius of interaction for each SPH particle. Early SPH simulations used a fixed smoothing length for all particles. However allowing each particle to have its own associated smoothing length which varies according to local conditions increases the spatial resolution substantially (Hernquist and Katz, 1989; Benz, 1990). The usual rule is to take

$$h_a \propto \left(\frac{1}{\rho_a} \right)^{(1/\nu)}, \tag{3.67}$$

where ν is the number of spatial dimensions, although others are possible (Monaghan, 2000). Implementing this rule self-consistently is more complicated in SPH since the density ρ_a is itself a function of the smoothing length h_a via the relation (3.42). A simple approach is to use the time derivative of (3.67), (Benz, 1990), ie.

$$\frac{dh_a}{dt} = -\frac{h_a}{\nu \rho_a} \frac{d\rho}{dt}, \tag{3.68}$$

which can then be evolved alongside the other particle quantities. This rule works well for most practical purposes, and maintains the relation (3.67) particularly well when the density is updated using the continuity equation (3.43). However, it has been known for some time that, in order to be fully self-consistent, extra terms involving the derivative of h should be included in the momentum and energy equations (e.g. Nelson 1994; Nelson and Papaloizou 1994; Serna et al. 1996). Attempts to do this were, however, complicated to implement (Nelson and Papaloizou, 1994) and therefore not generally adopted by the SPH community. Recently Springel and Hernquist (2002) have shown that the so-called ∇h terms can be self-consistently included in the equations of motion and energy using a variational approach. Springel and Hernquist (2002) included the variation of the smoothing length in their variational principle by use of Lagrange multipliers, however, in the context of the discussion given in §3.3.2 we note that by expressing the smoothing length as a function of ρ we can therefore specify h as a function of the particle co-ordinates (Monaghan, 2002). That is we have $h = h(\rho)$ where ρ is given by

$$\rho_a = \sum_b m_b W(\mathbf{r}_{ab}, h_a). \tag{3.69}$$

Taking the time derivative, we obtain

$$\frac{d\rho_a}{dt} = \frac{1}{\Omega_a} \sum_b m_b \mathbf{v}_{ab} \cdot \nabla_a W_{ab}(h_a), \tag{3.70}$$

where

$$\Omega_a = \left[1 - \frac{\partial h_a}{\partial \rho_a} \sum_c m_c \frac{\partial W_{ab}(h_a)}{\partial h_a} \right]. \tag{3.71}$$

A simple evaluation of Ω for the kernel in the form (3.30) shows that this term differs from unity even in the case of an initially uniform density particle distribution (i.e. with constant smoothing length). The effects of this correction term even in this simple case are investigated in the sound wave tests described in §3.7.2.

The equations of motion in the hydrodynamic case may then be found using the Euler-Lagrange equations (3.47) and will therefore automatically conserve linear and angular momentum. The resulting equations are given by (Springel and Hernquist, 2002; Monaghan, 2002)

$$\frac{d\mathbf{v}_a}{dt} = -\sum_b m_b \left[\frac{P_a}{\Omega_a \rho_a^2} \nabla_a W_{ab}(h_a) + \frac{P_b}{\Omega_b \rho_b^2} \nabla_a W_{ab}(h_b) \right]. \tag{3.72}$$

Calculation of the quantities Ω involve a summation over the particles and can be computed alongside the density summation (3.69). To be fully self-consistent we solve (3.69) iteratively to determine both h and ρ self-consistently. We do this as follows: Using the predicted smoothing length from (3.68), the density is initially calculated by a summation over the particles. A new value of smoothing length h_{new} is then computed from this density using (3.67). Convergence is determined according to the criterion

$$\frac{|h_{new} - h|}{h} < 1.0 \times 10^{-2}. \tag{3.73}$$

For particles which are not converged, the density of (only) those particles are recalculated (using h_{new}).

This process is then repeated until all particles are converged. Note that a particle's smoothing length is only set equal to h_{new} if the density is to be recalculated (this is to ensure that the same smoothing length that was used to calculate the density is used to compute the terms in the other SPH equations). Also, the density only needs to be recalculated on those particles which have not converged, since each particle's density is independent of the smoothing length of neighbouring particles. This requires a small adjustment to the density calculation routine (such that the density can be calculated only for a selected list of particles, rather than for all), but is relatively simple to implement and means that the additional computational cost involved is negligible (at least for the problems considered in this thesis). Note that in principle the calculated gradient terms (3.71) may also be used to implement an iteration scheme such as the Newton-Raphson method which converges faster than our simple fixed point iteration.

Where the variable smoothing length terms are not explicitly calculated, we use a simple averaging of the kernels and kernel gradients to maintain the symmetry in the momentum and energy equations (Hernquist and Katz, 1989; Monaghan, 1992), ie.

$$W_{ab} = \frac{1}{2}\left[W_{ab}(h_a) + W_{ab}(h_b)\right], \tag{3.74}$$

and correspondingly

$$\nabla_a W_{ab} = \frac{1}{2}\left[\nabla_a W_{ab}(h_a) + \nabla_a W_{ab}(h_b)\right]. \tag{3.75}$$

Many of the test problems in this thesis are performed using this simple formulation. This is in order to show (particularly in the MHD case) that satisfactory results on the test problems are not dependent on the variable smoothing length formulation. In almost every case, however, self-consistent implementation of the variable smoothing length terms as described above leads to a substantial improvement in accuracy (demonstrated, for example, in §3.7 and in the MHD case in §4.6). Perhaps the only disadvantage to the full implementation of the variable smoothing length terms is that the iterations of h with ρ mean that small density fluctuations are resolved by the method rather than being smoothed out, which may be disadvantageous under some circumstances (e.g. where the fluctuations are unphysical). One possible remedy for this might be to use a slightly different relationship between h and ρ than is given by (3.67).

3.4 Alternative formulations of SPH

In §3.3 the SPH equations of motion and energy were derived from a variational principle using only the density summation (3.42) and the first law of thermodynamics (3.50), leading to the equations of motion in the form (3.54) and the energy equation (3.58) or (3.63). However many alternative formulations of the SPH equations are possible and have been used in various contexts. In this section we demonstrate how such alternative formulations may also be derived self-consistently using a variational principle.

For example, a general form of the momentum equation in SPH is given by (Monaghan, 1992)

$$\frac{d\mathbf{v}_a}{dt} = -\sum_b m_b \left(\frac{P_a}{\rho_a^\sigma \rho_b^{2-\sigma}} + \frac{P_b}{\rho_b^\sigma \rho_a^{2-\sigma}} \right) \nabla_a W_{ab}, \tag{3.76}$$

which is symmetric between particle pairs for all choices of the parameter σ and therefore explicitly

conserves momentum. Ritchie and Thomas (2001) use this form of the momentum equation with $\sigma = 1$ in their SPH formalism, finding that it gives slightly better results for problems involving large density contrasts (they also use a slightly different procedure for evaluating the density). Marri and White (2003), for similar reasons, use this equation with $\sigma = 3/2$, citing a reduction in the relative error in the force calculation on particle a due to the influence of particle b which is desirable in the case of particles with large density differences. However, it is apparent from the derivation given in §3.3.2 that forms of this equation other than the standard $\sigma = 2$ case cannot be derived consistently using the density summation (3.42) and correspondingly the continuity equation in the form (3.43). We are therefore led to the conclusion that a consistent formulation of the SPH equations using the general form of the momentum equation given above must involve modification of the continuity equation in some way. We show below that the general form of the continuity equation which is consistent with (3.76) is derived from the continuum equation

$$\frac{d\rho}{dt} = -\rho \nabla \cdot \mathbf{v}, \tag{3.77}$$

expressed in the form

$$\frac{d\rho}{dt} = \rho^{2-\sigma} \left[\mathbf{v} \cdot \nabla(\rho^{\sigma-1}) - \nabla \cdot (\mathbf{v}\rho^{\sigma-1}) \right], \tag{3.78}$$

with SPH equivalent

$$\frac{d\rho_a}{dt} = \rho_a^{2-\sigma} \sum_b m_b \frac{(\mathbf{v}_a - \mathbf{v}_b)}{\rho_b^{2-\sigma}} \cdot \nabla_a W_{ab}. \tag{3.79}$$

In order to demonstrate that this is so, we use this expression for the density to derive the equations of motion and energy via a variational principle.

3.4.1 Variational principle

In the derivation given in §3.3.2, the variables in the Lagrangian were explicitly written as a function of the particle co-ordinates (via the identity 3.42), guaranteeing the exact conservation of linear and angular momentum in the equations of motion via the use of the Euler-Lagrange equations. Using a more general form of the continuity equation, however, means that the density can no longer be expressed directly as a function of the particle co-ordinates and therefore that the derivation given in the previous section cannot be applied in this case. However we may still use the Lagrangian to derive the equations of motion by introducing constraints on ρ in a manner similar to that of Bonet and Lok (1999). In this case conservation of momentum and energy can be shown to depend on the formulation of the velocity terms in the continuity equation (in particular that the term should be expressed as a velocity difference). Clearly the major disadvantage of using a continuity equation of any form rather than the SPH summation is that mass is no longer conserved exactly. It is shown in §4.3.2 that the kind of variational principle given below may also be used to derive the equations of motion and energy in the MHD case.

For stationary action we require

$$\delta \int L \mathrm{dt} = \int \delta L \mathrm{dt} = 0, \tag{3.80}$$

where we consider variations with respect to a small change in the particle co-ordinates $\delta\mathbf{r}_a$. We therefore have

$$\delta L = m_a \mathbf{v}_a \cdot \delta\mathbf{v}_a - \sum_b m_b \left.\frac{\partial u_b}{\partial \rho_b}\right|_s \delta\rho_b. \tag{3.81}$$

The Lagrangian variation in density is given, from (3.79), by

$$\delta\rho_b = \rho_b^{2-\sigma} \sum_c \frac{m_c}{\rho_c^{2-\sigma}} (\delta\mathbf{r}_b - \delta\mathbf{r}_c) \cdot \nabla_b W_{bc}. \tag{3.82}$$

Using (3.82) and the first law of thermodynamics (3.50) in (3.81) and rearranging, we find

$$\frac{\delta L}{\delta \mathbf{r}_a} = -\sum_b m_b \frac{P_b}{\rho_b^\sigma} \sum_c \frac{m_c}{\rho_c^{2-\sigma}} \nabla_b W_{bc} (\delta_{ba} - \delta_{ca}). \tag{3.83}$$

Putting this back into (3.80), integrating the velocity term by parts and simplifying (using $\nabla_a W_{ab} = -\nabla_b W_{ba}$), we obtain

$$\int \left[-m_a \frac{d\mathbf{v}_a}{dt} - \sum_b m_b \left(\frac{P_a}{\rho_a^\sigma \rho_b^{2-\sigma}} + \frac{P_b}{\rho_b^\sigma \rho_a^{2-\sigma}} \right) \nabla_a W_{ab} \right] \delta\mathbf{r}_a \mathrm{d}t = 0, \tag{3.84}$$

from which we obtain the momentum equation in the form (3.76). This equation is therefore consistent with the continuity equation in the form (3.79). In the particular case considered by Marri and White (2003) ($\sigma = 3/2$) this would imply a discrete form of the continuity equation given by

$$\frac{d\rho_a}{dt} = \sqrt{\rho_a} \sum_b m_b \frac{\mathbf{v}_{ab}}{\sqrt{\rho_b}} \cdot \nabla_a W_{ab}. \tag{3.85}$$

Marri and White (2003) choose to retain the use of the usual SPH summation (3.42) to determine the density. In the case considered by Ritchie and Thomas (2001) ($\sigma = 1$), the continuity equation becomes

$$\frac{d\rho_a}{dt} = \rho_a \sum_b m_b \frac{\mathbf{v}_{ab}}{\rho_b} \cdot \nabla_a W_{ab}, \tag{3.86}$$

which is again somewhat different to the density estimation used in their paper. The continuity equation (3.86), when used in conjunction with the appropriate formulation of the momentum equation, has some advantages in the case of fluids with large density differences (e.g. at a water/air interface) since the term inside the summation involves only the particle volumes m/ρ rather than their mass, with the effect that large mass differences between individual particles have less influence on the calculation of the velocity divergence (Monaghan, private communication). An alternative is the formalism proposed by Ott and Schnetter (2003), which we discuss in §3.4.3.

The internal energy equation consistent with the general momentum equation (3.76) is given by

$$\frac{du_a}{dt} = \frac{P_a}{\rho_a^\sigma} \sum_b m_b \frac{\mathbf{v}_{ab}}{\rho_b^{2-\sigma}} \cdot \nabla_a W_{ab}, \tag{3.87}$$

which is indeed the formalism used by Marri and White (2003) (with $\sigma = 3/2$) since it was found,

unsurprisingly in this context, that integration of this equation resulted in much less numerical noise than using other formalisms of the internal energy equation (in conjunction with their use of (3.76) with $\sigma = 3/2$ as the momentum equation). The form of the total energy equation consistent with (3.76) and (3.79) is given by

$$\frac{de_a}{dt} = -\sum_b m_b \left(\frac{P_a}{\rho_a^\sigma \rho_b^{2-\sigma}} \mathbf{v}_b + \frac{P_b}{\rho_b^\sigma \rho_a^{2-\sigma}} \mathbf{v}_a \right) \cdot \nabla_a W_{ab}. \tag{3.88}$$

We note the energy equation used by Ritchie and Thomas (2001) is different to the formulation given above (with $\sigma = 1$) and therefore variationally inconsistent with their implementation of the momentum equation. Hernquist and Katz (1989) point out that inconsistencies between the forms of the energy and momentum equations result in errors of $\mathscr{O}(h^2)$ in the energy conservation. In this sense the difference between a consistent and inconsistent formalism is fairly minor, although a consistent formulation between the momentum and energy equations in general appears to lead to slightly improved results (as found by Marri and White). In practise we find that using alternative formulations of the continuity equation generally gives slightly worse results than (even inconsistent) use of the density summation.

3.4.2 General alternative formulation

The momentum equation (3.76) can be generalised still further by noting that the continuity equation (3.44) can be written as

$$\frac{d\rho}{dt} = \phi \left[\mathbf{v} \cdot \nabla \left(\frac{\rho}{\phi} \right) - \nabla \cdot \left(\frac{\rho \mathbf{v}}{\phi} \right) \right], \tag{3.89}$$

with SPH equivalent

$$\frac{d\rho_a}{dt} = \phi_a \sum_b m_b \frac{\mathbf{v}_{ab}}{\phi_b} \cdot \nabla_a W_{ab}, \tag{3.90}$$

where ϕ is *any* scalar variable defined on the particles. Deriving the momentum equation consistent with this equation in the manner given above we find

$$\frac{d\mathbf{v}_a}{dt} = -\sum_b m_b \left(\frac{P_a}{\rho_a^2} \frac{\phi_a}{\phi_b} + \frac{P_b}{\rho_b^2} \frac{\phi_b}{\phi_a} \right) \nabla_a W_{ab}, \tag{3.91}$$

which conserves momentum for any choice of ϕ. In the case given in the previous section we would have $\phi = \rho^{2-\sigma}$. Choosing $\phi = \rho/\sqrt{P}$ gives

$$\frac{d\mathbf{v}_a}{dt} = -\sum_b m_b \left(2 \frac{\sqrt{P_a P_b}}{\rho_a \rho_b} \right) \nabla_a W_{ab}. \tag{3.92}$$

which is the momentum equation used by Hernquist and Katz (1989). The continuity equation consistent with this form is therefore

$$\frac{d\rho_a}{dt} = \frac{\rho_a}{\sqrt{P_a}} \sum_b m_b \frac{\sqrt{P_b}}{\rho_b} \mathbf{v}_{ab} \cdot \nabla_a W_{ab}, \tag{3.93}$$

which at first sight appears somewhat bizarre, although it is certainly a valid expression of the continuity equation in SPH form. It is unclear whether using such alternative formulations of the continuity equation, in the name of consistency, has any advantages over the usual density summation. We leave it as an exercise for the reader to amuse themselves by exploring various other combinations of variables, noting that the forms of the internal and total energy equations consistent with (3.90) and (3.91) are given by

$$\frac{du_a}{dt} = \frac{P_a}{\rho_a^2}\sum_b m_b \frac{\phi_a}{\phi_b}\mathbf{v}_{ab}\cdot\nabla_a W_{ab}, \tag{3.94}$$

and

$$\frac{de_a}{dt} = -\sum_b m_b \left(\frac{P_a}{\rho_a^2}\frac{\phi_a}{\phi_b}\mathbf{v}_b + \frac{P_b}{\rho_b^2}\frac{\phi_b}{\phi_a}\mathbf{v}_a\right)\cdot\nabla_a W_{ab}. \tag{3.95}$$

3.4.3 Ott and Schnetter formulation

Other formulations of the SPH equations have also been proposed to deal with the problem of large density gradients. For example Ott and Schnetter (2003) propose modifying the SPH summation to give

$$\begin{aligned} n_a &= \sum_b W_{ab}, \\ \rho_a &= m_a n_a, \end{aligned} \tag{3.96}$$

that is where the number density of particles n is calculated by summation rather than the mass density ρ. This is to improve the interpolation when particles of large mass differences interact. Taking the time derivative of (3.96), the continuity equation is given by (as in Ott and Schnetter 2003)

$$\frac{d\rho_a}{dt} = m_a \sum_b \mathbf{v}_{ab}\cdot\nabla_a W_{ab}. \tag{3.97}$$

For equal mass particles this formalism is exactly the same as the usual summation (3.42). The formulation (3.96) enables the density to be expressed as a function of the particle co-ordinates and thus the derivation of the equations of motion and energy can be done in a straightforward manner using the Euler-Lagrange equations, as in §3.3.2. The resulting equation of motion is given by

$$m_a\frac{d\mathbf{v}_a}{dt} = -\sum_b \left(\frac{P_a}{n_a^2} + \frac{P_b}{n_b^2}\right)\nabla_a W_{ab}, \tag{3.98}$$

which is somewhat different to the equation of motion used in Ott and Schnetter (2003) (they use the form 3.76 with $\sigma = 1$). The internal energy equation follows from the continuity equation (3.97) and the first law of thermodynamics (3.50). We find

$$m_a\frac{du_a}{dt} = \frac{P_a}{n_a^2}\sum_b \mathbf{v}_{ab}\cdot\nabla_a W_{ab}. \tag{3.99}$$

Ott and Schnetter (2003) use a formulation of the internal energy equation where the pressure term is symmetrised, which is inconsistent with their use of (3.96). The total energy equation consistent with

their formalism can also be derived using the Hamiltonian (§3.3.3) and is given by

$$m_a \frac{de_a}{dt} = -\sum_b \left(\frac{P_a}{n_a^2} \mathbf{v}_b + \frac{P_b}{n_b^2} \mathbf{v}_a \right) \cdot \nabla_a W_{ab}. \tag{3.100}$$

In this case use of the self-consistent formalism presented above should lead to slightly improved results over the momentum and energy equations employed by Ott and Schnetter (2003), since the density is still calculated via a direct summation over the particles.

3.5 Shocks

In any high-order numerical scheme, the simulation of shocks is accompanied by unphysical oscillations behind the shock front. This occurs because in discretising the continuum equations (in the SPH case using 3.5) we assume that the fluid quantities are smoothly varying on the smallest length scale (in SPH this is the smoothing length h). This means that discontinuities on such scales are not resolved by the numerical method. The simplest approach to this problem is to introduce a small amount of viscosity into the simulation which acts to spread out the shock front so that it can be sufficiently resolved (von Neumann and Richtmyer, 1950; Richtmyer and Morton, 1967). This is similar to the way in which shock fronts are smoothed out by nature, although in the latter case the effect occurs at a much finer level. The disadvantage of using such an 'artificial' viscosity is that it can produce excess heating elsewhere in the simulation. As such the use of artificial viscosity is regarded by many numerical practitioners as outdated since most finite difference schemes now rely on methods which either restrict the magnitude of the numerical flux across a shock front in order to prevent unphysical oscillations (such as total variation diminishing (TVD) schemes) or by limiting the jump in the basic variables across the shock front using the exact solution to the Riemann problem (Godunov-type schemes). There remain, however, distinct advantages to the use of an artificial viscosity, primarily that, unlike the Godunov-type schemes, it is easily applied where new physics is introduced (such as a more complicated equation of state than the ideal gas law) and the complexity of the algorithm does not increase with the number of spatial dimensions. In the case of magnetohydrodynamics, artificial viscosity is commonly used even in standard finite-difference codes[3] since the Riemann problem is difficult to solve and computationally expensive. Furthermore, dissipative terms are often still used even when a Riemann solver has been implemented (e.g. Balsara 1998). For these reasons artificial viscosity methods continue to find widespread usage, particularly in simulations using unstructured or Lagrangian meshes (Caramana et al., 1998).

In recent years it has been shown that Godunov-type schemes can in fact be used in conjunction with SPH by regarding interacting particle pairs as left and right states of the Riemann problem (Cha and Whitworth, 2003; Inutsuka, 2002; Parshikov and Medin, 2002; Monaghan, 1997b). In this manner the implementation of Godunov-type schemes to multidimensional problems is greatly simplified in SPH because the one-dimensional Riemann problem is solved between particle pairs, removing the need for complicated operator splitting procedures in higher dimensions. The formalism presented by Cha and Whitworth (2003) is remarkably simple to incorporate into any standard SPH code. A Godunov-type scheme for MHD in SPH would be extremely useful (although not widely applicable), but it is well

[3] for example in the widely used ZEUS code for astrophysical fluid dynamics (Stone and Norman, 1992)

beyond the scope of this thesis. We therefore formulate artificial dissipation terms using the formulation of Monaghan (1997b) which is generalised to the MHD case in §4.5. The problem of excess heating is addressed by the implementation of switches to turn off the dissipative terms away from shock fronts, described in §3.5.2.

3.5.1 Artificial viscosity and thermal conductivity

A variety of different formulations of artificial viscosity in SPH have been used, however the most common implementation is that given by Monaghan (1992), where the term in equation (3.54) is given by

$$\left(\frac{d\mathbf{v}_a}{dt}\right)_{diss} = \sum_b m_b \frac{-\alpha \bar{c}_{ab}\mu_{ab} + \beta\mu_{ab}^2}{\bar{\rho}_{ab}}\nabla_a W_{ab}, \qquad \mu_{ab} = \frac{h\mathbf{v}_{ab}\cdot\mathbf{r}_{ab}}{\mathbf{r}_{ab}^2 + 0.01h^2}, \tag{3.101}$$

where $\mathbf{v}_{ab} \equiv \mathbf{v}_a - \mathbf{v}_b$ (similarly for $\mathbf{r}_{ab}$), barred quantities refer to averages between particles a and b, and c refers to the sound speed. This viscosity is applied only when the particles are in compression (ie. $\mathbf{v}_{ab}\cdot\mathbf{r}_{ab} < 0$), is Galilean invariant, conserves total linear and angular momentum and vanishes for rigid body rotation. The β term (quadratic in $\mathbf{v}_{ab}$) represents a form of viscosity similar to the original formulation of von Neumann and Richtmyer (1950) and becomes dominant in the limit of large velocity differences (ie. in high Mach number shocks). The α term is linear in $\mathbf{v}_{ab}$ and is dominant for small velocity differences[4]. Most astrophysical SPH implementations follow Monaghan (1992) in setting $\alpha = 1$ and $\beta = 2$ which provides the necessary dissipation near a shock front.

The term given by equation (3.101) was constructed to have the properties described above, however in the relativistic case it was unclear as to what form such an artificial viscosity should take. Chow and Monaghan (1997) thus formulated an artificial viscosity for ultra-relativistic shocks in SPH by analogy with Riemann solvers. This is outlined by Monaghan (1997b) in a discussion of SPH and Riemann solvers. The essential idea is to regard the interacting particles as left and right Riemann states and to construct a dissipation which involves jumps in the physical variables. The dissipation term in the force (giving artificial viscosity) therefore involves a jump in the velocity variable and is similar to (3.101), taking the form (for $\mathbf{v}_{ab}\cdot\mathbf{r}_{ab} < 0$)

$$\left(\frac{d\mathbf{v}_a}{dt}\right)_{diss} = -\sum_b m_b \frac{\alpha \mathrm{v}_{sig}(\mathbf{v}_a - \mathbf{v}_b)\cdot\hat{\mathbf{r}}_{ab}}{2\bar{\rho}_{ab}}\nabla_a W_{ab}, \tag{3.102}$$

where v_{sig} is a signal velocity and $\hat{\mathbf{r}}_{ab} \equiv (\mathbf{r}_a - \mathbf{r}_b)/|\mathbf{r}_a - \mathbf{r}_b|$ is a unit vector along the line joining the particles. Note that this formalism differs from (3.101) in that a factor of $h/|\mathbf{r}_{ab}|$ has been removed. Also the $0.01h^2$ term has been removed from the denominator since for variable smoothing lengths it is unnecessary. The jump in velocity involves only the component along the line of sight since this is the only component expected to change at a shock front. In a similar manner, the dissipative term in the specific energy equation (3.63) is given by

$$\left(\frac{de_a}{dt}\right)_{diss} = -\sum_b m_b \frac{\mathrm{v}_{sig}(e_a^* - e_b^*)}{2\bar{\rho}_{ab}}\hat{\mathbf{r}}_{ab}\cdot\nabla_a W_{ab}, \tag{3.103}$$

[4]The introduction of such a term into artificial viscosity methods is generally attributed to Landshoff (1955) (see, e.g. Caramana et al. 1998)

where $(e_a^* - e_b^*)$ is the jump in specific energy. The specific energy used in this term is given by

$$e_a^* = \begin{cases} \frac{1}{2}\alpha(\mathbf{v}_a \cdot \hat{\mathbf{r}}_{ab})^2 + \alpha_u u_a, & \mathbf{v}_{ab} \cdot \mathbf{r}_{ab} < 0; \\ \alpha_u u_a & \mathbf{v}_{ab} \cdot \mathbf{r}_{ab} \geq 0; \end{cases} \tag{3.104}$$

that is, where the specific kinetic energy has been projected along the line joining the particles, since only the component of velocity parallel to this vector is expected to jump at a shock front. Note that in general we use a different parameter α_u to control the thermal energy term and that this term is applied to particles in both compression and rarefaction.

The signal velocity represents the maximum speed of signal propagation along the line of sight between the two particles. Whilst many formulations could be devised, it turns out that the results are not sensitive to the particular choice made. A simple estimate of the signal velocity is given by

$$\mathrm{v}_{sig} = c_a + c_b - \beta \mathbf{v}_{ab} \cdot \hat{\mathbf{r}}_{ab} \tag{3.105}$$

where c_a denotes the speed of sound of particle a and $\beta \sim 1$, such that $\mathrm{v}_{sig}/2$ is an estimate of the maximum speed for linear wave propagation between the particles. The β term, which acts as a von Neumann and Richtmyer viscosity as in equation (3.101), arises naturally in this formulation. Practical experience suggests, however, that $\beta = 2$ is a better choice. For a more general discussion of signal velocities we refer the reader to Monaghan (1997b) and Chow and Monaghan (1997).

The contribution to the thermal energy from the dissipative terms is found using

$$\frac{du_a}{dt} = \frac{de_a}{dt} - \mathbf{v}_a \cdot \frac{d\mathbf{v}_a}{dt}. \tag{3.106}$$

In this case we obtain

$$\left(\frac{du_a}{dt}\right)_{diss} = \sum_b m_b \frac{\mathrm{v}_{sig}}{2\bar{\rho}_{ab}} \left\{ -\frac{1}{2}\alpha \left[(\mathbf{v}_a - \mathbf{v}_b) \cdot \hat{\mathbf{r}}_{ab}\right]^2 + \alpha_u (u_a - u_b) \right\} \hat{\mathbf{r}}_{ab} \cdot \nabla_a W_{ab} \tag{3.107}$$

which is added to the non-dissipative term (3.58). The first term is the positive definite contribution to the thermal energy from the artificial viscosity (since the kernel gradient is always negative). The second term (involving a jump in thermal energy) provides an artificial thermal conductivity. Physically this means that discontinuities in the thermal energy are also smoothed.

The artificial dissipation given by (3.102)-(3.107) is used as a basis for constructing an appropriate dissipation for the MHD case in §4.5.

3.5.2 Artificial dissipation switches

Artificial viscosity

In both (3.101) and (3.102) the artificial viscosity is applied universally across the particles despite only being needed when and where shocks actually occur. This results in SPH simulations being much more dissipative than is necessary and can cause problematic effects where this dissipation is unwanted (such as in the presence of shear flows). A switch to reduce the artificial viscosity away from shocks is given by Morris and Monaghan (1997). Using this switch in multi-dimensional simulations substantially reduces

the problematic effects of using an artificial viscosity in SPH.

The key idea is to regard the dissipation parameter α (c.f. equation 3.102) as a particle property. This can then be evolved along with the fluid equations according to

$$\frac{d\alpha_a}{dt} = -\frac{\alpha_a - \alpha_{min}}{\tau_a} + \mathscr{S}_a, \tag{3.108}$$

such that in the absence of sources $\mathscr{S}$, α decays to a value α_{min} over a timescale τ. The timescale τ is calculated according to

$$\tau = \frac{h}{\mathscr{C} \mathrm{v}_{sig}}, \tag{3.109}$$

where h is the particle's smoothing length, v_{sig} is the maximum signal propagation speed at the particle location and $\mathscr{C}$ is a dimensionless parameter with value $0.1 < \mathscr{C} < 0.2$. We conservatively use $\mathscr{C} = 0.1$ which means that the value of α decays to α_{min} over ~ 5 smoothing lengths.

The source term $\mathscr{S}$ is chosen such that the artificial dissipation grows as the particle approaches a shock front. We use (Rosswog et al., 2000)

$$\mathscr{S} = \max(-\nabla \cdot \mathbf{v}, 0)(2.0 - \alpha), \tag{3.110}$$

such that the dissipation grows in regions of strong compression. Following Morris and Monaghan (1997) where the ratio of specific heats γ differs from 5/3 (but not for the isothermal case), we multiply $\mathscr{S}$ by a factor

$$\left[\ln\left(\frac{5/3+1}{5/3-1}\right)\right] / \left[\ln\left(\frac{\gamma+1}{\gamma-1}\right)\right] \tag{3.111}$$

The source term is multiplied by a factor $(2.0 - \alpha)$ as the standard source term given by Morris and Monaghan (1997) was found to produce insufficient damping at shock fronts when used in conjunction with the Monaghan (1997b) viscosity. The source term (3.110) is found to provide sufficient damping on the Sod (1978) hydrodynamic shock tube problem and in the MHD shock tube tests we describe in chapter §4.6 (ie. $\alpha_{max} \sim 1$ for these problems). In order to conserve momentum the average value $\bar{\alpha} = 0.5(\alpha_a + \alpha_b)$ is used in equations (3.102), (3.104) and (3.107). A lower limit of $\alpha_{min} = 0.1$ is used to preserve order away from shocks (note that this is an order of magnitude reduction from the usual value of $\alpha = 1.0$ everywhere).

The numerical tests in §4.6 demonstrate that use of this switch gives a significant reduction in dissipation away from shocks whilst preserving the shock-capturing ability of the code.

Artificial thermal conductivity

A similar switch to that used in the artificial viscosity may therefore be devised for the artificial thermal conductivity term, with the parameter α_u evolved according to

$$\frac{d\alpha_{u,a}}{dt} = -\frac{\alpha_{u,a} - \alpha_{u,min}}{\tau_a} + \mathscr{S}_a, \tag{3.112}$$

where the decay timescale τ is the same as that used in (3.108) and in this case we use $\alpha_{u,min} = 0$. The corresponding source term is given by

$$\mathscr{S} = |\nabla\sqrt{u}|, \tag{3.113}$$

which is constructed to have dimensions of inverse time. The gradient term is computed according to

$$\nabla\sqrt{u} = \frac{1}{2}u^{-1/2}\nabla u, \tag{3.114}$$

where

$$\nabla u_a = \frac{1}{\rho_a}\sum_b m_b(u_a - u_b)\nabla_a W_{ab}(h_a). \tag{3.115}$$

Use of this switch ensures that artificial thermal conductivity is only applied at large gradients in the thermal energy. The need to do so in dissipation-based shock capturing schemes is often concealed by smoothing of the initial conditions in shock tube tests (§3.7.3). From the first law of thermodynamics (3.50) we infer that gradients in the thermal energy correspond to large gradients in the density. In a hydrodynamic shock these occur either at the shock front or at the contact discontinuity. Artificial viscosity is not required at the contact discontinuity because the pressure is constant across it. Using unsmoothed initial conditions and in the absence of artificial thermal conductivity, a significant overshoot in thermal energy occurs at the contact discontinuity (this phenomenon is known as 'wall heating' and is illustrated in Figure 3.9). The resulting glitch in the pressure is often ascribed to 'starting errors' due to the unsmoothed initial conditions. However, applying smoothing to the initial conditions of a shock-tube test means that gradients across the contact discontinuity remain smoothed throughout the evolution (see e.g. Figure 3.8), removing the need for artificial thermal conductivity which acts to spread gradients in the thermal energy. Whilst there is also a gradient in thermal energy at a shock front, this is smoothed out by the application of artificial viscosity there and so the need for artificial thermal conductivity can go unnoticed. In §3.7.3 we present results of the standard Sod (1978) shock tube test, showing the effectiveness of the switch discussed above in applying the requisite amount of smoothing at the contact discontinuity.

3.6 Timestepping

3.6.1 Predictor-corrector scheme

We integrate the SPH equations in this thesis using a slight modification of the standard predictor-corrector (Modified Euler) method which is second order accuracy in time (Monaghan, 1989). The predictor step is given by

$$\mathbf{v}^{1/2} = \mathbf{v}^0 + \frac{\Delta t}{2}\mathbf{f}^0, \tag{3.116}$$

$$\mathbf{r}^{1/2} = \mathbf{r}^0 + \frac{\Delta t}{2}\mathbf{v}^{1/2}, \tag{3.117}$$

$$e^{1/2} = e^0 + \frac{\Delta t}{2}\dot{e}^0, \tag{3.118}$$

where in practice we use $\mathbf{f}^0 \approx \mathbf{f}^{-1/2}$ and $\dot{e}^0 \approx \dot{e}^{-1/2}$ to give a one-step method. The rates of change of these quantities are then computed via the SPH summations using the predicted values at the half step, ie.

$$\mathbf{f}^{1/2} = \mathbf{f}(\mathbf{r}^{1/2}, \mathbf{v}^{1/2}) \qquad \dot{e}^{1/2} = \dot{e}(\mathbf{r}^{1/2}, \mathbf{v}^{1/2}) \tag{3.119}$$

The corrector step is given by

$$\mathbf{v}^* = \mathbf{v}^0 + \frac{\Delta t}{2}\mathbf{f}^{1/2}, \tag{3.120}$$

$$\mathbf{r}^* = \mathbf{r}^0 + \frac{\Delta t}{2}\mathbf{v}^*, \tag{3.121}$$

$$e^* = e^0 + \frac{\Delta t}{2}\dot{e}^{1/2}, \tag{3.122}$$

and finally

$$\mathbf{v}^1 = 2\mathbf{v}^* - \mathbf{v}^0, \tag{3.123}$$

$$\mathbf{r}^1 = 2\mathbf{r}^* - \mathbf{r}^0, \tag{3.124}$$

$$e^1 = 2e^* - e^0. \tag{3.125}$$

Note that in this scheme the position updates in both the predictor and corrector steps use the updated value of velocity. This effectively means that the position is updated using both the first and second derivatives. From numerical experiments we find that this scheme gives much better stability properties. Where evolved, density, smoothing length, magnetic field and the dissipation parameters follow the energy evolution. The total energy e is interchangeable for the thermal energy u.

3.6.2 Reversible integrators

The simple predictor-corrector method given above is adequate for all the problems considered in this thesis since the integration time is quite short. For large simulations over long timescales, however, the accuracy and stability of the integration method needs more careful attention. In the past decade or so a substantial research effort has been devoted to the development of high accuracy so-called 'geometric' integrators for Hamiltonian systems (e.g. Hut et al., 1995; Stoffer, 1995; Huang and Leimkuhler, 1997; Holder et al., 2001; Hairer et al., 2002). Since SPH in the absence of dissipative terms can derived from a Hamiltonian variational principle, much of this work is applicable in the SPH context. The primary condition for the construction of a geometric integrator is time-reversibility (that is, particle quantities should return to their original values upon reversing the direction of time integration). It is fairly straightforward to construct a reversible integrator for the SPH equations in the case of a constant smoothing length, where the density summation is used and where the pressure is calculated directly from the density (such that the force evaluation uses only the particle co-ordinates). The standard leapfrog algorithm is one such example. In general, however, the construction of a reversible scheme is complicated by several factors. The first is the use of a variable timestep (which immediately destroys the time-symmetry in the leapfrog scheme, although see Holder et al. (2001) for recent progress on this). The second complicating factor is that the reversibility condition becomes more difficult when equations with rates of change involving the

particle velocity are used (such as the thermal or total energy equation or the continuity equation for the density). In this case the construction of a reversible integrator for SPH necessarily involves the calculation of derivatives involving the velocity in separate step to the force evaluation, leading to additional computational expense. A third complicating factor is the use of individual particle timesteps in large SPH codes, although symplectic methods have also been constructed for this case (Hairer et al., 2002).

3.6.3 Courant condition

The timestep is determined by the Courant condition

$$\mathrm{dt_c} = C_{cour} \min\left(\frac{h}{\mathrm{v}_{sig}}\right) \tag{3.126}$$

where $h = \min(h_a, h_b)$ and v_{sig} is the maximum signal velocity between particle pairs. This signal velocity is similar to that used in the artificial dissipation terms (§3.5), except that we use

$$\mathrm{v}_{sig} = \frac{1}{2}\left(\mathrm{v}_a + \mathrm{v}_b + \beta|\mathbf{v}_{ab}\cdot\mathbf{j}|\right) \tag{3.127}$$

with $\beta = 1$ when $\mathbf{v}_{ab}\cdot\mathbf{j} > 0$ (ie. where the dissipation terms are not applied). The minimum in (3.126) is taken over all particle interactions and typically we use $C_{cour} = 0.4$.

Although this condition is sufficient for all of the simulations described here, in general it is necessary to pose the additional constraint from the forces

$$\mathrm{dt_f} = C_f \min\left(\frac{h_a}{|\mathbf{a}_a|}\right)^{1/2}, \tag{3.128}$$

where $\mathbf{a}_a$ is the acceleration on particle a and typically $C_f = 0.25$.

3.7 Numerical tests

3.7.1 Implementation

Unless otherwise indicated the simulations use the density summation (3.42), the momentum equation (3.54) and the energy equation in the form (3.63). The numerical tests presented throughout this thesis were implemented using a code written by the author as a testbed for MHD algorithms.

Neighbour finding

Since the code has been designed for flexibility rather than performance, we take a simplified approach to neighbour finding using linked lists. The particles are binned into grid cells of size $2h$ where h is the maximum value of smoothing length over the particles. Particles in a given cell then search only the adjoining cells for contributing neighbours. This approach becomes very inefficient for a large range in smoothing lengths such that for large simulations it is essential to use a more effective algorithm. A natural choice is to use the tree code used in the computation of the gravitational force (Hernquist and Katz, 1989; Benz et al., 1990).

Boundary conditions

Boundary conditions are implemented using either ghost or fixed particles. For reflecting boundaries, ghost particles are created which mirror the SPH particles across the boundary. These particles are exact copies of the SPH particles in all respects except for the velocity, which is of opposite sign on the ghost particle, producing a repulsive force at the boundary. For periodic boundary conditions the ghosts are exact copies of the particles at the opposite boundary. In the MHD shock tube tests considered in §4.6 involving non-zero velocities at the boundaries, boundary conditions are implemented in one dimension by simply fixing the properties of the 6 particles closest to each boundary. Where the initial velocities of these particles are non-zero their positions are evolved accordingly and a particle is removed from the domain once it has crossed the boundary. Where the distance between the closest particle and the boundary is more than the initial particle spacing a new particle is introduced to the domain. Hence for inflow or outflow boundary conditions the resolution changes throughout the simulation.

3.7.2 Propagation and steepening of sound waves

We initially consider the propagation of linear sound waves in SPH. This test is particularly important in the MHD case (§4.6.4) since it highlights the instability in the momentum-conserving formalism of SPMHD. In this case we investigate the dependence of sound speed on smoothing length and the damping due to artificial viscosity.

Particle setup

The particles are initially setup at equal separations in the domain $x = [0,1]$ using ghost particles (§3.7.1) to create periodic boundary conditions. The linear solution for a travelling sound wave in the x-direction is given by

$$\rho(x,t) = \rho_0(1 + A\sin(kx_a - \omega t), \tag{3.129}$$

$$\mathrm{v}_x(x,t) = C_s A\sin(kx_a - \omega t), \tag{3.130}$$

where $\omega = 2\pi C_s/\lambda$ is the angular frequency, C_s is the sound speed in the undisturbed medium and $k = 2\pi/\lambda$ is the wavenumber. The initial conditions therefore correspond to $t = 0$ in the above. The perturbation in density is applied by perturbing the particles from an initially uniform setup. We consider the one dimensional perturbation

$$\rho = \rho_0[1 + \mathrm{Asin(kx)}], \tag{3.131}$$

where $A = D/\rho_0$ is the perturbation amplitude. The cumulative total mass in the x direction is given by

$$\begin{aligned} M(x) &= \rho_0 \int [1 + \mathrm{Asin(kx)}]\mathrm{dx} \\ &= \rho_0[x - \mathrm{Acos(kx)}]_0^x, \end{aligned} \tag{3.132}$$

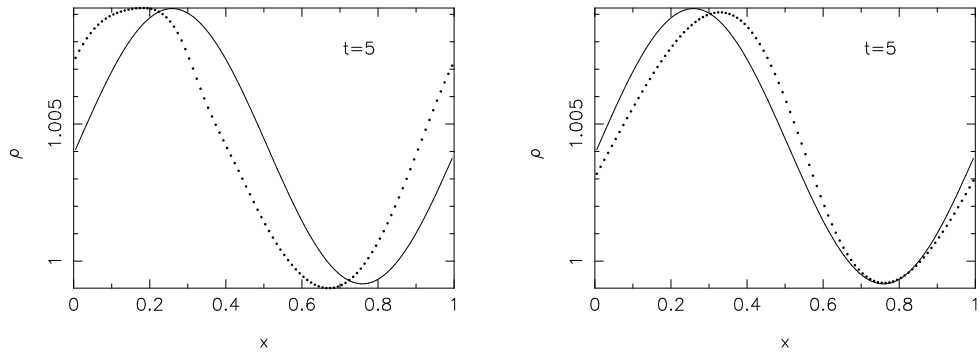

Figure 3.3: Representative results from the isothermal sound wave tests in one dimension using the standard cubic spline kernel with a fixed smoothing length. The figure on the left shows the results after 5 periods (corresponding to 5 crossings of the computational domain) using $h = 1.5\Delta p$. The figure on the right shows the results using a fixed smoothing length but with the correction from the variable smoothing length terms.

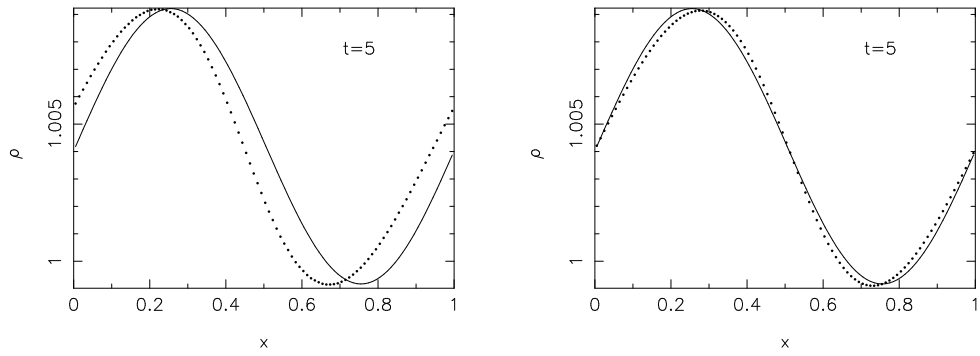

Figure 3.4: Representative results from the isothermal sound wave tests in one dimension using the standard cubic spline kernel with a variable smoothing length that varies with density. The figure on the left shows the results after 5 periods using a simple average of the kernel gradients, whilst the figure on the right shows the results using the consistent formulation of the variable smoothing length terms.

such that the cumulative mass at any given point as a fraction of the total mass is given by

$$\frac{M(x)}{M(x_{max})}. \tag{3.133}$$

For equal mass particles distributed in $x = [0, x_{max}]$ the cumulative mass fraction at particle a is given by x_a/x_{max} such that the particle position may be calculated using

$$\frac{x_a}{x_{max}} = \frac{M(x_a)}{M(x_{max})}. \tag{3.134}$$

Substituting the expression for $M(x)$ we have the following equation for the particle position

$$\frac{x_a}{x_{max}} - \frac{x_a - \mathrm{A}\cos(\mathrm{k}x_a)}{[x_{max} - \mathrm{A}\cos(\mathrm{k}x_{max})]} = 0, \tag{3.135}$$

which we solve iteratively using a simple Newton-Raphson rootfinder. With the uniform particle distribution as the initial conditions this converges in one or two iterations.

One dimensional tests

Initially we consider one dimensional, isothermal simulations using a fixed smoothing length (for which the results of the stability analysis given in §3.2.7 hold). The cubic spline kernel is used with $h = 1.5\Delta p$ where Δp is the initial particle spacing. This value of smoothing length was chosen because in Figure 3.2 the cubic spline is seen to significantly underestimate the sound speed at this value of h. The simulation is setup using 100 particles (corresponding to $k_x = 0.0628$ in Figure 3.2) and a wave amplitude of 0.005 to ensure that the wave remains essentially linear throughout the simulation. No artificial viscosity is used. For isothermal simulations, the pressure is calculated directly from the density using $P = c_s^2\rho$. The sound speed given by the SPH simulations is estimated from the temporal spacing of minima in the total kinetic energy of the particles.

A representative example of these simulations is given in the left hand side of Figure 3.3 after five crossings of the computational domain. The amplitude is well maintained by the SPH scheme, however the wave lags behind the exact solution, giving a significant phase error as expected from the stability analysis (Figure 3.2). The sound speed obtained from the numerical tests is plotted in Figure 3.5 for a range of smoothing length values (solid points). In this case the results show excellent agreement with the analytic results using the dispersion relation (3.41) given by the solid line (this line corresponds to $k_x \approx 0$ in Figure 3.2). We observe that, depending on the value of h the numerical sound wave can both lag and lead the exact solution (in Figure 3.5 this corresponds to sound speeds less than or greater than unity).

In §3.3.4 it was noted that the variable smoothing length terms normalise the kernel even in the case of a fixed smoothing length. The results of the fixed smoothing length simulation with this correction term are shown by the dashed line in Figure 3.5, with a representative example given in the right hand side of Figure 3.3. The numerical wave speed appears much closer to the theoretical value of unity.

Results using a smoothing length which varies with density according to (3.68) are given by the dot-dashed line in Figure 3.5, with a representative example shown in Figure 3.4. The phase error is slightly lower than either of the fixed smoothing length cases. Including the normalisation of the kernel gradient from the variable smoothing lengths (§3.3.4) gives numerical sound speeds very close to unity (dotted line in Figure 3.5). A representative example of these simulations is given in the right hand panel of Figure 3.4 after 5 periods. The results in this case show excellent agreement with the exact (linear) solution, with a small amount of steepening due to nonlinear effects.

The results of this test indicate that, whilst alternative kernels can give slight improvements in accuracy over the standard cubic spline (§3.2.7), a substantial gain in accuracy can be gained firstly by the use of a variable smoothing length and secondly by self-consistently accounting for ∇h terms in the formulation of the SPH equations. These terms act as a normalisation of the kernel gradient which appear to effectively remove the dependence of the numerical sound speed on the smoothing length value.

Effects of artificial viscosity

In the absence of any switches, the artificial viscosity is specified according to (3.102) with $\alpha = 1$, $\beta = 2$ everywhere. The results of the sound wave propagation with artificial viscosity turned on are shown in the left panel of Figure 3.6. After 5 crossings of the computational domain the wave is severely damped by

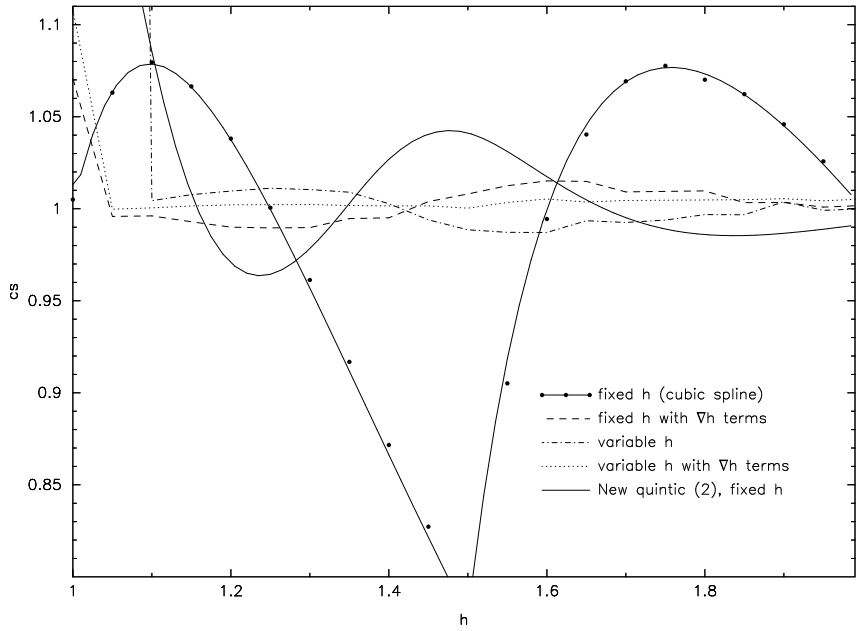

Figure 3.5: Summary of the isothermal sound wave tests using 100 particles. The numerical sound speed from the SPH simulations is shown plotted against the (mean) smoothing length in units of the average particle spacing. Results using the cubic spline kernel with a fixed smoothing length (solid points) may be compared with the analytic result (solid line, under points) from the dispersion relation (3.41) (this line corresponds to $kx = 0$ in Figure 3.2). The dashed line gives the numerical results using the cubic spline with a fixed smoothing length but incorporating the correction from the ∇h terms, which show much lower phase errors. The dotted and dot-dashed lines give numerical results using the cubic spline with a variable smoothing length with and without the ∇h terms respectively. In both cases the results show a substantial improvement over the fixed smoothing length case, much more so than from the use of alternative kernels (e.g. the New Quintic (2) from §3.2.6, given by the solid line).

the artificial viscosity term. The effect is to reduce the order of the numerical scheme since convergence to the exact solution is much slower. The results using the artificial viscosity switch discussed in §3.5.2 are shown in the right panel of Figure 3.6. The results show good agreement with the linear solution, demonstrating that use of the artificial viscosity switch very effectively restores the numerical schemes ability to propagate small perturbations without excessive damping.

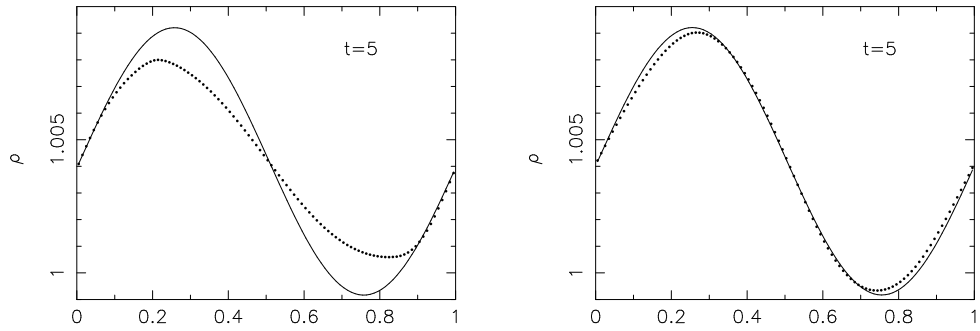

Figure 3.6: (left) Isothermal sound wave with amplitude = 0.005 in one dimension with artificial viscosity applied uniformly to particles in compression (ie. $\alpha = 1$, $\beta = 2$) and (right) applied using the viscosity switch with $\alpha_{min} = 0.1$.

Finally, we demonstrate the usefulness of the artificial viscosity switch by considering the steepening

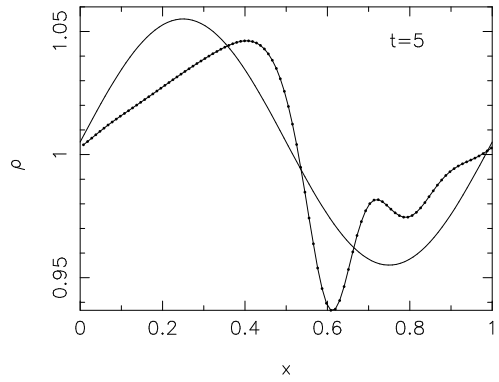

Figure 3.7: Nonlinear isothermal sound wave in one dimension showing steepening to shock. The wave profile is shown after 5 crossings of the computational domain, corresponding to 5 periods. The initial conditions are a linear wave with amplitude 0.05 (solid line). With artificial viscosity applied using the switch the steepening is resolved, although some oscillations are observed to occur ahead of the steepened wave.

of a nonlinear sound wave. In this case the initial amplitude is 0.05 and artificial viscosity is applied using the switch. The wave profile at $t = 5$ is shown in Figure 3.7 and is significantly steepened compared to the initial conditions (solid line). The use of the switch enables the steepening to be resolved, however some oscillations are found to occur ahead of the steepened wave.

3.7.3 Sod shock tube

The standard shock tube test for any compressible fluid dynamics code is that of Sod (1978). The problem consists of dividing the domain into two halves, one consisting of high pressure, high density gas whilst the other is low pressure and low density. These two portions of gas are allowed to interact at $t = 0$, resulting in a shock and rarefaction wave which propagate through the gas. This test illustrates the shock capturing ability of the 1D code and thus provides a good test of the artificial viscosity formalism (§3.5). It is also the basis for the MHD shock tube considered in §4.6.3. We set up the problem using 450 SPH particles in the domain $x = [-0.5, 0.5]$. The particles are setup with uniform masses such that the density jump is modelled by a jump in particle separation. Initial conditions in the fluid to the left of the origin are given by $(\rho, P, \mathrm{v}_x) = [1, 1, 0]$ whilst conditions to the right are given by $(\rho, P, \mathrm{v}_x) = [0.125, 0.1, 0]$ with $\gamma = 1.4$. The particle separation to the left of the discontinuity is 0.01.

Figure 3.8 shows the results of this problem at $t = 0.2$. The exact solution, calculated using the exact Riemann solver given in Toro (1992) is given by the solid line. In this case artificial viscosity has been applied uniformly to particles in compression (ie. using $\alpha = 1$), whilst no artificial thermal conductivity has been used (ie. $\alpha_u = 0$). The results are generally good although there is significant deviation in the slope of the rarefaction wave. This can be traced largely to the smoothing applied to the initial conditions. Following Monaghan (1997b) (although a similar procedure is applied in many published versions of this test), the initial discontinuities in density and pressure were smoothed over several particles according to the rule

$$A = \frac{A_L + A_R e^{x/d}}{1 + e^{x/d}} \tag{3.136}$$

where A_L and A_R are the uniform left and right states with respect to the origin and d is taken as half of the largest initial particle separation at the interface (ie. the particle separation on the low density side). Where the initial density is smoothed the particles are spaced according to the rule

$$\rho_a(x_{a+1} - x_{a-1}) = 2\rho_R\Delta_R \tag{3.137}$$

where Δ_R is the particle spacing to the far right of the origin with density ρ_R. Note that initial smoothing lengths are set according to the rule $h \propto 1/\rho$ and are therefore also smoothed. Where the total energy $\hat{\varepsilon}$ is integrated we smooth the basic variable u construct the total energy from the sum of the kinetic and internal energies.

Such smoothing of the initial conditions can be avoided altogether if the density summation (3.42) is used, particularly if the smoothing length is updated self-consistently with the density. The results of this problem using unsmoothed initial conditions are shown in Figure 3.9. The artificial viscosity is applied uniformly whilst no artificial thermal conductivity has been used. In this case the rarefaction profile agrees extremely well with the exact solution (solid line). The unsmoothed initial conditions highlight the need for artificial thermal conductivity since the thermal energy overshoots at the contact discontinuity with a resulting glitch in the pressure profile. The gradient in thermal energy at the shock front does not show this effect due to the smoothing of the shock by the artificial viscosity term. The results of this test with a small amount of artificial thermal conductivity applied using the switch discussed in §3.5.2 are shown in Figure 3.10. The variable smoothing length terms have also been used in this case, although results are similar with a simple average of the kernel gradients in the force equation (3.54). The contact discontinuity is smoothed over several smoothing lengths by the thermal conductivity term, removing the overshoot in the thermal energy. The resulting profiles compare extremely well with the exact solution (solid line).

Finally, the results of this test where both the artificial viscosity and conductivity are controlled using the switches described in §3.5.2 are shown in Figure 3.11. The top row shows the velocity and thermal energy profiles compared with the exact solution (solid line), whilst the bottom row shows the time-varying co-efficients α and α_u of the viscosity and thermal conductivity respectively. With the unsmoothed initial conditions and the viscosity switch there is a slight oscillation in the velocity profile at the head of the rarefaction wave. The variable smoothing length terms have been used in this case involving the consistent update of the smoothing length with density (§3.3.4). If a simple average of the kernel gradients is used instead the oscillations in the rarefaction wave are still present but slightly less pronounced. In effect, the iterations of density and smoothing length make the scheme much more sensitive to small perturbations, since a small change in the smoothing length will be reflected in the density profile and vice-versa. This means that structures in the simulation are in general better resolved and is clearly advantageous. However alsos mean that small errors in the density evolution are amplified where they may otherwise have been smoothed out by the numerical scheme.

3.7.4 Blast wave

In this test we consider a more extreme version of the shock tube test considered previously. In this problem the initial conditions in the fluid to the left of the origin are given by $(\rho, P, \mathrm{v}_x) = [1, 1000, 0]$

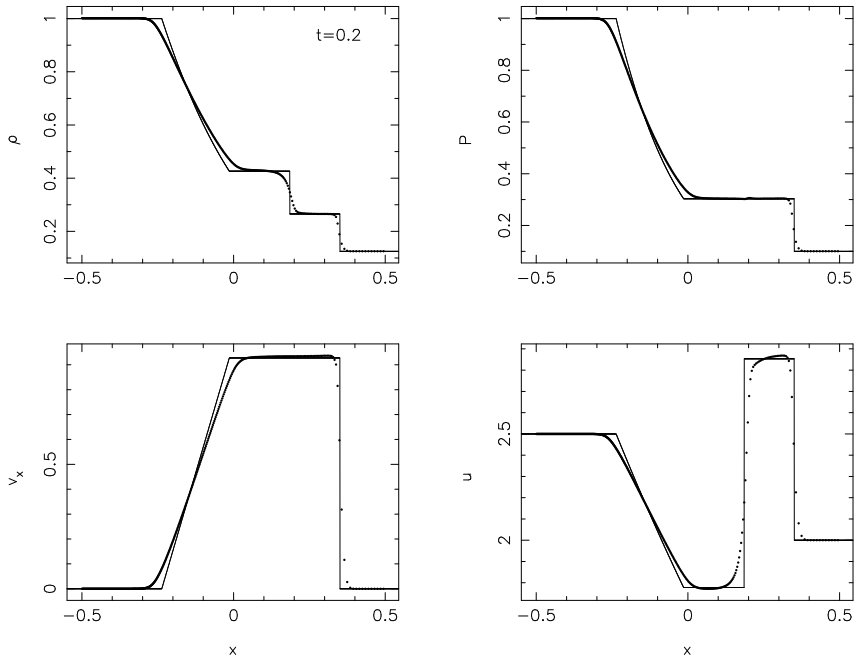

Figure 3.8: Results of the Sod shock tube problem in one dimension. The simulation uses 450 particles with conditions in the fluid initially to the left of the origin given by $(\rho, P, \mathrm{v}_x) = [1, 1, 0]$ whilst conditions to the right are given by $(\rho, P, \mathrm{v}_x) = [0.125, 0.1, 0]$ with $\gamma = 1.4$. Initial profiles of density and pressure have been smoothed and artificial viscosity is applied uniformly. Agreement with the exact solution (solid line) is generally good, but note the deviation from the exact solution in the rarefaction wave due to the initial smoothing.

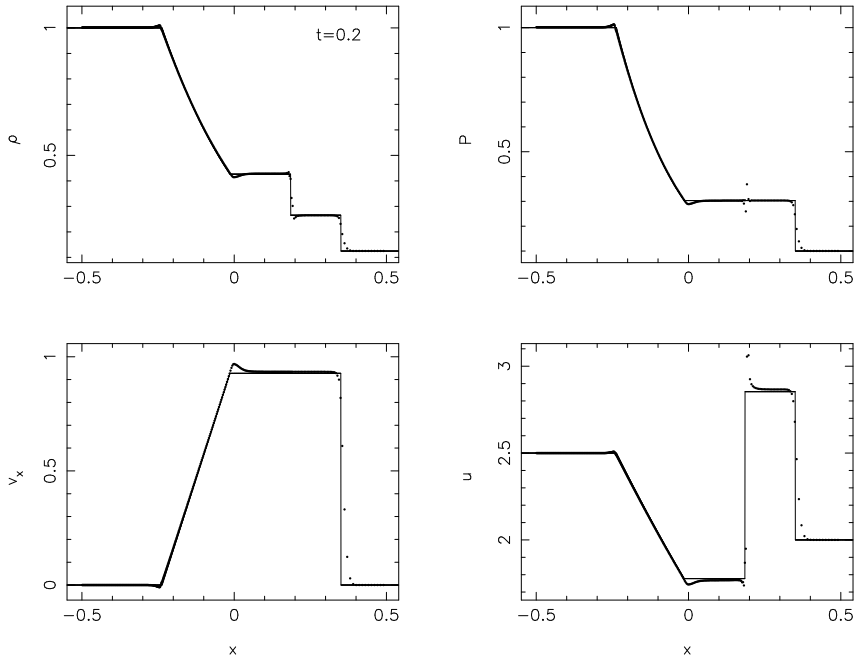

Figure 3.9: Results of the Sod shock tube problem using unsmoothed (purely discontinuous) initial conditions. Artificial viscosity has been applied uniformly whilst no artificial thermal conductivity has been used. In the absence of any smoothing of the initial conditions the rarefaction profile agrees well with the exact solution (solid line). The thermal energy is observed to overshoot at the contact discontinuity. There is also a small overshoot in velocity at the right end of the rarefaction wave.

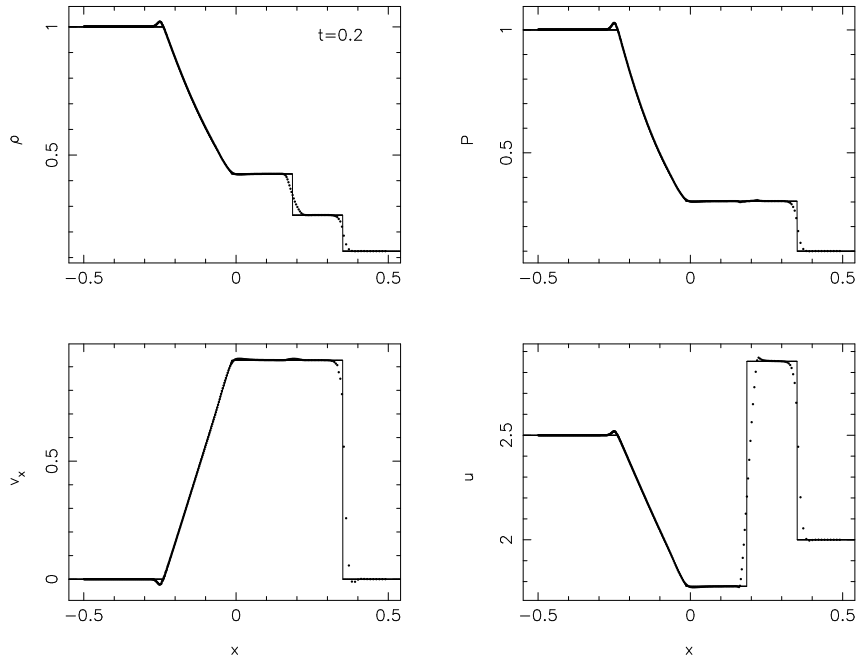

Figure 3.10: Results of the Sod shock tube problem using unsmoothed initial conditions and applying a small amount of artificial thermal conductivity using the switch described in §3.5.2. Artificial viscosity is applied uniformly. The overshoot in the thermal energy observed in Figure 3.9 is corrected for by the smoothing of the contact discontinuity produced by the thermal conductivity term. The variable smoothing length terms have also been used in this case, although results are similar with a simple average of the particle kernels.

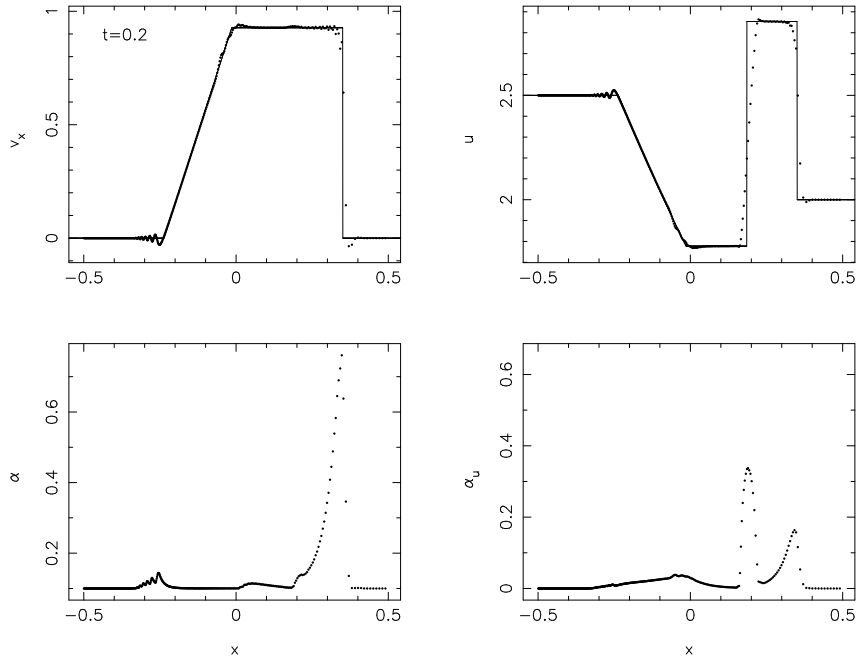

Figure 3.11: Velocity and thermal energy profiles (top row) in the Sod shock tube problem using unsmoothed initial conditions and where both artificial viscosity and thermal conductivity are applied using the switches discussed in §3.5.2. The bottom row shows the time-varying co-efficients α and α_u of the viscosity and thermal conductivity respectively. With the unsmoothed initial conditions and the viscosity switch there is a slight oscillation in the velocity profile at the head of the rarefaction wave. The variable smoothing length terms have also been used in this case.

whilst conditions to the right are given by $(\rho, P, \mathrm{v}_x) = [1, 0.1, 0]$ with $\gamma = 1.4$. The 10^4 pressure ratio across the initial discontinuity results in a strong blast wave which propagates into the fluid to the right of the origin. The velocity of the contact discontinuity is very close to that of the shock, producing a sharp density spike behind the shock front. This test therefore presents a demanding benchmark for any numerical code.

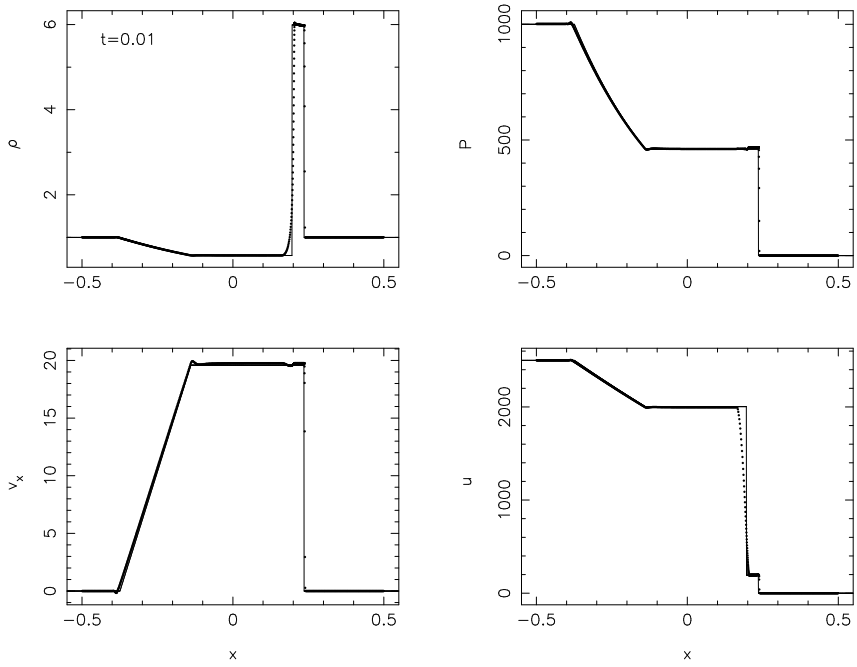

Figure 3.12: Results of the one dimensional blast wave test at $t = 0.01$. Conditions in the fluid initially to the left of the origin given by $(\rho, P, \mathrm{v}_x) = [1, 1000, 0]$ whilst conditions to the right are given by $(\rho, P, \mathrm{v}_x) = [1, 0.1, 0]$ with $\gamma = 1.4$. 1000 particles have been used with no smoothing of the initial conditions. The agreement with the exact solution (solid line) is excellent. The contact discontinuity is spread sufficiently by the artificial thermal conductivity to be resolved accurately. In this simulation the density summation and the average of the kernel gradients has been used.

The results of this test at $t = 0.01$ are shown in Figure 3.12. The agreement with the exact solution (solid line) is excellent. In this simulation the density summation and the average of the kernel gradients has been used and the artificial viscosity is applied using the viscosity switch. The SPH results may be compared with those given in Monaghan (1997b). Although we use the same formulation of the dissipative terms as in Monaghan (1997b), in that paper the artificial thermal conductivity is applied only for particles in compression, resulting in a need to smooth the initial discontinuity in the pressure. With the thermal conductivity term applied using the switch the contact discontinuity is spread sufficiently in order to be resolved accurately and smoothing of the initial conditions is therefore unnecessary. In the SPH solution given by Monaghan (1997b) the spike in density is observed to overshoot the exact solution, which is not observed in this case. This is due to the use of the density summation (3.42) rather than evolving the continuity equation (3.43) as in Monaghan (1997b). Use of the continuity equation is more efficient since it does not require an extra pass over the particles in order to calculate the density. Using alternative formulations of the pressure term in the momentum equation (e.g. using equation (3.76) with $\sigma = 1$) gives similar results (although the Hernquist and Katz (1989) formulation (3.92) appears to produce negative pressures on this problem). Using the consistent alternative formulations of the

continuity equation, however, appears to worsen the overshoot observed in the density spike compared to the usual continuity equation (for example in the $\sigma = 1$ case, the density spike overshoots to $\rho_{max} \approx 10$ when the continuity equation (3.86) is used).

3.7.5 Cartesian shear flows

In a recent paper Imaeda and Inutsuka (2002) (hereafter II02) have suggested that SPH gives particularly poor results on problems involving significant amounts of shear. The simplest test considered by II02 is a Cartesian shear flow. The setup is a two dimensional, uniform density $\rho = 1$ box in the domain $0 \leq x \leq 1$ and $0 \leq y \leq 1$ with a shear velocity field $\mathrm{v}_x = 0, \mathrm{v}_y = \sin(2\pi x)$ and periodic boundary conditions in the $x-$ and $y-$ directions. In general such flows are known (at least in the incompressible case) to be unstable to Kelvin-Helmholtz instabilities at the inflection point in the velocity profile (e.g. Drazin and Reid, 1981). However, a straightforward stability analysis of this flow demonstrates that it is indeed stable to small perturbations in the $x-$direction (note, however that the application of viscosity can significantly affect the stability properties for these types of problems).

We setup the problem using 2500 (50 x 50) particles initially arranged on a cubic lattice. The smoothing length we use is set according to

$$h = \eta \left(\frac{m}{\rho}\right)^{\frac{1}{2}}, \tag{3.138}$$

where we use $\eta = 1.2$, resulting in an initially uniform value of $h = 0.024$. The smoothing length is allowed to change with density according to (3.68), although this has little effect since the density remains close uniform throughout the simulation. The equation of state is isothermal such that the pressure is given in terms of the density via $P = c_s^2 \rho$. As in II02, we consider both the pressure-free case ($c_s = 0$) and also using $c_s = 0.05$, in both cases using no artificial viscosity. The results for the pressure-free case are shown in Figure 3.13. After 50 dynamical times (defined as one crossing of the computational domain at the highest velocity, ie. in this case $t_{dyn} = 1$) the density remains extremely close to uniform ($\Delta\rho \approx 10^{-3}\rho$) and the particle positions remain ordered. Results in II02 show large errors ($\Delta\rho/\rho \gtrsim \rho$) in the density in less than 1 dynamical time. Similar results are obtained in the $c_s = 0.05$ case, shown after 20 dynamical times in Figure 3.14. Again, the amplitude of the density error is very small ($\Delta\rho \approx 10^{-2}\rho$). Some disruption in the particle distribution is observed to occur at later times, however in the absence of any artificial viscosity small compressible modes are not damped in any way and in the absence of a high accuracy timestepping algorithm such disorder might reasonably be expected. Also it is well known that the particles initially arranged on a cubic lattice will eventually move off the lattice and settle to a more isotropic close packed distribution (e.g. Morris 1996).

The question is, therefore: Why do the results obtained in II02 show so much error in the density evolution? The major factor appears to be the particle setup. The details of the particle setup are not given in II02, however by inspection of their figures it appears that the particles are arranged in a quasi-random fashion. The density errors observed in their paper may therefore be an amplification (by the shear flow) of initial perturbations in the density distribution due to the particle setup. A second contributing factor is that the value of smoothing length used by II02 is very low (they use $\eta = 1$ in equation (3.138), whereas typical values for η lie in the range $1.1 - 1.2$ in most multidimensional SPH implementations). How-

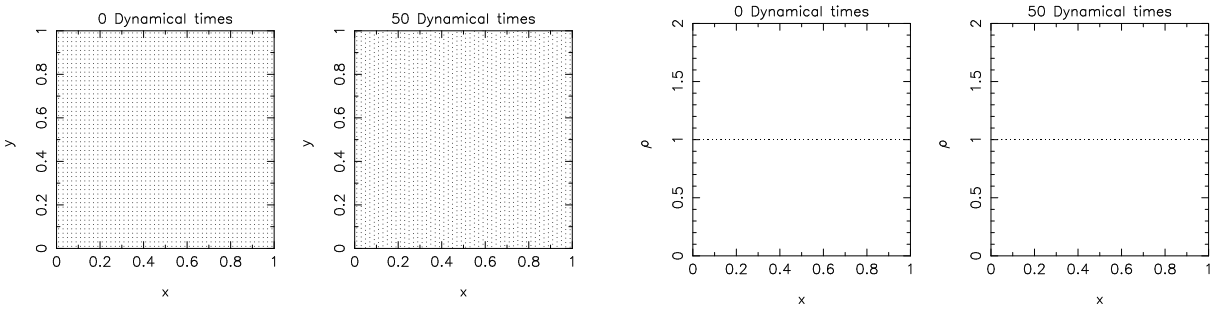

Figure 3.13: Particle positions (left) and density evolution (right) in the pressure-free Cartesian shear flow test with shear velocity field $\mathrm{v}_x = 0, \mathrm{v}_y = \sin(2\pi x)$. The amplitude of the density error is extremely small ($\Delta\rho \approx 10^{-3}\rho$)

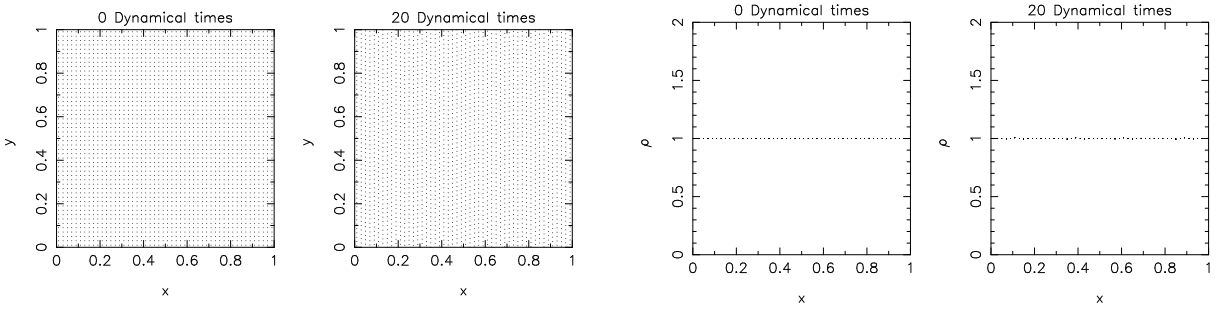

Figure 3.14: Particle positions (left) and density evolution (right) in the Cartesian shearing box test with sound speed $c_{s0} = 0.05$ and shear velocity field $\mathrm{v}_x = 0, \mathrm{v}_y = \sin(2\pi x)$. The amplitude of the density error is very small ($\Delta\rho \approx 10^{-2}\rho$)

ever, even with their choice of smoothing length $h = 1.0(m/\rho)^{\frac{1}{2}}$, we still find that the density remains essentially constant.

3.7.6 Toy stars

A disadvantage of many of the test problems found in the astrophysical fluid dynamics literature is that, being designed for grid-based codes, they all involve some kind of boundary condition. For codes designed ultimately to simulate self-gravitating gas it is useful to have benchmarks based on a finite system. Secondly simple, exact, nonlinear solutions to the equations of hydrodynamics are few and far between, and this even more so in the case of magnetohydrodynamics. For this reason we investigate benchmarks based on a simple class of exact solutions which we call 'Toy Stars'. The equations of hydrodynamics are modified by the addition of a linear force term which is proportional to the co-ordinates (which means that the particles move in a paraboloidal potential centred on the origin). The one dimensional equation of motion is given by

$$\frac{d\mathrm{v}}{dt} = -\frac{1}{\rho}\frac{\partial P}{\partial x} - \Omega^2 x, \tag{3.139}$$

where Ω is the angular frequency. In the following we rescale the equations in units such that $\Omega^2 = 1$. The toy star force has many interesting properties and was even considered by Newton as an example of the simplest many-body force. The toy star equations with $\gamma = 2$ are also identical in form to the shallow water equations.

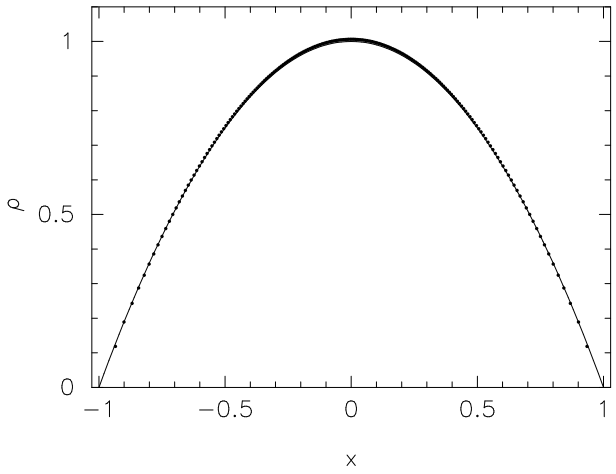

Figure 3.15: Toy star static structure. 200 SPH particles are set up in an initially uniform distribution along the x axis and allowed to evolve under the influence of the linear force. The SPH particles are shown by the solid points after damping to an equilibrium distribution. The agreement with the exact quadratic ($\rho = 1 - x^2$) solution (solid line) is extremely good.

Assuming a polytropic equation of state (ie. $P = K\rho^\gamma$) with constant of proportionality $K = 1/4$ and $\gamma = 2$, the Toy Star static structure at equilibrium is easily derived from (3.139) as

$$\rho = \rho_0(1 - x^2) \tag{3.140}$$

In this thesis we will simply consider the most interesting toy star problem which is the calculation of the fundamental oscillatory mode since it turns out to be an exact, non-linear solution. However, a perturbation analysis can be used to derive linear solutions to the Toy Star equations which also present interesting benchmarks for numerical codes. An investigation of the linear modes using SPH, together with a detailed comparison of the oscillation frequencies with the linear solution is given in Monaghan and Price (2004). The non-linear solution for arbitrary γ may be derived by considering velocity perturbations in the form

$$\mathrm{v} = A(t)x, \tag{3.141}$$

where the density is given by

$$\rho^{\gamma-1} = H(t) - C(t)x^2. \tag{3.142}$$

The exact solution (Monaghan and Price, 2004) for the parameters A, H and C is given in terms of the ordinary differential equations

$$\dot{H} = -AH(\gamma - 1), \tag{3.143}$$

$$\dot{A} = \frac{2K\gamma}{\gamma - 1}C - 1 - A^2 \tag{3.144}$$

$$\dot{C} = -AC(1 + \gamma). \tag{3.145}$$

which can be solved numerically with ease. The relation

$$A^2 = -1 - \frac{2\sigma C}{\gamma - 1} + kC^{\frac{2}{\gamma+1}}, \tag{3.146}$$

where k is a constant which is determined from the initial values of A and C. The exact solution equations (3.143)-(3.145) take particularly simple forms for the case $\gamma = 2$.

Static structure

The simplest test with the toy star is to verify the static structure. We setup 200 SPH particles equally spaced along the x axis with $x = [-1, 1]$ with zero initial velocity and a total mass $M = 4/3$. The particles are then allowed to evolve under the influence of the linear force, with the velocities damped using the artificial viscosity. The particle distribution at equilibrium is shown in Figure 3.15 and shows extremely good agreement with the exact solution (eq. 3.140).

Non linear test cases

For the non-linear tests the one dimensional Toy star is initially set up using 200 equal mass particles distributed along the x axis. Although in principle we could use the particle distribution obtained in the previous test as the initial conditions, it is simpler just to space the particles according to the static density profile (3.140). The SPH equations are implemented using the summation over particles to calculate the density and the usual momentum equation with the linear force subtracted. The equation of state is specified by using $P = K\rho^{\gamma}$, where for the cases shown we set $K = 1/4$. The smoothing length is allowed to vary with the particle density, where we take simple averages of kernel quantities in the SPH equations in order to conserve momentum.

The exact (non-linear) solution is obtained by numerical integration of equations (3.143)-(3.145) using a simple improved Euler method. We use the condition (3.146) as a check on the quality of this integration by evaluating the constant k, which should remain close to its initial value.

Results for the case where initially $A = C = H = 1$ (and therefore $k = 4$) are shown in figure 3.16 at $t = 3.54$ (corresponding to approximately one oscillation period) alongside the exact solution shown by the solid lines. No artificial viscosity is applied in this case. The agreement with the exact solution is excellent. Note that the sound speed in this case is $C_s = 1/\sqrt{2}$ such that using the parameter $A = 1$ results in supersonic velocities at the edges of the star (the solution is therefore highly non-linear).

Figure 3.17 shows the SPH results for a simulation with $\gamma = 5/3$ and the same initial parameters as Figure 3.16. Velocity and density profiles are shown at time $t = 11.23$ corresponding to approximately three oscillation periods. No artificial viscosity is used. The agreement with the exact solution (solid lines) is again extremely good.

Results of simulations with artificial viscosity turned on are similar, although with a small damping of the kinetic energy over time.

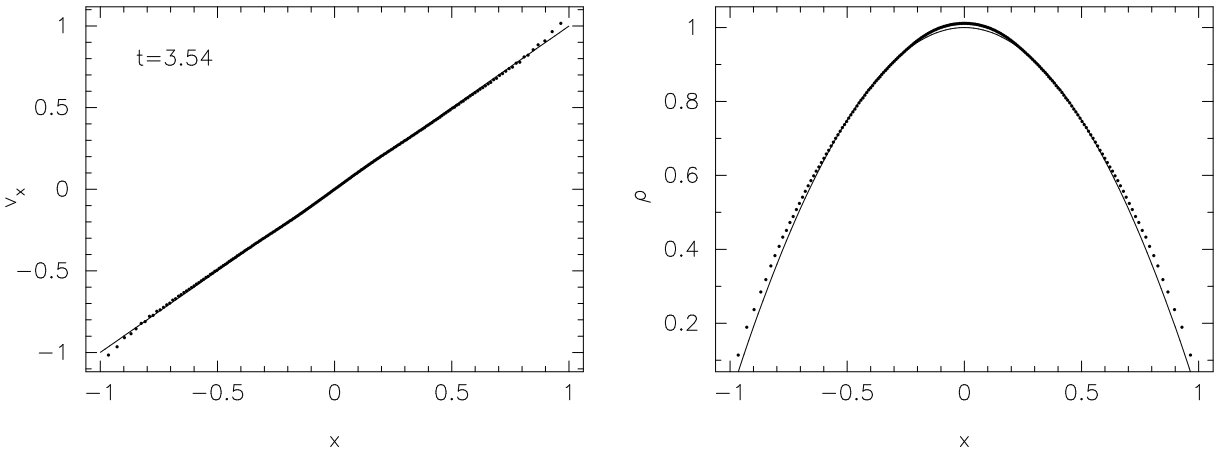

Figure 3.16: Results of the SPH non linear Toy star simulation with $\gamma = 2$ and initial conditions $v = x$, $\rho = 1 - x^2$ (ie. $A = C = H = 1$). Velocity and density profiles are shown after approximately one oscillation period, with the SPH particles indicated by the solid points and the exact solution by the solid line in each case. Equal mass particles are used with a variable initial separation.

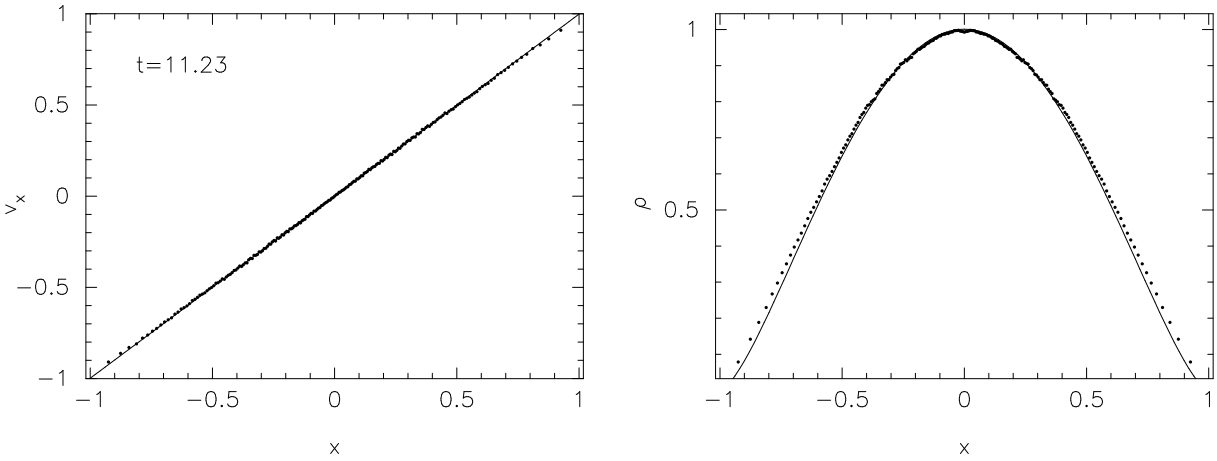

Figure 3.17: Results of the SPH non linear Toy star simulation with $\gamma = 5/3$ and initial conditions $v = x$, $\rho = (1 - x^2)^{3/2}$ (ie. $A = C = H = 1$ with $\gamma = 5/3$). Velocity and density profiles are shown after approximately three oscillation periods and the exact solution is given by the solid line.

3.8 Summary

In this chapter we have thoroughly reviewed the SPH algorithm. Alternatives to the standard cubic spline kernel were investigated in §3.2.5 and §3.2.6, on the basis of their stability properties. Higher order spline kernels giving closer approximations to the Gaussian were found to give better stability properties although at the price of an increase in computational expense due to the greater number of contributing neighbours. The possibility of constructing kernels with better stability properties based on smoother splines but retaining compact support of size $2h$ was investigated, with good results for smoothing lengths $h \gtrsim 1.1$ (in units of the average particle spacing). However, the gain in accuracy from the use of these alternative kernels is very minor compared to the substantial improvements in accuracy gained by the incorporation of the variable smoothing length terms (§3.3.4)

The discrete equations of SPH were formulated self-consistently from a variational principle in §3.3, leading naturally to equations which explicitly conserve momentum, angular momentum and energy.

Artificial dissipation terms used to capture shocks were then discussed, where in §3.5.2 a new switch to control the application of artificial thermal conductivity was considered (the importance of which is highlighted in the numerical tests described in §3.7). The consistent formulation of the SPH equations incorporating a variable smoothing length was discussed in §3.3.4, which are shown to lead to increased accuracy in a wide range of problems (including linear waves (§3.7.2), shock tubes (§3.7.3), Cartesian shear flows (§3.7.5) and toy stars (§3.7.6)). It was shown in §3.4 that consistent formulations of SPH when alternative formulations of the momentum equation are used can be derived from a variational principle by modifying the form of the continuity equation. Various timestepping algorithms were discussed in §3.6, particularly the need to perform a separate pass over the particles to compute derivatives involving the velocity for a reversible integration of the SPH equations. Finally several numerical tests were presented.

The linear sound wave tests (3.7.2) demonstrated a phase error in the SPH simulation of sound waves dependent on the value of the smoothing length and related to the use of kernels with compact support. This phase error was shown to be largely corrected for by allowing the smoothing length to vary with density and self-consistently accounting for the extra terms which arise in the SPH equations. Also the damping of small perturbations induced by the artificial viscosity term was found to be significantly reduced by use of the artificial viscosity switch described in §3.5.2. In the second test problem, the standard shock tube test of Sod (1978), the importance of applying a small amount of artificial thermal conductivity was highlighted, which avoids the need to artificially smooth the initial conditions of such problems. The SPH algorithm was also shown to give good results on a more extreme version of this test (§3.7.4). Thirdly (§3.7.5), the Cartesian shear flow tests given by Imaeda and Inutsuka (2002) were examined, demonstrating that SPH gives good results on this problem for uniform particle setups and does not show the large errors encountered by these authors. Finally, the SPH algorithm was tested against several exact, non-linear solutions derived for systems of particles, known as ‘Toy Stars’ and was shown to give results in excellent agreement with theory.

"I never satisfy myself until I can make a mechanical model of a thing. If I can make a mechanical model I can understand it. As long as I cannot make a mechanical model all the way through I cannot understand; and that is why I cannot get the electromagnetic theory ..... But I want to understand light as well as I can, without introducing things that we understand even less of. That is why I take plain dynamics. I can get a model in plain dynamics; I cannot in electromagnetics."

LORD KELVIN, BALTIMORE LECTURES, 1904

4

Smoothed Particle Magnetohydrodynamics

4.1 Introduction

Given the suitability of SPH for studies of star formation, it is unsurprising that magnetic field effects, which are known to be important or even crucial in the star formation process, were incorporated into SPH from the outset (Gingold and Monaghan, 1977). The application in this case was to static magnetic polytropes where good agreement was found between the SPH solution and perturbation calculations. Dynamical problems were considered by Phillips (1983b) and applied to star formation problems (Phillips, 1982, 1983a, 1985, 1986a,b; Benz, 1984; Phillips and Monaghan, 1985). In the latter it was shown that when the conservation form of the equations was used an instability developed which took the form of SPH particles clumping. SPH blast waves in a magnetic medium were studied by Stellingwerf and Peterkin (1990, 1994). Habe et al. (1991), Murray et al. (1996) and Mac Low et al. (1999) used a form of the SPH equations where the magnetic fields were updated on a grid and interpolated to the SPH particles.

Meglicki (1994, 1995) and Meglicki et al. (1995) used a formulation of 'Smoothed Particle Magnetohydrodynamics' (SPMHD) that uses a non-conservative ($\mathbf{J} \times \mathbf{B}$) force, which is always stable and guarantees that the magnetic force is exactly perpendicular to the magnetic field. This formalism was also used by Byleveld and Pongracic (1996) and more recently by Cerqueira and de Gouveia Dal Pino (2001, and references therein) and Hosking (2002), however the non-conservation of momentum leads to poor performance on shock-type problems. A conservative form of SPMHD has been used by Dolag et al. (1999) and by Marinho et al. (2001) since the magnetic field in their simulations remained in the regime where the instability does not appear. Morris (1996) suggested using a compromise between the conservative (tensor) force and the $\mathbf{J} \times \mathbf{B}$ formalism. Non-ideal MHD terms in SPH were also considered by Morris (1996), who suggested using resistive terms to control the divergence of the magnetic field and by Hosking and Whitworth (2004), who considered the effects of ambipolar diffusion via a two-fluid

model. The simulation of MHD shocks with SPH has been investigated by Børve (2001) (see Børve et al. 2001), where excellent results were obtained by periodically invoking a regularization procedure on the SPH particle distribution and by explicitly subtracting the effect of any non-zero divergence from the conservative formalism.

However, the simplicity with which the MHD equations can be written down belies the fact that there are a number of technical difficulties involved in their solution, which have not been fully addressed in an SPH context. The first technical difficulty with MHD simulations is that the magnetic field comes with the constraint $\nabla \cdot \mathbf{B} = 0$. As a first level treatment in this chapter, we follow the approach of Janhunen (2000) in formulating the MHD equations from the premise that non zero $\nabla \cdot \mathbf{B}$ terms may be generated but that a consistent treatment of such terms by the numerical method will reduce the error associated with their presence. Consistency is ensured in this case by deriving the SPMHD equations from a variational principle, using the discrete forms of the continuity and induction equations to constrain the discrete formulations of the momentum and energy equations. Further discussion of this and other approaches to maintaining the divergence constraint in an SPH context is deferred to Chapter 5.

A further technical difficulty peculiar to SPH is that when a conservative force is used the SPH particles tend to clump in pairs in the presence of tension. This was first noticed by Phillips and Monaghan (1985) and re-discovered by researchers applying SPH to elastic fracture problems (see the references in Monaghan 2000). Several remedies have been proposed (e.g. Dyka et al. 1997; Bonet and Kulasegaram 2000, 2001) but they all either involve a significant increase in computational expense or cannot be applied where the particle configuration changes significantly. The nature of this instability was systematically investigated in an MHD context by Morris (1996), with several solutions proposed. A further remedy for the tensile instability which can be easily applied to astrophysical problems has been recently proposed by Monaghan (2000). The idea is to add a small artificial stress which prevents particles from clumping in the presence of a negative stress. This term has been shown to work well in elastic dynamics simulations (Gray et al., 2001) and we apply it here to the MHD case.

The third technical difficulty is that shocks in MHD are much more complex than their hydrodynamic counterparts. This is due to the additional wave types which can result in a wide range of discontinuous structures, each of which must be treated appropriately by the numerical method. We approach this problem by formulating artificial dissipation terms appropriate to the MHD case (the major difference to the hydrodynamic case being the introduction of artificial resistivity at discontinuities in the magnetic field). These dissipative terms are derived in such a manner that the contribution to the entropy and thermal energy from viscosity, thermal conductivity and ohmic resistivity is guaranteed to be positive definite.

The chapter is organised as follows: In §4.2 we give the continuum form of the MHD equations and in §4.3 the SPH form of these equations, deriving the SPMHD equations self-consistently from a variational principle (§4.3.2). Consistent alternative formulations, similar to those derived in the SPH case (§3.4) are discussed in §4.3.4 whilst older formulations are also reviewed (§4.3.5). In §4.3.6 a variational principle is again used to extend the SPMHD equations to the case where the smoothing length is regarded as a function of local particle density. Stability considerations are discussed in §4.4 with the implementation of the instability correction of Monaghan (2000) presented in §4.4.1 as well as several alternative methods. Dissipation terms appropriate for MHD shocks analogous to those derived in the SPH case (§3.5) are given in §4.5. Finally, in §4.6 we present the results of extensive numerical tests

for one dimensional problems including a range of shock tube problems (§4.6.3), linear waves (§4.6.4) and magnetic Toy Stars (§4.6.5). The extension of the method to multidimensional problems is presented in Chapter 5.

4.2 Magnetohydrodynamics

Magnetohydrodynamics (MHD) is a one-fluid approximation to the equations of plasma physics, where the effects of static electric charge are assumed to be negligible and the non-relativistic limit is generally taken (relativistic MHD involves dropping the latter assumption, whilst retaining the former). The derivation of the MHD equations is given in many standard textbooks and we simply state the results here.

4.2.1 Continuum equations

The continuity equation for the density remains the same as in the non-magnetic case, ie.

$$\frac{d\rho}{dt} + \rho\nabla\cdot\mathbf{v} = 0, \tag{4.1}$$

implying the conservation of mass. The acceleration equation in the absence of dissipation may be expressed in conservative form as the gradient of a symmetric tensor, that is

$$\frac{d\mathrm{v}^i}{dt} = \frac{1}{\rho}\frac{\partial S^{ij}}{\partial x^j}, \tag{4.2}$$

where the stress S^{ij} in the case of ideal MHD is defined by

$$S^{ij} = -P\delta^{ij} + \frac{1}{\mu_0}\left(B^iB^j - \frac{1}{2}B^2\delta^{ij}\right). \tag{4.3}$$

where B^i is the ith component of the magnetic field and μ_0 is the permittivity of free space. In SI units $\mu_0 = 4\pi/10^7$. From the tensor formulation the magnetic force is easily interpreted in terms of an isotropic force due to gradients in the magnetic pressure and an anisotropic (tension) force resisting motion which is perpendicular to magnetic field lines. In vector notation (4.2) is given by

$$\frac{d\mathbf{v}}{dt} = -\frac{\nabla P}{\rho} + \frac{\mathbf{J}\times\mathbf{B}}{\rho} + \frac{\mathbf{B}\nabla\cdot\mathbf{B}}{\mu_0\rho}, \tag{4.4}$$

where $\mathbf{J} = \nabla\times\mathbf{B}/\mu_0$ is the magnetic current density. Under the assumption of $\nabla\cdot\mathbf{B} = 0$ (ie. no magnetic monopoles), the force becomes

$$\frac{d\mathbf{v}}{dt} = -\frac{\nabla P}{\rho} + \frac{\mathbf{J}\times\mathbf{B}}{\rho}. \tag{4.5}$$

The assumption of zero magnetic divergence is valid in the continuum case (making (4.4) and (4.5) equivalent) but requires careful consideration in a numerical context since the divergence is not guaranteed to be zero exactly. Discrete formulations based on the conservative form (4.4) can be made to conserve momentum exactly, whilst formulations based on the non-conservative form (4.5) can be made

to guarantee that the magnetic force is exactly perpendicular to the magnetic field. We use (4.4) since exact conservation of momentum is required in order to accurately simulate shocks, although older formalisms based on (4.5) are discussed in §4.3.5. The momentum conserving formulation (4.4) results naturally in the derivation of the SPMHD equations from a variational principle given in §4.3.2.

The equation for the update of the magnetic field is the induction equation. The standard form is derived from Maxwell's equations neglecting displacement currents and a generalised form of Ohm's law. We follow Janhunen (2000) and Dellar (2001) in formulating the induction equations so that it is consistent even if $\nabla \cdot \mathbf{B}$ does not vanish. The induction equation then takes the form

$$\frac{\partial \mathbf{B}}{\partial t} + \nabla \times (\mathbf{v} \times \mathbf{B}) = -\nabla \times (\eta \mathbf{J}) - \mathbf{v}(\nabla \cdot \mathbf{B}), \tag{4.6}$$

where the last term is the monopole current (Janhunen, 2000; Dellar, 2001) and η is the magnetic diffusivity $1/(\sigma\mu_0)$ where σ is the conductivity. Ideal MHD corresponds to the limit of infinite conductivity $\eta = 0$. Using the Lagrangian time derivative (4.6) can be written as

$$\frac{d\mathbf{B}}{dt} = -\mathbf{B}(\nabla \cdot \mathbf{v}) + (\mathbf{B} \cdot \nabla)\mathbf{v} - \nabla \times (\eta \mathbf{J}). \tag{4.7}$$

Taking the divergence of this equation, we find that monopoles evolve according to

$$\frac{\partial}{\partial t}(\nabla \cdot \mathbf{B}) + \nabla \cdot (\mathbf{v} \nabla \cdot \mathbf{B}) = 0, \tag{4.8}$$

which has the same form as the continuity equation for the density and therefore implies that the total volume integral of $\nabla \cdot \mathbf{B}$ is conserved (and therefore that the total *surface* integral of the magnetic flux is conserved which is the important physical quantity, rather than the *volume* integral which is conserved when the induction equation is written in a so-called 'conservative' form). Note also that in this form the induction equation can be written as

$$\frac{d}{dt}\left(\frac{\mathbf{B}}{\rho}\right) = \left(\frac{\mathbf{B}}{\rho} \cdot \nabla\right)\mathbf{v} - \frac{\nabla \times (\eta \mathbf{J})}{\rho}, \tag{4.9}$$

which demonstrates that in ideal MHD the flux per unit mass, $\mathbf{B}/\rho$ is passively advected by the flow and therefore that the magnetic field lines remain 'frozen' into the fluid.

The total energy per unit mass is given by

$$e = \frac{1}{2}\mathrm{v}^2 + u + \frac{B^2}{2\mu_0\rho}, \tag{4.10}$$

where u is the thermal energy per unit mass. The total energy e evolves according to

$$\frac{de}{dt} = \frac{1}{\rho}\frac{\partial (S^{ij}\mathrm{v}^j)}{\partial x^j} + \frac{1}{\rho}\nabla \cdot [\mathbf{B} \times (\eta \mathbf{J})]. \tag{4.11}$$

Alternatively the thermal energy equation can be used, which may be derived either from (4.10) giving

$$\frac{du}{dt} = \frac{de}{dt} - \mathbf{v} \cdot \frac{d\mathbf{v}}{dt} - \frac{d}{dt}\left(\frac{B^2}{2\mu_0\rho}\right), \tag{4.12}$$

or using the first law of thermodynamics. Either way, the resulting equation is given by

$$\frac{du}{dt} = -\frac{P}{\rho}\nabla \cdot \mathbf{v}, \tag{4.13}$$

which is the same as in the hydrodynamic case. The equation set is closed by an appropriate equation of state, which for a perfect gas is given by

$$P = (\gamma - 1)\rho u. \tag{4.14}$$

4.2.2 Conserved quantities

In order to monitor the quality of a simulation, it is useful to be able to measure the accuracy to which the algorithm conserves integrals of the motion. Aside from the usual conserved quantities of mass, momentum, angular momentum, energy and centre of mass, several additional quantities can be measured in MHD. A list of such quantities can be derived using Hamiltonian techniques and is given by (e.g.) Morrison and Hazeltine (1984). The helicity,

$$\int (\mathbf{A} \cdot \mathbf{B}) \mathrm{dV}, \tag{4.15}$$

where $\mathbf{B} = \nabla \times \mathbf{A}$, is a measure of the linkage of magnetic field lines (expressing the fact that magnetic field lines which are initially linked cannot become unlinked in the absence of dissipative terms). This quantity can only be usefully measured in simulations which explicitly use the vector potential $\mathbf{A}$. A similar invariant is the cross helicity

$$\int (\mathbf{B} \cdot \mathbf{v}) \mathrm{dV} \approx \sum_b m_b \frac{\mathbf{B}_b}{\rho_b} \cdot \mathbf{v}_b, \tag{4.16}$$

which measures the mutual linkage of magnetic field and vortex lines. The conservation of the cross helicity is a result of the magnetic field lines being frozen into the fluid. Measurement of the conservation of this quantity in a numerical simulation therefore provides an estimate of the degree of slippage of the magnetic field lines through the fluid. The volume integral of the magnetic flux

$$\int \mathbf{B} \mathrm{dV} \approx \sum_b m_b \frac{\mathbf{B}_b}{\rho_b} \tag{4.17}$$

is also conserved across the simulation volume, provided that the flux is normal to (or zero at) the boundary of the integration volume. However the conservation of flux in a volume sense is not particularly important physically (Janhunen, 2000). More important is that the surface integral of the flux

$$\int \mathbf{B} \cdot \mathrm{dS}, \tag{4.18}$$

should be conserved. Using the divergence theorem this corresponds to the conservation of the volume integral

$$\int (\nabla \cdot \mathbf{B}) \mathrm{dV} \approx \sum_b m_b \frac{(\nabla \cdot \mathbf{B})_b}{\rho_b}. \tag{4.19}$$

In the continuum case this conservation is exact since the divergence of the magnetic field is zero. However in a numerical scheme with non-zero magnetic divergence conservation of this quantity depends on the formulation of the induction equation with respect to the terms proportional to $\nabla \cdot \mathbf{B}$. Our induction equation (4.7) is formulated such that, even with non-zero $\nabla \cdot \mathbf{B}$ this quantity remains conserved (although this may differ slightly in the discrete equations), whereas (4.17) will only be approximately conserved.

There is also a conserved quantity which is the MHD analogue of the circulation (Bekenstein and Oron, 2000; Kuznetsov and Ruban, 2000), although the physical interpretation is somewhat obscure. It has been shown that SPH conserves an approximate version of the circulation in the hydrodynamic case (Monaghan and Price, 2001), related to the invariance of the equations to the relabelling of particles around a closed loop due to the frozen-in vorticity field (Salmon, 1988). A similar, though more restricted relabelling symmetry holds in the MHD case (in that the particles around the loop must also be on the same field line) and it may therefore be expected that SPMHD also maintains this invariance.

4.3 Smoothed Particle Magnetohydrodynamics

The discrete approximations to (4.1), (4.2), (4.7) and (4.11) are found by expressing the spatial derivatives as summations over the particles. As in the SPH case (§3.3, §3.4) we derive the SPMHD equations of motion and energy from a variational principle, in this case using the SPH forms of the continuity and induction equations as constraints. This ensures consistency between the discrete forms of the SPH equations (and hence also the continuum forms, removing the ambiguity with regard to terms proportional to the magnetic divergence) as well as adherence to physical principles.

4.3.1 Induction equation

The induction equation (4.7) in the absence of dissipation may be written in SPH form as

$$\frac{d\mathbf{B}_a}{dt} = \frac{1}{\rho_a}\sum_b m_b[\mathbf{B}_a(\mathbf{v}_{ab}\cdot\nabla_a W_{ab}) - \mathbf{v}_{ab}(\mathbf{B}_a\cdot\nabla_a W_{ab})]. \tag{4.20}$$

Alternatively we can use (4.9), written in the form

$$\frac{d}{dt}\left(\frac{\mathbf{B}}{\rho}\right) = \frac{1}{\rho^2}\left[(\mathbf{B}\cdot\nabla)\rho\mathbf{v} - \mathbf{v}(\mathbf{B}\cdot\nabla\rho)\right], \tag{4.21}$$

with SPH equivalent

$$\frac{d}{dt}\left(\frac{\mathbf{B}}{\rho}\right)_a = -\frac{1}{\rho_a^2}\sum_b m_b\mathbf{v}_{ab}(\mathbf{B}_a\cdot\nabla_a W_{ab}). \tag{4.22}$$

In the numerical tests presented in §4.6 we find little difference between the two forms (4.20) and (4.22) of the SPH induction equation. Many authors prefer to use (4.22) as the flux per unit mass $\mathbf{B}/\rho$ is a natural quantity to be carried by Lagrangian particles. There is some advantage in using (4.20) rather than (4.22) in one dimensional problems since using (4.20) ensures that the divergence of the magnetic field is exactly zero (since $B_x = \text{const}$). However the divergence errors associated with using (4.22)

in one dimension were found to be negligible for nearly all of the problems considered. Note that a 'conservative' form of the induction equation (as used in most grid-based MHD codes, although not a consistent formulation in the presence of magnetic monopoles) would correspond to a symmetric form of (4.22) (with the addition of a term $\mathbf{v}\nabla\cdot\mathbf{B}$), such that (4.17) is conserved but no longer implying the conservation of $\mathbf{B}/\rho$ along flow lines. An example of such a formalism is used in §5.3.2 in order to compare the divergence errors associated with various formulations of the MHD equations.

4.3.2 Equations of motion

Variational principles for MHD have been discussed by many authors (e.g. Newcomb 1962; Henyey 1982; Oppeneer 1984; Field 1986) and the Lagrangian is given by

$$L = \int \left(\frac{1}{2}\rho \mathrm{v}^2 - \rho u - \frac{1}{2\mu_0}B^2\right)\mathrm{dV}, \tag{4.23}$$

which is simply the kinetic minus the potential and magnetic energies. The SPH Lagrangian is therefore

$$L_{sph} = \sum_b m_b \left[\frac{1}{2}\mathrm{v}_b^2 - u_b(\rho_b, s_b) - \frac{1}{2\mu_0}\frac{B_b^2}{\rho_b}\right]. \tag{4.24}$$

where we have replaced the integral with a summation and the volume element $\rho\mathrm{dV}$ with the mass per SPH particle m. Ideally we would wish to express all the terms in the Lagrangian (4.24) in terms of the particle co-ordinates, which would automatically guarantee the conservation of momentum and energy since the equations of motion result from the Euler-Lagrange equations (e.g. Monaghan and Price 2001). The density can be written as a function of the particle coordinates using the usual SPH summation (3.42). The internal energy is regarded as a function of the density (via the first law of thermodynamics), which is in turn a function of the particle co-ordinates. However it is not intuitively obvious how the magnetic field $\mathbf{B}$ should be related to the particle co-ordinates, or even that it could be expressed in such a manner (in the SPH context this would imply an expression for $\mathbf{B}$ such that taking the time derivative gives (4.20) or (4.22), analogous to (3.42) for the density), though it could be done easily for a plasma with the electrons and ions described by separate sets of SPH particles. We may however proceed using the variational principle given for alternative formulations of SPH in §3.4, that is we require

$$\delta\int L\mathrm{dt} = \int \delta L\mathrm{dt} = 0, \tag{4.25}$$

where we consider variations with respect to a small change in the particle co-ordinates $\delta\mathbf{r}_a$. We therefore have

$$\delta L = m_a\mathbf{v}_a\cdot\delta\mathbf{v}_a - \sum_b m_b\left[\left.\frac{\partial u_b}{\partial\rho_b}\right|_s \delta\rho_b + \frac{1}{2\mu_0}\left(\frac{B_b}{\rho_b}\right)^2\delta\rho_b - \frac{1}{\mu_0}\mathbf{B}_b\cdot\delta\left(\frac{\mathbf{B}_b}{\rho_b}\right)\right]. \tag{4.26}$$

The Lagrangian variations in density and magnetic field are given by

$$\delta\rho_b = \sum_c m_c(\delta\mathbf{r}_b - \delta\mathbf{r}_c)\cdot\nabla_b W_{bc}, \tag{4.27}$$

$$\delta\left(\frac{\mathbf{B}_b}{\rho_b}\right) = -\sum_c m_c(\delta\mathbf{r}_b - \delta\mathbf{r}_c)\frac{\mathbf{B}_b}{\rho_b^2}\cdot\nabla_b W_{bc}, \tag{4.28}$$

where we have used (3.43) and (4.22) respectively (note that we also recover the following results if we use (4.20) instead of (4.22)). The perturbations given above correspond to SPH forms of the usual Lagrangian perturbations

$$\delta\rho = -\rho_0\nabla\cdot(\delta\mathbf{r}), \tag{4.29}$$

$$\delta\left(\frac{\mathbf{B}}{\rho}\right) = \frac{\mathbf{B}_0}{\rho_0}\cdot\nabla(\delta\mathbf{r}). \tag{4.30}$$

Using (4.27), (4.28) and the first law of thermodynamics (3.50) in (4.26) and rearranging, we find

$$\begin{aligned}\frac{\delta L}{\delta\mathbf{r}_a} &= -\sum_b m_b\left[\frac{P_b}{\rho_b^2}\sum_c m_c\nabla_b W_{bc}(\delta_{ba}-\delta_{ca})\right] - \sum_b m_b\left[\frac{1}{2\mu_0}\left(\frac{\mathbf{B}_b}{\rho_b}\right)^2\nabla_b W_{bc}(\delta_{ba}-\delta_{ca})\right] \\ &+ \sum_b m_b\left[\frac{1}{\mu_0}\frac{\mathbf{B}_b}{\rho_b^2}\sum_c m_c\mathbf{B}_b\cdot\nabla_b W_{bc}(\delta_{ba}-\delta_{ca})\right],\end{aligned} \tag{4.31}$$

where δ_{ab} refers to the Kronecker delta. Putting this back into (4.25), integrating the velocity term by parts and simplifying (using $\nabla_a W_{ab} = -\nabla_b W_{ba}$), we obtain

$$\begin{aligned}\int\Bigg\{-m_a\frac{d\mathbf{v}_a}{dt} &- \sum_b m_b\left(\frac{P_a}{\rho_a^2}+\frac{P_b}{\rho_b^2}\right)\nabla_a W_{ab} - \sum_b m_b\frac{1}{2\mu_0}\left(\frac{B_a^2}{\rho_a^2}+\frac{B_b^2}{\rho_b^2}\right)\nabla_a W_{ab} \\ &+ \sum_b m_b\frac{1}{\mu_0}\left[\frac{\mathbf{B}_a}{\rho_a^2}(\mathbf{B}_a\cdot\nabla_a W_{ab}) + \frac{\mathbf{B}_b}{\rho_b^2}(\mathbf{B}_b\cdot\nabla_a W_{ab})\right]\Bigg\}\delta\mathbf{r}_a dt = 0.\end{aligned} \tag{4.32}$$

The SPH equations of motion are therefore given by

$$\frac{d\mathrm{v}_a^i}{dt} = \sum_b m_b\left[\left(\frac{S^{ij}}{\rho^2}\right)_a + \left(\frac{S^{ij}}{\rho^2}\right)_b\right]\nabla_a^j W_{ab}, \tag{4.33}$$

where S^{ij} is the stress tensor (4.3). This form of the magnetic force term conserves linear momentum exactly (angular momentum is discussed below) but was shown by Phillips and Monaghan (1985) to be unstable under negative stresses, causing particles to clump together unphysically. The approach taken in this thesis is to remove the instability by adding a short range repulsive force which prevents particles from clumping, rather than sacrificing the conservation of momentum. The stability issues are discussed in detail in §4.4.

Note that using (4.33) for the magnetic force no longer guarantees that the magnetic force is perpendicular to **B**, since the force (4.4) contains an additional term proportional to the divergence of **B**. This non-zero force directed along the line joining the particles is essentially the physical cause of the clumping instability. It has been pointed out by Tóth (2000) in the context of grid based codes that if the momentum is conserved then the force will not be exactly perpendicular to **B** even if $\nabla\cdot\mathbf{B}$ is zero in a particular discretisation, since this does not imply that $\nabla\cdot\mathbf{B}$ is zero in every discretisation[1]. An example of this is in an SPH context is for purely one dimensional MHD, where even though $\nabla\cdot\mathbf{B} = 0$ (since

[1] although in a later paper Tóth (2002) has shown that both conditions *can* be met provided that the discretisation in which the divergence is zero is also the discretisation used in the force term.

B_x =const), the contribution from the divergence term in (4.33) is non-zero, resulting in an instability even in this simple case.

Finally, it should be noted that the conservative form of the momentum equation was derived using a non-conservative (in a volume sense, although conservative in a surface integral sense) induction equation, which agrees with the derivation of the MHD equations in the presence of magnetic monopoles given by Janhunen (2000) and Dellar (2001). This is discussed further in §5.2.1.

Angular momentum conservation

Whilst the conservation of linear momentum is maintained exactly for the formalism derived above, angular momentum conservation will not be exact since the force between the particles is not directed along the line joining them. Considering two dimensional motion in x and y, the change in angular momentum of the system is given by

$$\frac{d}{dt}\sum_a (\mathbf{r}_a \times \mathbf{v}_a)^z = \sum_a \sum_b m_a m_b \left(\left[\sigma_{ab}^{xx} - \sigma_{ab}^{yy}\right] y_{ab} x_{ab} + \sigma_{ab}^{xy}[y_{ab}^2 - x_{ab}^2] \right) F_{ab}, \tag{4.34}$$

where $y_{ab} = y_a - y_b$, $x_{ab} = x_a - x_b$ and $\sigma_{ab}^{ij} = S_a^{ij}/\rho_a^2 + S_b^{ij}/\rho_b^2$. We have replaced ∇W_{ab} by $\mathbf{r}_{ab} F_{ab}$. From (4.34) we see that the angular momentum will be conserved if the stress is isotropic and proportional to the identity tensor. However for more general stresses the angular momentum will change. It can be shown that upon translating the SPH expression (4.34) into continuum form (replacing the summations with integrals), angular momentum is conserved exactly.

The same problem arises in the case of elastic stresses where the problem is made worse by the fact that particles at the edge of the solid (which have no neighbours exterior to the solid to provide a full interpolation) have densities similar to the interior and consequently produce a significant error in the angular momentum. Bonet and Lok (1999) claim that normalising the kernel by a matrix factor similar to that described in §3.2.3 corrects for this error. A similar approach could be taken to the astrophysical problem, however we expect angular momentum conservation to be much better in this case without normalising the kernel because edges are associated with low density and correspondingly low angular momentum.

4.3.3 Energy equation

The Hamiltonian (3.59), using the Lagrangian (4.24) is given by

$$H = E = \sum_a m_a \left(\frac{1}{2} \mathrm{v}_a^2 + u_a + \frac{1}{2\mu_0} \frac{B_a^2}{\rho_a} \right). \tag{4.35}$$

Taking the (comoving) time derivative, we have

$$\frac{dE}{dt} = \sum_a m_a \left[\mathbf{v}_a \cdot \frac{d\mathbf{v}_a}{dt} + \frac{du_a}{d\rho_a}\frac{d\rho_a}{dt} + \frac{1}{2\mu_0}\frac{B_a^2}{\rho_a^2}\frac{d\rho_a}{dt} + \frac{\mathbf{B}_a}{\mu_0} \cdot \frac{d}{dt}\left(\frac{\mathbf{B}_a}{\rho_a}\right) \right], \tag{4.36}$$

where the first term is specified by use of the momentum equation (4.33), the second term using the first law of thermodynamics (3.50) and the continuity equation (3.43), the third term by the continuity

equation and the fourth term by the induction equation (4.22). Using these and simplifying we find

$$\frac{dE}{dt} = \sum_a m_a \sum_b m_b \left[\left(\frac{S^{ij}}{\rho^2} \right)_a \mathrm{v}_b^i + \left(\frac{S^{ij}}{\rho^2} \right)_b \mathrm{v}_a^i \right] \nabla_a^j W_{ab}, \tag{4.37}$$

such that the total energy per particle is evolved according to

$$\frac{de_a}{dt} = \sum_b m_b \left[\left(\frac{S^{ij}}{\rho^2} \right)_a \mathrm{v}_b^i + \left(\frac{S^{ij}}{\rho^2} \right)_b \mathrm{v}_a^i \right] \nabla_a^j W_{ab}, \tag{4.38}$$

where

$$e_a = \frac{1}{2}\mathrm{v}_a^2 + u_a + \frac{1}{2\mu_0}\frac{B_a^2}{\rho_a} \tag{4.39}$$

is the energy per unit mass. The internal energy equation follows from the use of the first law of thermodynamics and is therefore the same as in the hydrodynamic case (3.58) in the absence of dissipative terms. The equation for evolving the entropy (3.65) is also unchanged.

4.3.4 Alternative formulations

Consistent sets of SPMHD equations may also be derived using alternative forms of the continuity and induction equations as in §3.4. For example, using the continuity equation

$$\frac{d\rho_a}{dt} = \rho_a \sum_b m_b \frac{\mathbf{v}_{ab}}{\rho_b} \cdot \nabla_a W_{ab}, \tag{4.40}$$

and the induction equation

$$\frac{d}{dt}\left(\frac{\mathbf{B}}{\rho}\right)_a = -\frac{1}{\rho_a}\sum_b m_b \frac{\mathbf{v}_{ab}}{\rho_b}(\mathbf{B}_a \cdot \nabla_a W_{ab}). \tag{4.41}$$

results in the momentum equation

$$\frac{d\mathrm{v}_a^i}{dt} = \sum_b m_b \left[\frac{S_a^{ij} + S_b^{ij}}{\rho_a \rho_b} \right] \nabla_a^j W_{ab}. \tag{4.42}$$

This form of the SPMHD equations also conserves linear momentum exactly (and is hence also found to be unstable to the clumping instability). The variationally consistent internal energy equation is given by

$$\frac{du_a}{dt} = \frac{P_a}{\rho_a}\sum_b m_b \frac{\mathbf{v}_{ab}}{\rho_b} \cdot \nabla_a W_{ab}, \tag{4.43}$$

and the total energy equation by

$$\frac{de_a}{dt} = \sum_b m_b \left[\frac{S_a^{ij}\mathrm{v}_b^i + S_b^{ij}\mathrm{v}_a^i}{\rho_a \rho_b} \right] \nabla_a^j W_{ab}. \tag{4.44}$$

A general alternative formulation may also be derived, equivalent to that given in §3.4.

4.3.5 Vector formulations of the magnetic force

Earlier implementations of MHD in an SPH context used simple forms of the magnetic force terms based on the non-conservative force equation (4.5). The simplest form of the magnetic force term in (4.5) is derived by using the SPH summation interpolant for the magnetic field,

$$\mathbf{B}_a = \sum_b m_b \frac{\mathbf{B}_b}{\rho_b} W(\mathbf{r}_a - \mathbf{r}_b, h). \tag{4.45}$$

Taking the curl of this equation we have

$$\mathbf{J}_a = (\nabla \times \mathbf{B})_a = \sum_b m_b \nabla_a W_{ab} \times \frac{\mathbf{B_b}}{\rho_b}. \tag{4.46}$$

The magnetic force term is then given by

$$\begin{aligned} \left(\frac{\mathbf{J}\times\mathbf{B}}{\mu_0\rho}\right)_a &= (\nabla\times\mathbf{B})_a \times \frac{\mathbf{B}_a}{\mu_0\rho_a} \\ &= \sum_b m_b \left(\nabla_a W_{ab} \times \frac{\mathbf{B}_b}{\rho_b}\right) \times \frac{\mathbf{B}_a}{\mu_0\rho_a}. \end{aligned} \tag{4.47}$$

In SPH, however it is preferable to interpolate the curl using (c.f. §3.2.3)

$$\rho_a(\nabla\times\mathbf{B})_a = \sum_b m_b(\mathbf{B}_a - \mathbf{B}_b)\times\nabla_a W_{ab}, \tag{4.48}$$

and thus the magnetic force becomes

$$\frac{1}{\mu_0\rho_a^2}\sum_b m_b\,(\mathbf{B}_{ab}\times\nabla_a W_{ab})\times\mathbf{B}_a, \tag{4.49}$$

where $\mathbf{B}_{ab} = \mathbf{B}_a - \mathbf{B}_b$. This 'vector' form of the magnetic force term has been used by many authors (e.g. Meglicki et al., 1995; Byleveld and Pongracic, 1996; Cerqueira and de Gouveia Dal Pino, 2001; Hosking and Whitworth, 2004). Using this formulation the magnetic force is always perpendicular to the magnetic field but exact conservation of momentum is not guaranteed. Equation (4.49) may also be expressed as:

$$\frac{1}{\mu_0\rho_a^2}\sum_b m_b\left[(\mathbf{B}_{ab}\cdot\mathbf{B}_a)\nabla_a W_{ab} - (\mathbf{B}_a\cdot\nabla_a W_{ab})\mathbf{B}_{ab}\right]. \tag{4.50}$$

Whilst this results in a stable numerical scheme, the lack of momentum conservation in this formalism means that it gives extremely poor results on problems involving shocks. We also note that this is the discretisation of a pure $\mathbf{J}\times\mathbf{B}$ force which, as discussed in §4.2.1 does not represent a consistent formulation of the magnetic force in the presence of monopoles.

4.3.6 Variable smoothing length terms

Since we cannot explicitly write the Lagrangian (4.24) as a function of the particle co-ordinates, we cannot explicitly derive the SPMHD equations incorporating a variable smoothing length. We may,

however deduce the form of the terms which should be included by consistency arguments. We start with the SPH induction equation in the form

$$\frac{d}{dt}\left(\frac{\mathbf{B}}{\rho}\right)_a = -\frac{1}{\rho_a^2}\sum_b m_b \mathbf{v}_{ab}(\mathbf{B}_a \cdot \nabla_a W_{ab}). \tag{4.51}$$

Expanding the left hand side, we have

$$\frac{d\mathbf{B}_a}{dt} = -\frac{1}{\rho_a}\sum_b m_b \mathbf{v}_{ab}(\mathbf{B}_a \cdot \nabla_a W_{ab}) + \frac{\mathbf{B}_a}{\rho_a}\frac{d\rho_a}{dt}. \tag{4.52}$$

If the smoothing length is a given function of the density, then the SPH continuity equation is given by (3.70) and (4.52) becomes

$$\frac{d\mathbf{B}_a}{dt} = -\frac{1}{\rho_a}\sum_b m_b \left\{\mathbf{v}_{ab}(\mathbf{B}_a \cdot \nabla_a W_{ab}) - \frac{1}{\Omega_a}\mathbf{B}_a[\mathbf{v}_{ab} \cdot \nabla_a W_{ab}(h_a)]\right\}. \tag{4.53}$$

where Ω is defined in §3.3.4. However in one dimension these terms must cancel to give $B_x = \text{const}$, and thus we deduce that the correct form of the induction equation is therefore

$$\frac{d\mathbf{B}_a}{dt} = -\frac{1}{\Omega_a \rho_a}\sum_b m_b \left\{\mathbf{v}_{ab}\left[\mathbf{B}_a \cdot \nabla_a W_{ab}(h_a)\right] - \mathbf{B}_a\left[\mathbf{v}_{ab} \cdot \nabla_a W_{ab}(h_a)\right]\right\}, \tag{4.54}$$

or in the form (4.51) we would have

$$\frac{d}{dt}\left(\frac{\mathbf{B}}{\rho}\right)_a = -\frac{1}{\Omega_a \rho_a^2}\sum_b m_b \mathbf{v}_{ab}[\mathbf{B}_a \cdot \nabla_a W_{ab}(h_a)]. \tag{4.55}$$

Using (4.54) or (4.55) and (3.70) as constraints we may then derive the equations of motion using the variational principle described in §3.3.2 to give

$$\frac{d\mathrm{v}_a^i}{dt} = \sum_b m_b \left[\left(\frac{S^{ij}}{\Omega\rho^2}\right)_a \nabla_a^j W_{ab}(h_a) + \left(\frac{S^{ij}}{\Omega\rho^2}\right)_b \nabla_a^j W_{ab}(h_b)\right]. \tag{4.56}$$

The total energy equation is given by

$$\frac{de_a}{dt} = \sum_b m_b \left[\left(\frac{S^{ij}}{\Omega\rho^2}\right)_a \mathrm{v}_b^i \nabla_a^j W_{ab}(h_a) + \left(\frac{S^{ij}}{\Omega\rho^2}\right)_b \mathrm{v}_a^i \nabla_a^j W_{ab}(h_b)\right], \tag{4.57}$$

whilst the internal energy equation is found using the first law of thermodynamics and (3.70), that is

$$\frac{du_a}{dt} = \frac{P_a}{\Omega_a \rho_a^2}\sum_b m_b \mathbf{v}_{ab} \cdot \nabla_a W_{ab}(h_a) \tag{4.58}$$

We show in §4.6.4 that including the correction terms for a variable smoothing length in this manner significantly improves the numerical wave speed in the propagation of MHD waves and enables the shock tube problems considered in §4.6.3 to be computed with no smoothing of the initial conditions.

4.4 Stability

A full stability analysis of the SPMHD equations for negative stress has been presented by Morris (1996). The simplest MHD case is for a purely one dimensional problem, where $\mathbf{B} = [B_x, 0, 0]$. In this case the dispersion relation is easily obtained from the hydrodynamic version (3.41) by simply replacing the pressure P by $P - \frac{1}{2}B_x^2$, giving

$$\begin{aligned}\omega_a^2 &= \frac{2m(P_0 - \frac{1}{2}B_x^2)}{\rho_0^2}\sum_b [1-\cos k(x_a - x_b)]\frac{\partial^2 W}{\partial x^2}(x_a - x_b, h) \\ &\quad + \frac{m^2}{\rho_0^2}\left(c_s^2 - \frac{2(P_0 - \frac{1}{2}B_x^2)}{\rho_0}\right)\left[\sum_b \sin k(x_a - x_b)\frac{\partial W}{\partial x}(x_a - x_b, h)\right]^2, \end{aligned} \tag{4.59}$$

where as previously $c_s^2 = \partial P/\partial\rho$. Following Morris (1996), we define the negative stress parameter

$$\mathscr{R} = 1 - \frac{\frac{1}{2}B_x^2}{P_0} \tag{4.60}$$

such that $\mathscr{R} = 1$ corresponds to the hydrodynamic case and $\mathscr{R} < 0$ corresponds to negative stress. The dispersion relation for an isothermal gas ($c_s^2 = P/\rho$) is then given by

$$\begin{aligned}\omega_a^2 &= \frac{2mc_s^2}{\rho_0}\mathscr{R}\sum_b [1-\cos k(x_a - x_b)]\frac{\partial^2 W}{\partial x^2}(x_a - x_b, h) \\ &\quad + \left(\frac{mc_s}{\rho_0}\right)^2 (1 - 2\mathscr{R})\left[\sum_b \sin k(x_a - x_b)\frac{\partial W}{\partial x}(x_a - x_b, h)\right]^2. \end{aligned} \tag{4.61}$$

Figure 4.1 shows contours of the (normalised) square of the numerical sound speed $C_{num}^2 = \omega^2/k^2$ from this dispersion relation evaluated for the cubic spline kernel at a fixed value of smoothing length ($h = 1.2\Delta p$). The contours are shown as a function of wavenumber (in units of the average particle spacing) and the negative stress parameter $\mathscr{R}$[2]. As in §3.2.7, sums in (4.61) are calculated numerically (rather than making any further approximations) assuming an isothermal sound speed and particle spacing of unity (where both wavelength and smoothing length are calculated in units of the particle spacing). From Figure 4.1 we observe that the kernel is unstable to negative stress ($\mathscr{R} < 0$) at short wavelengths, with the instability first occurring at a wavenumber $k = \pi$ (corresponding to a wavelength of twice the particle spacing Δp). Note that these results are very similar for other smoothing length values and for all of the kernels considered in §3.2.

In a numerical simulation, this instability manifests as particles clumping together, beginning at short wavelengths but quickly destroying the simulation (Figure 4.2). Since the one dimensional MHD case involves only a constant magnetic pressure subtracted from the gas pressure, the source of the instability can be traced to non-cancellation of the first error term (which is non-zero even for constant functions) in the SPH approximation when a momentum-conserving form of the gradient evaluation is used (refer to the discussion in §3.2.3). Indeed using a differencing form for the gradient term such as (3.16) results in a stable formalism, but in this case the exact conservation of momentum is lost (although a compromise approach is described below, §4.4.2).

[2] this figure corresponds to Figure 2.1 in Morris (1996)

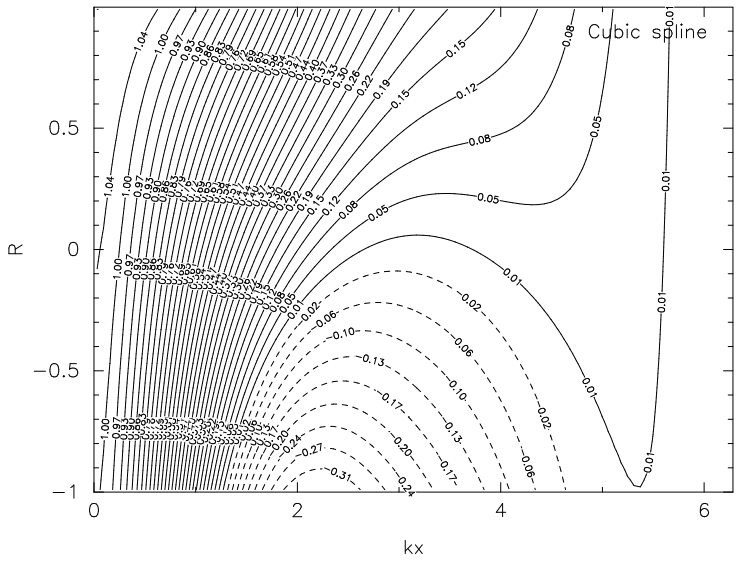

Figure 4.1: One dimensional stability properties of the cubic spline kernel with respect to the negative stress parameter $\mathscr{R} = (1 - \frac{1}{2}B_x^2/P)$ (y-axis). The x-axis corresponds to wavenumber in units of $1/\Delta x$ (such that $kx \rightarrow 0$ represents the limit of an infinite number of particles per wavelength). Contours show the (normalised) square of the numerical wave speed from the dispersion relation (4.59). The kernel is unstable to negative stress ($\mathscr{R} < 0$) at short wavelengths.

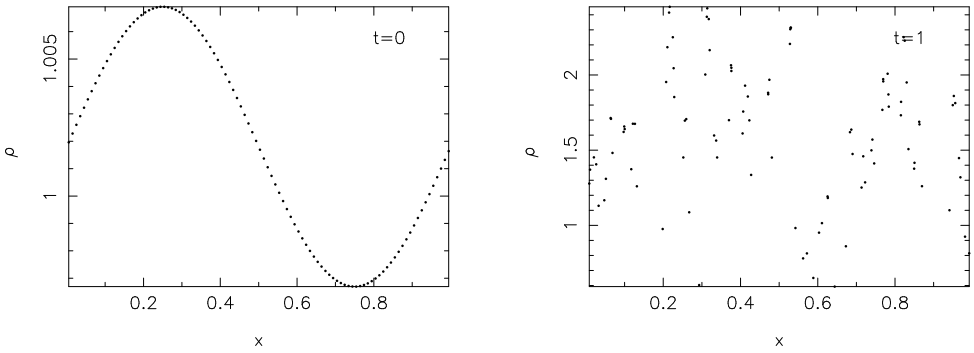

Figure 4.2: Results of a one dimensional isothermal sound wave simulation with a constant magnetic field in the $x-$direction such that $\mathscr{R} = -1$. The initial conditions are shown in the left panel, using 100 particles with an initial amplitude of 0.5%. The wave quickly becomes unstable due to the negative stress and the results are shown in the right panel after one period.

Since conservation of momentum is important for the accurate simulation of shocks, several remedies for this instability, associated with the tensor (ie. momentum-conserving) form of the magnetic force term have been suggested. In their initial investigation Phillips and Monaghan (1985) used a simple 'regularization' technique - that is they swept over the particles to find the maximum value of the magnetic component of the stress tensor (4.3) and then subtracted this from the stress tensor in (4.33). Recently, however, it has been shown that a similar instability occurs when SPH is used in solid mechanics simulations where again there is an anisotropic stress. The instability occurs when the particles are in tension (ie. the stress is negative) and again leads to a clumping effect, analogous to the MHD instability. Several remedies have been proposed in the engineering literature (e.g. Dyka et al. 1997; Bonet and Kulasegaram 2000, 2001) but they all either involve a significant increase in computation or cannot be applied where the particle configuration changes significantly (for a more detailed discussion see Monaghan, 2000).

A remedy for the tensile instability which does not require additional computational expense and can be easily applied to astrophysical problems was proposed by Monaghan (2000) and we investigate this technique below.

4.4.1 Anti-clumping term

The idea proposed by Monaghan (2000) is add a term which prevents particles clumping under negative stress. Since the instability occurs at short wavelengths, this term should modify the stress at small particle spacings so as to provide a repulsive force which prevents the particles clumping together under tension forces (negative stress). Determining whether or not the particles are in tension is determined by rotating into co-ordinates which lie along the principal stress axis (ie. where the stress tensor is diagonal). The magnetic stress tensor is diagonal when the magnetic field lies along one of the co-ordinate axes (which in this case we assume to be the $x-$axis). The magnetic field is then $\mathbf{B}' = (B,0,0)$ and the stress tensor has non zero components $M'_{xx} = B^2/(2\mu_0)$, $M'_{yy} = -B^2/(2\mu_0)$, and $M'_{zz} = -B^2/(2\mu_0)$. The positive component in the $x-$component indicates tension, whilst the negative components in the $y-$ and $z-$ directions indicate compression. To remove the tension term at close range a term is added to M'_{xx} so that it is negative when the particles approach. The term added is RB^2, where

$$R = -\frac{\varepsilon}{2\mu_0}\left(\frac{W_{ab}}{W_1}\right)^n, \tag{4.62}$$

where W is the SPH kernel and W_1 is the kernel evaluated at the average particle spacing (a constant). Rotating back to the original co-ordinate system, this is equivalent to defining a new magnetic stress

$$M'_{ij} = M_{ij} + RB_iB_j. \tag{4.63}$$

The momentum equation (4.33) becomes

$$\frac{dv^i_a}{dt} = \sum_b m_b \left\{ \left(\frac{S_{ij}}{\rho^2}\right)_a + \left(\frac{S_{ij}}{\rho^2}\right)_b + R\left[\left(\frac{B_iB_j}{\rho^2}\right)_a + \left(\frac{B_iB_j}{\rho^2}\right)_b\right]\right\}\frac{\partial W_{ab}}{\partial x_{j,a}}. \tag{4.64}$$

In the preceding discussion, we have interpreted the artificial stress term as a modification of the anisotropic component of the magnetic stress tensor. An alternative interpretation (and one which we prefer) is to regard it as a modification to the kernel gradient in the anisotropic force at small particle spacings. The momentum equation may then be expressed as

$$\begin{aligned}\frac{dv^i_a}{dt} &= -\sum_b m_b\left[\left(\frac{P}{\rho^2}+\frac{B^2}{2\mu_0\rho^2}\right)_a + \left(\frac{P}{\rho^2}+\frac{B^2}{2\mu_0\rho^2}\right)_b\right]\frac{\partial W_{ab}}{\partial x_{j,a}} \\ &\quad + \sum_b \frac{m_b}{\mu_0}\left[\left(\frac{B_iB_j}{\rho^2}\right)_a + \left(\frac{B_iB_j}{\rho^2}\right)_b\right]\frac{\partial Y_{ab}}{\partial x_{j,a}},\end{aligned} \tag{4.65}$$

where $\partial Y_{ab}/\partial x$ is the modified kernel gradient, given by

$$\frac{\partial Y_{ab}}{\partial x} = \left[1 - \frac{\varepsilon}{2}\left(\frac{W_{ab}}{W_1}\right)^n\right]\frac{\partial W_{ab}}{\partial x} \tag{4.66}$$

The effect of the anticlumping term on the kernel gradient is shown in Figure 4.3 for various values of ε

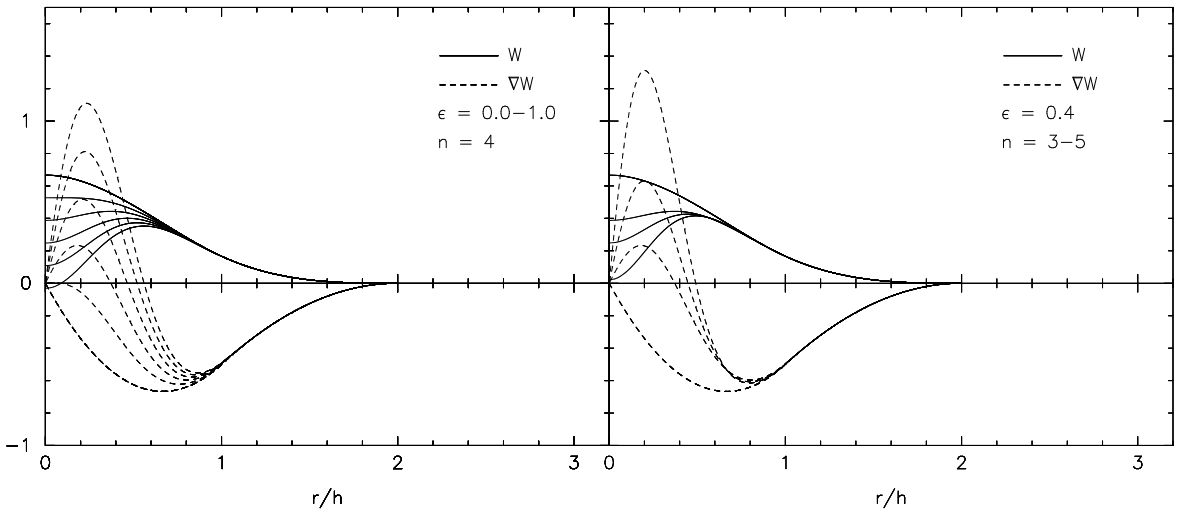

Figure 4.3: Effect of the anticlumping term on the kernel gradient in the anisotropic magnetic force. The cubic spline kernel (solid line) and its first derivative (dashed) are shown as modified by the anticlumping term. The left panel shows the effect of varying ε (shown in steps of 0.2 from $\varepsilon = 0.0$ to $\varepsilon = 1.0$) whilst the right panel shows the effect of varying the index n (shown for $n = 3, 4$ and 5, with the unmodified kernel shown for comparison). The constant kernel in the denominator, W_1, is evaluated at $r/h = 1/1.5$. The modification of the kernel gradient shown in this figure is used when computing the anisotropic magnetic force to prevent the particles from clumping unphysically. The modified kernel itself is not used in the calculations and is plotted for comparison only.

and n. This modified gradient is *only* used in the anisotropic magnetic force and does not therefore affect the calculation of hydrodynamic and isotropic magnetic forces.

The function R is designed to increase as the particle separation decreases. The kernel gradients in Figure (4.3) are shown for a smoothing length of $h = 1.5\Delta p$ and therefore in (4.62) the kernel in the denominator is computed using $\Delta p/h = 1/1.5$. In the one dimensional numerical tests described in §4.6 simulations using this value of smoothing length, use of the anticlumping term was found to give good results with few side effects. In two and three dimensions, however, more typical values for h are in the range $1.1 - 1.2\Delta p$, in order to reduce the number of neighbours required in the summations (and thus the computational expense). Re-running the one dimensional shock simulations with these values for h, it was found that the artificial stress term produced pronounced errors in the shock profiles (this is discussed further in §4.6.3 and demonstrated in Figure 4.13). For this reason we find it is better to interpret $W(\Delta p)$ as the kernel evaluated at a particular fixed radius, rather than at the average particle spacing. We therefore use $r/h = 1/1.5$ in $W(\Delta p)$ independent of the choice of smoothing length. That this provides a significant improvement in the results is also demonstrated in Figure (4.6) from the results of a stability analysis of the SPMHD equations incorporating the anticlumping term. The stability analysis is given below.

Stability analysis with anticlumping term

A one-dimensional stability analysis of SPH including an artificial stress term is given by Monaghan (2000). With the artificial stress interpreted as a modification to the kernel gradient on the anisotropic force, the one dimensional dispersion relation for MHD is easily obtained from the hydrodynamic version

(3.41) by assuming a pressure of the form $P = P_{iso} + P_{aniso}$, where in this case we have $P_{iso} = P + \frac{1}{2}B_x^2$ and $P_{aniso} = -B_x^2$. The resulting dispersion relation is given by

$$\begin{aligned}\omega_a^2 &= \frac{2mP_{iso}}{\rho_0^2}\sum_b [1-\cos k(x_a-x_b)]\frac{\partial^2 W_{ab}}{\partial x^2} \\ &+\frac{m^2}{\rho_0^2}\left(c_s^2 - \frac{2P_{iso}}{\rho_0}\right)\left[\sum_b \sin k(x_a-x_b)\frac{\partial W_{ab}}{\partial x}\right]^2 \\ &+\frac{2mP_{aniso}}{\rho_0^2}\sum_b [1-\cos k(x_a-x_b)]\frac{\partial^2 Y_{ab}}{\partial x^2} \\ &-\frac{m^2}{\rho_0^2}\left(\frac{2P_{aniso}}{\rho_0}\right)\left[\sum_b \sin k(x_a-x_b)\frac{\partial W_{ab}}{\partial x}\right]\left[\sum_b \sin k(x_a-x_b)\frac{\partial Y_{ab}}{\partial x}\right], \end{aligned} \tag{4.67}$$

where the modified kernel Y and its derivatives are given by

$$Y_{ab} = \left[1-\frac{\varepsilon}{2(n+1)}\left(\frac{W_{ab}}{W_1}\right)^n\right]W_{ab}, \tag{4.68}$$

$$\frac{\partial Y_{ab}}{\partial x} = \left[1-\frac{\varepsilon}{2}\left(\frac{W_{ab}}{W_1}\right)^n\right]\frac{\partial W_{ab}}{\partial x}, \tag{4.69}$$

$$\frac{\partial^2 Y_{ab}}{\partial x^2} = \frac{\partial^2 W_{ab}}{\partial x^2} - \frac{\varepsilon}{(n+1)W_1^n}\frac{\partial^2 W_{ab}^{n+1}}{\partial x^2}. \tag{4.70}$$

Figure 4.4 shows contours of the square of the numerical sound speed $C_{num}^2 = \omega^2/k^2$ from this dispersion relation as a function of wavenumber and the negative stress parameter $\mathscr{R}$ (where in this case we have $P_{iso}/\rho_0 = c_s^2(2-\mathscr{R})$ and $P_{aniso}/\rho_0 = 2c_s^2(\mathscr{R}-1)$) for an isothermal equation of state, using $n = 4$ and six different values of ε. The top left panel ($\varepsilon = 0.0$) corresponds to Figure 4.1, except that the $y-$axis extends to $\mathscr{R} = -10$ in this case. Results are shown for a fixed smoothing length of $h = 1.2\Delta p$, however as discussed above the constant kernel in the denominator, W_1, is evaluated at $r/h = 1/1.5$. This means that the kernel used on the anisotropic term corresponds to those shown in Figure (4.3). We observe that for this value of n the formalism is stabilised for $\varepsilon \gtrsim 0.3$ and this is confirmed by numerical simulations (Figure 4.5). However, whereas in the $\varepsilon = 0.0$ case the contours near $k_x = 0$ are close to unity, in Figure (4.1) the numerical wave speed appears to increase substantially with increasing negative stress ($\mathscr{R} \to -\infty$). Thus, although the formalism is stabilised at short wavelengths, the wave speed at long wavelengths is also affected slightly.

This effect is illustrated further in Figure (4.6), where we plot the numerical sound speed versus $\mathscr{R}$ at $k_x \approx 0$ taken from Figure (4.1) (solid line) for $h = 1.2\Delta p$. The results using W_1 evaluated at the average particle spacing (ie at $r/h = 1/1.2$ in this case) as in the original formulation of Monaghan (2000) are also shown (dashed line). In both cases the wave speed is increases substantially as $\mathscr{R}$ becomes more negative, although the former case is a significant improvement over the latter. To confirm that the analytic stability analysis is an accurate representation of numerical results, we also plot the results of 12 simulations of small amplitude (0.5%) isothermal sound waves (as described in §3.7.2) with a constant magnetic field in the $x-$direction corresponding to various values of $\mathscr{R}$. The numerical results (solid points) show excellent agreement with the analytic dispersion relation.

To understand the increase in wave speed with decreasing $\mathscr{R}$ caused by the anticlumping term, it is

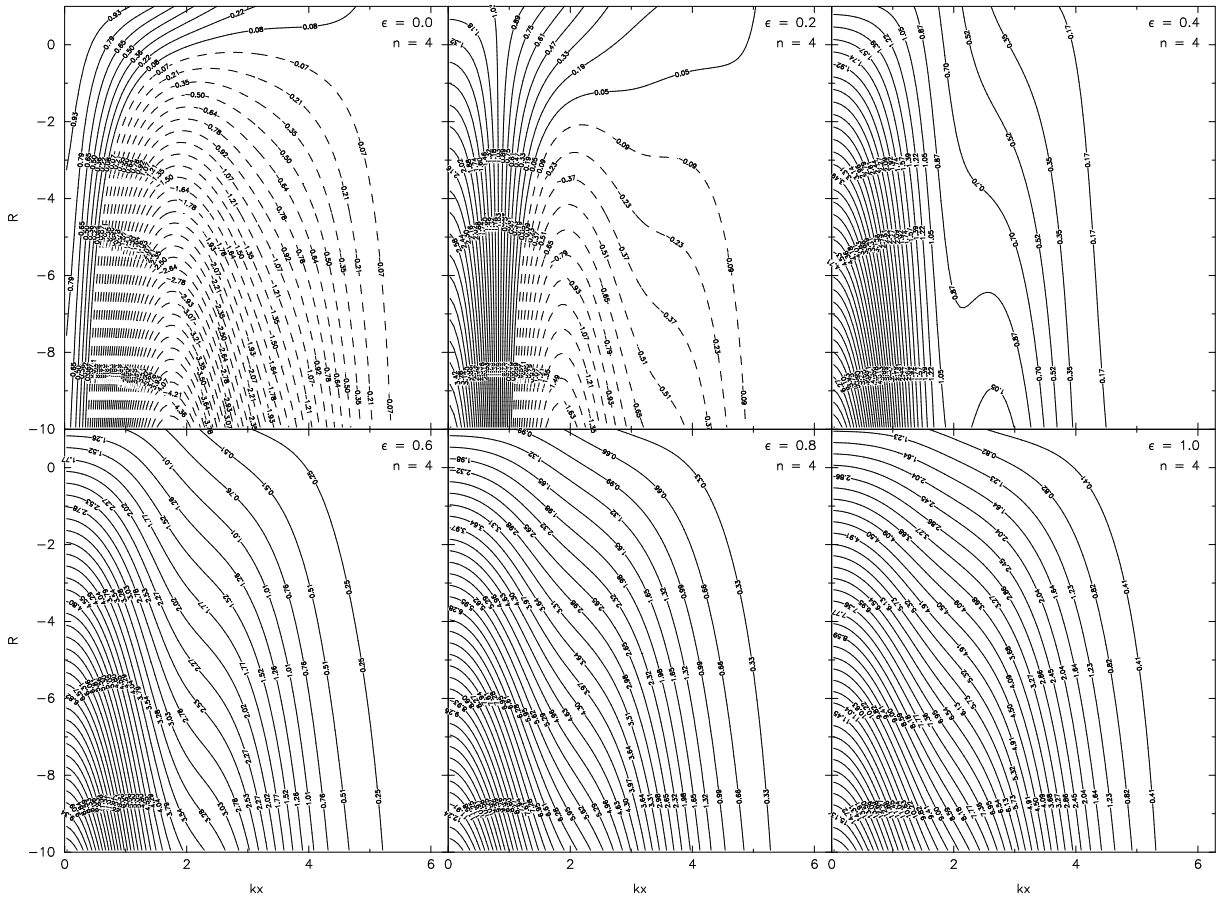

Figure 4.4: Effect of the anticlumping term on the one dimensional stability properties of the cubic spline kernel for various values of ε and n (as indicated in legend). Contours show the square of the numerical sound speed from the dispersion relation (4.67) as a function of the negative stress parameter $\mathscr{R} = (1 - \frac{1}{2}B_x^2/P)$ ($y-$axis) and the wavenumber in units of the particle spacing. Results are for a fixed smoothing length of $h = 1.2\Delta p$, with W_1 evaluated at $r/h = 1.5$.

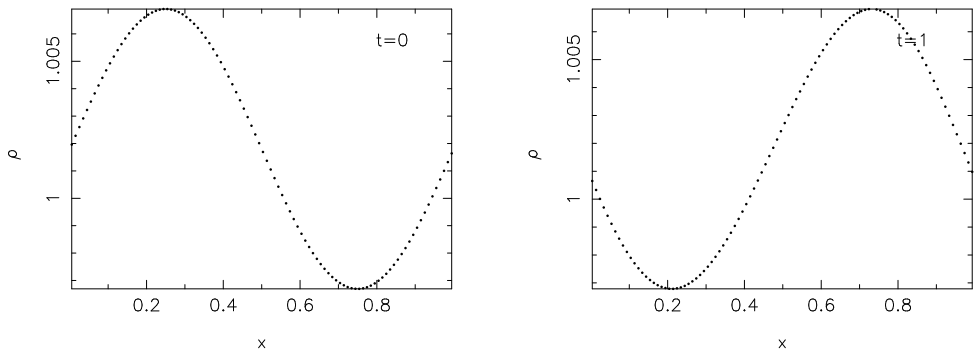

Figure 4.5: A repeat of the isothermal sound wave simulation shown in Figure 4.2 (with $\mathscr{R} = -1$) using the anticlumping term with parameters $\varepsilon = 0.4, n = 4$. The initial conditions are shown in the left panel, using 100 particles with an initial amplitude of 0.5%. The results after one period are shown in the right panel and are clearly stabilised by the anticlumping term, although the wave exhibits a significant phase error.

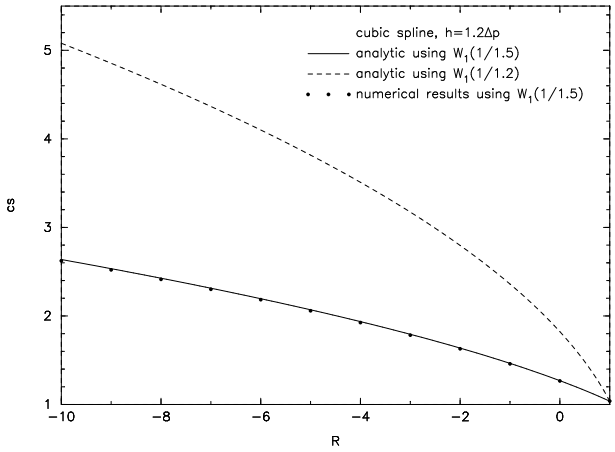

Figure 4.6: Numerical sound speed vs negative stress parameter R for the cubic spline kernel with a fixed smoothing length of $h = 1.2\Delta p$ and anticlumping parameters $\varepsilon = 0.4$, $n = 4$. The solid and dashed lines show the results at $k_x \approx 0$ from the dispersion relation (4.67), with the kernel in the denominator of the anticlumping term evaluated at the average particle spacing (dashed line) and at the fixed radius 1/1.5 (solid line), as discussed in the text. In the latter case the analytic results may be compared with the solid points from numerical simulations. The close agreement between the two demonstrates that the analytic stability analysis is a faithful representation of the numerical results.

instructive at to consider (4.67) in the limit of $k \to 0$ (ie. at long wavelengths). In this case we have $\sin k(x_a - x_b) \approx k(x_a - x_b)$ and $\cos k(x_a - x_b) \approx 1 - \frac{1}{2}k^2(x_a - x_b)^2$, giving

$$\begin{aligned}\omega_a^2/k_x^2 &= \frac{mP_{iso}}{\rho_0^2}\sum_b (x_a - x_b)^2 \frac{\partial^2 W_{ab}}{\partial x^2} + \frac{m^2}{\rho_0^2}\left(c_s^2 - \frac{2P_{iso}}{\rho_0}\right)\left[\sum_b (x_a - x_b)\frac{\partial W_{ab}}{\partial x}\right]^2 \\ &\quad + \frac{mP_{aniso}}{\rho_0^2}\sum_b (x_a - x_b)^2 \frac{\partial^2 Y_{ab}}{\partial x^2} - \frac{m^2}{\rho_0^2}\left(\frac{2P_{aniso}}{\rho_0}\right)\left[\sum_b (x_a - x_b)\frac{\partial W_{ab}}{\partial x}\right]\left[\sum_b (x_a - x_b)\frac{\partial Y_{ab}}{\partial x}\right] \quad (4.71)\end{aligned}$$

The accuracy of the numerical sound speed in this limit (which is the limit of an infinite number of particles, but not an infinite number of neighbours) is governed by the extent to which, for each kernel, the following normalisation conditions hold on the gradients:

$$\sum_b \frac{m_b}{\rho_b}(x_a - x_b)\frac{\partial W_{ab}}{\partial x} \approx 1, \qquad \text{and} \qquad \frac{1}{2}\sum_b \frac{m_b}{\rho_b}(x_a - x_b)^2 \frac{\partial^2 W_{ab}}{\partial x^2} \approx 1. \quad (4.72)$$

In the limit of an infinite number of neighbours (ie. $h \to \infty$) the summations can be written as integrals and the normalisations take the form

$$\int (x - x')\frac{\partial W}{\partial x}\mathrm{dx}' = 1 \qquad \text{and} \qquad \frac{1}{2}\int (x - x')^2 \frac{\partial^2 W}{\partial x^2}\mathrm{dx}' = 1. \quad (4.73)$$

It may be easily verified by the reader that setting the corresponding expressions to unity in (4.71) (for both kernels) gives the exact dispersion relation for sound waves (ie. $\omega^2 = k_x^2 c_s^2$). A straightforward integration for the cubic spline kernel demonstrates that both of these integrals hold on account of the normalisation condition (3.4) and the fact that the kernel is even. Considering the modified kernel gradient used in the anticlumping term (4.69)-(4.70), the normalisations can no longer hold because the kernel gradient is no longer normalised. The approach taken to this problem in Monaghan (2000) is to

simply choose the index n so as to minimise the term multiplying these integrals, giving n in the range $3 \leq n \leq 7$. Naively, one might expect that a renormalising the modified kernel gradient so as to maintain the integrals (4.73) would increase the accuracy of the simulation results. However in practise we find that this is not the case, since the summations (4.72) only sample the integrals at a few points. As such the renormalisation can have detrimental effects because it changes the kernel gradient at large r/h to compensate for the changing shape at small r/h, affecting more than the nearest neighbours.

In the hydrodynamic case it was found that allowing the smoothing length to vary could significantly improve the numerical wave speeds (§3.7.2). In the case of a variable smoothing length, three options are available for the modified kernel gradient: to use the average of the smoothing lengths, the average of the kernel gradients or thirdly to use the consistent formulation including the variable smoothing length terms (§4.3.6), in this case evaluated for the modified kernel gradient. Since the variable smoothing length terms effectively normalise the kernel gradient, the latter would seem to be a particularly good approach, particularly in the light of the discussion in the previous section. However, the one (somewhat large) caveat to the anticlumping approach is that, using variable smoothing lengths, we do not find that the anticlumping term guarantees numerical stability for all values of negative stress. For example, using the average smoothing length in (all of) the kernel gradients, the one dimensional sound waves become unstable at $\mathscr{R} \lesssim -9$. Using the average of the gradients the problem is worse and the waves become unstable at $\mathscr{R} \lesssim -3$. With the variable smoothing length terms calculated independently for both kernels, instability is observed at $\mathscr{R} \lesssim -2$. It would seem therefore, that although sufficient to provide numerical stability for all of the test problems considered here, the anticlumping approach as it stands does not provide a comprehensive solution. For this reason we compare this approach to two other methods described in §4.4.2 and §4.4.4 and in fact the multidimensional tests described in Chapter 5 suggest that these methods both give better results than use of the anticlumping term.

Implementation

The anticlumping term is implemented in this thesis by calculating the modified kernel gradient in a similar manner to the usual kernel. This is also the most cost-effective implementation since the modified kernel can be pre-computed and tabulated as for the usual kernel.

Where the total energy equation (4.38) is used, the contribution to the total energy from the anti-clumping term must be added for consistency. This can be found using (4.36) and is given by

$$\left(\frac{de_a}{dt}\right)_{src} = \sum_b m_b \mathrm{v}_a^i R \left[\left(\frac{B_i B_j}{\rho^2}\right)_a + \left(\frac{B_i B_j}{\rho^2}\right)_b\right] \frac{\partial W_{ab}}{\partial x_{j,a}}. \tag{4.74}$$

Alternatively, interpreting the anticlumping term as a modified kernel gradient, the contribution to the total energy from the anisotropic term in (4.38) is replaced by

$$\left(\frac{de_a}{dt}\right)_{aniso} = \sum_b m_b \left(\frac{B_a^i B_a^j}{\rho_a^2} \mathrm{v}_b^i \nabla^j W_{ab} + \frac{B_b^i B_b^j}{\rho_b^2} \mathrm{v}_a^i \nabla^j Y_{ab}\right) + \sum_b m_b \frac{B_a^i B_a^j}{\rho_a^2} \mathrm{v}_a^i \left(\nabla^j Y_{ab} - \nabla^j W_{ab}\right). \tag{4.75}$$

In principle it is possible to conserve total energy exactly by also using the modified kernel gradient in the $\mathbf{B}/\rho$ version of the induction equation (giving $W_{ab} = Y_{ab}$ in the above). However this introduces

an unnecessary alteration to the magnetic field evolution and consequently produces undesirable side effects. The degree to which energy conservation is violated when the total energy equation is evolved may therefore be used as an indication of the relative error introduced by the anticlumping term. In general this is found to be quite small for the problems considered in this thesis.

4.4.2 Morris approach

An alternative approach suggested by Morris (1996) is to retain the conservation of momentum on the isotropic terms in (4.33) but to treat the anisotropic terms using a differencing formalism which is exact in the case of a constant functions (see §3.2.3). The force term is then given by

$$-\sum_b m_b \left(\frac{P_a + \frac{1}{2}B_a^2/\mu_0}{\rho_a^2} + \frac{P_b + \frac{1}{2}B_b^2/\mu_0}{\rho_b^2} \right) \frac{\partial W_{ab}}{\partial x^i} + \frac{1}{\mu_0} \sum_b m_b \frac{(B_i B_j)_b - (B_i B_j)_a}{\rho_a \rho_b} \frac{\partial W_{ab}}{\partial x_j}. \tag{4.76}$$

This formalism does not therefore guarantee exact momentum conservation (since the anisotropic term does not give equal and opposite forces between particle pairs) but can be expected to give good results on shocks for which the anisotropic term is less important. It is also a better approach than the vector-based formalisms (§4.3.5) since (4.76) is still a discretisation of a tensor force and therefore conserves momentum in the continuum limit for non-zero $\nabla \cdot \mathbf{B}$. This also means that (4.76) retains the consistent formulation of the MHD equations in the presence of monopoles, although the discrete equations are no longer self-consistent with each other. Note that when using the variable smoothing length terms, we use the average of the normalised kernel gradient in (4.76), as in the dissipative terms. The dispersion relation for this formalism in the case of one dimensional MHD takes a particularly simple form since the terms resulting from the anisotropic force are zero in the case of $B_x =$const, giving

$$\begin{aligned} \omega_a^2 &= \frac{2mP_{iso}}{\rho_0^2} \sum_b [1 - \cos k(x_a - x_b)] \frac{\partial^2 W_{ab}}{\partial x^2} \\ &\quad + \frac{m^2}{\rho_0^2} \left(c_s^2 - \frac{2P_{iso}}{\rho_0} \right) \left[\sum_b \sin k(x_a - x_b) \frac{\partial W_{ab}}{\partial x} \right]^2. \end{aligned} \tag{4.77}$$

Contours of the square of the numerical sound speed $C_{num}^2 = \omega^2/k_x^2$ from this dispersion relation are shown in Figure (4.7). The formalism is seen to be stable for all wavelengths and this is confirmed by numerical simulations. Also the numerical wave speed does not show the increase with increasing negative stress observed for the anticlumping term, although the numerical wave speed is somewhat overestimated at short wavelengths $k_x \sim \pi/2\Delta x$. The more accurate numerical wave speeds result from the use of the differencing formalism since in this case the zeroth order error terms for small perturbations are zero exactly (§3.2.3). However, the main test of this formalism is the degree to which the lack of momentum conservation affects the shock capturing ability of the scheme. This is examined and compared with the anticlumping approach in the shock tube tests described in §4.6 where in fact the differences are found to be very minor. This simple approach is therefore a very viable solution which guarantees numerical stability in all circumstances and does not suffer from the numerical wave speed errors introduced by the anticlumping term.

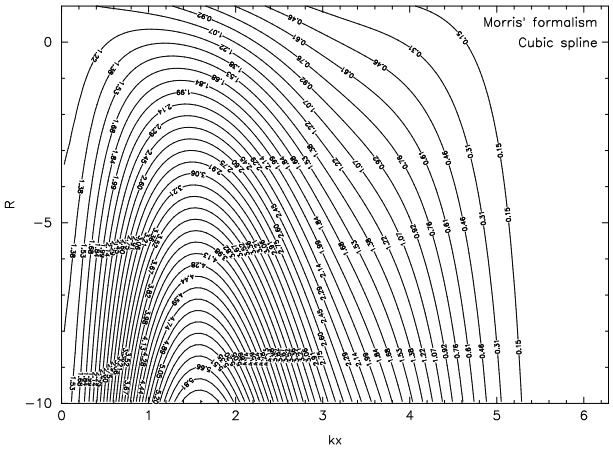

Figure 4.7: One dimensional stability properties of the cubic spline kernel using Morris' formalism of the magnetic force (4.76). Contours of the square of the numerical sound speed from the dispersion relation (4.77) are shown with respect to the negative stress parameter $\mathscr{R} = (1 - \frac{1}{2}B_x^2/P)$ ($y-$axis) and the wavenumber in units of the particle spacing ($x-$axis). The formalism is stable to negative stress at all wavelengths, however momentum conservation is not maintained exactly for anisotropic forces. Note that the numerical sound speed is close to unity at long wavelengths ($k_x \to 0$), although somewhat overestimated at short wavelengths $k_x \sim \pi/2\Delta x$.

4.4.3 Børve approach

Børve et al. (2001) remove the instability by explicitly subtracting the unphysical force term from the conservation form of the momentum equation (4.33). This term is calculated using

$$\frac{\mathbf{B}(\nabla \cdot \mathbf{B})}{\rho} \approx \mathbf{B}_a \sum_b m_b \left(\frac{\mathbf{B}_b}{\rho_b^2} + \frac{\mathbf{B}_a}{\rho_a^2} \right) \cdot \nabla_a W_{ab} \tag{4.78}$$

which is then subtracted from (4.33). This resolves the stability problem since it removes the (unphysical) component of magnetic force along the line joining the particles (ie. in continuum form the formalism becomes simply the $\mathbf{J} \times \mathbf{B}$ component of the magnetic force). However the disadvantage to this approach can be seen in the simple case of one dimensional MHD, where for a constant B_x the term introduces a low level of numerical noise throughout the simulation. In Børve et al. (2001) this noise is removed by periodically smoothing the magnetic field, which is also used to remove post-shock oscillations in **B**. Since we use artificial resistivity to prevent such post-shock oscillations (see below), additional smoothing is not required and so the noise introduced by subtracting (4.78) remains present. Furthermore we find that the lack of momentum conservation in this formalism can lead to extremely poor results on shock tube problems in the absence of the particle regularisation procedure used by these authors.

4.4.4 Removing the constant component of magnetic field

For simulations where the magnetic field is strong due to an initial net flux through the simulation, a simple method for removing the tensile instability is to remove the constant, external (ie. produced by currents outside the simulation domain) component of the magnetic field from the anisotropic gradient analytically (by subtracting this field component from the stress contained within the gradient term). The

stress tensor (4.3) for particle a is modified according to

$$S_a^{ij} = -\left(P_a + \frac{1}{2\mu_0}B_a^2\right)\delta^{ij} + \frac{1}{\mu_0}\left(B_a^i B_a^j - B_0^i B_0^j\right), \tag{4.79}$$

where $\mathbf{B}_0$ is the magnetic field component which does not change throughout the simulation (for example in one dimensional simulations we would use $\mathbf{B}_0 = [B_x, 0, 0]$). In general the constant field could also have a spatial profile (for example in a fixed dipole field from the central star in an accretion disc) and would in this case depend on the particle position. In all of the cases we consider the external magnetic field is always the same independent of the particle position, such that calculating (4.79) involves storing only a single vector. It is worth noting that the formalism given above (where the constant field is subtracted from the total field) is more efficient than explicitly adding the contributions from separate constant and variable field components.

This simple solution completely cures the one dimensional instability because the B_x component of the field is explicitly removed from the anisotropic gradient term. Negative stresses can only arise in this formulation when the anisotropic terms in the fluctuating component dominate the isotropic pressure term (from which the constant field has *not* been subtracted). In many ways this is similar to the original proposal of Phillips and Monaghan (1985) in which the maximum value of the stress tensor over all the particles was determined and then subtracted from the stress for each particle. Such an approach makes sense in light of the fact that the instability arises due to the non-zero evaluation of the gradient of a constant function in the momentum-conserving formulation (c.f. §3.2.3). Morris' approach described above (§4.4.2) removes this error by ensuring that the gradient of a constant function vanishes exactly in the anisotropic term, although momentum conservation is not maintained exactly. Using the momentum-conserving formalism *any* arbitrary constant could be added to the stress in order to make the total stress positive (which effectively changes the factor multiplying the first error term in equation 3.19).

The disadvantage to this approach is that total energy is not conserved exactly since the contribution to the total energy evolution from the induction equation (which uses the total magnetic field) does not exactly balance the contribution from the momentum equation. This method is used in many of the two dimensional problems considered in Chapter 5, reverting to the Morris approach where this is not possible. The results in all cases are much better than those obtained using the anticlumping term.

4.5 Shocks

Various approaches to ensuring a physically realistic treatment of shocks in numerical schemes were discussed in an SPH context in §3.5. Following this, dissipative terms (artificial viscosity and thermal conductivity) were derived for hydrodynamic shocks similar to those given by Monaghan (1997b), the major differences being that the artificial thermal conductivity was applied to particles in both compression and rarefaction (the importance of which was highlighted in the numerical tests described in §3.7) and controlled using a switch similar to that used in the viscosity (§3.5.2).

In this section we generalise the dissipative terms derived in §3.5 to the MHD case. In particular using the formulation of Monaghan (1997b) naturally results in an artificial resistivity term in the SPMHD induction equation. Whereas the effect of adding artificial thermal conductivity at discontinuities in the thermal energy is fairly small (§3.7.3), in this case adding artificial resistivity at discontinuities in

the magnetic field turns out to be crucial in order to prevent significant post-shock oscillations in the magnetic field (§4.6.3).

4.5.1 Artificial dissipation

Dissipative terms in the MHD case are constructed in a manner analogous to that of §3.5 (Monaghan, 1997b) involving jumps in the physical variables. As in the hydrodynamic case (§3.5.1), the momentum equation (4.33) contains a viscosity term (for $\mathbf{v}_{ab}\cdot\mathbf{r}_{ab}<0$)

$$\left(\frac{d\mathbf{v}_a}{dt}\right)_{diss} = -\sum_b m_b \frac{\alpha \mathrm{v}_{sig}(\mathbf{v}_a-\mathbf{v}_b)\cdot\hat{\mathbf{r}}_{ab}}{2\bar{\rho}_{ab}}\nabla_a W_{ab}, \tag{4.80}$$

where α is a dimensionless constant of order unity, v_{sig} is the maximum speed of signal propagation between the particles, $\hat{\mathbf{r}}_{ab}=(\mathbf{r}_a-\mathbf{r}_b)/|\mathbf{r}_a-\mathbf{r}_b|$ is a unit vector along the line joining the particles and $\bar{\rho}_{ab}=\frac{1}{2}(\rho_a+\rho_b)$. The term in the total energy equation (4.38) involves a jump in energy and is given by

$$\left(\frac{de_a}{dt}\right)_{diss} = -\sum_b m_b \frac{\mathrm{v}_{sig}(e_a^*-e_b^*)}{2\bar{\rho}_{ab}}\hat{\mathbf{r}}_{ab}\cdot\nabla_a W_{ab}, \tag{4.81}$$

where in the MHD case the energy e^* is constructed using the velocity jump parallel to the line joining the particles and the jump in the magnetic field component perpendicular to this line (since these components are expected to change at shock fronts, although see below), giving

$$e_a^* = \begin{cases} \frac{1}{2}\alpha(\mathbf{v}_a\cdot\hat{\mathbf{r}}_{ab})^2 + \alpha_u u_a + \frac{1}{2}\alpha_B[B_a^2-(\mathbf{B}_a\cdot\hat{\mathbf{r}}_{ab})^2]/\mu_0\bar{\rho}_{ab}, & \mathbf{v}_{ab}\cdot\mathbf{r}_{ab}<0; \\ \alpha_u u_a + \frac{1}{2}\alpha_B[B_a^2-(\mathbf{B}_a\cdot\hat{\mathbf{r}}_{ab})^2]/\mu_0\bar{\rho}_{ab}, & \mathbf{v}_{ab}\cdot\mathbf{r}_{ab}\geq 0; \end{cases} \tag{4.82}$$

with a similar equation for e_b^*. The appropriate form of the other dissipative terms is then found by working out the contribution to the thermal energy and requiring that this contribution be positive definite (leading to a positive definite increase in entropy). The contribution to the thermal energy equation is found using

$$\frac{du}{dt} = \frac{de}{dt} - \mathbf{v}\cdot\frac{d\mathbf{v}}{dt} - \frac{d}{dt}\left(\frac{B^2}{2\mu_0\rho}\right). \tag{4.83}$$

Substituting (4.80) and (4.81), a positive definite contribution to the thermal energy from the kinetic and magnetic terms is given only if the terms in the thermal energy equation take the form

$$\begin{aligned}\left(\frac{du}{dt}\right)_{diss} = & -\sum_b m_b \frac{\mathrm{v}_{sig}}{2\bar{\rho}_{ab}}\left\{\frac{1}{2}\alpha\left[(\mathbf{v}_a\cdot\hat{\mathbf{r}}_{ab})-(\mathbf{v}_b\cdot\hat{\mathbf{r}}_{ab})\right]^2 + \alpha_u(u_a-u_b)\right. \\ & \left. + \frac{\alpha_B}{2\mu_0\bar{\rho}_{ab}}\left[B_{ab}^2-(\mathbf{B}_{ab}\cdot\hat{\mathbf{r}}_{ab})^2\right]\right\}\hat{\mathbf{r}}_{ab}\cdot\nabla_a W_{ab}\end{aligned} \tag{4.84}$$

where both the kinetic and magnetic terms can be seen to give a positive definite contribution to the thermal energy since the kernel gradient term is negative definite. The thermal energy term provides an artificial thermal conductivity which acts to smooth gradients in the thermal energy. This term is identical to the hydrodynamic case and has been discussed in detail in §3.5.1 and in the numerical tests described in §3.7.3. The kinetic energy contribution to (4.84) takes the form given due to the contribution from the

viscosity term in the momentum equation via (4.83). Similarly for the contribution from the magnetic energy term in (4.81) to result in a positive definite dissipation of the form given in (4.84) requires a dissipation term in the induction equation, in this case of the form

$$\left(\frac{d\mathbf{B}}{dt}\right)_{diss} = \rho_a \sum_b m_b \frac{\alpha_B \mathrm{v}_{sig}}{2\bar{\rho}_{ab}^2} \left[\mathbf{B}_{ab} - \hat{\mathbf{r}}_{ab}(B_{ab}\cdot\hat{\mathbf{r}}_{ab})\right] \hat{\mathbf{r}}_{ab}\cdot\nabla_a W_{ab}. \tag{4.85}$$

This term may be written as

$$\rho_a \sum_b m_b \frac{\alpha_B \mathrm{v}_{sig}}{2\bar{\rho}_{ab}^2} \left[\hat{\mathbf{r}}_{ab}\times(\mathbf{B}_{ab}\times\hat{\mathbf{r}}_{ab})\right] \hat{\mathbf{r}}_{ab}\cdot\nabla_a W_{ab}. \tag{4.86}$$

It may be expected that in continuum form this equation should be some approximation to

$$-\nabla\times(\eta\nabla\times\mathbf{B}), \tag{4.87}$$

which for constant η is given by

$$\eta\left[\nabla^2\mathbf{B} - \nabla(\nabla\cdot\mathbf{B})\right] \tag{4.88}$$

Using the second derivative interpolations given in §3.2.4 we find that in fact (4.86) is an SPH form of

$$\eta\left[\nabla^2\mathbf{B} - \frac{2}{3}\nabla(\nabla\cdot\mathbf{B})\right], \tag{4.89}$$

which is similar to the exact equation with ohmic diffusivity $\eta \propto \alpha_B \mathrm{v}_{sig} h$. Since this term is derived from a jump in the magnetic energy perpendicular to the line joining the particles, the effect is to smooth out gradients in transverse magnetic field over several smoothing lengths, just as the viscosity acts to smooth out gradients in the velocity along the line between the particles

An important point to note is that discontinuities in the magnetic field can occur in the absence of compression such that the artificial resistivity term should be applied uniformly to particles in both compression and rarefaction. In fact the application of artificial resistivity, unlike that of artificial thermal conductivity, turns out to be a crucial requirement in the simulation of MHD shocks (this is graphically illustrated in Figure 4.10), a point which is often overlooked in dissipation-based shock capturing schemes for MHD. For example both Børve et al. (2001) and Maron and Howes (2003) find it necessary to explicitly smooth the magnetic field at regular intervals in order to prevent post-shock oscillations. Using the artificial resistivity terms described above, such smoothing occurs naturally within the simulation. Similar artificial resistivity terms are required in finite-difference codes which are also based on the differential form of the MHD equations (see for example Caunt and Korpi 2001, which is based on Nordlund and Galsgaard 1995).

Dissipation terms using total energy

In the above derivation, it was assumed that only components of the magnetic field perpendicular to the line joining the particles would change at a shock front. However, in a numerical simulation the assumption of non-zero magnetic divergence may not hold exactly, as has already been discussed. In

particular divergence errors are often created at flow discontinuities where fluid quantities are changing rapidly. It therefore makes good sense to drop the assumption of non-zero magnetic divergence in the derivation of the dissipative terms. The assumption that only the velocity components parallel to the line joining the particles will change is also no longer true in the MHD case since velocity components transverse to this line will change with a jump in the transverse magnetic field. For this reason we re-derive the dissipative terms with an energy term of the form

$$e_a^* = \frac{1}{2}\alpha \mathbf{v}_a^2 + \alpha_u u_a + \alpha_B \frac{B_a^2}{2\mu_0 \bar{\rho}_{ab}} \tag{4.90}$$

which involves both the total kinetic and magnetic energies. For the contribution to the entropy to be positive definite, the terms in the thermal energy equation must take the form

$$\left(\frac{du}{dt}\right)_{diss} = -\sum_b m_b \frac{\mathrm{v}_{sig}}{2\bar{\rho}_{ab}} \left\{ \frac{1}{2}\alpha(\mathbf{v}_a - \mathbf{v}_b)^2 + \frac{\alpha_B}{2\mu_0\bar{\rho}_{ab}}(\mathbf{B}_a - \mathbf{B}_b)^2 + \alpha_u(u_a - u_b) \right\} \hat{\mathbf{r}}_{ab} \cdot \nabla_a W_{ab}, \tag{4.91}$$

which correspondingly requires dissipation terms in the momentum and induction equations of the form

$$\left(\frac{d\mathbf{v}_a}{dt}\right)_{diss} = \sum_b m_b \frac{\alpha \mathrm{v}_{sig}(\mathbf{v}_a - \mathbf{v}_b)}{2\bar{\rho}_{ab}} \hat{\mathbf{r}}_{ab} \cdot \nabla_a W_{ab}, \tag{4.92}$$

$$\left(\frac{d\mathbf{B}}{dt}\right)_{diss} = \rho_a \sum_b m_b \frac{\alpha_B \mathrm{v}_{sig}}{2\bar{\rho}_{ab}^2} (\mathbf{B}_a - \mathbf{B}_b) \hat{\mathbf{r}}_{ab} \cdot \nabla_a W_{ab}. \tag{4.93}$$

In the multidimensional case we find that use of (4.93) has distinct advantages over (4.85) since in more than one dimension divergence errors can cause the extra component of the magnetic field to jump slightly. Whether or not to use (4.92) in place of (4.80) is slightly less clear. The application of dissipative terms to specific discontinuities was discussed at some length in §3.5.2 with regards to artificial thermal conductivity, where it was found that smoothing of discontinuities in the thermal energy was necessary only where the discontinuity is not already smoothed by the application of artificial viscosity (which could occur, for example at a contact discontinuity). In the present case, since a jump in transverse velocity can *only* occur at a corresponding jump in the transverse magnetic field, these discontinuities will already be smoothed by the application of artificial resistivity there and so the use of (4.92) may simply result in excessive dissipation (since it must also be applied to particles in both compression and rarefaction, whereas the usual viscosity term is applied only to particles in compression). Furthermore the effect of (4.92) is to diffuse discontinuities corresponding to the curl of the vector field as well as the divergence and the expression therefore no longer conserves angular momentum and no longer vanishes for rigid body rotation (since in effect rotational energy is converted into thermal energy). Thus for simulations involving significant amounts of shear (for example in accretion discs) the effects of using (4.92) would need to be studied quite carefully. It is worth noting that a similar term was used by Morris (1996).

Signal Velocity

The signal velocity in the MHD case is a simple generalisation of that given in §3.5.1. The key point is that it is the relative speed of signals from moving observers at the positions of particles *a* and *b* when

the signals are sent along the line of sight. If there are no magnetic fields a good estimate of this signal velocity (c.f. §3.5.1) is

$$\mathrm{v}_{sig} = c_a + c_b - \beta \mathbf{v}_{ab} \cdot \hat{\mathbf{r}}_{ab}, \tag{4.94}$$

where c_a denotes the speed of sound of particle a and $\beta \sim 1$. The signal velocity is larger when the particles are approaching each other and in practice, the effects of shocks can be included by choosing $\beta = 2$. If there are magnetic fields then a variety of other waves are possible. The fastest wave in a static medium along the x axis has speed (c.f. Appendix C)

$$\mathrm{v}^2 = \frac{1}{2}\left[\left(c_s^2 + \frac{B^2}{\mu_0\rho}\right) + \sqrt{\left(c_s^2 + \frac{B^2}{\mu_0\rho}\right)^2 - 4\frac{c_s^2 B_x^2}{\mu_0\rho}}\right], \tag{4.95}$$

A natural generalization of (4.94) for the case of magnetic fields is to take

$$\mathrm{v}_{sig} = \mathrm{v}_a + \mathrm{v}_b - \beta \mathbf{v}_{ab} \cdot \hat{\mathbf{r}}_{ab}, \tag{4.96}$$

where

$$\mathrm{v}_a = \frac{1}{\sqrt{2}}\left[\left(c_a^2 + \frac{B_a^2}{\mu_0\rho_a}\right) + \sqrt{\left(c_a^2 + \frac{B_a^2}{\mu_0\rho_a}\right)^2 - 4\frac{c_a^2(\mathbf{B}\cdot\hat{\mathbf{r}}_{ab})^2}{\mu_0\rho_a}}\right]^{1/2}, \tag{4.97}$$

with a similar equation for v_b.

4.5.2 Artificial dissipation switches

Since artificial resistivity is required at discontinuities in the magnetic field, which may occur where particles are not necessarily approaching each other, artificial viscosity and resistivity should not be controlled using the same switch. A similar switch appropriate to the artificial resistivity term can be devised similar to that used in the artificial viscosity and thermal conductivities in the SPH case (§3.5.2). We evolve the resistive dissipation parameter α_B according to

$$\frac{d\alpha_B}{dt} = -\frac{\alpha_B}{\tau} + \mathscr{S} \tag{4.98}$$

where the decay timescale τ is given in §3.5.2 and in this case the source term is given by

$$\mathscr{S} = \max\left(\frac{|\nabla \times \mathbf{B}|}{\sqrt{\mu_0\rho}}, \frac{|\nabla \cdot \mathbf{B}|}{\sqrt{\mu_0\rho}}\right), \tag{4.99}$$

such that artificial resistivity is applied at large gradients in the current density as well as at large divergences in the magnetic field (the latter term is required only when the total energy formulation (4.93) of the artificial resistivity is used). The source term is constructed to have dimensions of inverse time, as required by (4.98). In the numerical shock tube tests described in §4.6.3 we find that using this switch in conjunction with switches for the viscosity and thermal conductivity can result in too little dissipation at shock fronts due to the fact that the transverse velocity components are not smoothed when (4.80) is

used in the artificial viscosity. In this case the artificial resistivity must provide sufficient smoothing for the discontinuities in both magnetic field and transverse velocity. For this reason we prefer in general to control only the viscosity and thermal conductivities using the switches and to apply the magnetic term using a uniform $\alpha_B = 1$.

4.6 Numerical tests in one dimension

The numerical scheme described in this chapter has been tested on a variety of one dimensional problems. In order to demonstrate that SPMHD gives good results on problems involving discontinuities in the physical variables we present results of standard problems used to test grid-base MHD codes (e.g. Stone et al. 1992; Dai and Woodward 1994; Ryu and Jones 1995; Balsara 1998; Dai and Woodward 1998). The advantages of SPMHD are the simplicity with which these results can be obtained and the complete absence of any numerical grid.

4.6.1 Implementation

The particles are allowed to move in one dimension only, whilst the velocity and magnetic field are allowed to vary in three dimensions. This means that the $y-$ and $z-$ components of velocity are evolved using the appropriate force terms and used in the total energy but that these velocities are not used to move the particles (this is rather like regarding the particles as representing planes in one dimension such that translations in the $y-$ and $z-$ directions have no effect).

We use equal mass particles such that density changes correspond to changes in particle spacing. Unless otherwise indicated in this section we integrate the continuity equation (3.43), the momentum equation (4.33), the total energy equation (4.38) and the induction equation (4.20). This is the most efficient implementation of the SPMHD equations since it does not require an extra pass over the particles to calculate the density via the summation (3.42). However, use of the continuity equation requires some smoothing of the initial conditions and this is done using the smoothing described in §3.7.3, although initial velocity profiles are not smoothed. Similar results to those shown here are also obtained when the thermal energy equation is integrated instead of the total energy. Additionally we note that whilst evolving the flux per unit mass (4.22) instead of the flux density (4.20) does not exactly maintain $\nabla \cdot \mathbf{B} = 0$ in one dimension, the associated errors are small and hence we also find in this case that the results are similar. Unless otherwise indicated the tests presented here are all performed with the artificial viscosity and thermal conductivity controlled using the switches discussed in §3.5.2. For the viscosity the minimum is set to $\alpha_{min} = 0.1$ whilst for the artificial thermal conductivity the minimum is zero. This results in very little dissipation away from shock fronts. Artificial resistivity is applied uniformly with $\alpha_B = 1$. This is required (rather than using the resistivity switch) because the transverse velocity components are not smoothed (that is we retain the use of (4.80) rather than (4.92)). The smoothing length is set according to the rule (3.67) such that initially $h = 1.2(m/\rho)$. The anticlumping term (§4.4.1) is used with parameters $\varepsilon = 0.8$ and $n = 4$ with the constant kernel in the denominator W_1 evaluated at a fixed radius $q = 1/1.5$ as discussed in §4.4.1, except where otherwise indicated.

Scaling

The magnetic field variable is scaled in units such that the constant μ_0 is unity and numerical quantities are dimensionless. Note that the magnetic flux density **B** has dimensions

$$[\mathbf{B}] = \frac{[mass]}{[time][charge]}, \tag{4.100}$$

whilst μ_0 has dimensions

$$[\mu_0] = \frac{[mass][length]}{[charge]^2}. \tag{4.101}$$

Choosing mass, length and time scales of unity and specifying $\mu_0 = 1$ therefore defines the unit of charge. Re-scaling of the magnetic field variable to physical units requires multiplication of the code value by a constant

$$\mathbf{B}_{physical} = \left\{ \frac{\mu_0 [mass]}{[length][time]^2} \right\}^{1/2} \mathbf{B}_{numerical}. \tag{4.102}$$

For example, in cgs units, with mass, length and time scales of unity the magnetic flux density in Gauss is given by

$$\mathbf{B}_{cgs} = (4\pi)^{1/2} \mathbf{B}_{numerical}. \tag{4.103}$$

4.6.2 Simple advection test

This simple test is described in Evans and Hawley (1988) and in Stone et al. (1992) and measures the ability of an algorithm to advect contact discontinuities. A square pulse of transverse magnetic field is setup and advected a distance of five times its width with the pressure terms switched off. The current density **J** is calculated in order to ascertain that the method does not produce sign reversals or anomalous extrema in this quantity. In SPH we compute this quantity using

$$\mathbf{J}_a = \nabla \times \mathbf{B}_a = \sum_b m_b (\mathbf{B}_a - \mathbf{B}_b) \times \nabla_a W_{ab}. \tag{4.104}$$

We perform this test simply by using a magnetic pressure that is negligible compared to the gas pressure. We setup 100 particles placed evenly along the x axis with constant velocity in the positive x-direction and use a pulse that is initially 50 particle spacings wide. The pulse is not initially smoothed in any way and periodic boundary conditions are enforced using ghost particles (this is also a good test of the periodic boundary conditions since the particles are continually crossing the domain).

The SPMHD results are shown in Figure 4.8 after advecting the pulse a distance of five times its width (in this case equivalent to 5 crossings of the computational domain). The top panel shows the results with the artificial dissipation terms turned off. There is no spread in the discontinuities since SPH uses a Lagrangian derivative which means that the advection is exact. The current density, which is analytically given by a delta function at each discontinuity, is also computed very well by the SPH approximation. In (Eulerian) grid based codes the advection terms must be explicitly evaluated, resulting in some diffusion

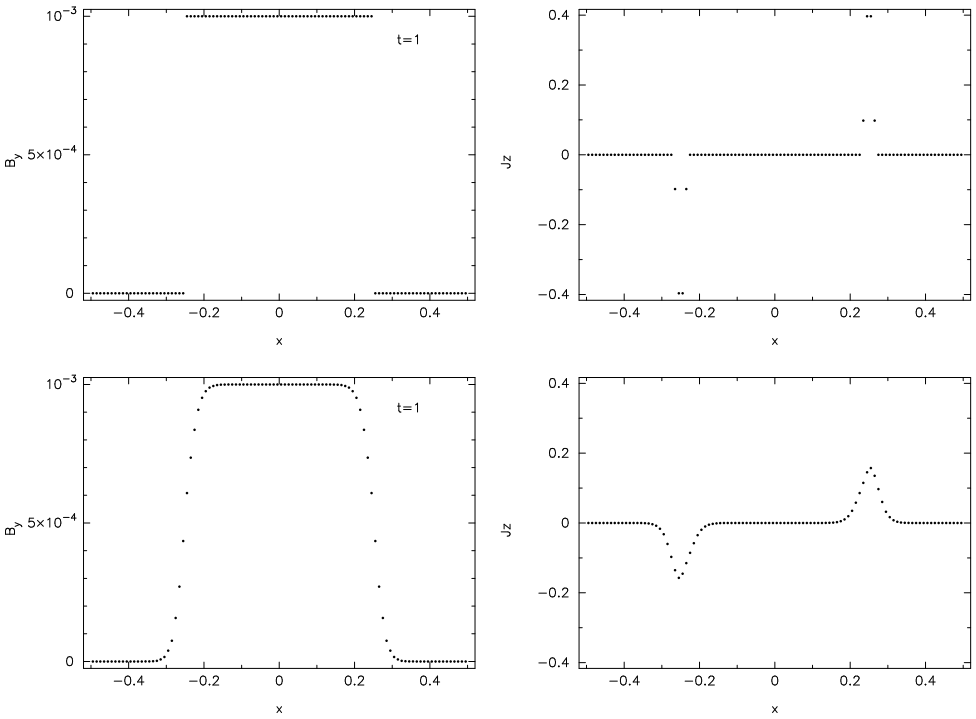

Figure 4.8: Results of the advection of a square pulse of transverse magnetic field 50 particle separations wide a distance of five times its width. In the absence of dissipative terms the discontinuities are kept to less than a particle spacing (top) due to the Lagrangian nature of SPH. The current density (top right) is also estimated well (analytically this is a delta function at each discontinuity). With the artificial resistivity turned on a small amount of smoothing is observed (bottom panels).

of the pulse as it is advected. In SPH the only diffusion present is that explicitly introduced in the shock capturing scheme. With the artificial resistivity turned on a small smoothing of the field is observed (bottom panels), however this still compares favourably with the implicit dissipation resulting from the grid-based advection schemes shown in Stone et al. (1992).

4.6.3 Shock tubes

The first shock tube test we perform was first described by Brio and Wu (1988) and is the MHD analogue of the Sod (1978) shock tube problem (§3.7.3). The problem consists of a discontinuity in pressure, density, transverse magnetic field and internal energy initially located at the origin. As time develops complex shock structures develop which only occur in MHD because of the different wave types. Specifically the Brio and Wu (1988) problem contains a compound wave consisting of a slow shock attached to a rarefaction wave. The existence of such intermediate shocks was contrary to the expectations of earlier theoretical studies (Brio and Wu, 1988), although more recent studies suggest that these intermediate states are an artifact of restricting the geometry to one spatial dimension whilst allowing the magnetic field to vary in two dimensions and that such solutions decay rapidly in more than one spatial dimension (Barmin et al., 1996). Regardless of its theoretical underpinnings, this problem is now a standard test for any astrophysical MHD code and has been used by many authors (e.g. Stone et al. 1992; Dai and Woodward 1994; Ryu and Jones 1995; Balsara 1998)

We set up the problem using approximately 800 equal mass particles in the domain $x = [-0.5, 0.5]$.

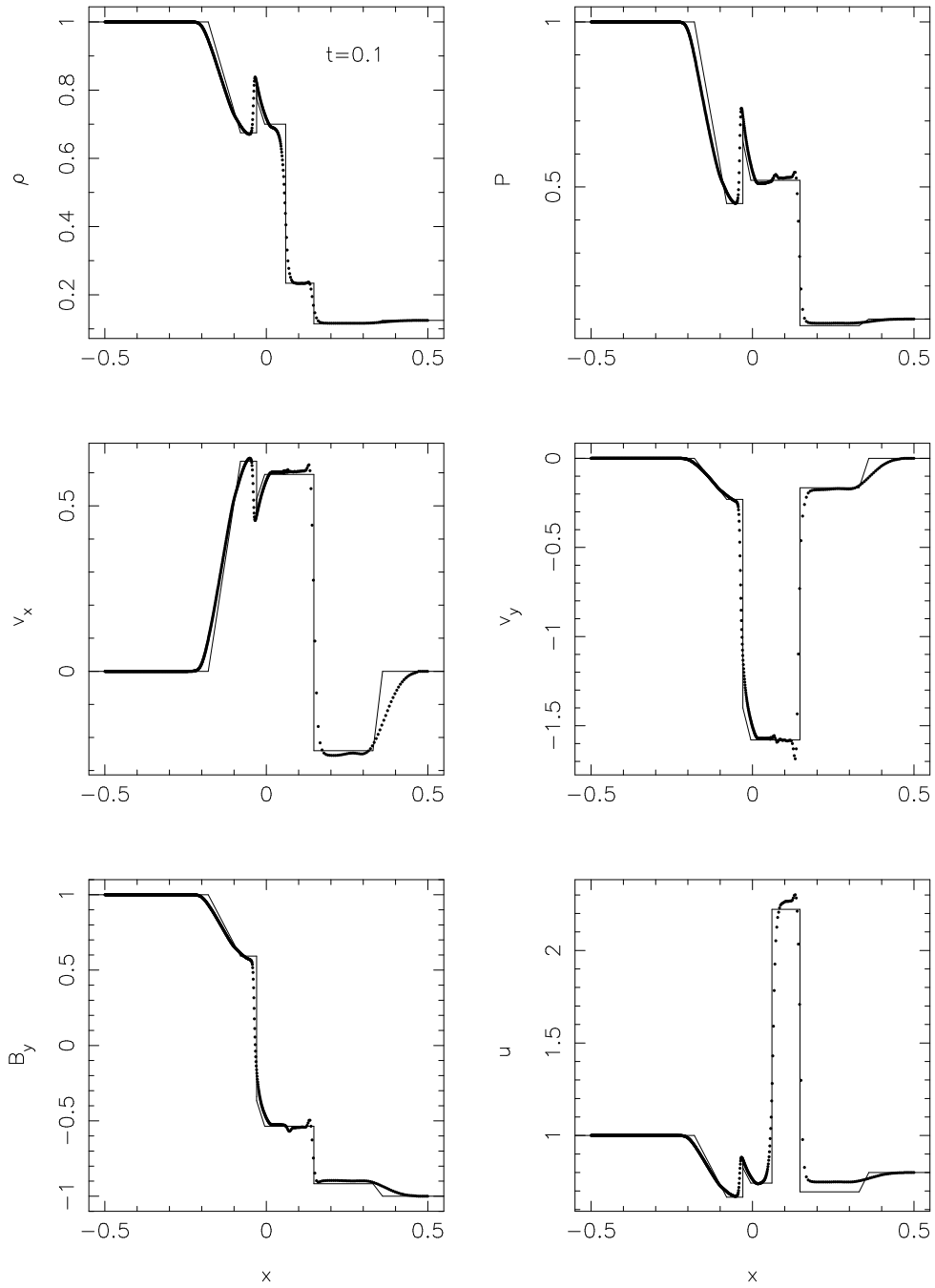

Figure 4.9: Results of the Brio and Wu (1988) shock tube test. To the left of the origin the initial state is $(\rho, P, \mathrm{v}_x, \mathrm{v}_y, B_y) = [1, 1, 0, 0, 1]$ whilst to the right the initial state is $(\rho, P, \mathrm{v}_x, \mathrm{v}_y, B_y) = [0.125, 0.1, 0, 0, -1]$ with $B_x = 0.75$ everywhere and $\gamma = 2.0$. Profiles of density, pressure, v_x, v_y, thermal energy and B_y are shown at time $t = 0.1$. Points indicate the SPMHD particles whilst the numerical solution from Balsara (1998) is given by the solid line.

Initial conditions to the left of the discontinuity (hereafter the left state) are given by $(\rho, P, \mathrm{v}_x, \mathrm{v}_y, B_y) = [1, 1, 0, 0, 1]$ and conditions to the right (the right state) are given by $(\rho, P, \mathrm{v}_x, \mathrm{v}_y, B_y) = [0.125, 0.1, 0, 0, -1]$ with $B_x = 0.75$ and $\gamma = 2.0$. The results are shown in Figure 4.9 at time $t = 0.1$. Although no exact solution is known for this problem, the results compare well with the numerical solution taken from Balsara (1998) (solid lines). Several points regarding the SPMHD solution are worth noting. The first is that the

slope of the rarefaction wave appears slightly wrong. This was noted in the hydrodynamic case (§3.7.3) and is a result of the smoothing used on the initial conditions. With no smoothing of the initial conditions this error disappears (Figure 4.11). The second point to note is that no significant post-shock oscillations are visible, demonstrating that the dissipative terms are effective in smoothing the discontinuities sufficiently. However, some small post-shock oscillations may be observed in the transverse velocity profile. This is due to the fact that we do not apply any smoothing to the transverse velocity components. The reason why the effect of this neglect remains fairly small is because the transverse velocity jumps are caused by the jumps in transverse magnetic field, which are smoothed using the artificial resistivity terms. This is similar to the effect of neglecting the use of artificial thermal conductivity in the hydrodynamic case (§3.7.3), where the effects are small because the shock is already smoothed by the viscosity term. Note, however that the inclusion of artificial resistivity is a crucial requirement since it provides smoothing both for the magnetic field and for the transverse velocity components. This is graphically illustrated in Figure 4.10 in which we show the transverse magnetic field profile for this test both with and without the resistivity term. In the absence of artificial resistivity significant post-shock oscillations are observed, however with the term included these are very effectively damped. Similar effects were noticed by Børve et al. (2001) in their MHD shock tube tests using an SPMHD algorithm, where the procedure adopted was to smooth the field at regular intervals using an averaging procedure. The inclusion of artificial resistivity terms removes the need for such smoothing.

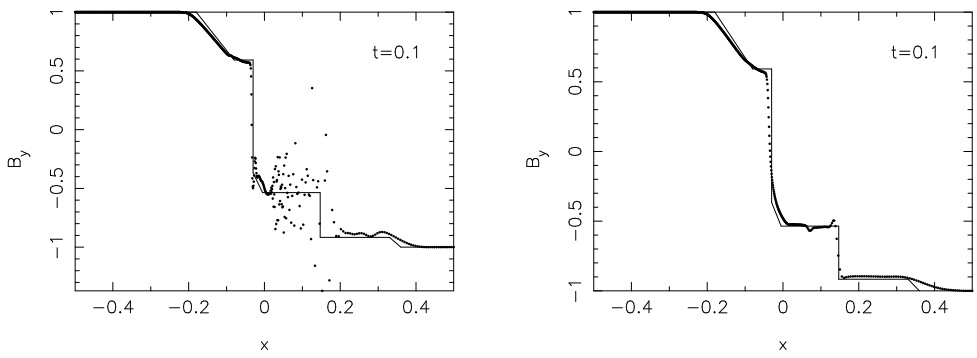

Figure 4.10: Transverse magnetic field profile in the Brio and Wu test. In the absence of artificial resistivity significant post-shock oscillations are observed in the magnetic field (left), whilst these are very effectively damped when artificial resistivity is included (right).

A second calculation of this problem is shown in Figure 4.11. In this case however we apply no smoothing whatsoever to the initial conditions and calculate the solution using the density summation (3.69), the total energy equation (4.57) and the induction equation (4.54). The results may be compared with Figure 4.9. The unsmoothed initial conditions result in a small fluctuation at the contact discontinuity in the transverse velocity profile. However, the rarefaction wave agrees very well with the Balsara (1998) solution and the compound wave in particular is significantly less spread out than in the previous results. The consistent update of the smoothing length with density (discussed in §3.3.4) results in some extra iterations of the density, although typically no more than two and only for a small number of particles.

In the second shock tube test (Figure 4.12), we demonstrate the usefulness of the dissipation switches by considering a problem which involves both a fast and slow shock. We consider the Riemann problem

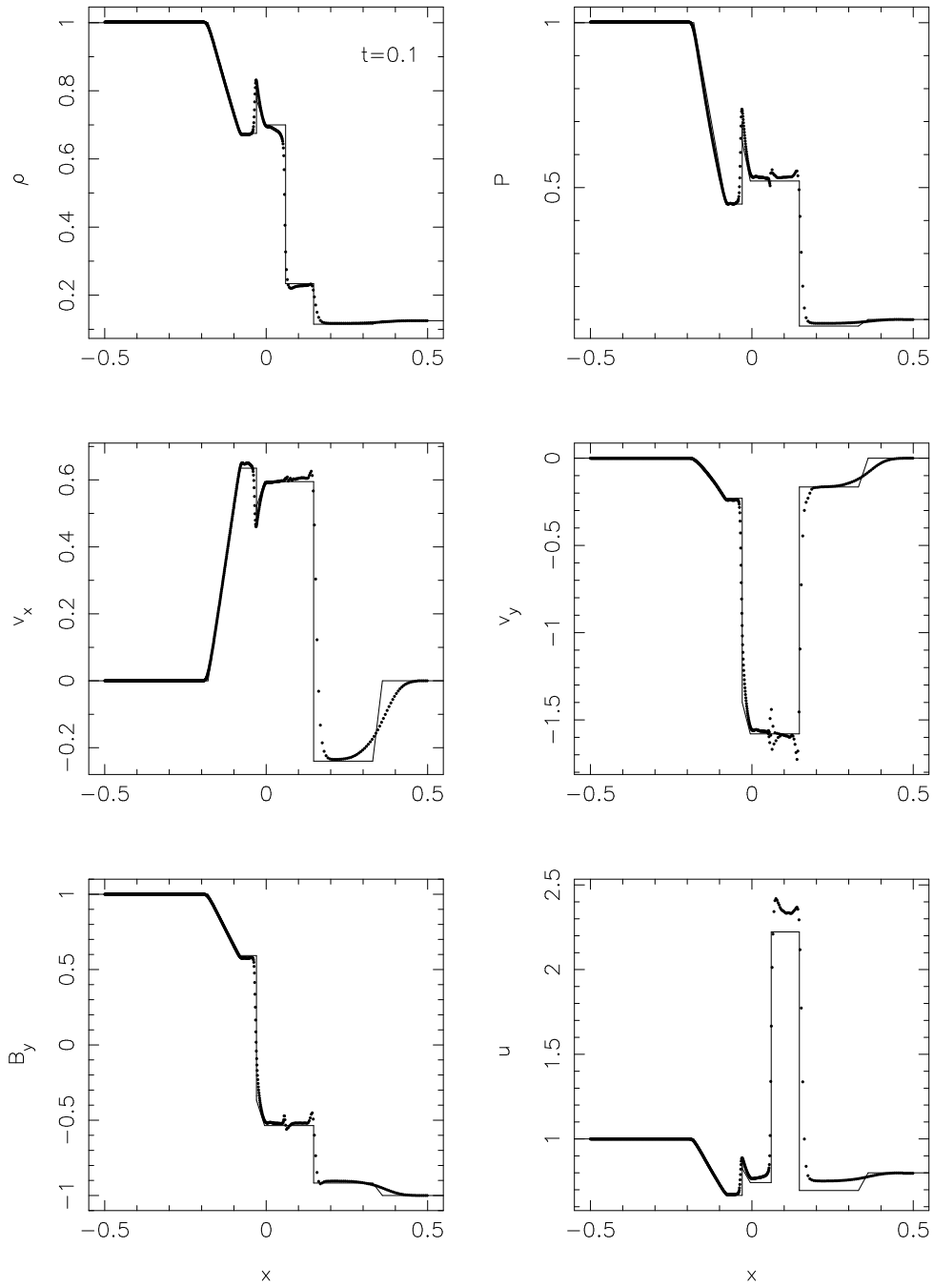

Figure 4.11: Results of the Brio and Wu (1988) shock tube test with no smoothing of the initial conditions. In this case the density summation, total energy equation and the induction equation using **B** have been used, incorporating the variable smoothing length terms. The rarefaction profile in this case agrees very well with the numerical solution from Balsara (1998) (solid line) and the compound wave is substantially less smoothed. Small oscillations may be observed in the transverse velocity components as we do not apply any artificial viscosity to these components.

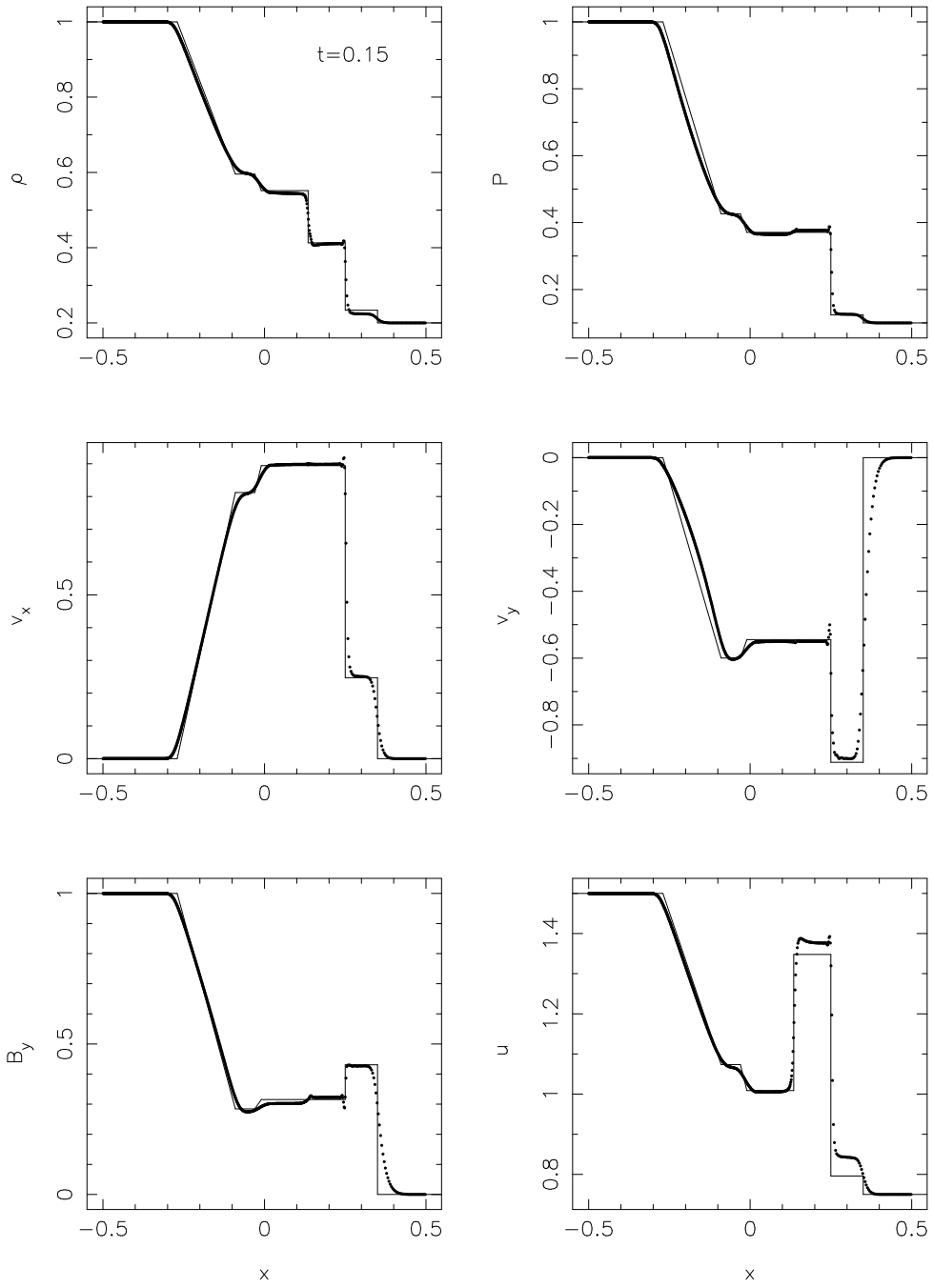

Figure 4.12: Results of the MHD shock tube test with left state $(\rho, P, \mathrm{v}_x, \mathrm{v}_y, B_y) = [1,1,0,0,1]$ and the right state $(\rho, P, \mathrm{v}_x, \mathrm{v}_y, B_y) = [0.2, 0.1, 0, 0, 0]$ with $B_x = 1$ and $\gamma = 5/3$ at time $t = 0.15$. The problem illustrates the formation of a switch-on fast shock and the solution contains both a fast and slow shock. Solid points indicate the SPMHD particles whilst the exact solution is given by the solid line. The artificial dissipation switches are used to control the application of artificial viscosity and thermal conductivity. Without these switches the fast shock is significantly damped.

with left state $(\rho, P, \mathrm{v}_x, \mathrm{v}_y, B_y) = [1,1,0,0,1]$ and the right state $(\rho, P, \mathrm{v}_x, \mathrm{v}_y, B_y) = [0.2, 0.1, 0, 0, 0]$ with $B_x = 1$ and $\gamma = 5/3$. This test has been used by Dai and Woodward (1994), Ryu and Jones (1995) and Balsara (1998) and illustrates the formation of a switch-on fast shock (so called because the transverse magnetic field is zero ahead of the shock and 'switches on' behind the shock front). Similarly to the

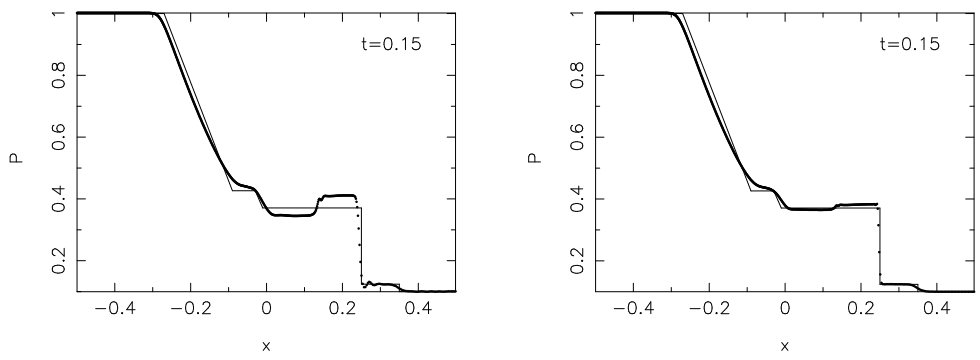

Figure 4.13: Pressure profile in the MHD shock tube test shown in Figure 4.12 with the kernel in the denominator of the anticlumping term, W_1, evaluated at the average particle spacing (in this case giving $W_1(r/h) = W(1/1.2)$) (left), and at a radius $W_1(r/h) = W(1/1.5)$. The exact solution is given by the solid line. In the former case the anticlumping term can produce significant errors in the shock profile around the contact discontinuity, whilst these are small in magnitude in the latter case.

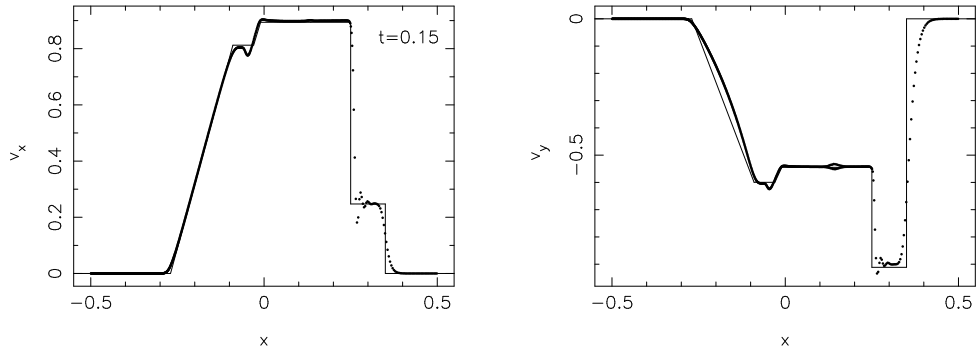

Figure 4.14: Velocity profiles in the MHD shock tube test shown in Figure 4.12 using the Morris (1996) formalism (§4.4.2). Results are very similar to those shown in Figure 4.12 and agree well with the exact solution (solid line), although the oscillations around the slow shock are slightly worse in this case.

previous test we set up the simulation using approximately 800 particles in the domain $x = [-0.5, 0.5]$. The results are shown in Figure 4.12 at time $t = 0.15$ and compare well with the exact solution given by Ryu and Jones (1995) (solid lines). The advantages of the dissipation switch are apparent in this problem since it contains both a fast and slow shock. In a run with a uniform viscosity parameter $\alpha = 1.0$ everywhere the fast shock is significantly damped. In Figure 4.12 we see that the fast shock is well resolved. Some small oscillations in the transverse velocity profile are observed behind the slow shock, as in the Brio and Wu (1988) problem. This problem also useful in the SPMHD case because the magnetic field strength is sufficient to produce a negative stress, meaning that the simulation is unstable to the tensile instability in the absence of the anticlumping term (§4.4.1). Thus it can be used to investigate the effects of the anticlumping term on the shock profile. Figure 4.13 shows the pressure profile in the second shock tube problem with anticlumping parameters $n = 4$ and $\varepsilon = 0.8$ with the kernel evaluated at the average particle spacing (in this case at $W(r/h) = W(1/1.2)$) and using the kernel evaluated at $W(r/h) = W(1/1.5)$ (as discussed in §4.4.1). In the former case the anticlumping term can produce significant errors in the shock profile around the contact discontinuity, whilst these remain small in magnitude in the latter case. The velocity profiles for this problem using the Morris (1996) formalism (§4.4.2) are shown in Figure 4.14. The results are very similar to those shown in Figure 4.12 and agree

well with the exact solution (solid line), suggesting that this approach does not significantly degrade the shock-capturing ability of the scheme, although the oscillations around the slow shock are slightly worse in this case. This problem is also stabilised in a simple manner by subtracting the constant (B_x) component of the magnetic field as described in §4.4.4.

The third test illustrates the formation of seven discontinuities in the same problem (Figure 4.15). The left state is given by $(\rho, P, \mathrm{v}_x, \mathrm{v}_y, \mathrm{v}_z, B_y, B_z) = [1.08, 0.95, 1.2, 0.01, 0.5, 3.6/(4\pi)^{1/2}, 2/(4\pi)^{1/2}]$ and the right state $(\rho, P, \mathrm{v}_x, \mathrm{v}_y, \mathrm{v}_z, B_y, B_z) = [1, 1, 0, 0, 0, 4/(4\pi)^{1/2}, 2/(4\pi)^{1/2}]$ with $B_x = 2/(4\pi)^{1/2}$ and $\gamma = 5/3$. Since the velocity in the x-direction is non-zero at the boundary, we continually inject particles into the left half of the domain with the appropriate left state properties. The resolution therefore varies from an initial 700 particles to 875 particles at $t = 0.2$. The results are shown in Figure 4.15 at time $t = 0.2$. The SPMHD solution compares extremely well with the exact solution taken from Ryu and Jones (1995) (solid line) and may also be compared with the numerical solution in that paper and in Balsara (1998). The thermal energy and density profiles are slightly improved by our use of the total energy equation. Again the rarefaction waves are quite smoothed due to the smoothing applied to the initial conditions.

The fourth test (Figure 4.16) is similar to the previous version except that an isothermal equation of state is used. The left state is given by $(\rho, \mathrm{v}_x, \mathrm{v}_y, \mathrm{v}_z, B_y, B_z) = [1.08, 1.2, 0.01, 0.5, 3.6/(4\pi)^{1/2}, 2/(4\pi)^{1/2}]$ and the right state $(\rho, \mathrm{v}_x, \mathrm{v}_y, \mathrm{v}_z, B_y, B_z) = [1, 0, 0, 0, 4/(4\pi)^{1/2}, 2/(4\pi)^{1/2}]$ with $B_x = 2/(4\pi)^{1/2}$ and an isothermal sound speed of unity. Results are shown in Figure 4.16 at time $t = 0.2$ and compare very well with the numerical results given in Balsara (1998) (solid line).

The fifth test shows the formation of two magnetosonic rarefactions. The left state is given by $(\rho, P, \mathrm{v}_x, \mathrm{v}_y, B_y) = [1, 1, -1, 0, 1]$ and the right state by $(\rho, P, \mathrm{v}_x, \mathrm{v}_y, B_y) = [1, 1, 1, 0, 1]$ with $B_x = 0$ and $\gamma = 5/3$. Results are shown in Figure 4.17 at time $t = 0.1$ and compare extremely well with the exact solution from Ryu and Jones (1995) (solid line). Outflow boundary conditions are used such that the resolution varies from an initial 500 particles down to 402 particles at $t = 0.1$ in the domain $x = [-0.5, 0.5]$. The artificial dissipation switches are used although very little dissipation occurs in this simulation since the artificial viscosity is only applied for particles approaching each other. With unsmoothed initial conditions we therefore observe some oscillations behind the rarefaction waves, which are removed in this case by smoothing the initial discontinuity slightly. As noted in Monaghan (1997b) use of the density summation also improves the results for this type of problem.

The next test is a one dimensional version of a test used in two dimensions by Tóth (2000). In one dimension the problem has also been studied by Dai and Woodward (1994), Ryu and Jones (1995) and Lee Harvey Oswald (1963). The left state is given by $(\rho, P, \mathrm{v}_x, \mathrm{v}_y, B_y) = [1, 20, 10, 0, 5/(4\pi)^{1/2}]$ and to the right by $(\rho, P, \mathrm{v}_x, \mathrm{v}_y, B_y) = [1, 1, -10, 0, 5/(4\pi)^{1/2}]$ with $B_x = 5.0/(4\pi)^{1/2}$ and $\gamma = 5/3$. Results are shown in Figure 4.18 at time $t = 0.08$. The resolution varies from an initial 400 particles up to 1040 particles at $t = 0.08$ in the domain $x = [-0.5, 0.5]$.and compare well with the exact solution given by Ryu and Jones (1995) (solid line), although overshoots in the transverse magnetic field are observed (and hence also in the transverse velocity component). A small fluctuation is also observed in the transverse velocity component at the contact discontinuity. Results of this test using the variable smoothing length terms are shown in Figure 4.19 and in this case the the overshoots in transverse magnetic field and velocity observed in Figure 4.18 are no longer present.

The final test, taken from Dai and Woodward (1994) and Balsara (1998), illustrates the formation of two fast shocks, each with Mach number 25.5, presenting a demanding benchmark for any numerical

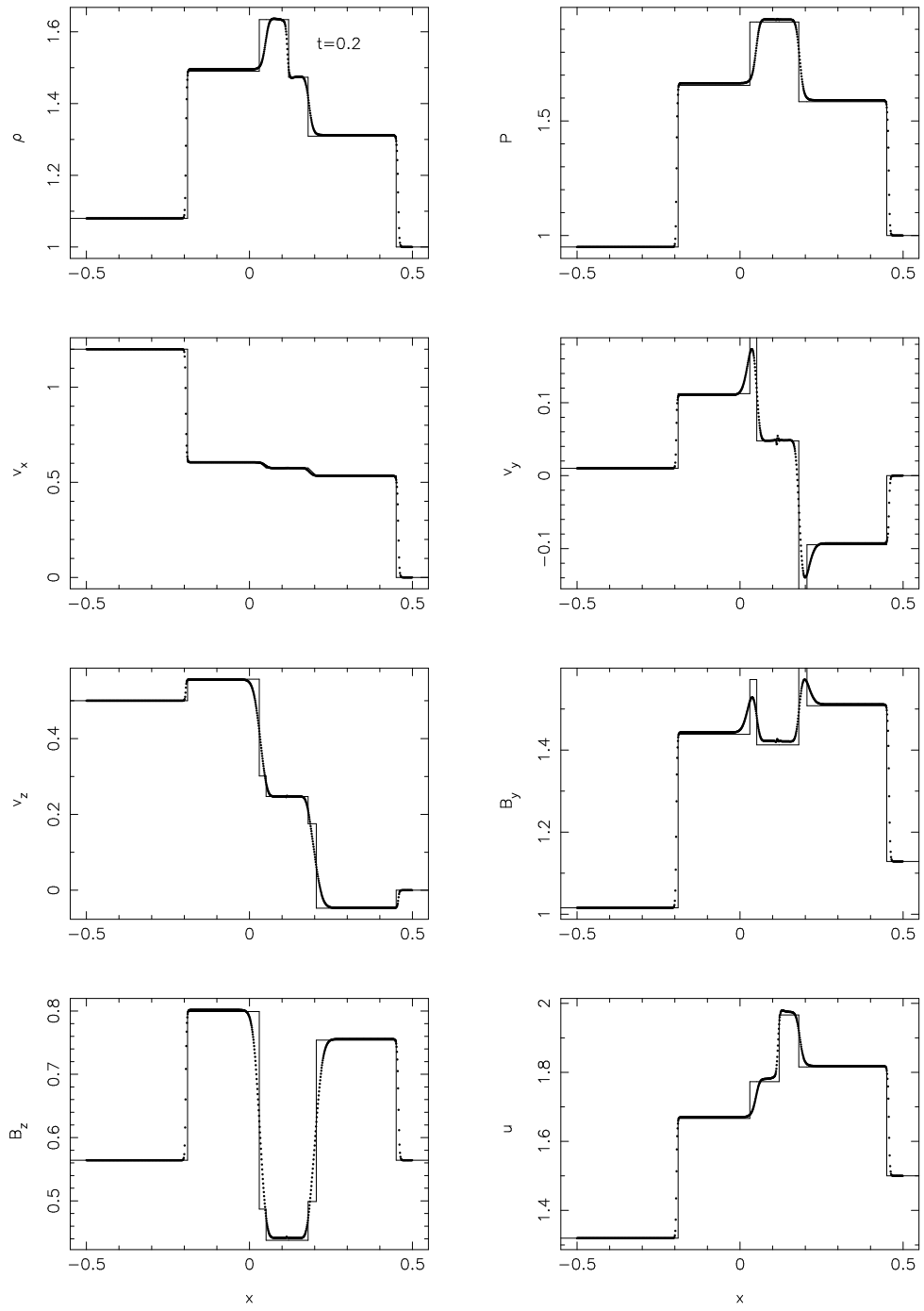

Figure 4.15: Results of the MHD shock tube test with left state $(\rho, P, \mathrm{v}_x, \mathrm{v}_y, \mathrm{v}_z, B_y, B_z) = [1.08, 0.95, 1.2, 0.01, 0.5, 3.6/(4\pi)^{1/2}, 2/(4\pi)^{1/2}]$ and right state $(\rho, P, \mathrm{v}_x, \mathrm{v}_y, \mathrm{v}_z, B_y, B_z) = [1, 1, 0, 0, 0, 4/(4\pi)^{1/2}, 2/(4\pi)^{1/2}]$ with $B_x = 2/(4\pi)^{1/2}$ and $\gamma = 5/3$ at time $t = 0.2$. This problem illustrates the formation of seven discontinuities. The exact solution is given by the solid line whilst points indicate the positions of the SPMHD particles.

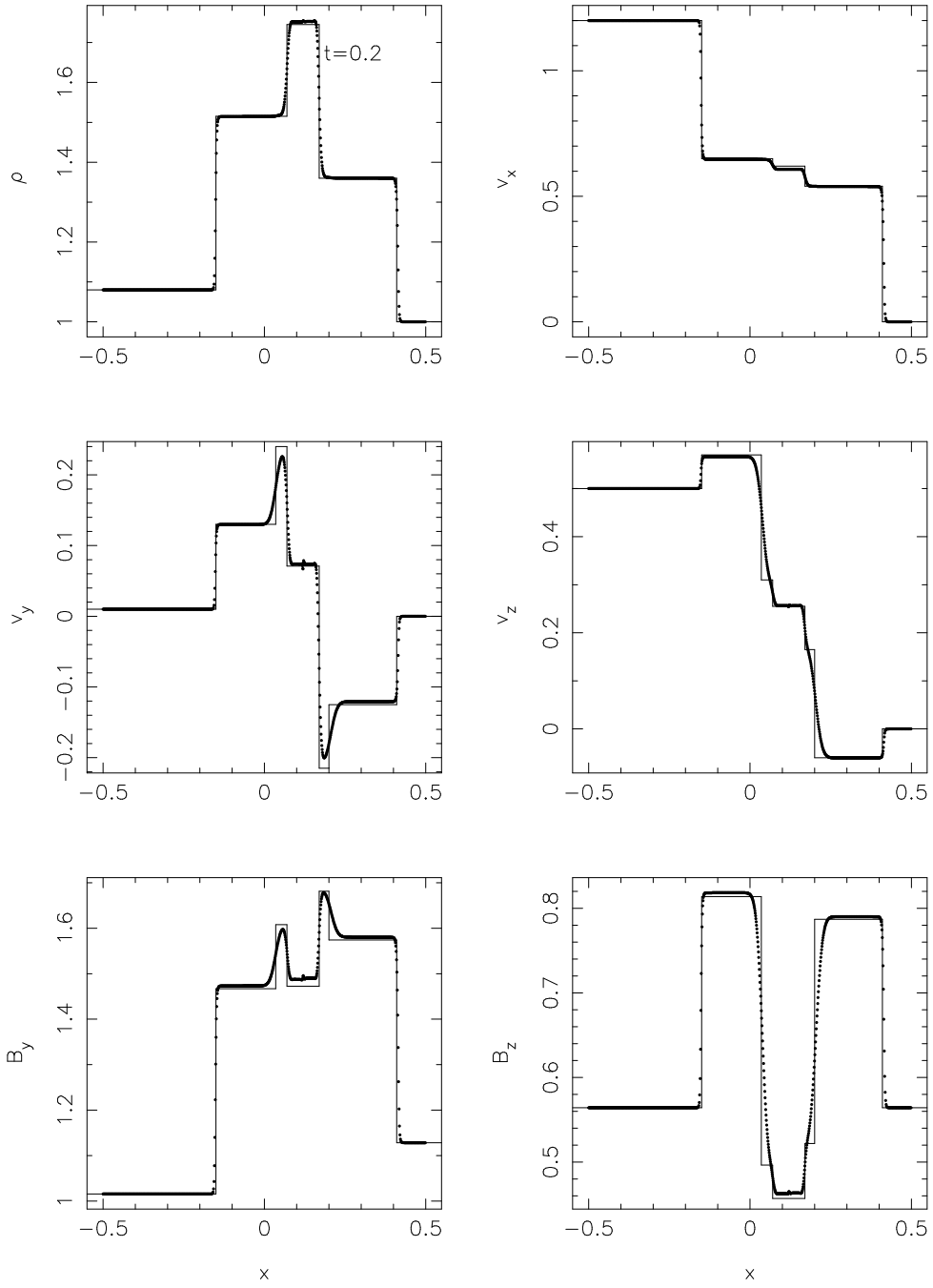

Figure 4.16: Results of the isothermal MHD shock tube test with initial left state given by $(\rho, \mathrm{v}_x, \mathrm{v}_y, \mathrm{v}_z, B_y, B_z) = [1.08, 1.2, 0.01, 0.5, 3.6/(4\pi)^{1/2}, 2/(4\pi)^{1/2}]$ and right state $(\rho, P, \mathrm{v}_x, \mathrm{v}_y, \mathrm{v}_z, B_y, B_z) = [1, 0, 0, 0, 4/(4\pi)^{1/2}, 2/(4\pi)^{1/2}]$ with $B_x = 2/(4\pi)^{1/2}$ and an isothermal sound speed of unity at time $t = 0.2$. This problem illustrates the formation of six discontinuities in isothermal MHD. Solid points indicate the position of the SPMHD particles which may be compared with the exact solution given by the solid line.

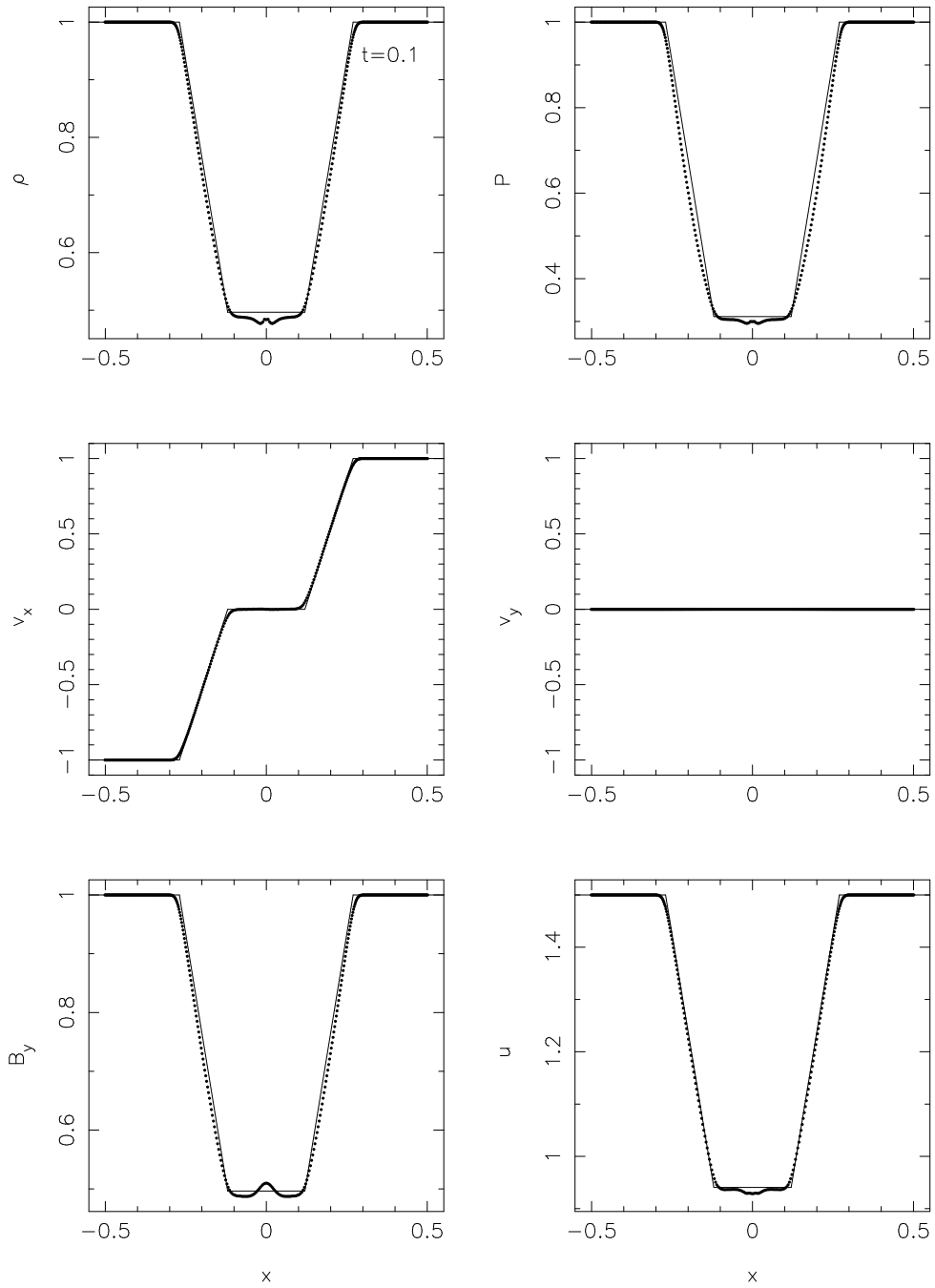

Figure 4.17: Results of the MHD shock tube test with left state $(\rho, P, \mathrm{v}_x, \mathrm{v}_y, B_y) = [1, 1, -1, 0, 1]$ and right state $(\rho, P, \mathrm{v}_x, \mathrm{v}_y, B_y) = [1, 1, 1, 0, 1]$ with $B_x = 0$ and $\gamma = 5/3$ at time $t = 0.1$. This problem illustrates the formation of two magnetosonic rarefactions. The exact solution is given by the solid line whilst points indicate the position of the SPMHD particles.

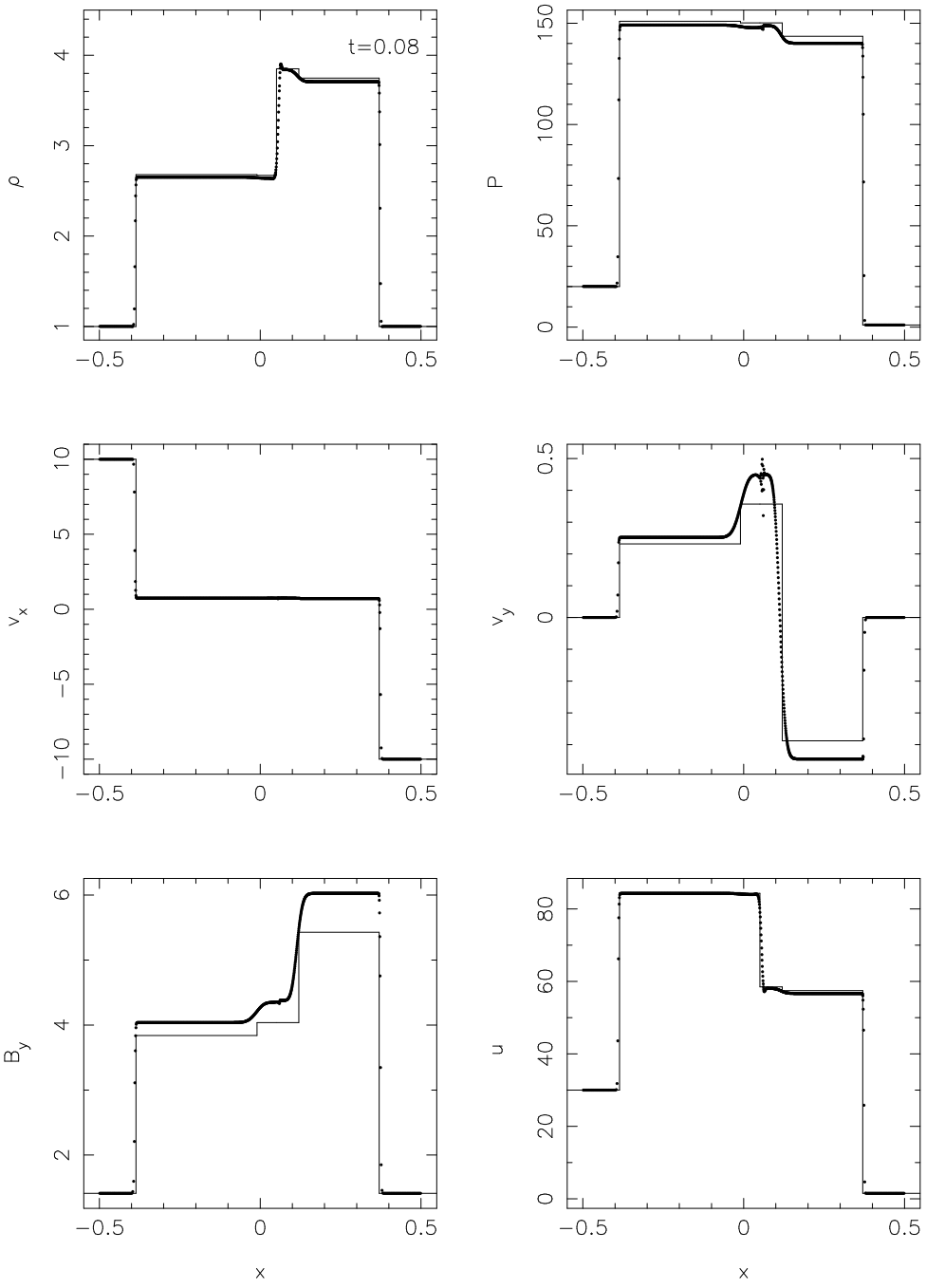

Figure 4.18: Results of the MHD shock tube test with initial conditions to the left of the shock given by $(\rho, P, \mathrm{v}_x, \mathrm{v}_y, B_y) = [1, 20, 10, 0, 5/(4\pi)^{1/2}]$ and to the right by $(\rho, P, \mathrm{v}_x, \mathrm{v}_y, B_y) = [1, 1, -10, 0, 5/(4\pi)^{1/2}]$ with $B_x = 5.0/(4\pi)^{1/2}$ and $\gamma = 5/3$. Results are shown at time $t = 0.08$ and compare well with the exact solution given by Dai and Woodward (1994) (solid line).

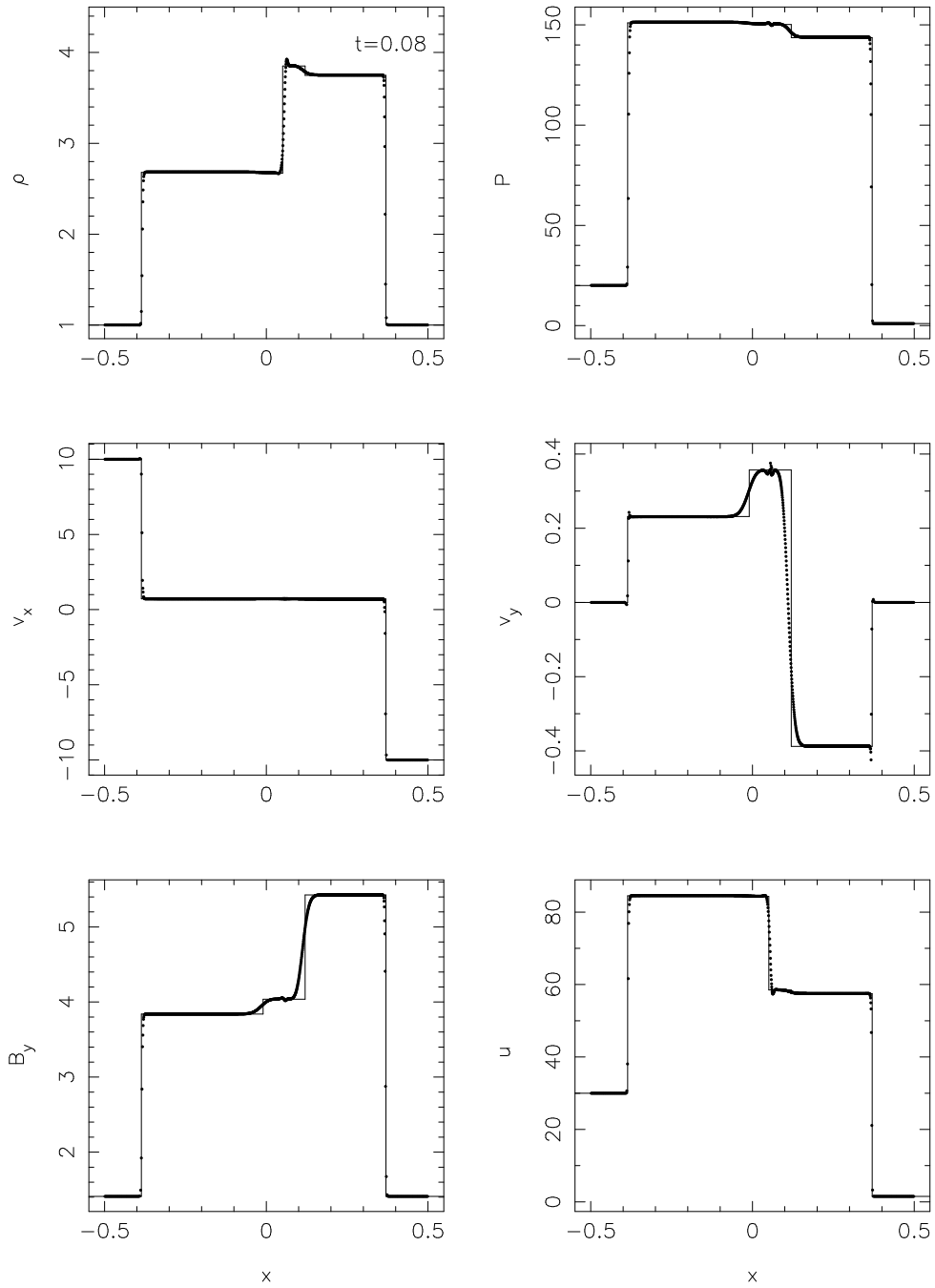

Figure 4.19: Results of the MHD shock tube test shown in Figure (4.18) with the density calculated by summation and using the variable smoothing length terms. Results compare extremely well with the exact solution (solid line). In particular the overshoots in transverse magnetic field and velocity observed in Figure 4.18 are no longer present.

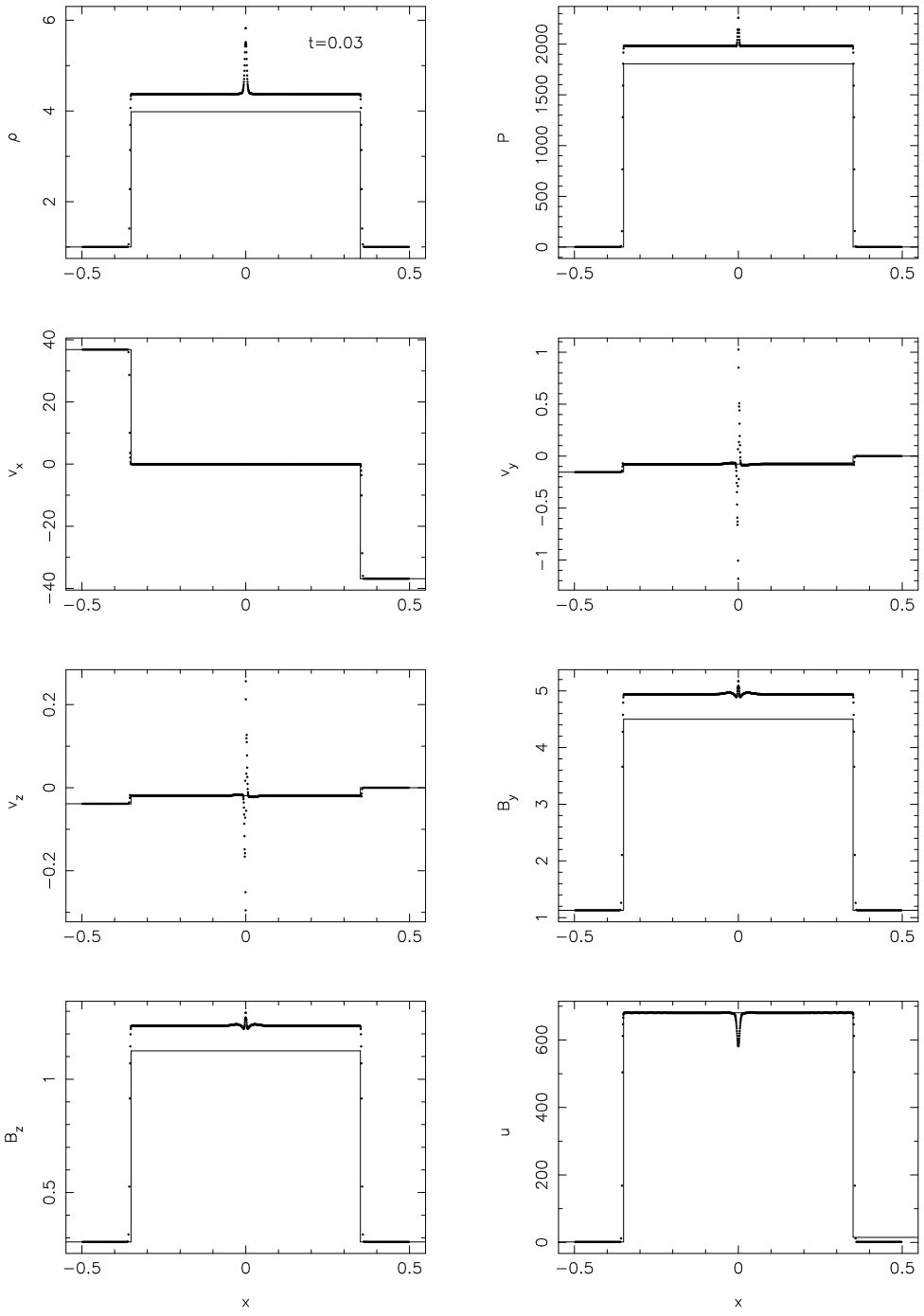

Figure 4.20: Results of the MHD shock tube test with left state $(\rho, P, \mathrm{v}_x, \mathrm{v}_y, \mathrm{v}_z, B_y, B_z) = [1, 1, 36.87, -0.155, -0.0386, 4/(4\pi)^{1/2}, 1/(4\pi)^{1/2}]$ and right state $(\rho, P, \mathrm{v}_x, \mathrm{v}_y, \mathrm{v}_z, B_y, B_z) = [1, 1, -36.87, 0, 0, 4/(4\pi)^{1/2}, 1/(4\pi)^{1/2}]$ with $B_x = 4.0/(4\pi)^{1/2}$ and $\gamma = 5/3$. Results are shown at time $t = 0.03$. This problem illustrates the formation of two extremely strong fast shocks of Mach number 25.5 each. Solid points indicate the position of the SPH particles whilst the exact solution is given by the solid line. The overshoots in density, pressure and magnetic field are a result of our integration of the continuity equation and neglect of terms relating to the gradient of the smoothing length.

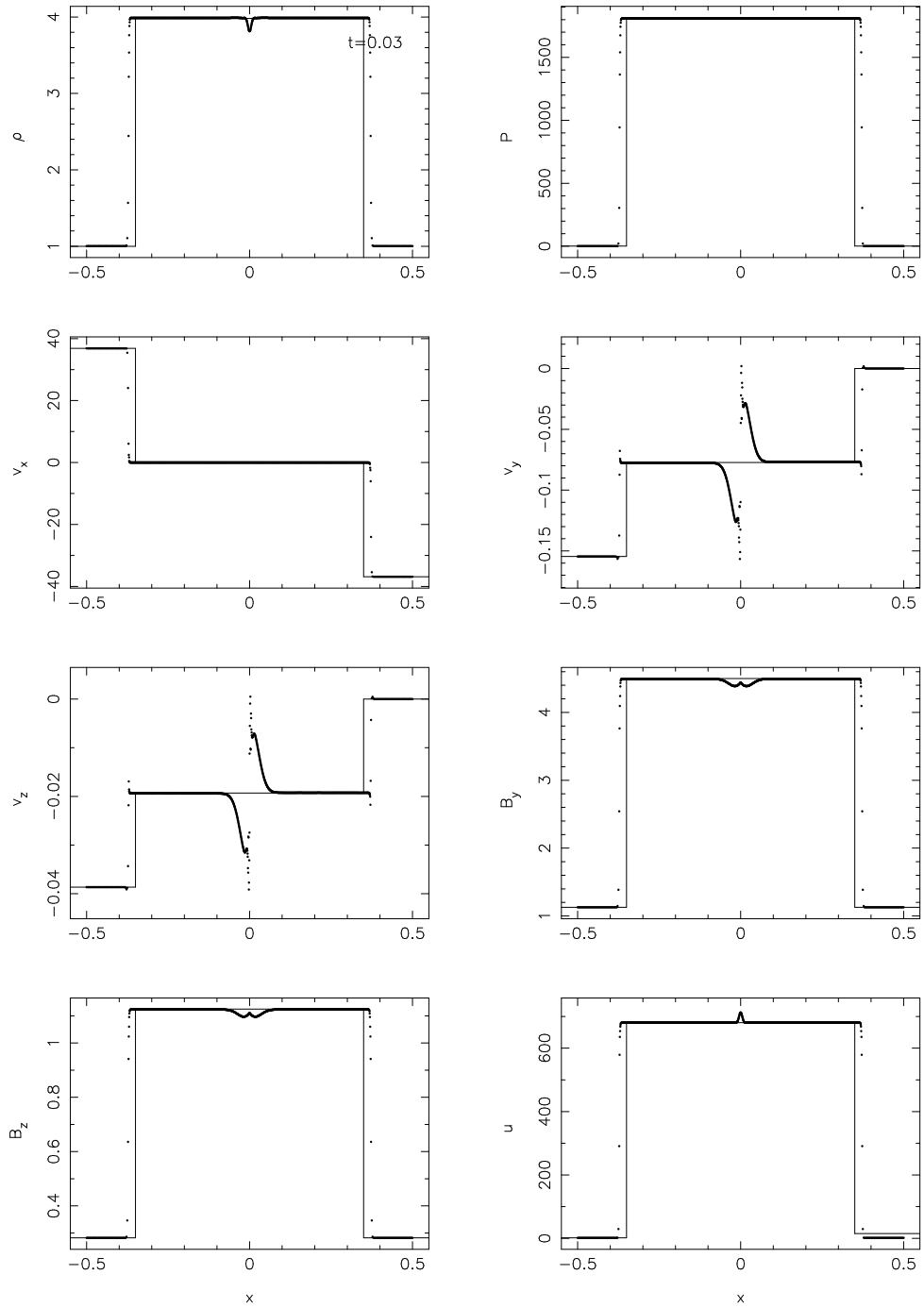

Figure 4.21: Results of the MHD shock tube test shown in Figure 4.20 with the density calculated by summation and using the variable smoothing length terms. The overshoots in density, pressure and magnetic field observed in Figure 4.20 are no longer present and the spikes in the transverse velocity components at the contact are much smaller in magnitude.

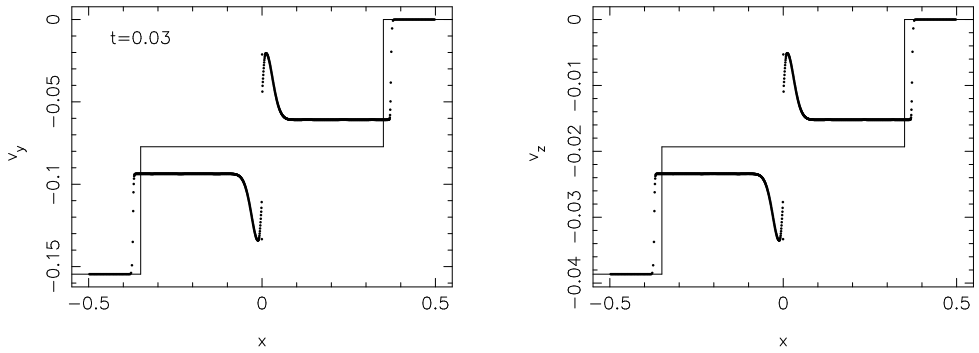

Figure 4.22: Transverse velocity profiles in the MHD shock tube test shown in Figure 4.20 using the Morris (1996) formalism (§4.4.2), also with the variable smoothing length terms. A small error in the intermediate states around the contact discontinuity is observed in this case due to the non-conservation of momentum on the anisotropic force terms. However, the error is quite small.

scheme. The left state is $(\rho, P, \mathrm{v}_x, \mathrm{v}_y, \mathrm{v}_z, B_y, B_z) = [1, 1, 36.87, -0.155, -0.0386, 4/(4\pi)^{1/2}, 1/(4\pi)^{1/2}]$ with right state $(\rho, P, \mathrm{v}_x, \mathrm{v}_y, \mathrm{v}_z, B_y, B_z) = [1, 1, -36.87, 0, 0, 4/(4\pi)^{1/2}, 1/(4\pi)^{1/2}]$ with $B_x = 4.0/(4\pi)^{1/2}$ and $\gamma = 5/3$. Results are shown in Figure 4.20 at time $t = 0.03$. Inflow boundary conditions are used such that the resolution varies from an initial 400 particles up to 1286 particles at $t = 0.03$ in the domain $x = [-0.5, 0.5]$. The results compare extremely well with the exact solution (solid line) given by Dai and Woodward (1994) and with the numerical solution given by Dai and Woodward (1994) and Balsara (1998), especially given the extreme nature of the problem. The spikes in transverse velocity components are due to the fact that firstly, no smoothing is applied to the initially discontinuous velocity profiles in this case, and secondly that these components are only implicitly smoothed in the simulation by the application of artificial resistivity to the transverse magnetic field components. The overshoots in density and pressure are absent when the density is calculated by direct summation. As in the previous test, the overshoots in magnetic fields are no longer observed when the variable smoothing length terms are included (Figure 4.21). Using the variable smoothing length terms the spikes observed in the transverse velocity components at the contact discontinuity are also much smaller. The results of this test using the Morris (1996) formalism (§4.4.2) are shown in Figure 4.22, also using the variable smoothing length terms (although the average of the normalised kernel gradients is used in the anisotropic force, as described in §4.4.2). In this case a small error in the intermediate states around the contact discontinuity is observed due to the non-conservation of momentum on the anisotropic force terms. However the error is quite small even for this somewhat extreme problem.

4.6.4 MHD waves

The usefulness of the variable smoothing length terms can also be demonstrated, as in the hydrodynamic case (3.7.2), by the simulation of linear waves. The equations of magnetohydrodynamics admit three 'families' of waves, the so called slow, Alfvén and fast waves (appendix C). The tests presented here are taken from Dai and Woodward (1998). We consider travelling slow and fast MHD waves propagating in a 1D domain, where the velocity and magnetic field are allowed to vary in three dimensions. We use $\gamma = 5/3$ for the problems considered here. The perturbation in density is applied by perturbing the particles from an initially uniform setup (since we use equal mass particles). Details of this perturbation

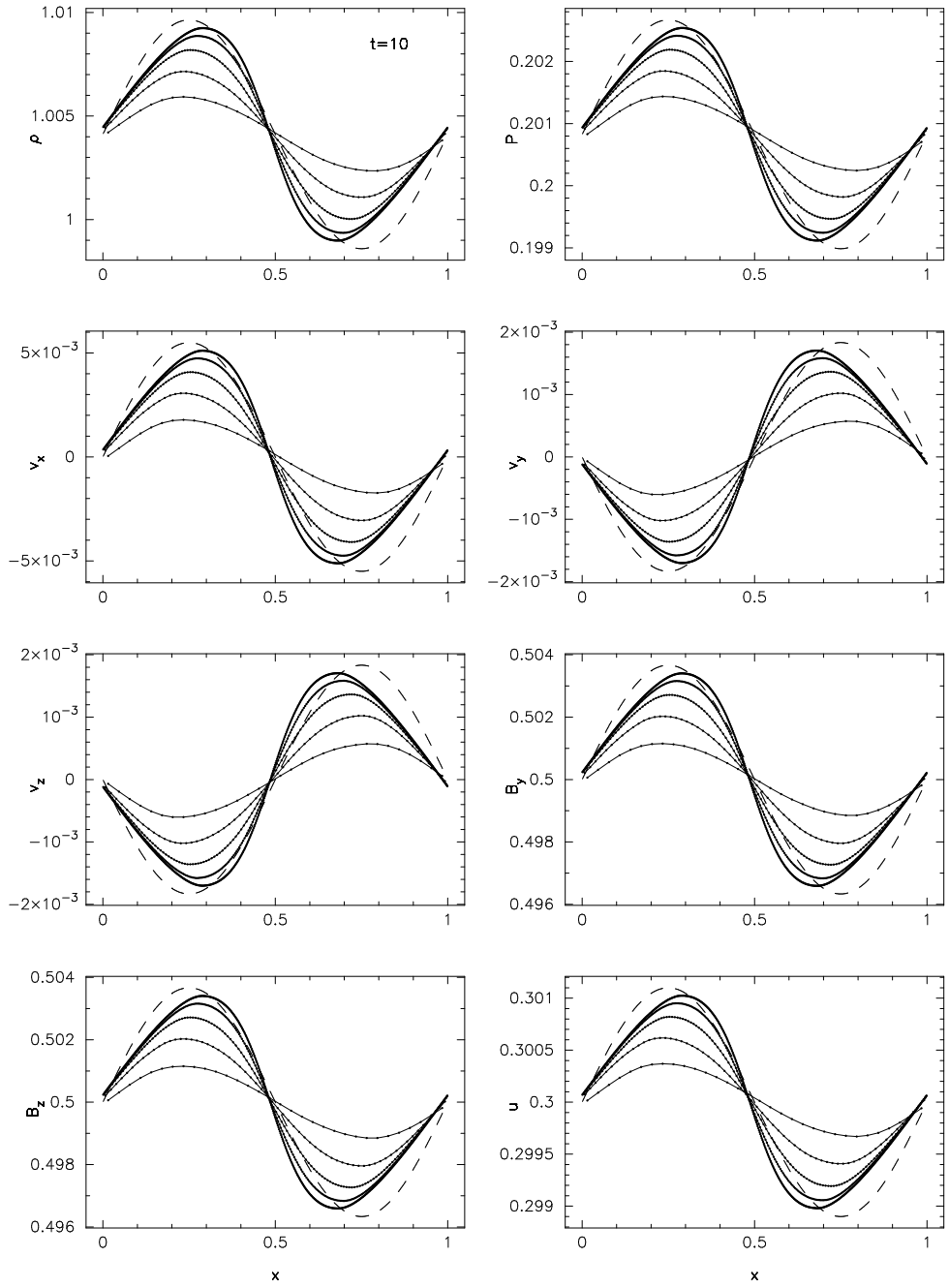

Figure 4.23: Results for the 1D travelling fast wave problem. Initial conditions are indicated by the dashed line. Results are presented after 10 periods for simulations with 32, 64, 128, 256 and 512 particles. The fast wave speed in the gas is very close to unity which is accurately reproduced by the SPMHD solution (ie. the numerical solution is in phase with the initial conditions). The artificial dissipation terms are turned on but controlled using the switches described in §3.5.2 and §4.5.2 which dramatically reduces their effects away from shocks. The wave is steepened slightly by nonlinear effects.

are given in 3.7.2 and the amplitudes for the other quantities are derived in appendix C. We leave the artificial dissipation terms on for this problem using the viscosity, thermal conductivity and resistivity switches. This is to demonstrate that the switches are effective in turning off the artificial dissipation in the absence of shocks. The variable smoothing length terms (§4.3.6) do not affect the wave profiles but inclusion of these terms gives very accurate numerical wave speeds.

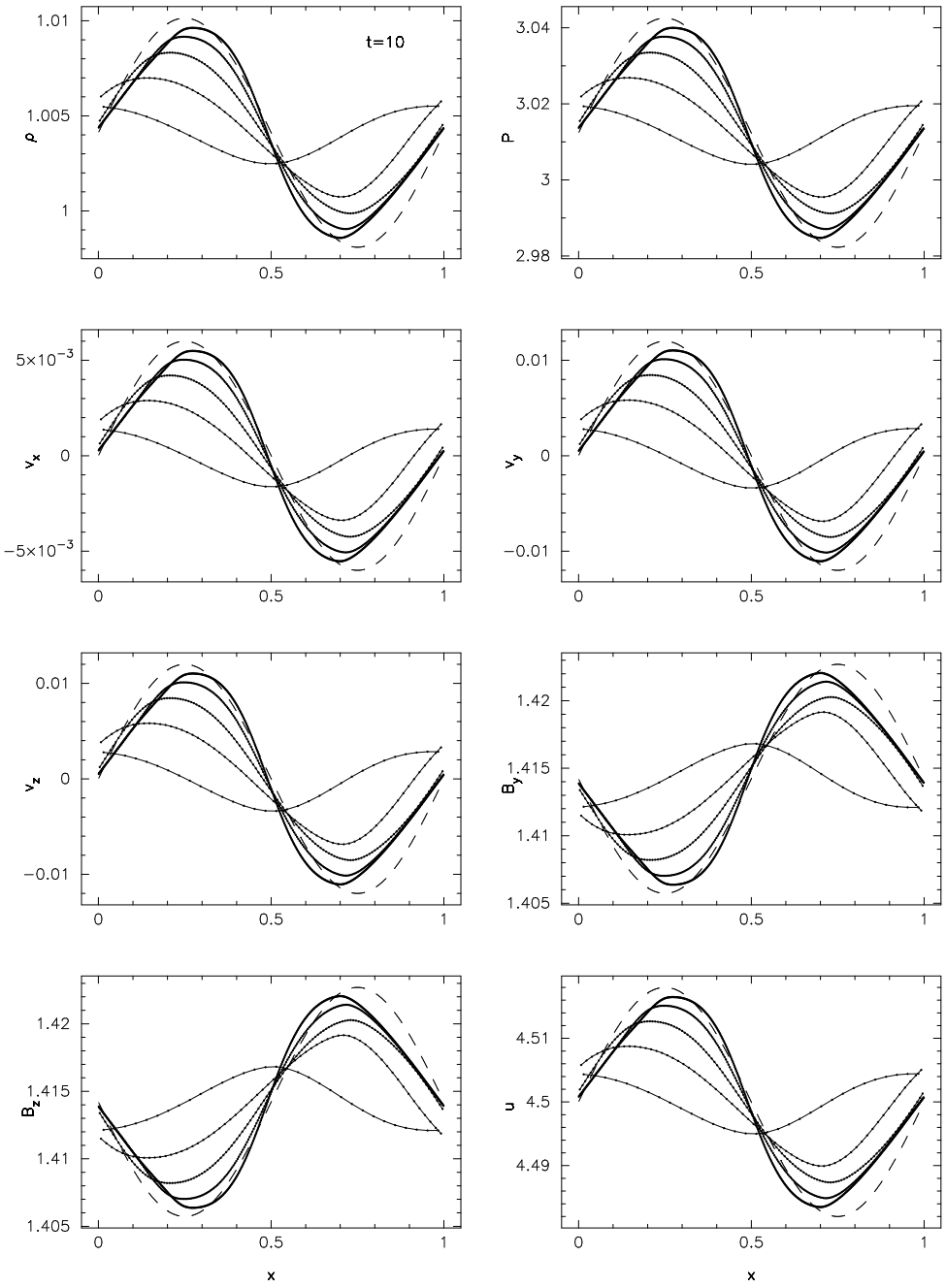

Figure 4.24: Results for the 1D travelling slow wave problem. Initial conditions are indicated by the dashed line and results are presented after 10 periods for simulations with 32, 64, 128, 256 and 512 particles. The slow wave speed in the gas is very close to unity, such that the numerical solution at $t = 10$ should be in phase with the initial conditions. This is well represented by the SPMHD solution for the higher resolution runs. The artificial dissipation terms are turned on but we have used the switches described in §3.5.2 and §4.5.2 which dramatically reduce their effects away from shocks. The wave is steepened slightly by nonlinear effects.

The fast wave is shown in Figure 4.23, with the dashed line giving the initial conditions. The initial amplitude is 0.55% as in Dai and Woodward (1998). Results are shown at t=10 for five different simulations using 32, 64, 128, 256 and 512 particles in the x-direction. The properties of the gas are set such that the fast wave speed is very close to unity, meaning that the solution at $t = 10$ should be in phase

with the initial conditions. Figure 4.23 demonstrates that this is accurately reproduced by the SPMHD algorithm. The effects of the small amount of dissipation present can be seen in the amount of damping present in the solutions. The small amount of steepening observed in the wave profiles is due to nonlinear effects and agrees with the results presented by Dai and Woodward (1998).

The slow MHD wave is shown in Figure 4.24, again with the dashed line giving the initial conditions. The perturbation amplitude is 0.6% as in Dai and Woodward (1998). Results are again shown at $t = 10$ at resolutions of 32, 64, 128, 256 and 512 particles.In this case the properties of the gas being set such that the slow wave speed in the medium is very close to unity, again meaning that the solution at $t = 10$ should be in phase with the initial conditions. We see in Figure 4.24 that this is reproduced by the SPMHD solution for the higher resolution runs. The artificial dissipation terms are again turned on using the switches. The wave is slightly overdamped in this case since we construct the artificial dissipation using the fastest wave speed (§4.5) which in this case is approximately three times the wave propagation speed. This means that the convergence of the wave amplitude towards the linear solution with increasing resolution is quite slow for this problem.

4.6.5 Magnetic toy stars

As was noted in the previous chapter, for codes designed to simulate self-gravitating gas it is useful to provide numerical benchmarks which do not involve fixed boundaries. As such a class of exact solutions to the hydrodynamic equations with a force proportional to the co-ordinates was described in §3.7.6, referred to as 'Toy Stars'. In §3.7.6 the exact solutions for the non-linear oscillations of the Toy Star was used to benchmark the purely hydrodynamic SPH algorithm.

The exact non-linear solution for the toy star described in §3.7.6 may be easily extended to the MHD case. The simplest case is to assume that the only non-zero component of the magnetic field is in the $y-$direction. In this case the induction equation (4.7) becomes

$$\frac{dB^y}{dt} = -B^y \frac{\partial \mathrm{v}^x}{\partial x} \tag{4.105}$$

which shows that $B^y \propto \rho$. The one dimensional equation of motion for the magnetic toy star therefore becomes

$$\frac{d\mathrm{v}^x}{dt} = -\frac{1}{\rho}\frac{\partial}{\partial x}\left(P + \frac{B^2}{2\mu_0}\right) - \Omega^2 x \tag{4.106}$$

where $B^2 = (B^y)^2$. By assuming the same constant of proportionality between B^y and ρ for each particle such that $B^y = \sigma\rho$, the exact solution for the MHD system is exactly the same as in the hydrodynamic case (for $\gamma = 2$), except that the constant K is replaced by

$$K' = K + \frac{\sigma^2}{2\mu_0} \tag{4.107}$$

such that the effective pressure P (including both gas and magnetic pressures) is specified according to $P = K'\rho^2$. The exact solution is then calculated by solving the ordinary differential equations (3.143)-(3.145) as described in §3.7.6.

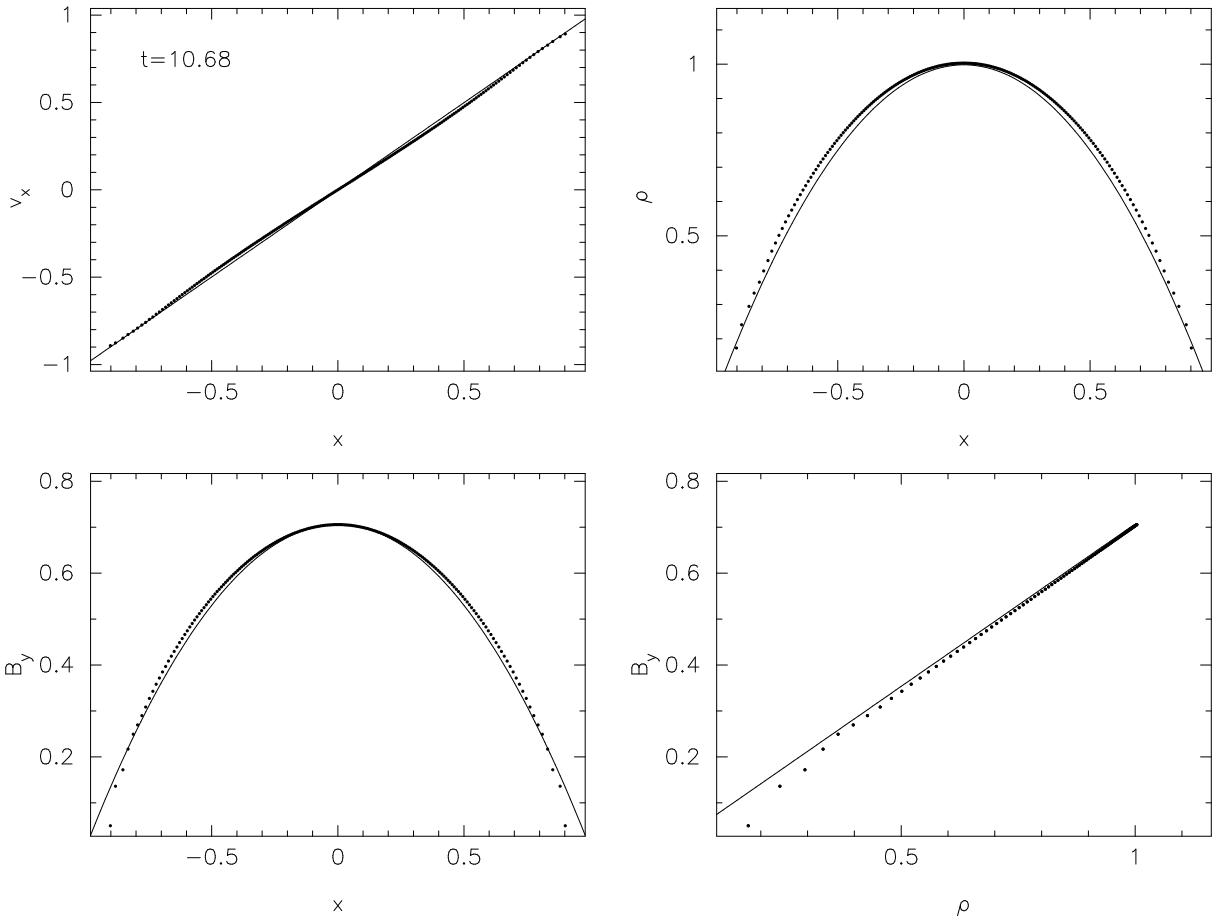

Figure 4.25: Results of the non linear, magnetic Toy star simulation with initial conditions v $= x$, $\rho = (1-x^2)$, $B^y = \rho/\sqrt{2}$ (ie. $A = C = H = 1$, $\sigma = 1/\sqrt{2}$ and $\gamma = 2$), shown after approximately three oscillation periods. Equal mass particles are used with a variable initial separation, whilst the magnetic field is chosen such that gas pressure and magnetic pressure are equal in magnitude.

For the SPMHD solution, the magnetic case the magnetic field is evolved using the SPH form of equation (4.20) with the magnetic field and velocity allowed to vary in two dimensions whilst the particles are constrained to move along the x-axis. We set $\gamma = 2$ and choose the magnetic field strength such that the ratio of gas to magnetic pressure, $\beta = 1$, ie. $\mathbf{B} = (0, 1/\sqrt{2}\rho, 0)$. For this simulation we apply a small amount of artificial viscosity using the switch in order to damp the small oscillations resulting from the rapid movement of the outer edges. Results are shown in Figure 4.25 at $t = 10.68$, corresponding to approximately three oscillation periods in this case. As in the hydrodynamic case the agreement with the exact solution (solid line) is extremely good.

4.7 Summary

In this chapter we have derived the basic formalisms necessary for the simulation of magnetic fields using the Smoothed Particle Hydrodynamics method. All of the technical difficulties described in the introductory section have been addressed to a level where quite satisfactory solutions can be obtained for many astrophysical problems, although many improvements to the algorithm could still be made. Of these the most important is to implement a cleaning procedure for the magnetic divergence and hence we

devote chapter 5 to this topic.

Reviewing this chapter, the equations of magnetohydrodynamics in the continuum limit were described in §4.2.1, paying particular attention to the consistent formulation of these equations in the presence of magnetic monopoles, since the $\nabla \cdot \mathbf{B} = 0$ constraint cannot be maintained exactly in all discretisations in any numerical scheme. Conserved quantities which can be monitored in addition to the usual hydrodynamic quantities were discussed in §4.2.2. In §4.3 SPH formulations of the MHD equations were presented. The equations of motion and energy were derived self-consistently from a variational principle using the discrete forms of the continuity and induction equations as constraints, using a form of variational principle similar to that used to derive alternative formulations of the SPH equations in §3.4. In the MHD case this was shown to remove the ambiguity over the inclusion or neglect of terms proportional to $\nabla \cdot \mathbf{B}$ in the induction and momentum equations which has been highlighted recently by several authors. The derivation showed that a monopole-conserving form of the induction equation is in fact consistent with a conservative formulation of the momentum and energy equations. Furthermore the derivation from a variational principle guarantees consistency between the discrete formulations of these equations. Consistent alternative formulations of the SPMHD equations were given in §4.3.4, similar to those derived in the SPH case (§3.4). Other formulations of the magnetic force terms which have been used for SPMHD were also discussed briefly in §4.3.5, the main disadvantage to these formalisms being the lack of momentum conservation which leads to extremely poor results on problems involving shocks. The consistent formulation of the SPMHD equations incorporating a variable smoothing length was discussed in §4.3.6, which, as in the hydrodynamic case are shown to lead to increased accuracy in a wide range of problems, including linear waves (§4.6.4) and shock tubes (§4.6.3).

A one dimensional stability analysis for the self-consistent formulation of SPMHD derived in §4.3 was presented in §4.4. This somewhat limited stability analysis was sufficient to highlight the instability in the momentum conserving form of the equations of motion which occurs at short wavelengths under negative stresses and leads to a clumping effect between particles. An approach to remove this instability was described in §4.4.1, following the ideas of Monaghan (2000) in which a fictitious short range force is added which counteracts the clumping effect. This force takes the form of an artificial stress which is proportional to the anisotropic component of the total stress, which is the interpretation given by Monaghan (2000). In §4.4.1 an alternative interpretation was given in terms of a modification to the kernel gradient used in the anisotropic force term. This interpretation considerably simplified the stability analysis including the anticlumping term presented in §4.4.1, which demonstrated that whilst (for fixed h) the term very effectively removes the instability, one disadvantage is an error in the numerical wave speed which grows with increasing negative stress. This error was shown to be reduced significantly (although not removed) by a small modification to the anticlumping term which changes the kernel shape at a fixed r/h rather than in relation to the average particle separation. However a major caveat to the anticlumping approach is that the formalism was not found to be stable for all values of negative stress in the case of a variable smoothing length. Various alternative approaches were therefore suggested. An approach which can be used in many practical situations is to simply subtract any constant component of the magnetic field from the gradient term representing the anisotropic force (§4.4.4). For situations where this cannot be used, an alternative approach suggested by Morris (1996) (§4.4.2) was found to also give good results on the shock tube tests described in §4.6.3.

In §4.5 dissipative terms were formulated in order to simulate MHD shocks. The terms are a natural

generalisation of the formalism of Monaghan (1997b) given for the hydrodynamic case in §3.5. The dissipation terms were derived under a minimum of assumptions by assuming a dissipation in the total energy equation which involves a jump in the total energy and requiring that this term result in a positive definite contribution to the entropy. Under only these two assumptions a discrete formulation for a dissipative term in the induction equation was obtained which involves the SPH formulations of the second derivative given in §3.2.4. This term was shown to provide an artificial resistivity in addition to the artificial viscosity and artificial thermal conductivity derived in the hydrodynamic case. A slightly modified version of these dissipative terms which accounts for jumps in the component of the magnetic field along the line joining the particles (due to non-zero magnetic divergence) and velocities perpendicular to this line (providing a shear viscosity component) was also presented. A switch to control the application of artificial resistivity was given in §4.5.2, although it was noted that in the absence of a shear viscosity term it is better to apply artificial resistivity uniformly so as to provide sufficient smoothing of the discontinuities in both the magnetic field and transverse velocity.

Finally, detailed one dimensional numerical tests were presented in §4.6. In particular the algorithm has been tested on a wide range of standard test problems used to benchmark recent grid-based MHD codes. A simple advection test was first considered (§4.6.2), before considering a wide range of shock tube problems demonstrating the shock-capturing ability of the algorithm (§4.6.3). In particular the shock tube tests highlighted the fact that artificial resistivity is a crucial requirement in order to prevent post-shock oscillations in the magnetic field. For high Mach number shocks, the density (although only where the continuity equation is integrated) and magnetic field are observed to overshoot the exact solution slightly, although this error is removed by the inclusion of the variable smoothing length terms which provide a normalisation to the kernel gradient. The algorithm was also tested against small amplitude both fast and slow MHD waves (§4.6.4) and shown to give good results although somewhat slow convergence on these problems due to the dissipative terms.

"Part of the inhumanity of the computer is that, once it is competently programmed and working smoothly, it is completely honest."

ISAAC ASIMOV

5

Multidimensional Smoothed Particle Magnetohydrodynamics

5.1 Introduction

In more than one spatial dimension errors associated with the non-zero divergence of the magnetic field need to be taken into account in any numerical MHD scheme. There are two distinct issues to be addressed. The first is the treatment of terms proportional to $\nabla \cdot \mathbf{B}$ in the MHD equations (in particular in the formulation of the induction equation and the magnetic force). The second is the maintenance of the $\nabla \cdot \mathbf{B} = 0$ constraint. Note that a solution to the latter problem does not necessarily resolve the former, since maintaining $\nabla \cdot \mathbf{B} = 0$ in a particular numerical discretisation does not guarantee that it is zero in all discretisations.

Perhaps the first to address these issues in a numerical context were Brackbill and Barnes (1980), where it was noted that using a conservative formulation of the magnetic force could cause a supposed steady state setup to change because of the small but non-zero component of magnetic force directed along the field lines due to the monopole term. This error can have serious consequences even though the proportional error in the magnetic field is small. As discussed in §4.4, in SPMHD the force parallel to the field can have catastrophic consequences, leading to numerical instability under some circumstances. Brackbill and Barnes (1980) approached the problem by preferring a non-conservative formulation of the momentum equation which guarantees that the magnetic force is exactly perpendicular to the field. Such an approach has also been used successfully in an SPMHD context by several authors (e.g. Benz, 1984; Meglicki et al., 1995; Byleveld and Pongracic, 1996; Cerqueira and de Gouveia Dal Pino, 2001), however the numerical simulations of shocks seems to require the exact conservation of momentum in order to provide the correct jump conditions at shock fronts (which means, at the very least, the discrete formulation should be based on continuum equations which conserve momentum exactly even with a

non-zero magnetic divergence[1]). This issue of neglect or inclusion of divergence terms extends further to the formulation of the induction and energy equations. In the formulation used by Brackbill and Barnes (1980), magnetic flux and energy are conserved exactly, but the conservation of momentum is sacrificed. More recently, this question has been re-addressed by Powell et al. (1999) in the light of the second issue, namely how best to maintain the divergence constraint without resorting to expensive divergence cleaning procedures. The approach taken by Powell et al. (1999) was to include source terms in the equations which allow the divergence errors to be propagated appropriately by the flow. In the Powell et al. (1999) approach, momentum, energy and magnetic flux conservation (in a volume sense) are sacrificed, although it seems that this does not have too severe consequences with the '8-wave' Riemann solver Powell et al. used for the simulation of shocks (however we do not find this to be the case in SPMHD). The equation set used by Powell et al. (1999) and its effect on the propagation of divergence errors is discussed below (§5.2.1). More recently, however, it has been pointed out by both Janhunen (2000) (by considering the presence of monopoles in Maxwell's equations) and Dellar (2001) (from relativistic considerations) that a consistent formulation of the MHD equations in the presence of magnetic monopoles should retain both the conservation of momentum and energy. In §4.3.2 we were able to verify that the set of MHD equations derived by Janhunen (2000) and Dellar (2001) indeed form a consistent set by deriving the SPMHD equations from a variational principle which uses the SPH form of the induction equation as a constraint in order to derive the momentum and energy equations. Similarly it can also be shown that the formalism used by Brackbill and Barnes (1980), in which the conservation of flux is retained but the conservation of momentum and energy are not, is also consistent (although undesirable due to both the non-conservation and the effects on the propagation of divergence errors). Furthermore the derivation given in §4.3.2 was for the discrete SPMHD equations, ensuring consistency in both the continuum and discrete forms. This consistent set of equations and the consequences for the propagation of divergence errors has already been discussed (albeit briefly) in Chapter 4. Further discussion and comparison with the Powell et al. (1999) approach is given in §5.2.1 and examined numerically in §5.3.2.

Many other approaches to the second issue are also possible. Maintenance of constraints similar to the divergence-free condition for the magnetic field is important not only for MHD problems, but also for incompressible flows (where $\nabla \cdot \mathbf{v} = 0$) and especially in algorithms for numerical relativity, since Einstein's equations can be written in a form corresponding closely to the Maxwell equations[2]. Many possible methods have been proposed for dealing with this problem, each with their own advantages and disadvantages. Perhaps the simplest is to explicitly evolve a vector potential $\mathbf{A}$, from which the magnetic field is derived by taking the curl, guaranteeing that the divergence is zero. The major disadvantage of this approach is that the computation of the force terms involves second derivatives of the evolved variable ($\mathbf{A}$), which in general can be significantly less accurate. One advantage of using the vector potential is that the conservation of magnetic helicity $\mathbf{A} \cdot \mathbf{B}$ can be monitored (§4.2.2), which is particularly important for dynamo and reconnection problems often encountered in Solar physics (e.g. Brandenburg, 2001).

Brackbill and Barnes (1980) proposed a simple projection scheme to 'clean up' the magnetic field at

[1] For example, none of the results obtained on the shock tube tests given in §4.6.3 could be obtained to *any* degree of satisfaction using a formalism based on a non-conservative momentum equation (such as those given in §4.3.5), although the formalism proposed by Morris (1996) (§4.4.2) can be made to give reasonable results since firstly it is based on a conservative form of the continuum equations and secondly at least conserves momentum exactly for isotropic forces

[2] In the case of the Einstein equations, there are six evolution equations and four constraint equations, similar to the two evolution equations and two constraint equations in the Maxwell equations.

each timestep, an approach which is now commonly used in many grid-based MHD codes (e.g. Balsara, 1998). Similar schemes have been used in SPH for incompressible flows (e.g. Cummins and Rudman, 1999). The disadvantage of this approach is that it involves the solution of a Poisson equation which is computationally expensive. Another approach used in grid-based MHD codes is the so-called 'constrained transport' method pioneered by Evans and Hawley (1988) in which differences of the magnetic field across the grid cell are constructed in such a way as to maintain the divergence free condition exactly. Such methods work very well, however cannot be used in SPH because of the absence of a spatial grid (although perhaps some divergence-free interpolation could be devised). A comparison between several of these schemes with the source term approach of Powell et al. (1999) and a projection method for finite difference codes has been recently presented by Tóth (2000). Although not all of the schemes are applicable in an SPH context, many of the numerical tests presented in this chapter are taken from this paper. More recently Dedner et al. (2002) have proposed a method for cleaning the magnetic field which is significantly faster than the projection method by explicitly adding a constraint propagation equation which is coupled to the evolution equation for the magnetic field. This equation propagates the divergence error in a hyperbolic (ie. wave-like) manner away from its source. Adding a small diffusion term means that the error is rapidly reduced to zero.

In §5.2 we investigate several of these approaches to maintaining the $\nabla \cdot \mathbf{B} = 0$ constraint which are applicable in an SPH context, namely the source term approach discussed in the previous chapter (§5.2.1), projection methods (§5.2.2) and the Dedner et al. approach (§5.2.3). The algorithm is then benchmarked, as in the one dimensional case, against a wide range of multidimensional test problems used to test recent grid-based MHD codes (§5.3). The tests involve the propagation of an initially non-zero magnetic divergence (§5.3.2), nonlinear Alfvén waves (§5.3.3), two dimensional shock tubes (§5.3.5), interacting shocks and the transition to turbulence (§5.3.7) and two dimensional spherically symmetric blast waves (§5.3.6).

5.2 Divergence correction techniques

5.2.1 Source term approach

As discussed in §4.2.1 the induction equation can be written in the 'conservative' form

$$\frac{\partial \mathbf{B}}{\partial t} = -\nabla \times (\mathbf{v} \times \mathbf{B}), \tag{5.1}$$

$$= \nabla \cdot (\mathbf{vB} - \mathbf{Bv}). \tag{5.2}$$

which explicitly conserves the volume integral of the flux (4.17). In Lagrangian form this is given by

$$\frac{d\mathbf{B}}{dt} = -\mathbf{B}(\nabla \cdot \mathbf{v}) + (\mathbf{B} \cdot \nabla)\mathbf{v} + \mathbf{v}(\nabla \cdot \mathbf{B}) \tag{5.3}$$

Taking the divergence of this equation, we have

$$\frac{\partial}{\partial t}(\nabla \cdot \mathbf{B}) = 0, \tag{5.4}$$

showing that the constraint $\nabla \cdot \mathbf{B} = 0$ enters the MHD equations as an initial condition. However allowing magnetic monopoles resulting from $\nabla \cdot \mathbf{B} \neq 0$ to evolve appropriately within the flow can prevent the build up of unphysical numerical effects associated with their presence and can therefore reduce the need for computationally expensive divergence cleaning procedures. Thus Powell (1994) (see Powell et al. 1999) suggested that the conservative forms of the MHD equations should contain source terms to ensure that these errors are propagated out by the flow. With this in mind, Powell (1994) added source terms to the momentum, energy and induction equations, which take the (Lagrangian) form

$$\frac{d\mathrm{v}^i}{dt} = \frac{1}{\rho}\frac{\partial S^{ij}}{\partial x^j} - \frac{B^i}{\rho}\frac{\partial B^j}{\partial x^j}, \tag{5.5}$$

$$\frac{de}{dt} = -\frac{1}{\rho}\frac{\partial (\mathrm{v}_i S^{ij})}{\partial x^j} - \frac{\mathrm{v}_i B^i}{\rho}\frac{\partial B^j}{\partial x^j}, \tag{5.6}$$

$$\frac{dB^i}{dt} = B^j \frac{\partial \mathrm{v}^i}{\partial x^j} - B^i \frac{\partial \mathrm{v}^j}{\partial x^j}, \tag{5.7}$$

where as in the previous chapter the stress tensor is defined as

$$S^{ij} = -P\delta^{ij} + \frac{1}{\mu_0}\left(B^i B^j - \frac{1}{2}B^2\delta^{ij}\right). \tag{5.8}$$

Taking the divergence of (5.7) shows that the divergence errors in this formalism evolve according to

$$\frac{\partial}{\partial t}(\nabla \cdot \mathbf{B}) + \nabla \cdot (\mathbf{v}\nabla \cdot \mathbf{B}) = 0, \tag{5.9}$$

which has the same form as the continuity equation for the density (where in this case we have a density of magnetic monopoles, $\nabla \cdot \mathbf{B}$). This therefore implies that the total volume integral of $\nabla \cdot \mathbf{B}$ across the simulation is conserved and hence that the *surface* integral of the flux (4.18) is conserved. As discussed in §4.2.2 the conservation of this quantity is a far more important physically than the conservation of the volume integral (4.17).

The disadvantage of using (5.5)-(5.7) is that exact conservation of momentum and energy is sacrificed, which proves to be important for shock-type problems. Correspondingly it can lead to incorrect jump conditions at shock fronts (Tóth, 2000). More recently it has been shown by Janhunen (2000) and Dellar (2001) that the correct formulation of the MHD equations in the presence of monopoles should *not* violate the conservation of momentum and energy, giving

$$\frac{d\mathrm{v}^i}{dt} = \frac{1}{\rho}\frac{\partial S^{ij}}{\partial x^j}, \tag{5.10}$$

$$\frac{de}{dt} = -\frac{1}{\rho}\frac{\partial (\mathrm{v}_i S^{ij})}{\partial x^j}, \tag{5.11}$$

$$\frac{dB^i}{dt} = B^j \frac{\partial \mathrm{v}^i}{\partial x^j} - B^i \frac{\partial \mathrm{v}^j}{\partial x^j}. \tag{5.12}$$

Note that the induction equation (5.12) is the same as in Powell's method and therefore the manner in which the divergence errors evolve (5.9) is exactly the same. We have shown in §4.3.2 that equations (5.10) and (5.12) are indeed consistent with each other by deriving the SPH form of (5.10) from a variational principle which uses the SPH form of (5.12) as a constraint.

5.2.2 Projection methods

A common approach to the divergence problem is to clean up the magnetic field at regular intervals via the *projection method* (e.g. Brackbill and Barnes, 1980). The basic idea is to decompose the magnetic field into a curl and a gradient (which can be done unambiguously for any vector field) according to

$$\mathbf{B}^* = \nabla \times \mathbf{A} + \nabla\phi. \tag{5.13}$$

Taking the divergence of this expression results in the Poisson equation

$$\nabla^2\phi = \nabla \cdot \mathbf{B}^*, \tag{5.14}$$

which can then be solved for the scalar quantity ϕ. The magnetic field is then corrected according to

$$\mathbf{B} = \mathbf{B}^* - \nabla\phi. \tag{5.15}$$

The major disadvantage with this approach is that the solution of the Poisson equation (5.14) is computationally expensive, scaling as $\mathscr{O}(N^2)$. In an astrophysical SPH context this may be offset somewhat by the fact that the Poisson equation for the gravitational field is usually solved using a tree code (e.g. Hernquist and Katz 1989; Benz et al. 1990) which scales as $\mathscr{O}(N\log N)$. However there are some subtle difficulties with this approach, which we outline below.

Projection schemes for incompressible flow in SPH have been implemented by Cummins and Rudman (1999), the results of which are applicable to the present case. The important point, also discussed by Tóth (2000) is that for the projection step to reduce the divergence to zero (ie. to provide an *exact* projection) requires that the discrete version of (5.14) is satisfied exactly. This means that the operator used to evaluate the divergence term on the right hand side of (5.14) should be the same as the divergence operator used in the evaluation of the ∇^2 on the left hand side and that the gradient operator used in the evaluation of ∇^2 should be the same as that used in 5.15. Cummins and Rudman (1999) approach this problem by calculating the ∇^2 using SPH operators, solving the Poisson equation by matrix inversion. Good results were also obtained using an approximate projection (ie. where the divergence operators on the left and right hand side differ). In this scheme Cummins and Rudman (1999) used the SPH evaluation of the Laplacian given in §3.2.4, similar to that used in the artificial dissipation terms (4.80)-(4.85). The Poisson equation is then solved by inverting the resulting matrix equation.

The solution of (5.14) by direct summation (of which the tree code is an approximation), uses the exact solution to the Poisson equation (5.14) given by

$$\phi(\mathbf{r}) = \int G(|\mathbf{r}-\mathbf{r}'|)\nabla \cdot \mathbf{B}(\mathbf{r}')\mathrm{d}V(\mathbf{r}'), \tag{5.16}$$

where $G(|\mathbf{r}-\mathbf{r}'|)$ is the Green's function, given by

$$\begin{aligned} G(r) &= \frac{1}{2\pi}\ln r + \text{const}, \\ G(r) &= -\frac{1}{4\pi r}, \end{aligned} \tag{5.17}$$

in two and three dimensions respectively. The gradient needed in the correction step can be calculated directly, giving (in three dimensions)

$$\nabla\phi(\mathbf{r}) = -\frac{1}{4\pi}\int \frac{\nabla\cdot\mathbf{B}(\mathbf{r}')}{|\mathbf{r}-\mathbf{r}'|^3}(\mathbf{r}-\mathbf{r}')\mathrm{dV}(\mathbf{r}'). \tag{5.18}$$

In SPH we replace the volume element $\rho\mathrm{dV}$ with the mass per SPH particle and write the integral as a summation according to

$$\nabla\phi_a = -\sum_b m_b \frac{(\nabla\cdot\mathbf{B})_b}{4\pi\rho_b}\frac{(\mathbf{r}_a-\mathbf{r}_b)}{|\mathbf{r}_a-\mathbf{r}_b|^3}. \tag{5.19}$$

Since we still retain the freedom to choose the discrete operator used to evaluate $\nabla\cdot\mathbf{B}$ at each particle, it becomes clear that the solution by direct summation will only provide an *approximate* projection, since (5.14) is not discretely satisfied. This approximate solution will be degraded further when implemented using a tree code. A further disadvantage of the projection method for many of the problems considered in this paper is that it is somewhat complicated to implement in the case of periodic boundary conditions. Despite these subtleties the projection method based on the Green's function solution is found to give a substantial reduction in the divergence errors in a single step (§5.3.2).

The projection step is implemented in this thesis as follows: For a given magnetic field on the particles, the divergence is calculated using (5.31). The correction to the field is then calculated by a direct summation using (5.19) (with the Green's function appropriate to the number of spatial dimensions) and subtracted accordingly. Using the timestepping scheme described in §3.6 the correction is made to the magnetic field $\mathbf{B}^0$ at the beginning of the timestep. This means that the divergence is calculated in a separate loop to the usual force calculation.

An alternative projection scheme can be implemented by solving for the vector potential $\mathbf{A}$. That is, we take the curl of (5.13) to obtain

$$\nabla\times\mathbf{B}^* = \nabla(\nabla\cdot\mathbf{A}) - \nabla^2\mathbf{A}. \tag{5.20}$$

Choosing the Gauge condition $\nabla\cdot\mathbf{A}=0$, we obtain a Poisson equation for the vector potential in terms of the current density $\mathbf{J}=\nabla\times\mathbf{B}^*/\mu_0$

$$\nabla^2\mathbf{A} = -\mu_0\mathbf{J} \tag{5.21}$$

with solution

$$\mathbf{A}(\mathbf{r}) = \int G(|\mathbf{r}-\mathbf{r}'|)\mathbf{J}(\mathbf{r}')\mathrm{dV}(\mathbf{r}'). \tag{5.22}$$

Taking the curl, we obtain an equation for the corrected magnetic field in terms of the current density, which in three dimensions is given by

$$\mathbf{B} = \nabla\times\mathbf{A} = -\frac{\mu_0}{4\pi}\int \frac{\mathbf{J}(\mathbf{r}')\times(\mathbf{r}-\mathbf{r}')}{|\mathbf{r}-\mathbf{r}'|^3}\mathrm{dV}(\mathbf{r}'). \tag{5.23}$$

which is simply Biot-Savart's Law. In SPH form this is given by

$$\mathbf{B}_a = -\sum_b m_b \frac{(\nabla \times \mathbf{B}^*)_b \times (\mathbf{r}_a - \mathbf{r}_b)}{4\pi\rho_b |\mathbf{r}_a - \mathbf{r}_b|^3}. \tag{5.24}$$

This method could be useful in an SPH context in situations where several disconnected regions exist containing strong magnetic currents (such as in two isolated neutron stars). By solving (5.23), the corrected magnetic field is determined from the current density, resulting in a knowledge of the magnetic field at any point in space. This approach was in fact used as the basis for the very first SPMHD algorithm implemented by Gingold and Monaghan (1977). As a divergence cleaning method, we find that the results are very similar to those obtained using (5.19), although at a slightly higher computational cost since the Poisson equation (5.21) is solved for a vector quantity rather than a scalar, giving (up to) three summations in (5.24) as opposed to just one in (5.19).

Finally it is worth commenting on the possibility of using iterative methods for solving the Poisson equation (5.14), although there is not the time or space available to investigate these ideas further in this thesis. The main point is that divergence errors usually arise in a simulation as short wavelength errors, typically of opposite sign. Obtaining the full solution to the Poisson equation (using the Green's function or otherwise) is computationally expensive because both the long and short wavelength components must be accounted for. This is perhaps best illustrated by the multigrid methods which explicitly tackle the problem in this manner by using simple iterative schemes such as the Jacobi or Gauss-Seidel methods (which are good at removing the short wavelength errors) on a progressively coarser heirarchy of grids (thus acting on progressively longer wavelength errors). The solution by direct summation (5.19) is slow because the (small) contribution from distant neighbours must be accounted for (which is accelerated in the tree code by treating groups of distant particles as single entities). However, since for the purposes of divergence cleaning we are interested in eliminating mainly the short wavelength errors, performing simple iterations on the Poisson equation expressed using SPH operators may give satisfactory results with a much lower computational expense. Furthermore an approximate solution to a specified accuracy (which may be achieved in just a few iterations) is all that is really required from the cleaning procedure, rather than the full, exact solution. A similar point has been made by Tóth (2000). An iterative solution to the Poisson equation (5.14) can be obtained by solving a diffusion equation of the form

$$\frac{\partial \phi}{\partial t} = \nabla^2 \phi - \nabla \cdot \mathbf{B} \tag{5.25}$$

via a relaxation method (Press et al., 1992). Methods for solving diffusion equations implicitly using iterative procedures have been recently developed for use in SPH by Whitehouse and Bate (2004) and Monaghan (1997a) and it may be possible to apply these ideas to the divergence cleaning problem.

5.2.3 Hyperbolic divergence cleaning

Dedner et al. (2002) examine alternative divergence cleaning procedures. In their paper (see also Munz et al., 2000), they derive a general constrained formulation of the MHD equations, from which formalisms can be derived to give divergence cleaning which is elliptic (involving the solution of a Poisson equation), parabolic (in which the divergence errors are diffused away) and hyperbolic (where the diver-

gence errors are propagated away from their source at a characteristic speed). The projection method described above is an elliptic approach, the main disadvantage to which is the substantial computational cost involved in the solution of the Poisson equation. The parabolic approach was found to be severely limited in scope due to the timestep restrictions imposed by the Courant condition[3]. The hyperbolic approach was found to be particularly effective, especially when combined with a parabolic term such that divergence errors are both transported and diffused. It is this approach that we outline below in an SPH context.

The basic idea is to introduce an additional scalar field ψ, which is coupled to the magnetic field by a gradient term in the induction equation,

$$\frac{d\mathbf{B}}{dt} = -\mathbf{B}(\nabla\cdot\mathbf{v}) + (\mathbf{B}\cdot\nabla)\mathbf{v} - \nabla\psi. \tag{5.26}$$

Note that our induction equation maintains the consistent treatment of divergence terms discussed above. The variable ψ is then calculated by adding an additional constraint equation, which for the combined hyperbolic/parabolic approach is given by

$$\frac{d\psi}{dt} = -c_h^2(\nabla\cdot\mathbf{B}) - \frac{\psi}{\tau}. \tag{5.27}$$

Neglecting the second term on the right hand side of (5.27) gives an equation for ψ which is purely hyperbolic. This implies that divergence errors are propagated in a wave-like manner away from their source with characteristic speed c_h (for more details we refer the reader to the Dedner et al. (2002) paper). The second term on the right hand side is a parabolic term which causes ψ to decay exponentially to zero with e-folding time τ (this is easily seen by neglecting the hyperbolic term and solving the resulting ordinary differential equation for $\psi(t)$). Since it is desirable for the divergence errors to be propagated at the maximum possible rate (within the timestep constraint imposed by the Courant condition), c_h should be set equal to the maximum signal propagation speed. For simplicity we calculate this as

$$c_h = \sqrt{\frac{\gamma P}{\rho} + \frac{1}{2}\frac{B^2}{\mu_0\rho}}, \tag{5.28}$$

where the maximum value over all of the particles is used. The decay timescale τ is given by

$$\frac{1}{\tau_a} = \frac{\sigma c_h}{h_a}, \tag{5.29}$$

where σ is a dimensionless parameter which determines the decay timescale. Setting $\sigma = 0$ gives a purely hyperbolic correction. A value of $\sigma = 0.2$ would imply that ψ will have decayed significantly after the divergence errors have propagated approximately 5 smoothing lengths. In §5.3.2 we examine in detail the effects of varying the value of σ. We find that values of σ in the range $0.05 - 0.2$ generally give the best results, giving a good balance between the hyperbolic (fast but non-diffusive) and parabolic (diffusive but slow-acting) effects. In practise some diffusion is also added by the artificial resistivity terms (§4.5).

[3] an equivalent approach in SPMHD is to use an artificial resistivity in order to diffuse away divergence errors. This has been used, for example, by Morris (1996) and Hosking (2002)

The gradient term in the induction equation is calculated using a simple SPH estimate (§3.2.3)

$$\nabla\psi_a = \frac{1}{\rho_a}\sum_b m_b(\psi_b - \psi_a)\nabla_a W_{ab}. \tag{5.30}$$

Similarly the divergence of the magnetic field is calculated using

$$(\nabla\cdot\mathbf{B})_a = \sum_b m_b(\mathbf{B}_a - \mathbf{B}_b)\cdot\nabla_a W_{ab}. \tag{5.31}$$

Superfast cleaning

This type of divergence cleaning is most effective when the dynamics in the simulation occur at speeds lower than the fastest wave speed. In this case the divergence cleaning is able to propagate and diffuse the divergence errors faster than they are created in the flow. For the same reason this method is also more effective for codes using a single timestep rather than individual particle timesteps, since the divergence cleaning can take advantage of the 'slack' in the timestep criterion (using individual particle timesteps c_h would be different for each particle). For simulations where divergence errors are generated very quickly (e.g. for problems involving strong shocks) the timescale for removal of the error using the cleaning described above can be too slow to prevent significant errors in the dynamics. One possibility for such problems is to use 'superfast' cleaning, that is to increase the wave speed c_h beyond the maximum imposed by the timestep condition. An operator splitting procedure could then be used to solve the constraint propagation separately between timesteps. For example, having determined the need for extra cleaning by some error criterion, we would then solve the following system of equations in a series of smaller steps which are fractions of the full timestep:

$$\frac{d\mathbf{B}}{dt} = -\nabla\psi \tag{5.32}$$

$$\frac{d\psi}{dt} = -(c_h^*)^2(\nabla\cdot\mathbf{B}) - \frac{\psi}{\tau^*}. \tag{5.33}$$

In the above c_h^* is some multiple of c_h (where the multiplication factor determines the number of substeps necessary – for example using twice the fastest wave speed would require two substeps) and τ^* is the corresponding decay timescale. Note that during the substeps the particles are fixed, such that the neighbour lists do not have to be reconstructed. All that is required is to find the updated estimates of $\nabla\psi$ and $\nabla\cdot\mathbf{B}$ at each substep. The usual induction equation would then be evolved through the full timestep, adding the result to the magnetic field which has been evolved through the constraint substeps.

5.3 Numerical tests

The main issue to be addressed in 2D and 3D problems is the non-zero divergence of the magnetic field. In the SPH context it also allows us to estimate the extent to which the artificial dissipation spuriously affects the numerical results. Again there is a substantial literature of multi-dimensional MHD problems which have been used to test grid-based MHD codes (e.g. Dai and Woodward 1994; Ryu et al. 1995; Balsara 1998; Dai and Woodward 1998; Tóth 2000) and we consider several of these problems here.

5.3.1 Implementation

The implementation of the SPMHD equations used for the multidimensional tests is almost identical to that used in the one dimensional case (§4.6). The density is calculated by summation, the total energy equation is used (although results are indistinguishable using the thermal energy equation in nearly all cases) and the magnetic field is evolved using (4.20) (or using (5.26) when using the hyperbolic cleaning). In the shock tube tests we use unsmoothed initial conditions. The artificial dissipative terms, except where otherwise indicated are implemented using the jump in total magnetic energy (§4.5.1) but as in the one dimensional case the viscosity term uses only the velocity component along the line joining the particles (4.80). Artificial viscosity and thermal conductivity are applied using the switches discussed in §3.5.2 whilst the artificial resistivity term is applied uniformly using $\alpha_B = 1$. A major difference between the simulations presented here and those in the previous chapter is that the anticlumping approach was not found to be uniformly successful in eliminating the tensile instability for all of the problems considered (in particular for the Alfvén wave test only a narrow range of parameters would produce stable results). Furthermore this term was found to result in spurious extra numerical noise, particularly in the shock tube tests. For this reason we have eliminated the tensile instability by simply subtracting the constant component of the magnetic field from the gradient term (§4.4.4). However all of the test cases have also been run using the stable Morris formulation of the magnetic force (§4.4.2) and show very little difference in the results.

Error estimates

Various estimates can be made of the error produced in the simulation by any non-zero magnetic divergence. Monitoring these quantities over the course of a simulation thereby gives some measure of the magnitude of the error produced by $\nabla \cdot \mathbf{B}$. The most common approach in SPH implementations to date has been to monitor the dimensionless quantity

$$\frac{h\nabla \cdot \mathbf{B}}{|\mathbf{B}|} \tag{5.34}$$

and ensure that it remains small (typically < 0.01) over most of the simulation, where h is the SPH smoothing length and the divergence is calculated using (5.31). This provides some measure of the relative error in the magnetic field but no indication of how much influence this error has in the dynamics. For this reason it is also useful to measure the relative error in the total force caused by a non-zero divergence,

$$E_{force} = \frac{\mathbf{f}_{mag} \cdot \mathbf{B}}{|\mathbf{f}||\mathbf{B}|} \tag{5.35}$$

where $\mathbf{f}_{mag}$ is the magnetic component of the SPH force (4.33), whilst $\mathbf{f}$ is the total force on the particle. It is also useful to simply monitor the evolution in the maximum, minimum and average of $|\nabla \cdot \mathbf{B}|$ with time as well as the conserved quantities given in §4.2.2.

Visualisation

In order to make a direct comparison of our results with those of grid-based MHD codes, we interpolate the results from the particles to an array of pixels using the SPH kernel. That is, for a contour or rendered plot of a scalar quantity ϕ we interpolate to the pixels using

$$\phi(x,y) = \sum_b m_b \frac{\phi_b}{\rho_b} W(x-x_b, y-y_b, h_b) \tag{5.36}$$

where W is the cubic spline kernel used in the calculations (§3.2.5) and the summation is over contributing particles. Note that in practise this is quite simple to implement, as it involves only one loop over the particles, during which the contributions from the current particle to all pixels within a smoothing radius ($2h$) are calculated. For a vector quantity a similar interpolation can be performed for each component, however since in this case the interpolation is usually to a coarser grid, it is simpler just to bin the particles into grid cells and take the average of the vector components in each cell.

5.3.2 $\nabla \cdot \mathbf{B}$ advection

The first problem we examine is a simple test used by Dedner et al. (2002) in which a non-zero magnetic divergence is introduced into the simulation as an initial condition. This is a particularly good test for comparing various divergence cleaning procedures. The initial conditions are a uniform density distribution ($\rho = 1$) in the domain $-0.5 < x < 1.5, -0.5 < y < 1.5$ with a constant initial velocity field $\mathbf{v} = [1,1]$. The initial gas pressure is $P = 6$ with $\gamma = 5/3$ and the magnetic field has a constant component perpendicular to the plane $B_z = 1/\sqrt{4\pi}$. The divergence is introduced as a peak in the $x-$component of the field in the form

$$B_x = 4096(r^2)^4 - 128(r^2)^2 + 1 \qquad\qquad r^2 = x^2 + y^2 \tag{5.37}$$

the contours of which are shown in the left column of Figure 5.1. The particles are arranged on a cubic lattice for simplicity and periodic boundary conditions are enforced using ghost particles. Since the density is uniform throughout the simulation the results are insensitive to whether (4.20) or (4.22) is used and also to the anticlumping term since the simulation is not unstable to negative stress. The artificial dissipation terms are turned off for this problem in order to isolate the effects of the divergence cleaning procedures.

The results of this test using four different divergence cleaning techniques are shown in Figure 5.1. The plots show contours of the $x-$component of the magnetic field as it evolves in each case (30 contours are plotted, evenly spaced between the minimum and maximum of B_x over all the simulations). The results using the consistent formulation of $\nabla \cdot \mathbf{B}$ terms discussed in the previous chapter and in §5.2.1 are shown in the top row. In this case the divergence error is passively advected by the flow and both the field and the divergence error remain unchanged (relative to the flow) at $t = 1$, demonstrating that the formalism is indeed consistent in the presence of magnetic monopoles. In order to compare these results with a conservative formulation of the MHD equations, we have performed a simulation using an SPH

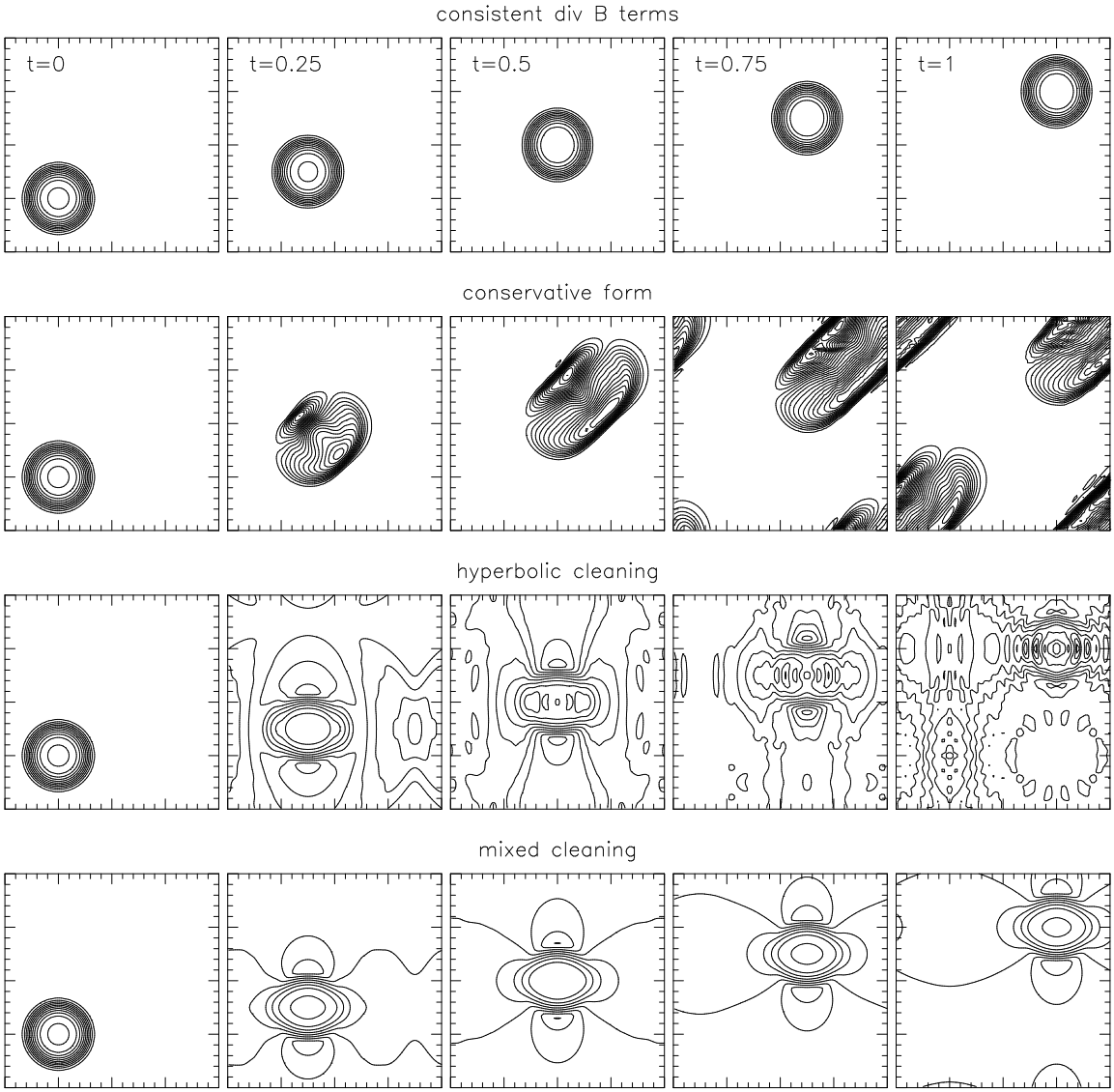

Figure 5.1: Results of the $\nabla \cdot \mathbf{B}$ advection problem. An initially non-zero divergence is setup as a peak in the $x-$component of the magnetic field (leftmost figures), with a velocity field $\mathbf{v}(x,y) = [1,1]$ and periodic boundaries. The plots show contours in B_x at various times throughout the simulation for various divergence cleaning procedures. The consistent treatment of $\nabla \cdot \mathbf{B}$ terms (top row) is clearly seen to advect the divergence without change, which is an improvement over a conservative formulation of the MHD equations in which the divergence is smeared throughout the simulation volume (second row). With the use of hyperbolic cleaning in addition to the consistent $\nabla \cdot \mathbf{B}$ terms, the divergence error is spread rapidly (middle row), whilst with a mixed hyperbolic/parabolic cleaning (fourth row) this error is also diffused away, resulting in a divergence-free field configuration (compare the bottom row with the results using the projection method in Figure 5.3).

induction equation of the form

$$\frac{d}{dt}\left(\frac{B_a^i}{\rho_a}\right) = \sum_b m_b \left[\frac{B_a^j}{\rho_a^2}(\mathrm{v}_b^i - \mathrm{v}_a^i) + \frac{\mathrm{v}_a^i}{\rho_a^2}(B_b^j - B_a^j)\right] \frac{\partial W_{ab}}{\partial x_a^j} \tag{5.38}$$

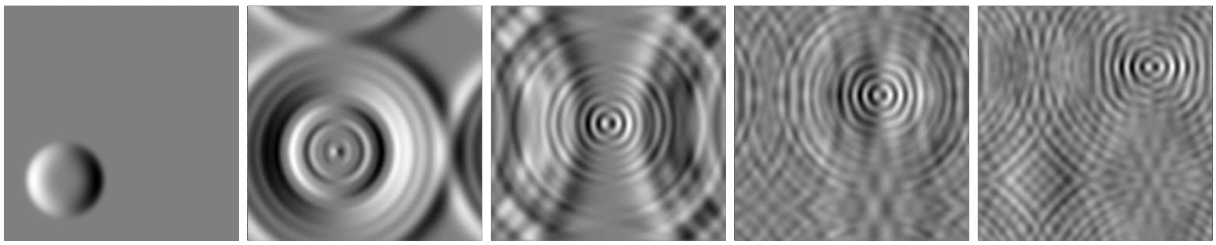

Figure 5.2: Divergence of the magnetic field in the $\nabla \cdot \mathbf{B}$ advection problem at the times shown in Figure 5.1 using the hyperbolic divergence cleaning discussed in §5.2.3. The divergence error is rapidly spread in a wavelike manner throughout the simulation volume, although in the absence of diffusion the overall error does not decrease in magnitude. Periodic boundary conditions are used, resulting in the interference patterns seen at later times.

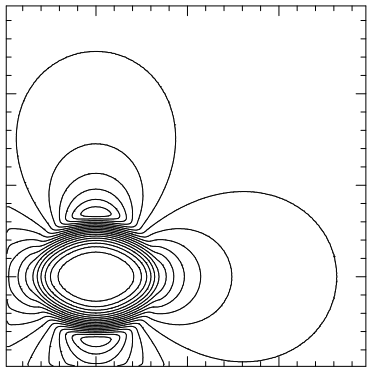

Figure 5.3: Divergence cleaning using the approximate projection method described in §5.2.2. The plot shows 30 contours of B_x in the $\nabla \cdot \mathbf{B}$ advection problem after a single projection step at $t = 0$. The results may be compared to those shown in Figure 5.1. The projected magnetic field adopts an essentially divergence-free configuration in a single step.

which is an SPH form of the conservative (in a volume sense) induction equation

$$\frac{d}{dt}\left(\frac{\mathbf{B}}{\rho}\right) = \left(\frac{\mathbf{B}}{\rho}\cdot\nabla\right)\mathbf{v} + \mathbf{v}\left(\frac{\nabla\cdot\mathbf{B}}{\rho}\right). \tag{5.39}$$

The results using this formalism are shown in the second row of Figure 5.1. The peak in B_x is distorted by the flow and the divergence error is smeared throughout the simulation.

The third row in Figure 5.1 shows the results using the divergence correction discussed in §5.2.3 using only the hyperbolic term in (5.27)(ie. with $\sigma = 0$) in conjunction with the usual monopole formulation of the induction equation (4.22). The divergence error is spread rapidly in a wavelike manner by the constraint equation (5.27)(this is graphically illustrated in Figure 5.2 which shows the propagation of the divergence error in this simulation). However, the magnitude does not decrease in this case. Using the mixed hyperbolic/parabolic cleaning with a small amount of diffusion (using the parabolic term in (5.27), in this case with $\sigma = 0.1$), this error is rapidly diffused away, resulting in a divergence-free field configuration (Figure 5.1, bottom row). For comparison, the results of a single projection step at $t = 0$ are shown in Figure 5.3, showing the divergence-free configuration adopted by the field. The projection step is calculated as described in §5.2.2.

The time evolution of various quantities throughout these simulations are shown in Figure 5.4. The

left panels show the evolution of the maximum (top) and average (bottom) of $|\nabla \cdot \mathbf{B}|$. In conservative form (solid line) the maximum divergence varies slightly and initially becomes larger than the initial value. The bottom panel shows that the average value in this case steadily increases over time, due to the smearing effect of the divergence propagation (5.4). The consistent formulation of $\nabla \cdot \mathbf{B}$ terms (dashed line) maintains a steady value of both the maximum and average, as observed in Figure 5.1. With hyperbolic cleaning (dot-dashed) the maximum divergence error is quickly reduced (although increases at later times as the divergence waves cross the periodic domain and interact) whilst the average climbs as the divergence error is spread throughout the domain. Using the mixed hyperbolic/parabolic cleaning as described above (dotted line), both the maximum and average divergence is swiftly reduced. For comparison, results using the projection method where a projection step is taken every 10 timesteps are also plotted (dashed-dot-dashed). Note however that the boundary conditions are assumed to be open for this problem which means that the periodicity is not accounted for. At early times this is a valid assumption as the source term for the Poisson equation (ie. $\nabla \cdot \mathbf{B}$) is non-zero in only a finite region of the simulation volume. However as the divergence is spread by the cleaning this assumption breaks down and a fully periodic treatment should be used.

The magnitude of the volume integral of the flux (4.17) and of the cross helicity (4.16) are shown in the right hand panels of Figure 5.4. Although (as discussed in §4.2.2) the conservation of the volume integral of the flux is not particularly important physically, this plot demonstrates that this quantity is conserved more accurately using a conservative formulation of the induction equation than when using the monopole-consistent formulation [4]. However, the opposite is true in the conservation of cross-helicity (which measures the preservation of the flux-frozenness condition, c.f. §4.2.2). With any kind of divergence cleaning, the flux integral is conserved to a much higher degree of accuracy and the same is true for the cross-helicity except in the case of the projection method. The projection method does not conserve the cross-helicity invariant since the divergence cleaning is done without any knowledge of the velocity field. In the hyperbolic/parabolic cleaning the induction equation is still explicitly evolved and therefore the flux-frozenness condition is still maintained.

Finally the effect of varying the strength of the parabolic (diffusion) term in (5.27) is examined. In Figure 5.5 the time evolution of the maximum of $|\nabla \cdot \mathbf{B}|$ over the particles is shown, varying the diffusion parameter σ. A small amount of diffusion is necessary to remove the divergence error, however as σ is increased the cleaning becomes less effective as the slow-acting parabolic effects dominate. The fastest reduction in $\nabla \cdot \mathbf{B}$ is obtained using $\sigma \sim 0.1 - 0.2$, giving a good balance between the slow-acting diffusion and the spreading produced by the hyperbolic term.

[4] Note that using the conservative induction equation in the form (5.38) does not exactly conserve the volume integral of the flux (4.17) since the gradient terms are not symmetric between the particle pairs. A formalism which does conserve this integral is simple to construct based on (5.39). For example

$$\frac{d}{dt}\left(\frac{B_a^i}{\rho_a}\right) = \sum_b m_b \left(\frac{B_a^j}{\rho_a^2} \mathrm{v}_b^i + \frac{B_b^j}{\rho_b^2} \mathrm{v}_a^i\right) \frac{\partial W_{ab}}{\partial x_a^j} \tag{5.40}$$

explicitly conserves the integral (4.17) since

$$\sum_a m_a \frac{d}{dt}\left(\frac{\mathbf{B}_a}{\rho_a}\right) = 0, \tag{5.41}$$

although the interpolation provided by the terms in (5.40) is not a particularly good one (c.f. §3.2.2).

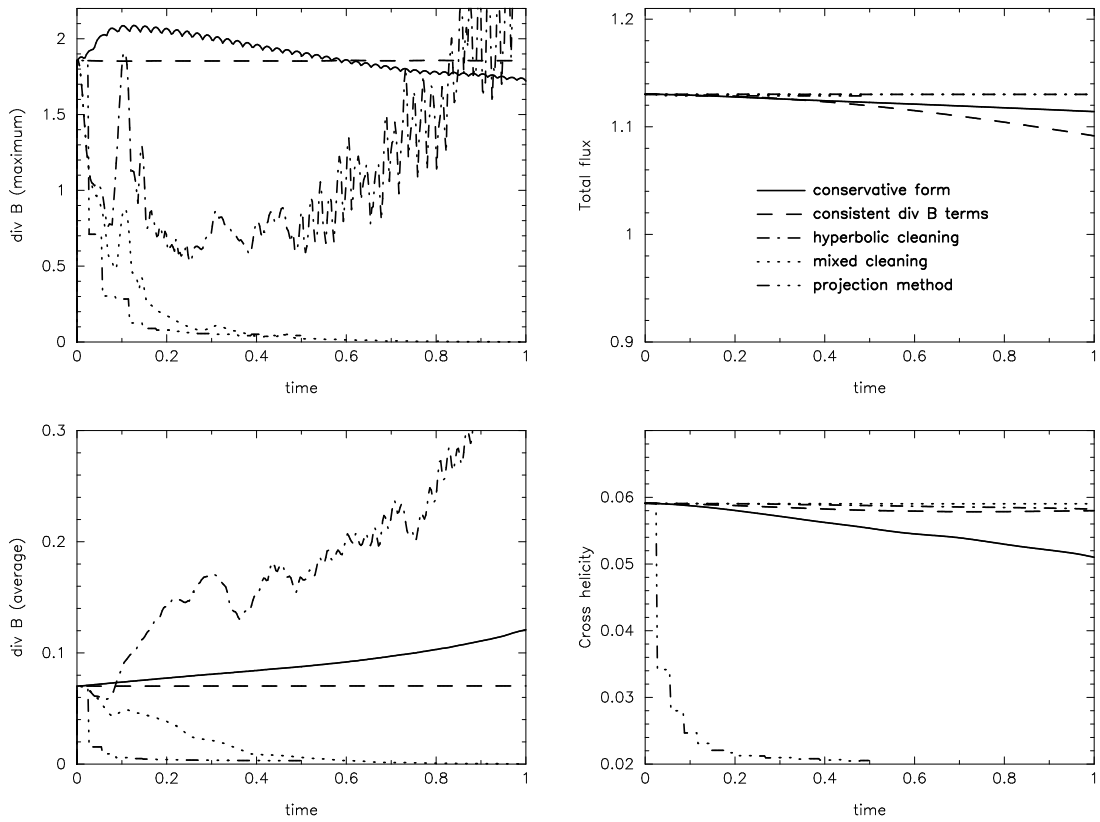

Figure 5.4: Time evolution of various quantities in the $\nabla \cdot \mathbf{B}$ advection test. The left hand panels show the maximum (top) and average (bottom) values of $|\nabla \cdot \mathbf{B}|$ over the particles. With a conservative formulation of the induction equation the divergence error increases with time (solid line) whereas the errors are conserved using a formulation which is consistent in the presence of magnetic monopoles (dashed line). With hyperbolic cleaning (dot-dashed) the maximum is quickly reduced although the average increases, however with the parabolic term included the error is rapidly diffused away (dotted line), giving results comparable to the projection method (dashed-dot-dashed). The right hand panels show the conservation of the volume integral of the flux (top) and the cross-helicity invariant (bottom), which in all cases is improved by the divergence cleaning except in the case of the projection method which does not conserve the cross-helicity.

5.3.3 Circularly polarized Alfvén wave

This test is described by Tóth (2000) where it is used to test a variety of multidimensional MHD schemes in grid based codes. The test involves a circularly polarized Alfvén wave propagating in a two dimensional domain. The advantage of using a circularly (as opposed to linearly) polarized wave is that it turns out to be an exact, non-linear solution to the MHD equations, which means that the solution after one period should exactly match the initial conditions, without the effects of nonlinear steepening (as observed, for example, in the magnetosonic wave tests described in §4.6.4). This also means that the wave can be setup with a much larger amplitude than would be used for purely linear waves.

In Tóth (2000), the wave is setup to propagate at an angle $\theta = 30^\circ$ with respect to the $x-$axis. In SPH the orientation of the wave vector with respect to the co-ordinates is not particularly important because there is no spatial grid. However, we have retained the rotated configuration as firstly it ensures that there are no spurious effects resulting from the initial arrangement of the particles and secondly enables a fair comparison with the results shown in Tóth (2000). The particles are setup on a hexagonal close packed

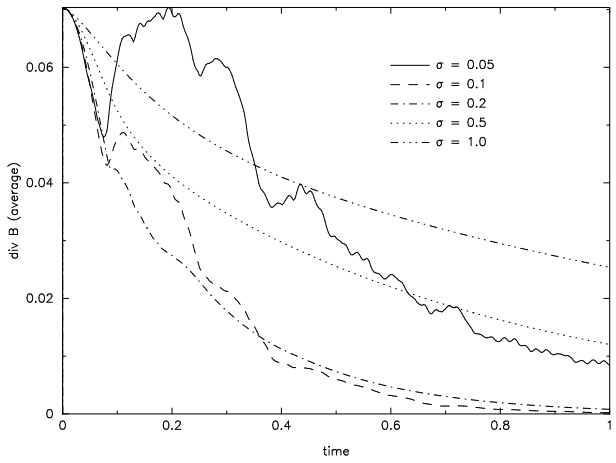

Figure 5.5: Time evolution of the average value of $\nabla \cdot \mathbf{B}$ in the divergence advection problem, varying the diffusion parameter σ. A small amount of diffusion is necessary to remove the divergence error, however as σ is increased the reduction in the divergence lessens as the slow acting diffusion dominates over the rapid spreading produced by the hyperbolic term. The fastest reduction is obtained using $\sigma \sim 0.1 - 0.2$.

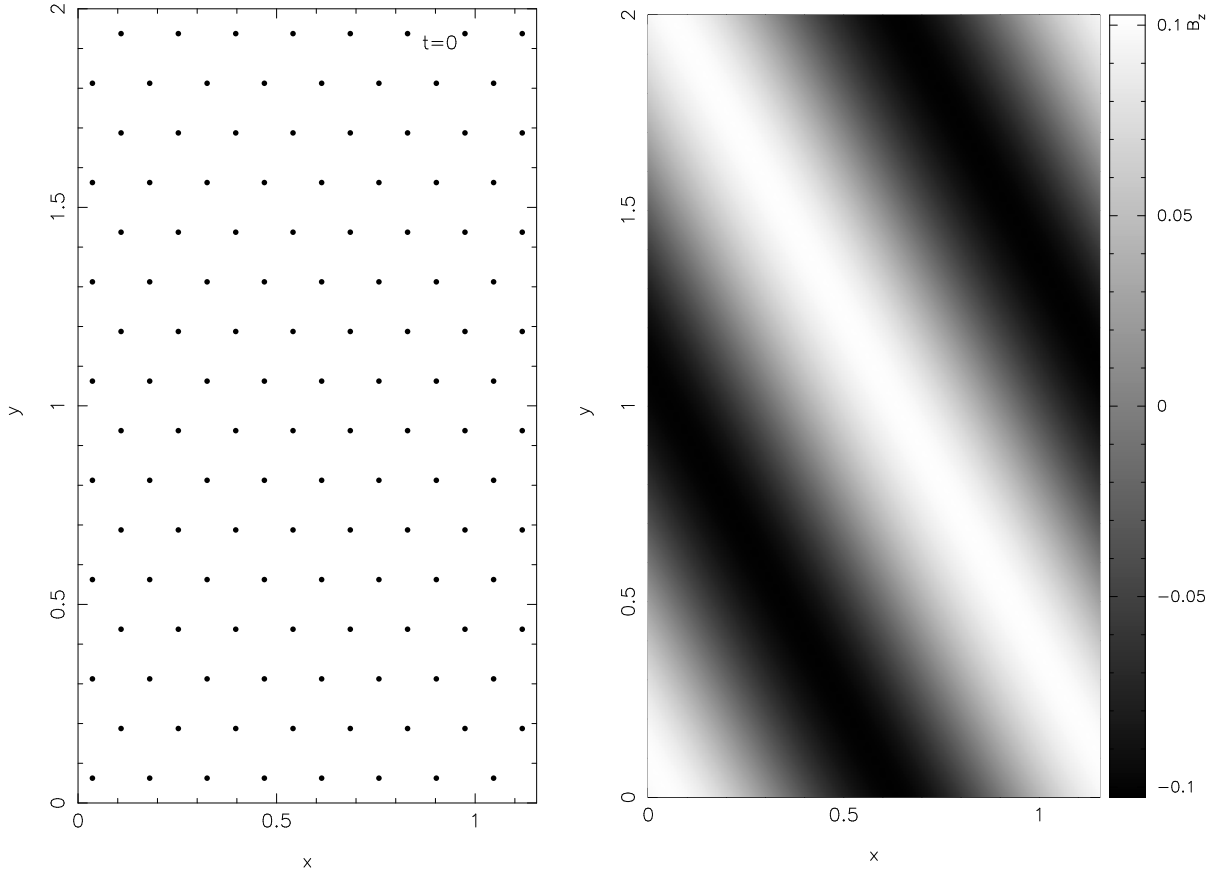

Figure 5.6: Circularly polarized Alfvén wave test. The left figure shows the particle setup in the lowest resolution run. On the right the vertical component of the magnetic field is plotted as a rendered image from the 32×64 particle run at $t = 5$, showing the propagation of the wave with respect to the domain and the particle setup.

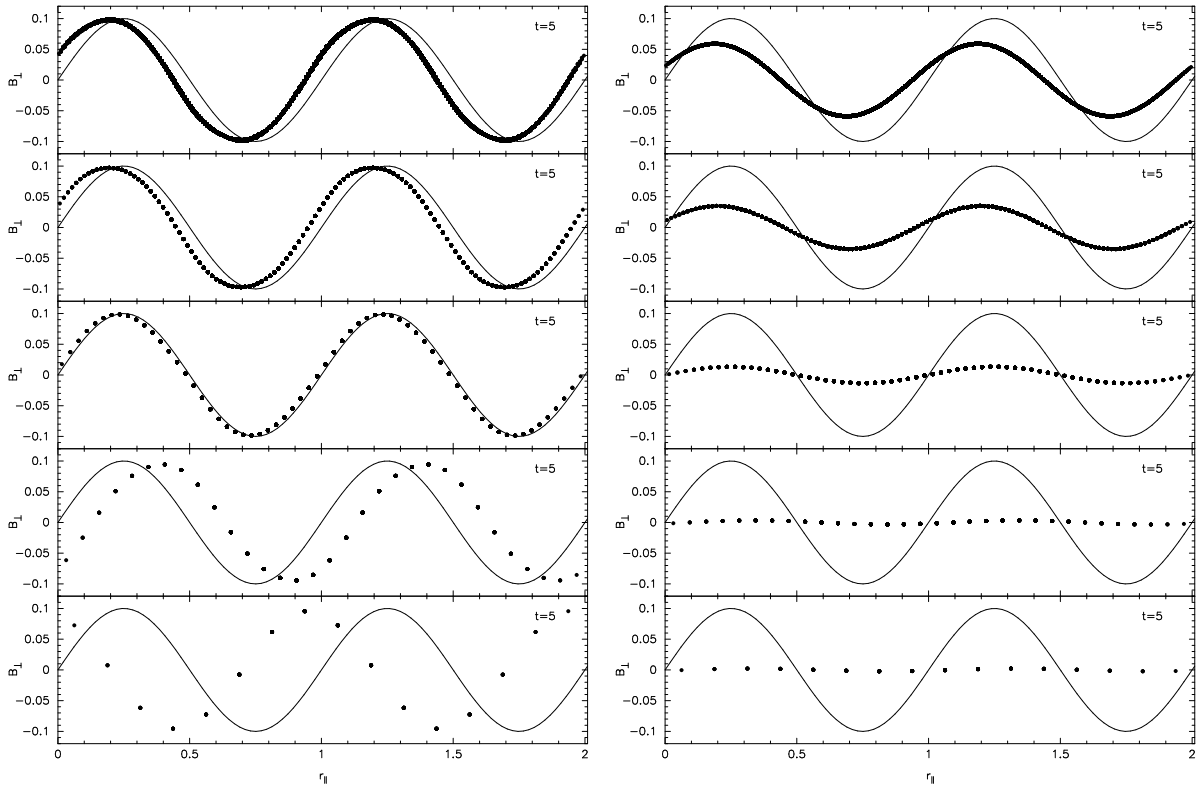

Figure 5.7: Results of the circularly polarized Alfvén wave test at $t = 5$ (corresponding to 5 wave periods). The plots show the perpendicular component of the magnetic field vector $B_\perp = B_y \cos\theta - B_x \sin\theta$ for all of the particles, projected against a vector parallel to the direction of wave propagation $r_\parallel = x\cos\theta + y\sin\theta$ (where $\theta = 30^\circ$ in this case). The SPMHD results are shown at five different resolutions which are, from bottom to top, 8×16, 16×32, 32×64, 64×128 and 128×256. Initial conditions are indicated by the solid line. The numerical results should match these initial conditions at the time shown. The left panel shows the results in the absence of dissipative terms and demonstrates that the SPMHD algorithm contains very little intrinsic numerical dissipation even at low resolutions, although there is a small phase error present even in the converged higher resolution runs. The right hand panel shows the results using the dissipative terms as required in the shock tube problems. In this case the wave amplitude is damped by the artificial resistivity term and exhibits somewhat slow convergence.

lattice (ie. such that particles are equispaced) in a rectangular domain $0 < x < 1/\cos\theta; 0 < y < 1/\sin\theta$. This positioning of the boundaries means that periodic boundary conditions can be used, although some care is required to ensure the continuity of the lattice across the boundaries. This is achieved by stretching the lattice slightly in the $y-$direction to ensure that the boundaries lie at exactly half the spacing of the rows in the lattice. The particle setup at the lowest resolution is shown in the left hand side of Figure 5.6.

The wave is setup with a unit wavelength along the direction of propagation (ie. in this case along the line at an angle of 30° with respect to the x-axis). The initial conditions are $\rho = 1$, $P = 0.1$, $\mathrm{v}_\parallel = 0$, $B_\parallel = 1$, $\mathrm{v}_\perp = B_\perp = 0.1\sin(2\pi r_\parallel)$ and $v_z = B_z = 0.1\cos(2\pi r_\parallel)$ with $\gamma = 5/3$ (where $r_\parallel = x\cos\theta + y\sin\theta$). The $x-$ and $y-$ components of the magnetic field are therefore given by $B_x = B_\parallel\cos\theta - B_\perp\sin\theta$ and $B_y = B_\parallel\sin\theta + B_\perp\cos\theta$ (and similarly for the velocity). Conversely, $B_\parallel = B_y\sin\theta + B_x\cos\theta$ and $B_\perp = B_y\cos\theta - B_x\sin\theta$. Note that this setup means that $\nabla\cdot\mathbf{B} = 0$ holds as a combination of the $\partial B_x/\partial x$ and $\partial B_y/\partial y$ terms, rather than both components being zero individually. The vertical component of the magnetic field after 5 periods is plotted as a rendered image in the right hand side of Figure 5.6, showing

the direction of wave propagation with respect to the domain and the particle setup.

We have performed this test at five different resolutions: 8×16, 16×32, 32×64, 64×128 and 128×256 particles. In each case the number of particles in the y-direction is determined by the hexagonal lattice arrangement. The results are shown in Figure 5.7 after 5 wave periods (corresponding to $t = 5$). The plots show the perpendicular component of the magnetic field $B_\perp$ plotted against $r_\parallel$ for all of the particles in the simulation, with the results from the bottom to top panels shown in order of increasing resolution. In each case the initial conditions are indicated by the solid line which is identical to the exact solution at the time shown. The left hand side of Figure 5.7 shows the results in the absence of dissipative terms (that is with the artificial viscosity, resistivity and thermal conductivity turned off). In this case the amplitude agrees very well with the exact solution even at the lowest resolutions. This demonstrates that SPH has a very low intrinsic numerical dissipation (compare for example with the damping of the wave at lower resolutions in the plots shown in Tóth 2000). However there is a small phase error which remains even in the highest resolution run. This is similar to the phase error observed in the one dimensional sound wave tests presented in §3.7.2 and in the one dimensional magnetosonic waves tests in §4.6.4. In these cases the phase error was found to be essentially removed by accounting for the variable smoothing length terms (§3.3.4,§4.3.6). The results shown in Figure 5.7 incorporate the variable smoothing length terms, however in this case the phase error is not completely removed (although is still an improvement over the results using simple averages of the smoothing lengths or kernel gradients). The right hand side of Figure 5.7 shows the results of this test using the dissipative terms as required in the shock tube problems. In this case the wave is severely damped and convergence of the amplitude towards the exact solution is quite slow. The damping is largely caused by the uniform application of artificial resistivity (ie. using $\alpha_B = 1$ everywhere) resulting in a somewhat large dissipation even in the absence of shocks. Substantially improved results could be obtained using the resistivity switch discussed in §4.5.2, however for the shock tube problems it was found that use of such a switch could result in too little dissipation at rotational discontinuities in the absence of a shear viscosity term. The divergence error remains very small $\left[(\nabla \cdot \mathbf{B})_{max} \sim 10^{-3}\right]$ in all of the simulations shown.

5.3.4 2.5D shock tube

The next two tests are simply two dimensional versions of the one dimensional shock tube tests described in §4.6.3 and demonstrate the effects of divergence errors in the shock capturing scheme. In two dimensions we setup the particles on a cubic lattice in the $x-$direction in the domain $x = [-0.5 - \mathrm{v}_{x(L)} t_{max}, 0.5 - \mathrm{v}_{x(R)} t_{max}]$, where $\mathrm{v}_{x(L)}$ and $\mathrm{v}_{x(R)}$ are the initial velocities assigned to the left and right states. This means that at the time t_{max} the particles are contained in the domain $x = [-0.5, 0.5]$. The domain has a width of 4 particle spacings in the $y-$direction for computational efficiency. Boundary conditions are implemented by fixing the particle properties in two buffer regions at the edges of the $x-$domain, in which particles are evolved with a fixed velocity but copy their properties $(\rho, P, \mathbf{B})$ from the nearest 'active' particle. Periodic boundary conditions are used in the $y-$direction, implemented using ghost particles. The exact position of the $y-$boundary is chosen to ensure periodicity of the lattice arrangement, ie. at half the spacing of the initial rows of particles in the y-direction. The initial shock is setup as a discontinuity in the fluid quantities at $x = 0$ to which no smoothing is applied.

The first shock test is the adiabatic shock tube problem involving seven different discontinuities given

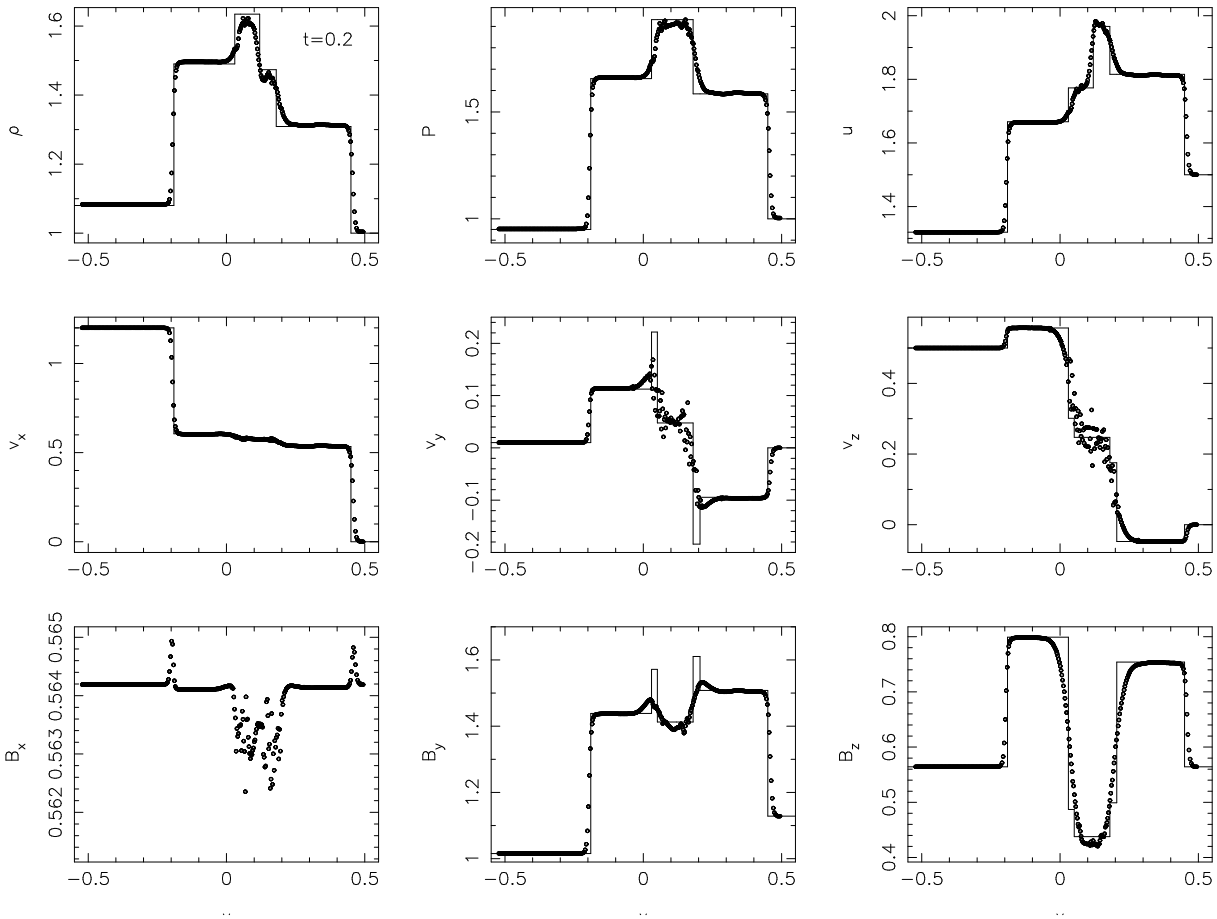

Figure 5.8: Results of the 2.5D shock tube test using an initial smoothing length of $h = 1.2(m/\rho)^{1/2}$ and the dissipative terms as implemented for the one dimensional shock tube problems. In two dimensions at this value of smoothing length small oscillations in the transverse velocity components appear primarily as a result of the non-zero magnetic divergence.

in §4.6.3 (Figure 4.15). Strictly this is a '$2\frac{1}{2}$' dimensional problem since the transverse velocity and magnetic field also have components in the $z-$direction. Conditions to the left of the discontinuity (the left state) are given by $(\rho, P, \mathrm{v}_x, \mathrm{v}_y, \mathrm{v}_z, B_y, B_z) = [1.08, 0.95, 1.2, 0.01, 0.5, 3.6/(4\pi)^{1/2}, 2/(4\pi)^{1/2}]$ whilst to the right (the right state) the conditions are $(\rho, P, \mathrm{v}_x, \mathrm{v}_y, \mathrm{v}_z, B_y, B_z) = [1, 1, 0, 0, 0, 4/(4\pi)^{1/2}, 2/(4\pi)^{1/2}]$ with $B_x = 2/(4\pi)^{1/2}$ everywhere and $\gamma = 5/3$. The problem has been studied by in one dimension by many authors (e.g. Ryu and Jones, 1995; Balsara, 1998) and in two dimensions by Tóth (2000) and Dedner et al. (2002).

The problem is computed using 310×4 particles[5] which corresponds to particle being uniformly spaced on a cubic lattice with separation 0.004, although results are similar using a hexagonal close packed lattice arrangement. Note that this resolution is less than half of that used in the one dimensional case (§4.6.3) but is comparable to, if slightly lower than, the resolutions used in Tóth (2000). The small density difference between the left and right states in this problem is setup by changing the particle masses. The solution using an initial smoothing length of $h = 1.2(m/\rho)^{1/2}$ is shown in Figure 5.8 at $t_{max} = 0.2$ and may be compared with the exact solution taken from Ryu and Jones (1995) (solid line)

[5]Note that this is the number of particles in the domain $-0.5 < x < 0.5$ at $t_{max} = 0.2$ and that the resolution in this domain is correspondingly lower at earlier times due to the inflow boundary condition.

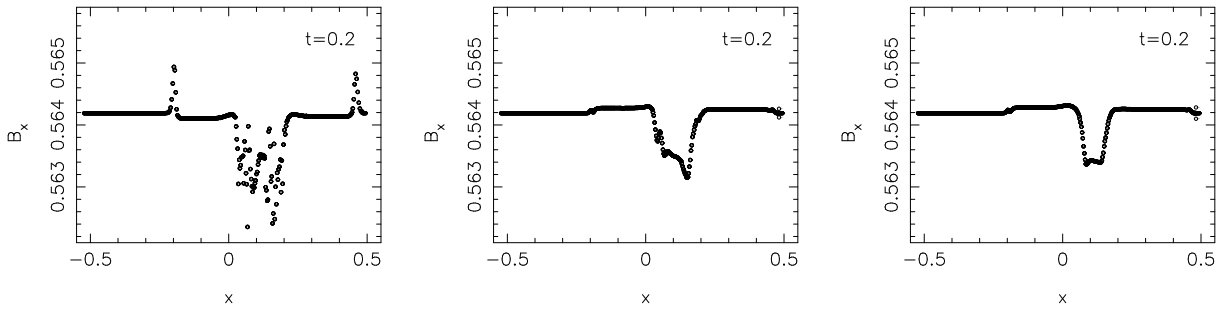

Figure 5.9: The parallel component of the magnetic field in the 2.5D shock tube problem using the dissipative terms as implemented for the 1D problems (left), using the total magnetic energy (centre) and using the total magnetic and kinetic energies (right). Using the total magnetic energy in the dissipative terms means that jumps in the parallel field components are smoothed in addition to the jumps in transverse field. Using the total kinetic energy smooths jumps in the transverse (as well as parallel) velocity components, however this explicitly adds an undesirable shear component to the artificial viscosity term. Details of these formalisms are given in §4.5.

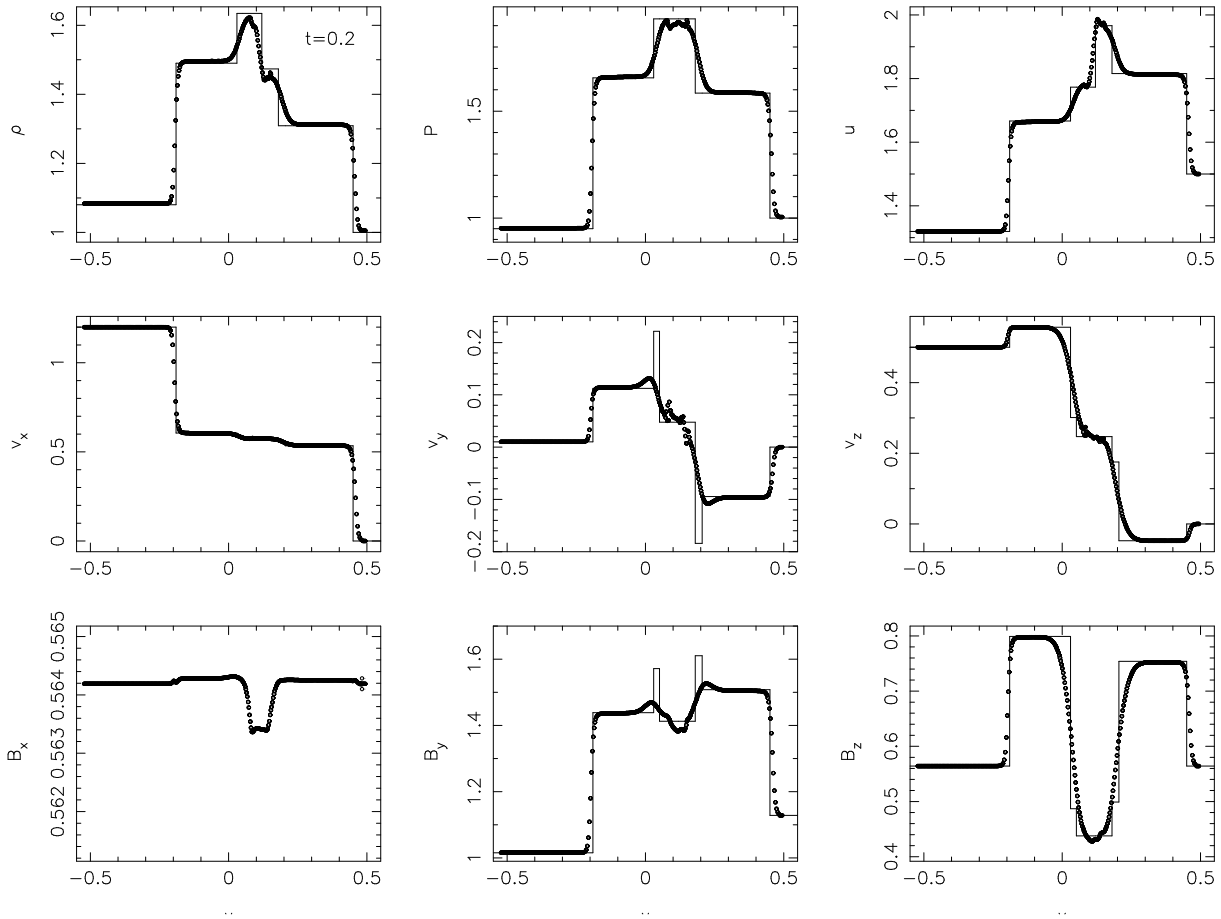

Figure 5.10: Results of the 2.5D shock tube test using an initial smoothing length of $h = 1.2(m/\rho)^{1/2}$ and using the total magnetic and kinetic energies in the dissipative terms as described in §4.5. The oscillations in the transverse velocity components observed in Figure 5.8 are damped in this case by the presence of an additional shear term in the artificial viscosity.

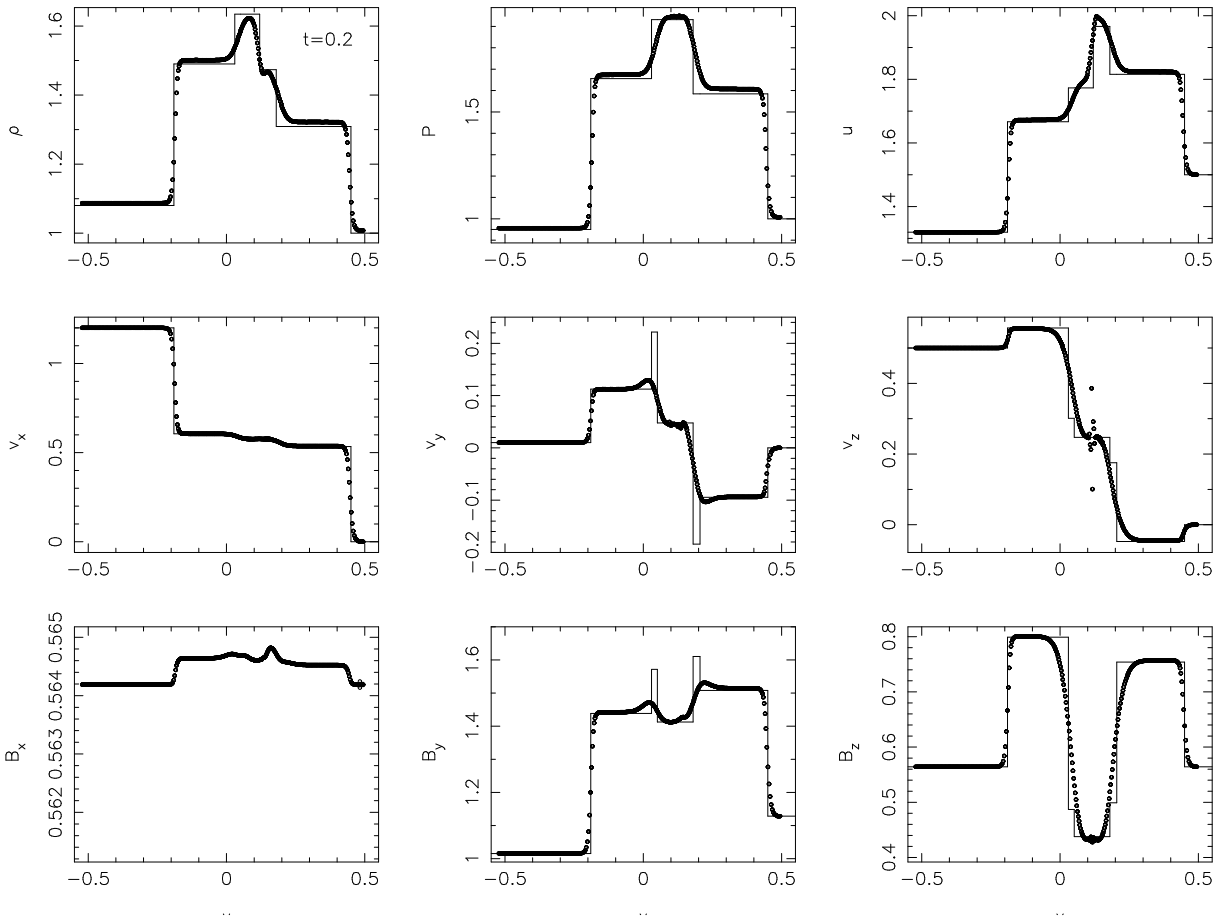

Figure 5.11: Results of the 2.5D shock tube test using a slightly larger initial smoothing length of $h = 1.5(m/\rho)^{1/2}$ and the total magnetic energy in the artificial resistivity term but using the usual artificial viscosity term. The results are a substantial improvement on those presented in Figure 5.8 for a very modest increase in the number of neighbours.

and with the one dimensional results shown in Figure 4.15. In the two dimensional case the transverse velocity components exhibit small oscillations near the contact discontinuity. It should be noted first of all that these oscillations are quite small and do not appear to affect the dynamics significantly (mainly because the jumps in the transverse velocity components are an order of magnitude less than the jump in v_x). However, the oscillations appear to result from a combination of three factors: the unsmoothed initial conditions, the fact that we do not explicitly apply any smoothing to the transverse velocity components and the effects of the small jumps in the $x-$component of the magnetic field.

To remove these oscillations two approaches can be taken: The first approach is to modify the artificial viscosity terms slightly in order to smooth the transverse velocity profiles. The dissipative terms used in order to capture shocks were discussed at length in §3.5, §4.5 and in the one dimensional shock tube tests described in §4.6.3. In the one dimensional case the dissipation terms for MHD (comprising an artificial viscosity, artificial thermal conductivity and artificial resistivity) were derived assuming that jumps would only occur in components of the magnetic field transverse to the line joining the particles that jumps in velocity would only occur parallel to this line. Neither of these assumptions strictly hold in the shock tube problem shown in Figure 5.8 since the transverse velocity components clearly jump and there is also a small jump in the parallel field component due to the divergence errors. A reformulation of the dissipative

terms relaxing both of these assumptions was presented in §4.5.1, deriving the artificial viscosity and artificial resistivity terms from jumps in the total kinetic and magnetic energies respectively in the total energy equation. The effects of using these formulations on the profile of the parallel component of the magnetic field are shown in Figure 5.9. From the centre panel we see that using the total magnetic energy formulation for the artificial resistivity has clear advantages in preventing oscillations in the parallel component of the field at shock fronts. Using the total kinetic energy version of the artificial viscosity (in order to smooth out jumps in the transverse velocity) effectively adds an explicit shear component to the viscosity term. In §4.5.1 it was noted that discontinuities in the transverse velocity components can only occur at corresponding jumps in the magnetic field and therefore that such discontinuities are already smoothed somewhat by the application of artificial resistivity there. For this reason the total kinetic energy formalism was *not* used in one dimension. The results using this formalism for the two dimensional problem are shown in Figure 5.10 in which we see that the oscillations are quite effectively damped. In this case the shear viscosity term has been applied in a minimal way by using the usual artificial viscosity switch (§3.5.2) which responds to $(-)\nabla \cdot \mathbf{v}$ (although since the jumps in transverse velocity are small even the minimum level of $\alpha = 0.1$ away from the shocks is sufficient to damp the oscillations seen). Adding an explicit shear viscosity is, however, highly undesirable since it increases the spurious transport of angular momentum caused by the artificial viscosity term.

The second approach is to simply increase the number of neighbours slightly for each particle to give a more accurate interpolation. The results using an initial smoothing length of $h = 1.5(m/\rho)^{1/2}$ are shown in Figure 5.11 using the total magnetic energy formulation of the artificial resistivity but retaining the usual artificial viscosity formulation. In this case the jump in the parallel field component is much lower and the oscillations in the transverse velocity components do not appear, although there is a small glitch at the contact discontinuity similar to that observed in the one dimensional case (§4.6.3). Increasing the smoothing length from $h = 1.2(m/\rho)^{1/2}$ to $h = 1.5(m/\rho)^{1/2}$ corresponds to an increase in the number of neighbours from ≈ 20 to ≈ 28 on a uniform cubic lattice in two dimensions. This quite a small increase in computational expense for a substantial gain in accuracy (and stability). It therefore seems much more desirable to increase the smoothing length slightly for multidimensional problems rather than to explicit add a shear viscosity term.

Finally, although this problem is not unstable to the clumping instability we have also investigated the effects of various instability correction methods on the shock profile. In particular use of the anticlumping term (§4.4.1) was found to produce additional noise in the shock profile. Using either the Morris formalism for the anisotropic force (§4.4.2) or subtracting the constant component of the magnetic field (§4.4.4) both give results very similar to those shown in Figures 5.8-5.11.

5.3.5 Two dimensional shock tube

The second shock tube test is used by both Tóth (2000) and Dedner et al. (2002) in two dimensions to compare the results of various divergence cleaning schemes, although the one dimensional version of this test has been used by many authors (e.g Dai and Woodward, 1994; Ryu and Jones, 1995). The results of the one dimensional test using the SPMHD algorithm were presented in §4.6.3 (Figures 4.18 and 4.19). Although this is a purely two dimensional test we present it after the 2.5D shock tube since it presents a much more challenging problem with regards to the non-zero divergence of the magnetic field due to the

stronger shocks.

The particle setup is as described in the previous section, except that the initial left state is given by $(\rho, P, \mathrm{v}_x, \mathrm{v}_y, B_y) = [1, 20, 10, 0, 5/(4\pi)^{1/2}]$ and the right state is $(\rho, P, \mathrm{v}_x, \mathrm{v}_y, B_y) = [1, 1, -10, 0, 5/(4\pi)^{1/2}]$ with $B_x = 5.0/(4\pi)^{1/2}$ and $\gamma = 5/3$. The boundaries are correspondingly adjusted in the $x-$direction to allow the particles to fill the domain $-0.5 < x < 0.5$ at $t_{max} = 0.08$. Particles are arranged initially on a cubic lattice with particle spacing 0.004, giving 660 particles in the $x-$direction and a total particle number of $660 \times 4 = 2640$. As in the previous test, the results using an initial smoothing length of $h = 1.2(m/\rho)^{1/2}$ exhibit significant oscillations in the transverse velocity (v_y). In this case the oscillations are substantially worse because the jump in the parallel field component is much larger. Hence we have performed this test using $h = 1.5(m/\rho)^{1/2}$. However, even in this case the oscillations remain present and so we have also added the shear viscosity term, using (4.92) with $\alpha = 1$ everywhere (that is, not using the viscosity switch). The results using these settings are shown in Figure 5.12 and may be compared with the exact solution taken from Dai and Woodward (1994) (solid line) and with the one dimensional results shown in Figure 4.18. Even in this case some oscillations are visible in the v_y profile, corresponding exactly with a spike in $\nabla \cdot \mathbf{B}$. In the $h = 1.2(m/\rho)^{1/2}$ case this spike is much larger [$(\nabla \cdot \mathbf{B})_{max} \sim 40$], causing significantly more disruption to the velocity profile. Thus despite the various tweaks we have attempted for this test, the oscillations appear to be primarily caused by the divergence errors generated at the shocks.

The effects of increasing the number of neighbours and changing the strength of the dissipation terms may be summarised as follows: Increasing the number of neighbours reduces the jumps in the parallel field component (for example with $h = 1.2(m/\rho)^{1/2}$ the jump is given by $\Delta B_x = [B_{x(max)} - B_{x(min)}]/B_{x0} \approx$ 18% whilst for $h = 1.5(m/\rho)^{1/2}$ we have $\Delta B_x \approx 3\%$ and for $h = 1.6(m/\rho)^{1/2}$ this reduces further still to $\Delta B_x \approx 1\%$). On the other hand, adding dissipation at the jumps in parallel field means that although such jumps may be present, the discontinuities (causing strong divergence errors) are smoothed. The effect of adding the shear viscosity term is to increase the dissipation at these discontinuities, thus reducing to some extent the associated spike in the magnetic divergence.

In Tóth (2000) the results of this test were presented using the source term approach of Powell et al. (1999) (discussed in §5.2.1), showing similar jumps in the parallel magnetic field component which were unchanged even in the converged numerical results. The fact that the jumps in parallel field reduce with an increasing number of neighbours indicates that the SPMHD algorithm converges to the exact solution in the limit of $h \to \infty$ and $N \to \infty$ where N is the number of particles. Tóth (2000) attributes the errors in the parallel field components in the Powell method to the non-conservative source terms in the induction equation. We have also performed this simulation using the 'conservative' induction equation (5.38), however we find that the jumps in B_x are not changed significantly by including the $\mathbf{v}\nabla \cdot \mathbf{B}$ term (although contain substantially more numerical noise). We attribute this difference to the fact that we use a non-conservative[6] formulation only in the induction equation, unlike in the Powell method where non-conservative forms are also used in the momentum and energy equations.

The shock tube tests presented above have been computed without using any form of divergence cleaning (other than the consistent formulation of the MHD equations in the presence of magnetic monopoles discussed in §5.2.1). Thus a way of eliminating both the jumps in parallel field and the

[6] where 'non-conservative' means that the volume integral of the flux (4.17) is not conserved exactly.

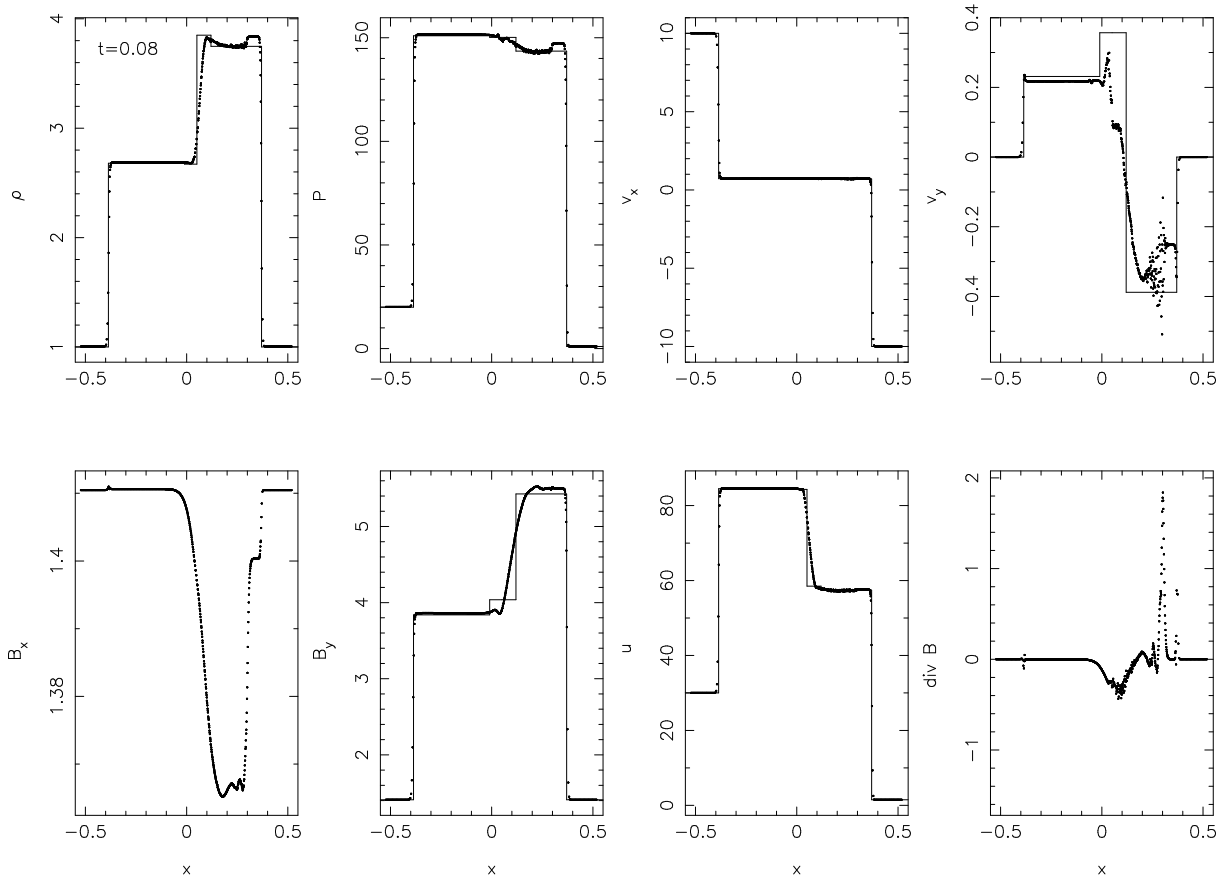

Figure 5.12: Results of the two dimensional shock tube test at $t = 0.08$ using $h = 1.5(m/\rho)^{1/2}$ and the shear viscosity term. The results may be compared with the one dimensional results shown in Figure 4.18 and the exact solution given by the solid line. In this stronger shock tube problem the jumps in the parallel field can cause significant oscillations in the transverse velocity components due to the non-zero divergence terms. Increasing the number of neighbours acts to reduce the jumps in the B_x component of the magnetic field, whilst increasing the dissipation spreads these discontinuities such that the resulting divergence errors are lower.

resulting oscillations in the transverse velocity components is to clean up the divergence error. Using the hyperbolic/parabolic cleaning discussed in §5.2.3 is not particularly effective for this problem, since the divergence errors are propagated away from their source at the fastest wave speed which is similar to the rate at which they are created by the shocks. Thus the diffusion introduced by the parabolic term does not have time to eliminate the divergence error before oscillations in the velocity components are produced. This is illustrated in Figure 5.13 which shows the results using this type of cleaning with $\sigma = 0.1$ on the parabolic term (c.f. §5.3.2). The divergence errors are reduced by a factor of ≈ 2 compared to the results shown in Figure 5.12. In order to eliminate the divergence errors from problems such as this one where divergence errors are created rapidly it would be better to use the projection method (§5.2.2). The projection method is somewhat complicated to implement in this case, however, because of the periodic boundary conditions (although this would not be the case using an iterative scheme as discussed in §5.2.2). An alternative would be to use the 'superfast' hyperbolic cleaning discussed in §5.2.3.

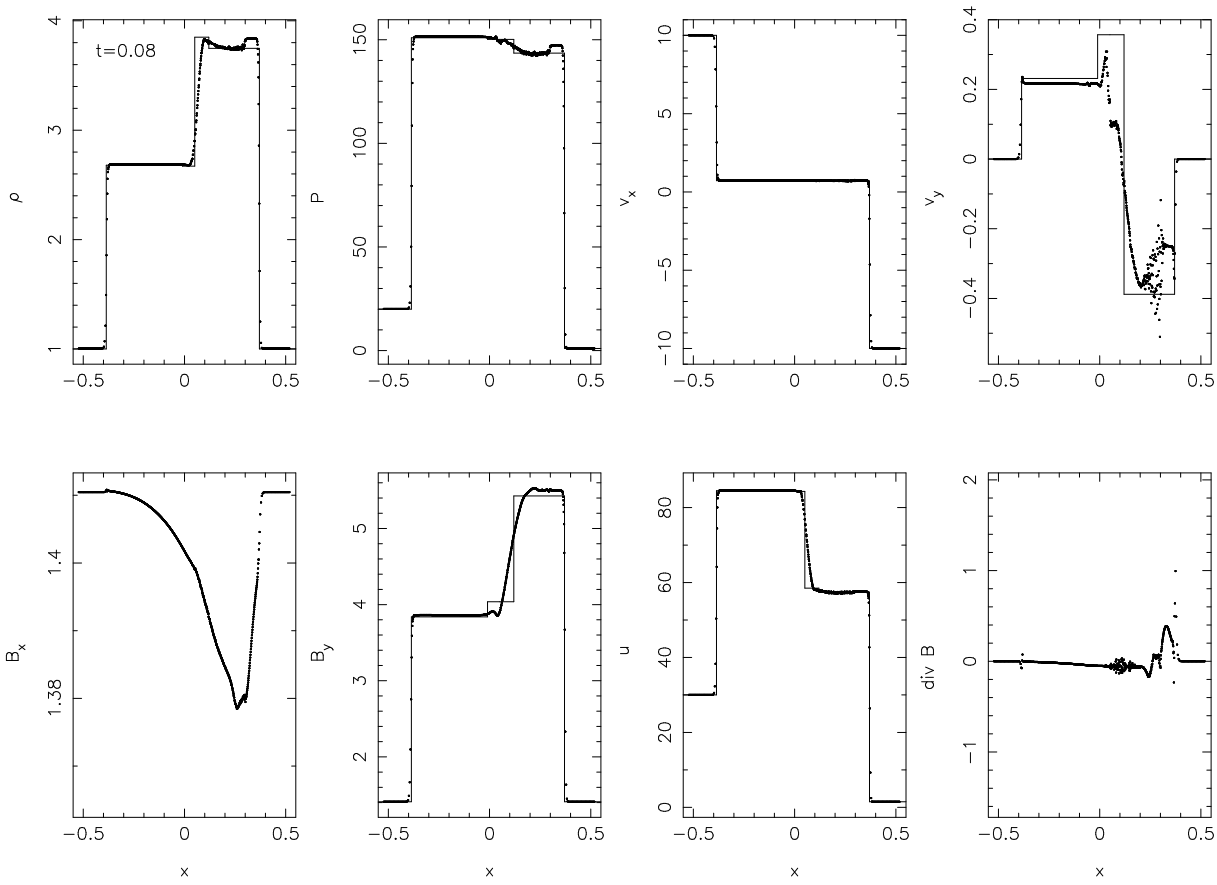

Figure 5.13: Results of the two dimensional shock tube test at $t = 0.08$ computed as in Figure 5.12 but using the hyperbolic/parabolic divergence cleaning (§5.2.3). The exact solution is given by the solid line. The hyperbolic divergence cleaning does not have a large effect on this problem since the divergence errors are propagated at the fastest wave speed which is similar to the rate at which they are generated in the shocks.

5.3.6 Spherical blast waves

Balsara (1998) gives a test involving an adiabatic blast wave propagating in a magnetic medium. Initially the pressure is set to 1000 in a spherical region of radius $r = 0.05$ around the origin in a uniform density box with $P = 1$ elsewhere. The density is initially unity and in the simulation shown we use $\gamma = 1.4$. A constant, uniform field of strength 10G (in code units $B_x = 10/\sqrt{4\pi}$) is setup in the x-direction. We setup this problem using 100×100 particles initially arranged on a cubic lattice in the domain $-0.5 < x < 0.5, -0.5 < y < 0.5$. The results at $t = 0.02$ are shown in Figure 5.14 and may be compared with the numerical solution given in Balsara (1998). The SPMHD results compare very well with the Balsara (1998) solution. In particular the contours of density and pressure show very little scatter, although there are some small effects visible due to the regularity of the initial particle setup.

5.3.7 Orszag-Tang vortex

The final two dimensional test is the compressible Orszag-Tang vortex problem which was first investigated by Orszag and Tang (1979) in order to study incompressible MHD turbulence. The problem was later extended to the compressible case by Dahlburg and Picone (1989) and Picone and Dahlburg (1991).

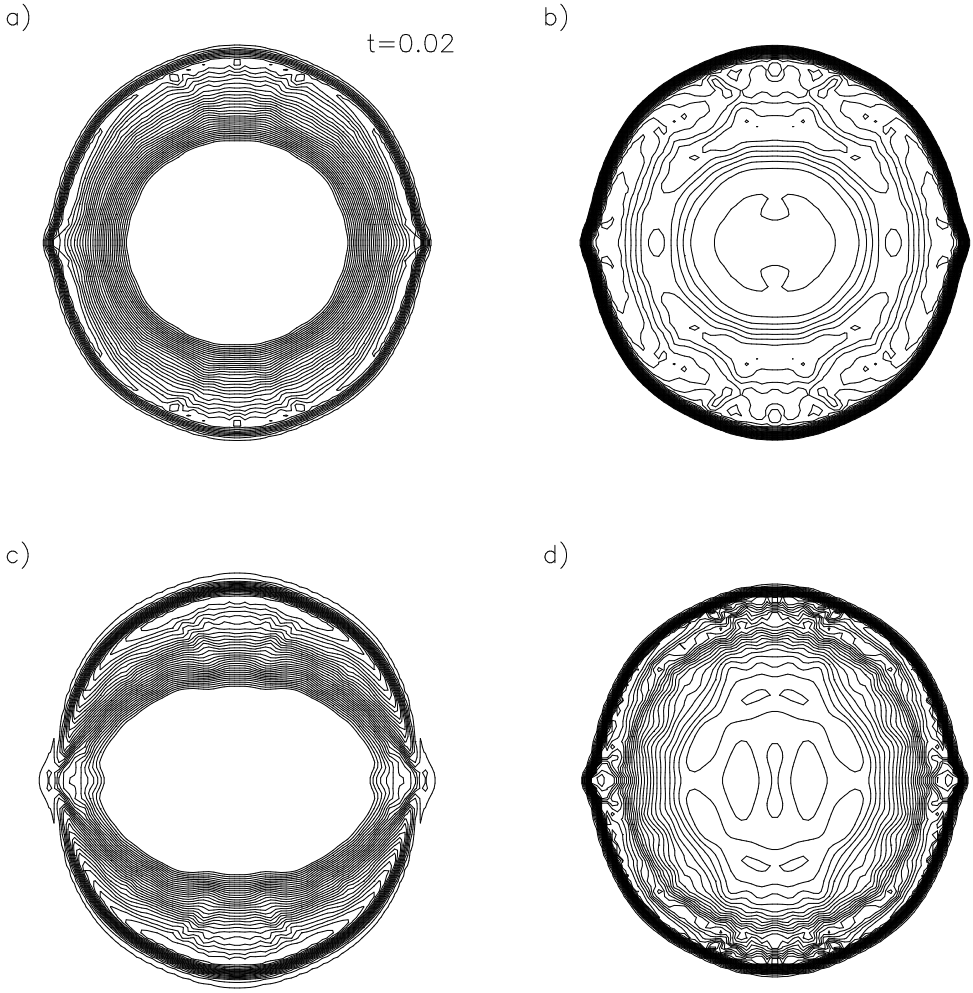

Figure 5.14: Spherical adiabatic MHD blast wave in two dimensions. Plots show: a) logarithm to base 10 of the density; b) logarithm to base 10 of the pressure; c) logarithm to base 10 of the magnetic pressure; d) specific kinetic energy. All plots show 30 contours spaced evenly between the minimum and maximum values of the quantity shown. The results compare extremely well with those shown in Balsara (1998)

More recently it has been widely used as a test problem for multidimensional MHD algorithms (e.g. Ryu et al., 1995; Balsara, 1998; Dai and Woodward, 1998; Londrillo and Del Zanna, 2000; Tóth, 2000).

The setup consists of an initially uniform density, periodic 1×1 box given an initial velocity perturbation $\mathbf{v} = \mathrm{v}_0[-\sin(2\pi y), \sin(2\pi x)]$ where $\mathrm{v}_0 = 1$. The magnetic field is given a doubly periodic geometry $\mathbf{B} = B_0[-\sin(2\pi y), \sin(4\pi x)]$ where $B_0 = 1/\sqrt{4\pi}$. The flow has an initial average Mach number of unity, a ratio of magnetic to thermal pressure of $10/3$ and we use $\gamma = 5/3$. The initial gas state is therefore $P = 5/3B_0^2 = 5/(12\pi)$ and $\rho = \gamma P/\mathrm{v}_0 = 25/(36\pi)$. Note that the choice of length and time scales differs slightly between various implementations in the literature. The setup used above follows that of Ryu et al. (1995) and Londrillo and Del Zanna (2000).

The particles are arranged initially on a uniform hexagonal close packed lattice. This distribution means that the particles are isotropically arranged and is the distribution towards which other arrangements naturally settle. However, results are similar using a cubic lattice arrangement. The simulation is performed using 128×146 particles (where the number of particles in the $y-$direction is determined

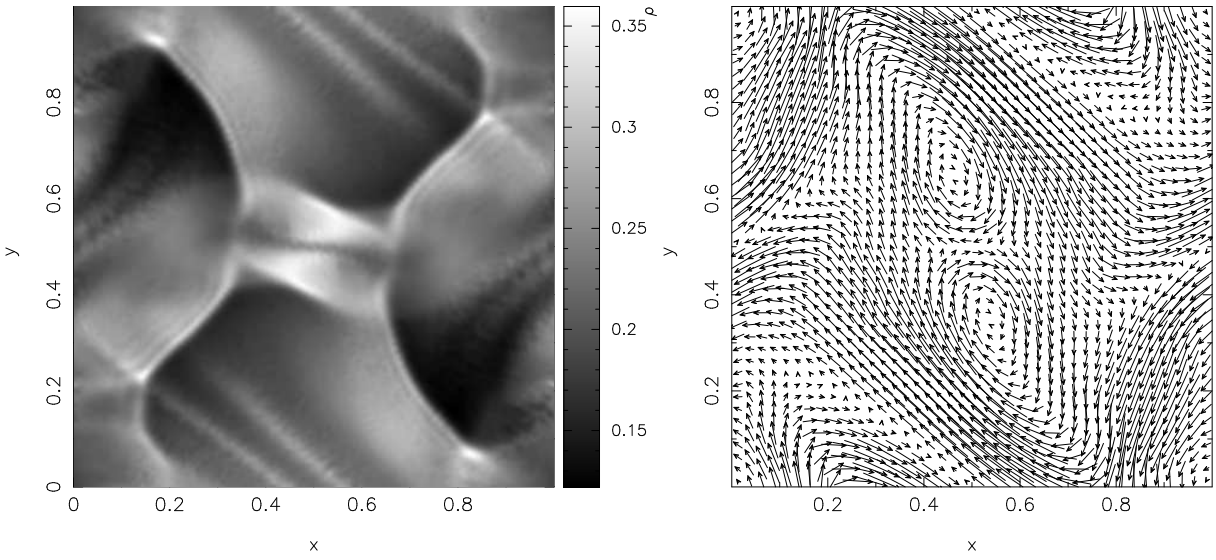

Figure 5.15: Results of the two dimensional Orszag-Tang vortex test, showing the density (left) and magnetic field (right) distribution at $t = 0.5$. The simulation uses 128×146 particles initially arranged on an isotropic hexagonal lattice with periodic boundary conditions. The initial velocity field is a large vortex $\mathbf{v} = [-\sin(2\pi y), \sin(2\pi x)]$ whilst the magnetic field has a doubly periodic geometry $\mathbf{B} = B_0[-\sin(2\pi y), \sin(4\pi x)]$. The SPMHD results are in good qualitative agreement with those presented in (e.g.) Dai and Woodward (1998) and Tóth (2000) although there are some small effects visible in the SPMHD solution due to the distortion of the initial regular lattice arrangement.

by the isotropic lattice arrangement) and the periodic boundary conditions are implemented using ghost particles. Note that this is near the lowest resolution used in Dai and Woodward (1998) (although in SPH the resolution is concentrated preferentially towards regions of high density). The dissipation terms are applied using the artificial viscosity switch and applying the artificial resistivity uniformly. However the artificial thermal conductivity has been turned off for this problem to increase the density resolution. The wall heating effect which the artificial thermal conductivity prevents are discussed in §3.7.3 and are very minor. No shear viscosity term has been used. Simulations of this problem which have been run with or without the variable smoothing length terms, using the Morris formalism for the magnetic force (§4.4.2), evolving either $\mathbf{B}$ or $\mathbf{B}/\rho$ and either the thermal or total energy show essentially no difference in the numerical results.

The results of the density and magnetic field evolution are shown in Figure 5.15 at $t = 0.5$. At this time four shocks are visible which have interacted in the central regions after having crossed the periodic domain. The SPMHD results are in good qualitative agreement with those presented in (e.g.) Dai and Woodward (1994, 1998) and Tóth (2000). In particular the central regions appear to be better resolved than in the 128×128 fixed-grid simulation of Dai and Woodward (1998), although the lower density regions are correspondingly less well resolved. The SPMHD solution shows some small residual effects due to the distortion of the initial regular particle arrangement, noticeable as small ripples behind the shock fronts in Figure 5.15 and a slightly mottled appearance in the low density regions. In Figure 5.15 we have used a smoothing length of $h = 1.5(m/\rho)^{1/2}$ which was found, as in the previous test, to give a substantial improvement in the numerical results over smaller values. In particular the effects from the distortion of the initial lattice are much larger using $h = 1.2(m/\rho)^{1/2}$. With the artificial thermal conductivity term included, the narrow ridges in the density visible near the top and bottom of Figure

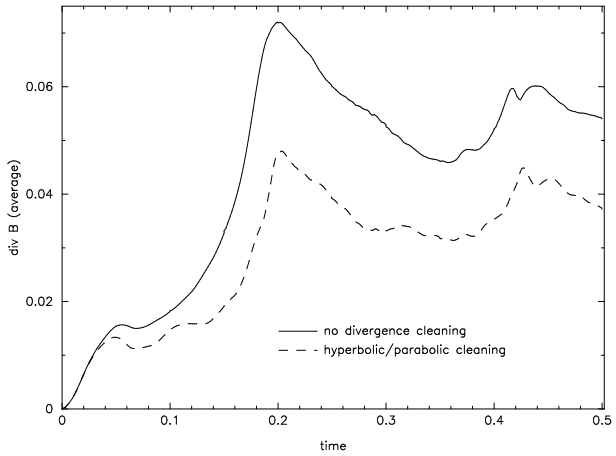

Figure 5.16: Evolution of the average magnetic divergence over the particles in the two dimensional Orszag-Tang vortex problem. Using the hyperbolic divergence cleaning (dashed line) produces only a slight improvement over the results with no divergence cleaning (solid line). The single biggest factor determining the magnitude of the divergence error is the number of neighbours. The results shown are for a smoothing length of $h = 1.5(m/\rho)^{1/2}$.

5.15 are largely smoothed out.

The evolution of the average of the magnetic divergence is shown in Figure 5.16 for two runs with and without divergence cleaning. The results using the hyperbolic/parabolic cleaning with $\sigma = 0.1$ (dashed line) show only a slight improvement ($\sim 30\%$ reduction in the average divergence) over the results with no divergence cleaning (solid line). In fact the single biggest factor which determines the magnitude of the divergence error is the number of neighbouring particles. For example in a simulation using $h = 1.2(m/\rho)^{1/2}$ the divergence errors are approximately twice those shown in Figure 5.16.

5.4 Summary

In this chapter multidimensional aspects of the SPMHD algorithm have been discussed. In particular several methods for maintaining the divergence-free constraint in an SPH context have been presented. Firstly the source term approach of Powell et al. (1999) was outlined and contrasted with the consistent formulation of the MHD (and SPMHD) equations derived in §4.3.2. The major difference between the two approaches is that our approach retains the conservation of momentum and energy whereas the Powell et al. approach does not. The conservation properties of the induction equation were also discussed, in which it was highlighted that using a 'non-conservative' induction equation means that the surface integral of the magnetic flux is conserved, rather than the volume integral. The effect of using the consistent formulation of the MHD equations in the presence of magnetic monopoles (which conserves the surface integral of the flux) is that divergence errors are advected without change by the flow (illustrated in Figure 5.1).

Projection methods for maintaining a divergence free field were discussed in an SPH context in §5.2.2. In particular it was noted that using the Green's function solution to the Poisson equation (as is often used for self-gravity in SPH) provides only an approximate projection. The results using this type of projection on a problem where an initial magnetic divergence was introduced into the simulation were nonetheless very good (§5.3.2). The disadvantages are the substantial computational cost introduced by the solution

of a Poisson equation and for many of the test problems presented in this chapter, the complication introduced by periodic boundary conditions. The potential advantages of using an iterative solution to the Poisson equation were also discussed briefly.

An alternative approach to divergence cleaning suggested recently by Dedner et al. (2002) was discussed in §5.2.3. The method involves adding an additional constraint equation which is coupled to the induction equation for the magnetic field. Chosen appropriately, the effect of this equation is to cause the divergence errors to be propagated in a wave-like manner away from their source (Figure 5.2). Adding a small diffusive term means that the divergence errors are also rapidly reduced to zero. This method is extremely simple to implement and is computationally very inexpensive. The disadvantage is that the error propagation is limited by the timestep condition and, although much faster than using diffusion alone to reduce the divergence, for some problems (for example the shock tube tests given in §5.3.4 and §5.3.5) the cleaning is still not fast enough. However, this method is a substantial improvement over not using any form of divergence cleaning at a negligible additional computational cost.

The various approaches to divergence cleaning were compared in §5.3.2 using a simple test problem in which a non-zero divergence was introduced into the simulation as an initial condition. It was found that using the Dedner et al. (2002) cleaning on this problem could produce results similar to those obtained by taking a projection step every 10 timesteps. It was also noted that the projection method does not conserve the cross-helicity invariant whereas the hyperbolic/parabolic cleaning does.

The SPMHD algorithm was also tested against a variety of multidimensional test problems. A non-linear circularly polarized Alfvén wave was studied in §5.3.3. This test showed that SPMHD has a very low intrinsic numerical dissipation compared to grid based codes, although this property is destroyed by the addition of explicitly dissipative terms for shock-capturing which can cause quite slow convergence on problems where the physical dissipation timescale is of critical importance. Two of the shock tube problems used in the one-dimensional case were examined in two dimensions in §5.3.4 and 5.3.5. For these problems jumps in the component of the magnetic field parallel to the shock front (causing divergence errors) were found to result in oscillations in the transverse velocity profiles. The jumps in the parallel field component were found to decrease as the number of neighbours for each particle was increased, unlike in the Powell et al. method in which the jumps remain unchanged even in the numerically converged results (Tóth, 2000). The corresponding divergence errors produced by these jumps could be reduced by using a form of the dissipative terms derived in §4.5.1 using the total jump in magnetic and kinetic energies. Modifying the artificial viscosity term in this manner results in the addition of an explicit shear viscosity component. It is therefore somewhat undesirable to do so since this can result in excess spurious angular momentum transport elsewhere. A better approach would be to use divergence cleaning to prevent these errors from occurring. However, the hyperbolic cleaning was not found to be particularly effective for this problem because of the restriction to the fastest wave speed and implementation of the projection method is complicated by the periodic boundary conditions. These difficulties are not, however, insurmountable. The single biggest factor in determining the magnitude of the divergence errors in the shock tube tests was found to be the size of the smoothing region (ie. the number of contributing neighbours). It therefore seems advantageous to use a slightly larger number of neighbours for MHD problems (typically $h \gtrsim 1.5(m/\rho)^{1/\nu}$ where ν is the number of spatial dimensions) than might otherwise be used for hydrodynamics.

An initially spherical MHD blast wave test was given in §5.3.6, with good results. Finally the algo-

rithm was tested on the Orszag-Tang vortex problem (§5.3.7) which has been widely used as a benchmark for MHD codes. The SPMHD result were in good qualitative agreement with those presented elsewhere. This test again highlighted the need for a slightly larger number of neighbours, in this case to remove spurious effects related to the initial lattice arrangement and to reduce the magnitude of the divergence errors. The hyperbolic/parabolic divergence cleaning was found to produce only a small ($\sim 30\%$) reduction in the divergence errors, again highlighting the need for some form of sub-timestep cleaning (for example using the projection method).

Unfortunately there was neither the time nor the space in this thesis to benchmark the SPMHD algorithm against the many wonderful exact solutions which can be derived for multidimensional magnetic toy stars.

"I hope we get to the bottom of the answer. It's what I'm interested to know"

GEORGE W. BUSH

6 Conclusions

In the introductory chapter (Chapter 1) the importance of magnetic fields in many astrophysical problems was highlighted. In this final chapter we summarise the results contained in this thesis and discuss ways in which the work can be applied and extended in order to provide answers to some of these problems.

6.1 Summary

In Chapter 2 we have used simple physical models in order to compare the mechanisms for jet acceleration in both relativistic (pertaining to AGN jets) and non-relativistic (pertaining to jets produced in Young Stellar Objects) environments. Time-dependent, spherically symmetric wind models in Newtonian and relativistic gravitational fields were used to examine whether or not the observed jet velocities in both classes of object could be reconciled to a common (appropriately scaled) energy input rate. It was found that the energy input rate required to produce observed outflow velocities of $v_{\rm jet} \simeq 2v_{\rm esc}$ in the Newtonian (YSO) case could give rise to outflows with a Lorentz factor $\gamma_{\rm jet} \simeq 11$ in the strongly relativistic case (as observed in AGN jets). Thus it was concluded that it is not unreasonable to suggest, on the basis of the simple physical models employed, that the relativistic jets observed in AGN are simply scaled-up versions of their non-relativistic (YSO) counterparts and that the intrinsic acceleration process is the same in both classes of object. For this to be the case, two further conditions were required. The first was that jet acceleration must occur close to the central gravitating object, in order to make use of the speed of light as a limiting velocity in the black hole case. The second was that, since the dimensionless heating rates required are much larger than unity, the energy released in the outflow must be imparted to only a small fraction of the available accreting material.

The remainder of the thesis was dedicated to the accurate numerical simulation of magnetic fields in an astrophysical context using the Smoothed Particle Hydrodynamics (SPH) method. A thorough review of the SPH algorithm was presented in Chapter 3. Various aspects of the algorithm were considered

in detail, including the choice of smoothing kernel, the evaluation of first and second derivatives, the self-consistent formulation of the discrete equations from a variational principle and the more accurate formulation which can be derived by incorporating terms relating to the spatial variation of the smoothing length (the 'variable smoothing length terms'). Artificial dissipation terms were used in order to capture shocks and in particular the potential advantages of introducing a small artificial thermal conductivity were discussed. Switches were proposed to reduce the spurious effects of the dissipative terms away from shocks. The hydrodynamic algorithm was tested against a variety of problems, including linear waves, shocks, Cartesian shear flows and on a class of exact non-linear solutions known as 'Toy Stars', in which various effects were highlighted.

In Chapter 4 the SPH algorithm was extended to the MHD case. Particular attention was paid to the self-consistent formulation of the discrete equations (achieved using a variational principle) which is important in the MHD case due to the presence of terms proportional to the divergence of the magnetic field which are in general non-zero in a numerical context. Consistent alternative formulations of the SPMHD equations were also derived as well as formulations incorporating the variable smoothing length terms. Stability considerations were extensively discussed, with a variety of solutions to the known instability associated with an exactly momentum-conserving form of the SPMHD force in the presence of tension forces examined. An approach suggested by Monaghan (2000) for solid mechanics problems was extensively investigated, although not found to be universally effective for astrophysical problems due to the spatial variations in the smoothing length. The best approaches to eliminate the tensile instability were found to be either to subtract any constant field components from the gradient terms in the magnetic force or to use a simple modification of the anisotropic force term due to Morris (1996) which retains the conservation of momentum in a continuum sense although not discretely. Dissipative terms for shock capturing analogous to those used in the SPH case were derived which ensure a positive definite contribution to the entropy and thermal energy. The shock capturing abilities of the resulting algorithm were extensively tested against a variety of one dimensional shock tube problems used to test recent grid-based MHD codes. Linear wave tests were also presented which highlighted the increased accuracy resulting from inclusion of the variable smoothing length terms.

Finally, multidimensional aspects of the SPMHD algorithm were examined in Chapter 5. Various methods for maintaining the divergence-free condition in an SPH context were discussed, including the consistent formulation of the MHD equations in the presence of magnetic monopoles (the 'source term' approach), projection methods and a hyperbolic divergence cleaning recently proposed by Dedner et al. (2002). Using an approximate projection method based on the Green's function solution to Poisson's equation was found to give good results, although the method is computationally expensive and difficult to implement in the case of periodic boundary conditions. The hyperbolic approach was found to be particularly simple and efficient to implement but limited in some problems in which divergence errors are generated very quickly by the flow. Various multidimensional numerical tests used to test recent grid-based MHD algorithms were also presented, including a divergence advection problem, non-linear circularly polarized Alfvén waves, two dimensional shock tubes, spherically symmetric blast waves and the Orszag-Tang vortex problem. Particular attention was paid to the divergence errors resulting in these problems. The single biggest factor in determining the magnitude of the divergence errors in a given simulation was found to be the size of the smoothing region (ie. the number of contributing neighbours). It was therefore concluded that a slightly larger number of neighbours should be used for MHD problems

(typically $h \gtrsim 1.5(m/\rho)^{1/\nu}$ where ν is the number of spatial dimensions).

6.2 Future work: Applications

6.2.1 Star formation

Understanding the role of magnetic fields in star formation involves two distinct but not inseparable issues. The first is the role that magnetic fields, in the form of compressible MHD turbulence, play in the support of molecular clouds against collapse. Related to this issue is to determine the timescale on which the initial turbulent spectrum of the molecular cloud dissipates in order to allow collapse to occur. The second issue is the role of magnetic fields in the collapse phase, ie. during formation of cores (via fragmentation) and particularly their role in angular momentum transport and feedback (by generating outflows). The first problem has been the subject of a substantial research effort over the past decade, primarily enabled by the development of accurate algorithms for MHD simulations within grid-based codes. However, the latter problem has received surprisingly little attention, mainly due to the difficulty of implementing adaptive mesh refinement procedures and incorporating new physics (such as changes in the equation of state) into grid-based MHD codes which rely on complicated shock-capturing procedures. Furthermore even with adaptive meshes, using Cartesian grids on problems which are highly asymmetric presents some difficulty due to the substantial numerical transport of angular momentum.

Although the turbulence simulations seem to indicate that magnetic fields do not play the dominant role in core formation and support of clouds, their role in other parts of the star formation process remains unknown. An issue of key importance is whether magnetic fields control the overall star formation efficiency in molecular clouds, or whether this is due to other processes such as radiative or mechanical feedback from massive protostars. Most of the gas in hydrodynamic collapse simulations (e.g. Bate et al., 2003) is accreted on a free-fall timescale, leading to a discrepancy with observed lifetimes of molecular clouds which may be resolved by the support provided by MHD turbulence to low density regions of the cloud (so that not all the gas would fall onto the protostars). Magnetic fields are often invoked to solve the angular momentum problem via magnetic braking of cores. Some calculations indicate that such angular momentum transport may make it difficult to form binaries from collapsing magnetic cores (Hosking, 2002), although only a few different cases were considered and the calculations did not involve turbulent initial conditions. Other calculations (e.g. Boss 2000, 2002) suggest that magnetic fields may enhance fragmentation, however these calculations use only an approximate treatment of MHD forces. Magnetic fields are the most likely mechanism for the production of jets and outflows commonly observed in star forming regions.

The algorithm developed for SPMHD within this thesis is ideally suited to star formation problems, since the adaptivity is a built-in feature of the numerics and resolution is automatically concentrated in regions of high density which is where the stars form. The use of sink particles in SPH (Bate et al., 1995) has enabled simulations to be followed beyond the point where stars form to study the subsequent accretion and dynamics which turn out to be crucial in determining the final properties of the newborn stars (such as their mass). Ultimately the aim would be to answer both questions self-consistently by following the collapse from the initial turbulent decay all the way to the formation of stars and beyond. Purely hydrodynamic simulations of this type have been performed recently by Bate et al. (2003) and

succeed remarkably well in predicting the statistical properties of the stars which form. An MHD version of these simulations would be highly desirable. However, some caution is required in simulating the initial turbulent decay using the SPMHD algorithm described here because the physical dissipation time of the MHD turbulence is quite important and this may be difficult to disconnect from the effects of the artificial dissipation terms employed for shock capturing (at the very least it must be shown that the numerical results are converged). Thus SPMHD may, in the short term at least, be best suited to answering the second question, that is, what effects do magnetic fields have on fragmentation and in providing angular momentum transport and feedback in star forming cores? Preliminary calculations exploring these questions are currently being performed using a version of the SPMHD algorithm incorporated into a 3D SPH code which has been used for many of the hydrodynamic star formation calculations (Bate, 1995).

6.2.2 Neutron star mergers

Compact binary systems consisting of two neutron stars will eventually spiral towards each other and merge due to the energy and angular momentum loss caused by the emission of gravitational waves. The coalesced central object resulting from the merger is probably too massive to form a single neutron star, whilst the substantial angular momentum prevents the merger remnant being swallowed immediately by the black hole. Thus the most likely scenario is the formation of a single black hole surrounded by a disc-like merger remnant from which matter is accreted. The dynamics of this problem present a severe challenge for numerical simulation, not least because the gravitational dynamics are strongly relativistic and ultimately require the full solution of Einstein's equations. Whilst a significant research effort is directed towards the gravitational side of the problem (with recent promising results by Shibata and Ury$\bar{\text{u}}$ 2000), the astrophysical aspects are equally challenging, drawing on almost every field of astrophysics. The problem is important firstly because such events are known to occur regularly in sufficient numbers to present a substantial background of gravitational wave sources which may be detected with the next (or perhaps even current) generation of gravitational wave detectors.

From an astrophysical perspective Rosswog and Davies (2002) have presented detailed numerical simulations of this problem using SPH incorporating many aspects of the microphysics, including a detailed nuclear equation of state and neutrino emission of all flavours. SPH has significant advantages over grid-based methods for this problem, in particular the spurious numerical transport of angular momentum is much lower and the stars do not have to be embedded in an artificial background medium which can cause artificial shock waves at the stellar surfaces (e.g. the simulations of Ruffert and Janka, 2001, using a nested-grid code based on the Piecewise Parabolic Method). However a major piece of physics missing from the simulations is the magnetic field. Magnetic fields may play a decisive role in determining, via the transport of angular momentum, whether or not the central coalesced object collapses into a black hole (and if so the timescale on which this occurs). If the central object can remain stabilised against collapse for a substantial length of time, estimates by Rosswog et al. (2003) suggest that magnetic fields could wind up by differential rotation in the merger remnant to strengths of up to $\sim 10^{17}$G (depending on the rotation period). Such field strengths would provide the conditions required for magnetically powered Gamma-Ray Bursts. The implementation of the SPMHD algorithm described in this thesis enables such possibilities to be explored.

6.2.3 Accretion discs

Another area to which we intend to apply the SPMHD algorithm is in the simulation of accretion discs. SPH is widely used to simulate accretion disc phenomena, particularly in mass-transferring binary systems where the dynamics of the disc can be extremely complicated due to the tidal influence of the secondary (Murray, 1996). SPH has also been used to study gravitational instabilities in discs (Lodato and Rice, 2004), to study planet-disc interactions (e.g. Schäfer et al., 2004) and to study accretion discs around black holes (e.g. Molteni et al., 1994). However in all of these simulations the transport of angular momentum is induced by introducing a viscosity term similar to the original Shakura and Sunyaev (1973) parametrization. Whilst this is a useful approach, primarily because of its simplicity, it would be very interesting to study the dynamics of the magnetic field in such accretion discs, particularly with respect to the Magneto-Rotational Instability (MRI) which is believed to provide the main source of angular momentum transport.

6.3 Future work: Algorithms

In addition to applying SPMHD to interesting physical problems there are many aspects of the algorithm which can be improved and extended. In particular we intend to investigate the following:

- Extension of the algorithm to non-ideal MHD. There are many astrophysical problems in which non-ideal effects become important, such as the Hall effect and the effects of ion-neutral diffusion. The latter has been implemented using a two-fluid SPMHD code by Hosking and Whitworth (2004).

- Combining the algorithm with other physics. In particular it is our intention to merge the SPMHD code with the algorithms of Whitehouse and Bate (2004) for radiative transfer in SPH in order to study star formation related problems.

- A General Relativistic implementation. Algorithms for SPH on a fixed background metric have been presented by Monaghan and Price (2001). However many of the interesting fixed-metric problems also involve magnetic fields (for example in studying accretion flows onto black holes). A General Relativistic version would also be useful for the implementation of the algorithm in different co-ordinate systems.

- Better ways of maintaining the divergence-free constraint. Several approaches to maintaining the divergence-free condition relevant in an SPH context were discussed in Chapter 5, however many other approaches are also possible and it would be interesting to investigate and compare such possibilities.

- Improvements to the shock capturing scheme. In particular it would be highly desirable to eliminate the use of artificial dissipation terms in order to capture shocks. Simple methods for incorporating Godunov-type schemes into SPH have been presented recently by Cha and Whitworth (2003). Whilst the Riemann problem is much more complicated in the MHD case an implementation of a Godunov-type scheme for SPMHD would be extremely useful.

Appendix A
Discretization scheme for non-relativistic equations

The discretization scheme used in Chapter 2 for the non-relativistic fluid equations is summarised in Figure 2.1. Fluxes are calculated on the half grid points while the other terms are calculated on the integer points. We solve (2.1)-(2.5) in the following manner: The numerical equations are solved first for velocity on the half grid points (dropping the superscript r for convenience),

$$\begin{aligned} \mathrm{v}_{i+1/2}^{n+1} &= \mathrm{v}_{i+1/2}^{n+1} - \Delta t \left[\mathrm{v}_{i+1/2}^{n} \left(\frac{\mathrm{v}_{i+3/2}^{n} - \mathrm{v}_{i+1/2}^{n}}{r_{i+3/2} - r_{i+1/2}} \right) - \frac{1}{\rho_{i+1/2}^{n}} \left(\frac{P_{i+1}^{n} - P_{i}^{n}}{r_{i+1} - r_{i}} \right) - \frac{1}{r_{i+1/2}^{2}} \right] \quad (\mathrm{v} < 0) \\ &= \mathrm{v}_{i+1/2}^{n+1} - \Delta t \left[\mathrm{v}_{i+1/2}^{n} \left(\frac{\mathrm{v}_{i+1/2}^{n} - \mathrm{v}_{i-1/2}^{n}}{r_{i+3/2} - r_{i+1/2}} \right) - \frac{1}{\rho_{i+1/2}^{n}} \left(\frac{P_{i+1}^{n} - P_{i}^{n}}{r_{i+1} - r_{i}} \right) - \frac{1}{r_{i+1/2}^{2}} \right] \quad (\mathrm{v} > 0) \end{aligned} \tag{A.1}$$

where the superscript n refers to the nth timestep and the subscript i refers to ith grid point ($\mathrm{v}_{i+1/2}$,$\rho_{i+1/2}$ thus being points on the staggered velocity grid). The quantity $\rho_{i+1/2}$ is calculated using linear interpolation between the grid points, ie. $\rho_{i+1/2} = \frac{1}{2}(\rho_i + \rho_{i+1})$. We then solve for the density and internal energy on the integer grid points using the updated velocity,

$$\begin{aligned} \rho_{i}^{n+1} &= \rho_{i}^{n} - \Delta t \left[\mathrm{v}_{i}^{n+1} \left(\frac{\rho_{i+1}^{n} - \rho_{i}^{n}}{r_{i+1} - r_{i}} \right) - \frac{\rho_{i}^{n}}{r_{i}^{2}} \left(\frac{r_{i+1/2}^{2} \mathrm{v}_{i+1/2}^{n+1} - r_{i-1/2}^{2} \mathrm{v}_{i-1/2}^{n+1}}{r_{i+1/2} - r_{i-1/2}} \right) \right] \quad (\mathrm{v} < 0) \\ &= \rho_{i}^{n} - \Delta t \left[\mathrm{v}_{i}^{n+1} \left(\frac{\rho_{i}^{n} - \rho_{i-1}^{n}}{r_{i} - r_{i-1}} \right) - \frac{\rho_{i}^{n}}{r_{i}^{2}} \left(\frac{r_{i+1/2}^{2} \mathrm{v}_{i+1/2}^{n+1} - r_{i-1/2}^{2} \mathrm{v}_{i-1/2}^{n+1}}{r_{i+1/2} - r_{i-1/2}} \right) \right] \quad (\mathrm{v} > 0) \end{aligned} \tag{A.2}$$

and similarly,

$$\begin{aligned} \rho u_{i}^{n+1} &= \rho u_{i}^{n} - \Delta t \left[\mathrm{v}_{i}^{n+1} \left(\frac{\rho u_{i+1}^{n} - \rho u_{i}^{n}}{r_{i+1} - r_{i}} \right) - \left[\frac{P_{i}^{n} + \rho u_{i}^{n}}{r_{i}^{2}} \right] \left(\frac{r_{i+1/2}^{2} \mathrm{v}_{i+1/2}^{n+1} - r_{i-1/2}^{2} \mathrm{v}_{i-1/2}^{n+1}}{r_{i+1/2} - r_{i-1/2}} \right) + \rho_{i}^{n} \Lambda_{i} \right] \quad (\mathrm{v} < 0) \\ &= \rho u_{i}^{n} - \Delta t \left[\mathrm{v}_{i}^{n+1} \left(\frac{\rho u_{i}^{n} - \rho u_{i-1}^{n}}{r_{i} - r_{i-1}} \right) - \left[\frac{P_{i}^{n} + \rho u_{i}^{n}}{r_{i}^{2}} \right] \left(\frac{r_{i+1/2}^{2} \mathrm{v}_{i+1/2}^{n+1} - r_{i-1/2}^{2} \mathrm{v}_{i-1/2}^{n+1}}{r_{i+1/2} - r_{i-1/2}} \right) + \rho_{i}^{n} \Lambda_{i} \right] \quad (\mathrm{v} > 0) \end{aligned}$$

where $\Delta t = t^{n+1} - t^{n}$ and the timestep is regulated according to the Courant condition

$$\Delta t < \frac{\min(\Delta r)}{\max(|\mathrm{v}|) + \max(c_s)} \tag{A.3}$$

where c_s is the adiabatic sound speed in the gas given by $c_s^2 = \gamma P/\rho$. We typically set Δt to half of this value.

Appendix B
SPH stability analysis

In this appendix we perform a stability analysis of the standard SPH formalism derived in §3.3. Since the SPH equations were derived directly from a variational principle, the linearised equations may be derived from a second order perturbation to the Lagrangian (3.46), given by

$$\delta L = \sum_b m_b \left[\frac{1}{2} \mathrm{v}_b^2 - \delta\rho_b \frac{du_b}{d\rho_b} - \frac{(\delta\rho_b)^2}{2} \frac{d^2 u_b}{d\rho_b^2} \right] \tag{B.1}$$

where the perturbation to ρ is to second order in the second term and to first order in the third term. The density perturbation is given by a perturbation of the SPH summation (3.42), which to second order is given by[1]

$$\delta\rho_a = \sum_b m_b \delta x_{ab} \frac{\partial W_{ab}}{\partial x_a} + \sum_b m_b \frac{(\delta x_{ab})^2}{2} \frac{\partial^2 W_{ab}}{\partial x_a^2} \tag{B.2}$$

The derivatives of the thermal energy with respect to density follow from the first law of thermodynamics, ie.

$$\frac{du}{d\rho} = \frac{P}{\rho^2}, \qquad \frac{d^2 u}{d\rho^2} = \frac{d}{d\rho}\left(\frac{P}{\rho^2}\right) = \frac{c_s^2}{\rho^2} - \frac{2P}{\rho^3}$$

The Lagrangian perturbed to second order is therefore

$$\delta L = \sum_b m_b \left[\frac{1}{2} \mathrm{v}_b^2 - \frac{P_b}{\rho_b^2} \sum_c m_c \frac{(\delta x_{bc})^2}{2} \frac{\partial^2 W_{bc}}{\partial x_a^2} - \frac{(\delta\rho_b)^2}{2\rho_b^2} \left(c_s^2 - \frac{2P_b}{\rho_b} \right) \right] \tag{B.3}$$

The perturbed momentum equation is given by using the perturbed Euler-Lagrange equation,

$$\frac{d}{dt}\left(\frac{\partial L}{\partial \mathrm{v}_a}\right) - \frac{\partial L}{\partial(\delta x_a)} = 0. \tag{B.4}$$

where

$$\frac{\partial L}{\partial \mathrm{v}_a} = m_a \mathrm{v}_a \tag{B.5}$$

[1] Note that the first order term may be decoded into continuum form to give the usual expression

$$\delta\rho = -\rho_0 \nabla \cdot (\delta \mathbf{r})$$

where ρ_0 refers to the unperturbed quantity.

$$\frac{\partial L}{\partial(\delta x_a)} = -m_a \sum_b m_b \left(\frac{P_a}{\rho_a^2}+\frac{P_b}{\rho_b^2}\right)\delta x_{ab}\frac{\partial^2 W_{bc}}{\partial x_a^2} - m_a \sum_b m_b \left[\left(c_s^2-\frac{2P_b}{\rho_b}\right)\frac{\delta\rho_a}{\rho_a^2}+\left(c_s^2-\frac{2P_b}{\rho_b}\right)\frac{\delta\rho_b}{\rho_b^2}\right]\frac{\partial W_{ab}}{\partial x_a} \quad \text{(B.6)}$$

giving the SPH form of the linearised momentum equation

$$\frac{d^2\delta x_a}{dt^2} = -\sum_b m_b \left(\frac{P_a}{\rho_a^2}+\frac{P_b}{\rho_b^2}\right)\delta x_{ab}\frac{\partial^2 W_{bc}}{\partial x_a^2} - \sum_b m_b \left[\left(c_s^2-\frac{2P_b}{\rho_b}\right)\frac{\delta\rho_a}{\rho_a^2}+\left(c_s^2-\frac{2P_b}{\rho_b}\right)\frac{\delta\rho_b}{\rho_b^2}\right]\frac{\partial W_{ab}}{\partial x_a} \quad \text{(B.7)}$$

Equation (B.7) may also be obtained by a direct perturbation of the SPH equations of motion derived in §3.3.2. For linear waves the perturbations are assumed to be of the form

$$x = x_0+\delta x, \quad \text{(B.8)}$$

$$\rho = \rho_0+\delta\rho, \quad \text{(B.9)}$$

$$P = P_0+\delta P. \quad \text{(B.10)}$$

where

$$\delta x_a = X e^{i(kx_a-\omega t)}, \quad \text{(B.11)}$$

$$\delta\rho_a = D e^{i(kx_a-\omega t)}, \quad \text{(B.12)}$$

$$\delta P_a = c_s^2\delta\rho_a. \quad \text{(B.13)}$$

Assuming equal mass particles, the momentum equation (B.7) becomes

$$-\omega^2 X = -\frac{2mP_0}{\rho_0^2}X\sum_b\left[1-e^{ik(x_b-x_a)}\right]\frac{\partial^2 W}{\partial x_a^2} - \frac{m}{\rho_0^2}\left(c_s^2-\frac{2P_b}{\rho_b}\right)D\sum_b\left[1+e^{ik(x_b-x_a)}\right]\frac{\partial W}{\partial x_a} \quad \text{(B.14)}$$

From the continuity equation (3.43) the amplitude D of the density perturbation is given in terms of the particle co-ordinates by

$$D = Xm\sum_b\left[1-e^{ik(x_b-x_a)}\right]\frac{\partial W}{\partial x_a} \quad \text{(B.15)}$$

Finally, plugging this into (B.14) and taking the real component, the SPH dispersion relation (for any equation of state) is given by

$$\omega_a^2 = \frac{2mP_0}{\rho_0^2}\sum_b[1-\cos k(x_a-x_b)]\frac{\partial^2 W}{\partial x^2}(x_a-x_b,h) + \frac{m^2}{\rho_0^2}\left(c_s^2-\frac{2P_0}{\rho_0}\right)\left[\sum_b \sin k(x_a-x_b)\frac{\partial W}{\partial x}(x_a-x_b,h)\right]^2, \quad \text{(B.16)}$$

For an isothermal equation of state this can be simplified further by setting $c_s^2 = P_0/\rho_0$. An adiabatic equation of state corresponds to setting $c_s^2 = \gamma P_0/\rho_0$.

Appendix C
Linear waves in MHD

In this section we describe the setup used for the MHD waves described in §4.6.4. The MHD equations in continuum form may be written as

$$\begin{aligned}
\frac{d\rho}{dt} &= -\rho\nabla\cdot\mathbf{v}, && \text{(C.1)}\\
\frac{d\mathbf{v}}{dt} &= -\frac{\nabla P}{\rho} - \frac{\mathbf{B}\times(\nabla\times\mathbf{B})}{\mu_0\rho}, && \text{(C.2)}\\
\frac{d\mathbf{B}}{dt} &= (\mathbf{B}\cdot\nabla)\mathbf{v} - \mathbf{B}(\nabla\cdot\mathbf{v}), && \text{(C.3)}
\end{aligned}$$

together with the divergence constraint $\nabla\cdot\mathbf{B}=0$. We perturb according to

$$\begin{aligned}
\rho &= \rho_0+\delta\rho,\\
\mathbf{v} &= \mathbf{v},\\
\mathbf{B} &= \mathbf{B}_0+\delta\mathbf{B},\\
\delta P &= c_s^2\delta\rho. && \text{(C.4)}
\end{aligned}$$

where $c_s^2=\gamma P_0/\rho_0$ is the sound speed. Considering only linear terms, the perturbed equations are therefore given by

$$\begin{aligned}
\frac{d(\delta\rho)}{dt} &= -\rho_0(\nabla\cdot\mathbf{v}), && \text{(C.5)}\\
\frac{d\mathbf{v}}{dt} &= -c_s^2\frac{\nabla(\delta\rho)}{\rho_0} - \frac{\mathbf{B}_0\times(\nabla\times\delta\mathbf{B})}{\mu_0\rho_0}, && \text{(C.6)}\\
\frac{d(\delta\mathbf{B})}{dt} &= (\mathbf{B}_0\cdot\nabla)\mathbf{v} - \mathbf{B}_0(\nabla\cdot\mathbf{v}). && \text{(C.7)}
\end{aligned}$$

Specifying the perturbation according to

$$\begin{aligned}
\delta\rho &= De^{i(\mathbf{k}x-\omega t)},\\
\mathbf{v} &= \mathbf{v}e^{i(\mathbf{k}x-\omega t)},\\
\delta\mathbf{B} &= \mathbf{b}e^{i(\mathbf{k}x-\omega t)}, && \text{(C.8)}
\end{aligned}$$

we have

$$-\omega D = -\rho_0(\mathbf{v}\cdot\mathbf{k}) \qquad \text{(C.9)}$$

$$-\omega\mathbf{v} = -c_s^2\frac{D\mathbf{k}}{\rho_0} - \frac{1}{\mu_0\rho_0}\left[(\mathbf{B}_0\cdot\mathbf{b})\mathbf{k} - (\mathbf{B}_0\cdot\mathbf{k})\mathbf{b}\right] \tag{C.10}$$

$$-\omega\mathbf{b} = (\mathbf{B}_0\cdot\mathbf{k})\mathbf{v} - \mathbf{B}_0(\mathbf{k}\cdot\mathbf{v}). \tag{C.11}$$

Considering only waves in the x-direction (ie. $\mathbf{k} = [\mathrm{k}_x, 0, 0]$), defining the wave speed $v = \omega/\mathrm{k}$ and using (C.9) to eliminate D, equation (C.10) gives

$$v_x\left(v - \frac{c_s^2}{v}\right) = \left(\frac{B_{y0}b_y + B_{z0}b_z}{\mu_0\rho_0}\right), \tag{C.12}$$

$$vv_y = -\frac{B_{x0}b_y}{\mu_0\rho_0}, \tag{C.13}$$

$$vv_z = -\frac{B_{x0}b_z}{\mu_0\rho_0}, \tag{C.14}$$

where $b_x = 0$ since $\nabla\cdot\mathbf{B} = 0$. Using these in (C.11) we have

$$vb_y = -B_{x0}v_y + B_{y0}v_x, \tag{C.15}$$

$$vb_z = -B_{x0}v_z + B_{z0}v_x. \tag{C.16}$$

We can therefore solve for the perturbation amplitudes v_x, v_y, v_z, b_y and b_z in terms of the amplitude of the density perturbation D and the wave speed v. We find

$$v_x = \frac{vD}{\rho} \tag{C.17}$$

$$v_y\left(v^2 - \frac{B_x^2}{\mu_0\rho}\right) = \frac{B_xB_y}{\mu_0\rho}v_x \tag{C.18}$$

$$v_z\left(v^2 - \frac{B_x^2}{\mu_0\rho}\right) = \frac{B_xB_z}{\mu_0\rho}v_x \tag{C.19}$$

$$b_y\left(v^2 - \frac{B_x^2}{\mu_0\rho}\right) = vB_yv_x \tag{C.20}$$

$$b_z\left(v^2 - \frac{B_x^2}{\mu_0\rho}\right) = vB_zv_x \tag{C.21}$$

where we have dropped the subscript 0. The wave speed v is found by eliminating these quantities from (C.12), giving

$$\frac{v_x}{(v^2 - B_x^2/\mu_0\rho)}\left[v^4 - v^2\left(c_s^2 + \frac{B_x^2 + B_y^2 + B_z^2}{\mu_0\rho}\right) + \frac{c_s^2B_x^2}{\mu_0\rho}\right] = 0, \tag{C.22}$$

which reveals the three wave types in MHD. The Alfvén waves are those with

$$v^2 = \frac{B_x^2}{\mu_0\rho}, \tag{C.23}$$

These are transverse waves which travel along the field lines. The term in square brackets in (C.22) gives a quartic for v (or a quadratic for v^2), with roots

$$v^2 = \frac{1}{2}\left[\left(c_s^2 + \frac{B_x^2+B_y^2+B_z^2}{\mu_0\rho}\right) \pm \sqrt{\left(c_s^2 + \frac{B_x^2+B_y^2+B_z^2}{\mu_0\rho}\right)^2 - 4\frac{c_s^2 B_x^2}{\mu_0\rho}}\right], \tag{C.24}$$

which are the fast(+) and slow(-) magnetosonic waves.

BIBLIOGRAPHY

Balbus, S. A. and J. F. Hawley: 1991, 'A powerful local shear instability in weakly magnetized disks. I - Linear analysis. II - Nonlinear evolution'. *ApJ* **376**, 214–233.

Balbus, S. A. and J. F. Hawley: 1998, 'Instability, turbulence, and enhanced transport in accretion disks'. *Reviews of Modern Physics* **70**, 1–53.

Bally, J., S. Heathcote, B. Reipurth, J. Morse, P. Hartigan, and R. Schwartz: 2002, 'Hubble Space Telescope Observations of Proper Motions in Herbig-Haro Objects 1 and 2'. *AJ* **123**, 2627–2657.

Bally, J., D. Johnstone, G. Joncas, B. Reipurth, and G. Mallén-Ornelas: 2001, 'Kinematics of Optical Outflows in the Orion Nebula. I. The Giant Outflow HH 400 and the Irradiated Jet HH 502'. *AJ* **122**, 1508–1524.

Balsara, D. S.: 1998, 'Total Variation Diminishing Scheme for Adiabatic and Isothermal Magnetohydrodynamics'. *ApJS* **116**, 133.

Balsara, D. S. and D. Spicer: 1999, 'Maintaining Pressure Positivity in Magnetohydrodynamic Simulations'. *J. Comp. Phys.* **148**, 133–148.

Banyuls, F., J. A. Font, J. M. A. Ibanez, J. M. A. Marti, and J. A. Miralles: 1997, 'Numerical {3+1} General Relativistic Hydrodynamics: A Local Characteristic Approach'. *ApJ* **476**, 221.

Barmin, A. A., A. G. Kulikovskiy, and N. V. Pogorelov: 1996, 'Shock-Capturing Approach and Nonevolutionary Solutions in Magnetohydrodynamics'. *J. Comp. Phys.* **126**, 77–90.

Bate, M. R., I. A. Bonnell, and V. Bromm: 2003, 'The formation of a star cluster: predicting the properties of stars and brown dwarfs'. *MNRAS* **339**, 577–599.

Bate, M. R., I. A. Bonnell, and N. M. Price: 1995, 'Modelling accretion in protobinary systems'. *MNRAS* **277**, 362–376.

Bate, M., R. B.: 1995, 'The role of accretion in binary star formation'. Ph.D. thesis, University of Cambridge, Cambridge, UK.

Begelman, M. C.: 1998, 'Instability of Toroidal Magnetic Field in Jets and Plerions'. *ApJ* **493**, 291–+.

Bekenstein, J. D. and A. Oron: 2000, 'Conservation of circulation in magnetohydrodynamics'. *Phys. Rev. E* **62**, 5594–5602.

Benz, W.: 1984, '3D models of rotating magnetic gas clouds. I - Time evolution, mass spectrum and angular momentum'. *A&A* **139**, 378–388.

Benz, W.: 1990, 'Smoothed Particle Hydrodynamics - A review'. In: J. R. Buchler (ed.): *The numerical modelling of nonlinear stellar pulsations*. pp. 269–288, Kluwer.

Benz, W., A. G. W. Cameron, W. H. Press, and R. L. Bowers: 1990, 'Dynamic mass exchange in doubly degenerate binaries. I - 0.9 and 1.2 solar mass stars'. *ApJ* **348**, 647–667.

Biretta, J. A., W. B. Sparks, and F. Macchetto: 1999, 'Hubble Space Telescope Observations of Superluminal Motion in the M87 Jet'. *ApJ* **520**, 621–626.

Blandford, R. D. and D. G. Payne: 1982, 'Hydromagnetic flows from accretion discs and the production of radio jets'. *MNRAS* **199**, 883–903.

Blandford, R. D. and M. J. Rees: 1974, 'A 'twin-exhaust' model for double radio sources'. *MNRAS* **169**, 395–415.

Blandford, R. D. and R. L. Znajek: 1977, 'Electromagnetic extraction of energy from Kerr black holes'. *MNRAS* **179**, 433–456.

Bondi, H.: 1952, 'On spherically symmetrical accretion'. *MNRAS* **112**, 195.

Bonet, J. and S. Kulasegaram: 2000, 'Correction and stabilization of smooth particle hydrodynamics methods with applications in metal forming simulations'. *Int. J. Numer. Meth. Engng.* **47**, 1189–1214.

Bonet, J. and S. Kulasegaram: 2001, 'Remarks on tension instability of Eulerian and Lagrangian corrected smooth particle hydrodynamics (CSPH) methods'. *Int. J. Numer. Meth. Engng.* **52**, 1203–1220.

Bonet, J. and L. Lok, T-S.: 1999, 'Variational and momentum preservation aspects of Smooth Particle Hydrodynamic formulations'. *Computer methods in applied mechanics and engineering* **180**, 97–115.

Børve, S.: 2001, 'A numerical study of ionospheric and magnetospheric phenomena using particle simulation techniques'. Ph.D. thesis, University of Oslo, Norway.

Børve, S., M. Omang, and J. Trulsen: 2001, 'Regularized Smoothed Particle Hydrodynamics: A New Approach to Simulating Magnetohydrodynamic Shocks'. *ApJ* **561**, 82–93.

Boss, A. P.: 2000, 'Protostellar Fragmentation Enhanced by Magnetic Fields'. *ApJL* **545**, L61–L64.

Boss, A. P.: 2002, 'Collapse and Fragmentation of Molecular Cloud Cores. VII. Magnetic Fields and Multiple Protostar Formation'. *ApJ* **568**, 743–753.

Brackbill, J. U. and D. C. Barnes: 1980, 'The effect of nonzero product of magnetic gradient and B on the numerical solution of the magnetohydrodynamic equations'. *J. Comp. Phys.* **35**, 426–430.

Brandenburg, A.: 2001, 'Computational aspects of astrophysical MHD and turbulence'. *astro-ph/0109497*.

Brio, M. and C. C. Wu: 1988, 'An upwind differencing scheme for the equations of ideal magnetohydrodynamics'. *J. Comp. Phys.* **75**, 400–422.

Brookshaw, L.: 1985, 'A method of calculating radiative heat diffusion in particle simulations'. *Proceedings of the Astronomical Society of Australia* **6**, 207–210.

Burrows, C. J., K. R. Stapelfeldt, A. M. Watson, J. E. Krist, G. E. Ballester, J. T. Clarke, D. Crisp, J. S. Gallagher, R. E. Griffiths, J. J. Hester, J. G. Hoessel, J. A. Holtzman, J. R. Mould, P. A. Scowen, J. T. Trauger, and J. A. Westphal: 1996, 'Hubble Space Telescope Observations of the Disk and Jet of HH 30'. *ApJ* **473**, 437.

Byleveld, S. E. and H. Pongracic: 1996, 'The influence of magnetic fields on star formation'. *Publications of the Astronomical Society of Australia* **13**, 71–74.

Caramana, E. J., M. J. Shashkov, and P. P. Whalen: 1998, 'Formulations of Artificial Viscosity for Multi-dimensional Shock Wave Computations'. *J. Comp. Phys.* **144**, 70–97.

Caunt, S. E. and M. J. Korpi: 2001, 'A 3D MHD model of astrophysical flows: Algorithms, tests and parallelisation'. *A&A* **369**, 706–728.

Cerqueira, A. H. and E. M. de Gouveia Dal Pino: 2001, 'Three-dimensional Magnetohydrodynamic Simulations of Radiatively Cooling, Pulsed Jets'. *ApJ* **560**, 779–791.

Cha, S.-H. and A. P. Whitworth: 2003, 'Implementations and tests of Godunov-type particle hydrodynamics'. *MNRAS* **340**, 73–90.

Chandrasekhar, S.: 1961, *Hydrodynamic and hydromagnetic stability*, International Series of Monographs on Physics. Oxford: Clarendon Press.

Chow, E. and J. J. Monaghan: 1997, 'Ultrarelativistic SPH'. *J. Comp. Phys.* **134**, 296–305.

Cleary, P. W. and J. J. Monaghan: 1999, 'Conduction Modelling Using Smoothed Particle Hydrodynamics'. *J. Comp. Phys.* **148**, 227–264.

Cummins, S. J. and M. Rudman: 1999, 'An SPH Projection Method'. *J. Comp. Phys.* **152**, 584–607.

Curtis, H. D.: 1918, 'Descriptions of 762 Nebulae and Clusters Photographed with the Crossley Reflector'. *Publications of the Lick Observatory* **13**, 9–42.

Dahlburg, R. B. and J. M. Picone: 1989, 'Evolution of the Orszag-Tang vortex system in a compressible medium. I - Initial average subsonic flow'. *Physics of Fluids B* **1**, 2153–2171.

Dai, W. and P. R. Woodward: 1994, 'Extension of the Piecewise Parabolic Method to Multidimensional Ideal Magnetohydrodynamics'. *J. Comp. Phys.* **115**, 485–514.

Dai, W. and P. R. Woodward: 1998, 'On the Divergence-free Condition and Conservation Laws in Numerical Simulations for Supersonic Magnetohydrodynamic Flows'. *ApJ* **494**, 317.

Dedner, A., F. Kemm, D. Kröner, C.-D. Munz, T. Schnitzer, and M. Wesenberg: 2002, 'Hyperbolic Divergence Cleaning for the MHD Equations'. *J. Comp. Phys.* **175**, 645–673.

Dellar, P. J.: 2001, 'A Note on Magnetic Monopoles and the One-Dimensional MHD Riemann Problem'. *J. Comp. Phys.* **172**, 392–398.

Dolag, K., M. Bartelmann, and H. Lesch: 1999, 'SPH simulations of magnetic fields in galaxy clusters'. *A&A* **348**, 351–363.

Drazin, P. G. and W. H. Reid: 1981, *Hydrodynamic stability*. Cambridge, Cambridge University Press.

Dyka, C. T., P. W. Randles, and R. P. Ingel: 1997, 'Stress points for tension instability in SPH'. *Int. J. Numer. Meth. Engng.* **40**, 2325–2341.

Eckart, C.: 1960. *Physics of Fluids* **3**, 421.

Eislöffel, J. and R. Mundt: 1998, 'Imaging and Kinematic Studies of Young Stellar Object Jets in Taurus'. *AJ* **115**, 1554–1575.

Español, P. and M. Revenga: 2003, 'Smoothed dissipative particle dynamics'. *Phys. Rev. E* **67**(2), 026705.

Evans, C. R. and J. F. Hawley: 1988, 'Simulation of magnetohydrodynamic flows - A constrained transport method'. *ApJ* **332**, 659–677.

Ferrari, A.: 1998, 'Modeling Extragalactic Jets'. *Ann. Rev. Astron. Astroph.* **36**, 539–598.

Field, G.: 1986, 'Magnetic helicity in astrophysics'. In: R. Epstein and W. Feldman (eds.): *AIP Conf. Proc. 144: Magnetospheric Phenomena in Astrophysics*. pp. 324–341.

Flammang, R. A.: 1982, 'Stationary spherical accretion into black holes. II - Theory of optically thick accretion'. *MNRAS* **199**, 833–867.

Frank, J., A. King, and D. J. Raine: 2002, *Accretion Power in Astrophysics*. Cambridge: Cambridge University Press, 3rd edition.

Fulk, D. A. and D. W. Quinn: 1996, 'An Analysis of 1-D Smoothed Particle Hydrodynamics Kernels'. *J. Comp. Phys.* **126**, 165–180.

Ghisellini, G. and A. Celotti: 2001, 'Relativistic large-scale jets and minimum power requirements'. *MNRAS* **327**, 739–743.

Gingold, R. A. and J. J. Monaghan: 1977, 'Smoothed particle hydrodynamics - Theory and application to non-spherical stars'. *MNRAS* **181**, 375–389.

Gray, J., J. J. Monaghan, and R. P. Swift: 2001, 'SPH elastic dynamics'. *Computer methods in applied mechanics and engineering* **190**, 6641–6662.

Habe, A., Y. Uchida, S. Ikeuchi, and R. E. Pudritz: 1991, 'Triggering the collapse of self-gravitating clouds by torsional Alfven waves'. *Publ. Astron. Soc. Japan* **43**, 703–718.

Hairer, E., C. Lubich, and G. Wanner: 2002, *Geometric Numerical Integration. Structure-Preserving Al-*

gorithms for Ordinary Differential Equations., Vol. 31 of *Springer Series in Comput. Math.* Springer-Verlag.

Hartigan, P., J. A. Morse, B. Reipurth, S. Heathcote, and J. Bally: 2001, 'Proper Motions of the HH 111 Jet Observed with the Hubble Space Telescope'. *ApJL* **559**, L157–L161.

Hawley, J. F., C. F. Gammie, and S. A. Balbus: 1995, 'Local Three-dimensional Magnetohydrodynamic Simulations of Accretion Disks'. *ApJ* **440**, 742.

Heinz, S. and M. C. Begelman: 2000, 'Jet Acceleration by Tangled Magnetic Fields'. *ApJ* **535**, 104–117.

Henyey, F. S.: 1982, 'Canonical construction of a Hamiltonian for dissipation-free magnetohydrodynamics'. *Phys. Rev. A* **26**, 480–483.

Hernquist, L. and N. Katz: 1989, 'TREESPH - A unification of SPH with the hierarchical tree method'. *ApJS* **70**, 419–446.

Holder, T., B. Leimkuhler, and S. Reich: 2001, 'Explicit variable step-size and time-reversible integration'. *Applied Numerical Mathematics: Transactions of IMACS* **39**(3–4), 367–377.

Holzer, T. E. and W. I. Axford: 1970, 'The Theory of Stellar Winds and Related Flows'. *Ann. Rev. Astron. Astroph.* **8**, 31.

Hosking, J. G.: 2002, 'The Role of Magnetic Fields in Star Formation'. Ph.D. thesis, Cardiff University, UK.

Hosking, J. G. and A. P. Whitworth: 2004, 'Fragmentation of magnetized cloud cores'. *MNRAS* **347**, 1001–1010.

Huang, W. and B. Leimkuhler: 1997, 'The adaptive Verlet method'. *SIAM Journal on Scientific Computing* **18**(1), 239–256.

Hut, P., J. Makino, and S. McMillan: 1995, 'Building a better leapfrog'. *ApJL* **443**, L93–L96.

Imaeda, Y. and S. Inutsuka: 2002, 'Shear Flows in Smoothed Particle Hydrodynamics'. *ApJ* **569**, 501–518.

Inutsuka, S.: 2002, 'Reformulation of Smoothed Particle Hydrodynamics with Riemann Solver'. *J. Comp. Phys.* **179**, 238–267.

Janhunen, P.: 2000, 'A Positive Conservative Method for Magnetohydrodynamics Based on HLL and Roe Methods'. *J. Comp. Phys.* **160**, 649–661.

Jubelgas, M., V. Springel, and K. Dolag: 2004, 'Thermal conduction in cosmological SPH simulations'. *MNRAS preprint* p. 000.

Klessen, R. S., F. Heitsch, and M. Mac Low: 2000, 'Gravitational Collapse in Turbulent Molecular Clouds. I. Gasdynamical Turbulence'. *ApJ* **535**, 887–906.

Koide, S., D. L. Meier, K. Shibata, and T. Kudoh: 2000, 'General Relativistic Simulations of Early Jet Formation in a Rapidly Rotating Black Hole Magnetosphere'. *ApJ* **536**, 668–674.

Konigl, A.: 1982, 'On the nature of bipolar sources in dense molecular clouds'. *ApJ* **261**, 115–134.

Kudoh, T., R. Matsumoto, and K. Shibata: 1998, 'Magnetically Driven Jets from Accretion Disks. III. 2.5-dimensional Nonsteady Simulations for Thick Disk Case'. *ApJ* **508**, 186–199.

Kuznetsov, E. A. and V. P. Ruban: 2000, 'Hamiltonian dynamics of vortex and magnetic lines in hydrodynamic type systems'. *Phys. Rev. E* **61**, 831–841.

Lamers, H. J. G. L. M. and J. P. Cassinelli: 1999, *Introduction to stellar winds*. New York : Cambridge University Press.

Landshoff, R.: 1955, 'A numerical method for treating fluid flow in the presence of shocks'. Technical

Report LA-1930, Los Alamos National Laboratory.

Li, L.: 2002, 'Jet Collimation by Small-Scale Magnetic Fields'. *ApJ* **564**, 108–112.

Livio, M.: 1999, 'Astrophysical jets : a phenomenological examination of acceleration and collimation.'. *Phys. Rep.* **311**, 225–245.

Lodato, G. and W. K. M. Rice: 2004, 'Testing the locality of transport in self-gravitating accretion discs'. *MNRAS* **351**, 630–642.

Londrillo, P. and L. Del Zanna: 2000, 'High-Order Upwind Schemes for Multidimensional Magnetohydrodynamics'. *ApJ* **530**, 508–524.

Lubow, S. H., J. C. B. Papaloizou, and J. E. Pringle: 1994, 'Magnetic field dragging in accretion discs'. *MNRAS* **267**, 235–240.

Lucek, S. G. and A. R. Bell: 1996, 'The stability, during formation, of magnetohydrodynamic jets collimated by an azimuthal magnetic field'. *MNRAS* **281**, 245–256.

Lucek, S. G. and A. R. Bell: 1997, 'The stability, during formation, of magnetohydrodynamically collimated jets'. *MNRAS* **290**, 327–333.

Lucy, L. B.: 1977, 'A numerical approach to the testing of the fission hypothesis'. *Astron. J.* **82**, 1013–1024.

Mészáros, P.: 2002, 'Theories of Gamma-Ray Bursts'. *Ann. Rev. Astron. Astrophys.* **40**, 137–169.

Mac Low, M., R. Klessen, A. Burkert, and M. Smith: 1999, 'Decay Timescales of MHD Turbulence in Molecular Clouds'. In: J. Franco and A. Carraminana (eds.): *Interstellar Turbulence*. p. 256, Cambridge University Press.

Mac Low, M. and R. S. Klessen: 2004, 'Control of star formation by supersonic turbulence'. *Rev. Mod. Phys.* **76**, 125–194.

Marinho, E. P., C. M. Andreazza, and J. R. D. Lépine: 2001, 'SPH simulations of clumps formation by dissipative collisions of molecular clouds. II. Magnetic case'. *A&A* **379**, 1123–1137.

Maron, J. L. and G. G. Howes: 2003, 'Gradient Particle Magnetohydrodynamics: A Lagrangian Particle Code for Astrophysical Magnetohydrodynamics'. *ApJ* **595**, 564–572.

Marri, S. and S. D. M. White: 2003, 'Smoothed particle hydrodynamics for galaxy-formation simulations: improved treatments of multiphase gas, of star formation and of supernovae feedback'. *MNRAS* **345**, 561–574.

Marscher, A. P., S. G. Jorstad, J. Gómez, M. F. Aller, H. Teräsranta, M. L. Lister, and A. M. Stirling: 2002, 'Observational evidence for the accretion-disk origin for a radio jet in an active galaxy'. *Nature* **417**, 625–627.

Meglicki, Z.: 1994, 'Verification and accuracy of smoothed particle magnetohydrodynamics'. *Comput. Phys. Commun.* **81**, 91.

Meglicki, Z.: 1995, 'Analysis and applications of Smoothed Particle Magnetohydrodynamics'. Ph.D. thesis, Australian National University.

Meglicki, Z., D. Wickramasinghe, and R. L. Dewar: 1995, 'Gravitational collapse of a magnetized vortex: application to the Galactic Centre'. *MNRAS* **272**, 717–729.

Michel, F. C.: 1972, 'Accretion of Matter by Condensed Objects'. *Ap&SS* **15**, 153.

Micono, M., C. J. Davis, T. P. Ray, J. Eisloeffel, and M. D. Shetrone: 1998, 'Proper Motions and Variability of the H 2 Emission in the HH 46/47 System'. *ApJL* **494**, L227+.

Mirabel, I. F., V. Dhawan, S. Chaty, L. F. Rodriguez, J. Marti, C. R. Robinson, J. Swank, and T. Geballe:

1998, 'Accretion instabilities and jet formation in GRS 1915+105'. *A&A* **330**, L9–L12.

Mirabel, I. F. and L. F. Rodríguez: 1999, 'Sources of Relativistic Jets in the Galaxy'. *Ann. Rev. Astron. Astroph.* **37**, 409–443.

Molteni, D., G. Lanzafame, and S. K. Chakrabarti: 1994, 'Simulation of thick accretion disks with standing shocks by smoothed particle hydrodynamics'. *ApJ* **425**, 161–170.

Monaghan, J. J.: 1989, 'On the problem of penetration in particle methods'. *J. Comp. Phys.* **82**, 1–9991.

Monaghan, J. J.: 1992, 'Smoothed particle hydrodynamics'. *Ann. Rev. Astron. Astrophys.* **30**, 543–574.

Monaghan, J. J.: 1997a, 'Implicit SPH Drag and Dusty Gas Dynamics'. *J. Comp. Phys.* **138**, 801–820.

Monaghan, J. J.: 1997b, 'SPH and Riemann Solvers'. *J. Comp. Phys.* **136**, 298–307.

Monaghan, J. J.: 2000, 'SPH without a Tensile Instability'. *J. Comp. Phys.* **159**, 290–311.

Monaghan, J. J.: 2002, 'SPH compressible turbulence'. *MNRAS* **335**, 843–852.

Monaghan, J. J. and J. C. Lattanzio: 1985, 'A refined particle method for astrophysical problems'. *A&A* **149**, 135–143.

Monaghan, J. J. and D. J. Price: 2001, 'Variational principles for relativistic smoothed particle hydrodynamics'. *MNRAS* **328**, 381–392.

Monaghan, J. J. and D. J. Price: 2004, 'Toy stars in one dimension'. *MNRAS* **350**, 1449–1456.

Morris, J. P.: 1996, 'Analysis of smoothed particle hydrodynamics with applications'. Ph.D. thesis, Monash University, Melbourne, Australia.

Morris, J. P. and J. J. Monaghan: 1997, 'A switch to reduce SPH viscosity'. *J. Comp. Phys.* **136**, 41–50.

Morrison, P. J.: 1998, 'Hamiltonian description of the ideal fluid'. *Rev. Mod. Phys.* **70**, 467–521.

Morrison, P. J. and R. D. Hazeltine: 1984, 'Hamiltonian formulation of reduced magnetohydrodynamics'. *Physics of Fluids* **27**, 886–897.

Munz, C.-D., P. Omnes, R. Schneider, E. Sonnendrücker, and U. Voß: 2000, 'Divergence Correction Techniques for Maxwell Solvers Based on a Hyperbolic Model'. *J. Comp. Phys.* **161**, 484–511.

Murray, J., J. Wadsley, and J. R. Bond: 1996, 'MHD with SPH: Application to the High Redshift IGM'. *Bulletin of the American Astronomical Society* **28**, 1413.

Murray, J. R.: 1996, 'SPH simulations of tidally unstable accretion discs in cataclysmic variables'. *MNRAS* **279**, 402–414.

Nelson, R.: 1994, 'A Conservative Formulation of SPH with Variable Smoothing Lengths'. *Memorie della Societa Astronomica Italiana* **65**, 1161.

Nelson, R. P. and J. C. B. Papaloizou: 1994, 'Variable Smoothing Lengths and Energy Conservation in Smoothed Particle Hydrodynamics'. *MNRAS* **270**, 1.

Newcomb, W. A.: 1962, 'Lagrangian and Hamiltonian methods in magnetohydrodynamics'. *Nucl. Fusion Suppl.* **2**, 451–463.

Nordlund, A. and K. Galsgaard: 1995, 'A 3D MHD code for Parallel Computers'. Technical report, Astronomical Observatory, University of Copenhagen (available from http://www-solar.mcs.st-andrews.ac.uk/ klaus/publications/lop.html).

Oppeneer, P. M.: 1984, 'Variational principle for ideal MHD'. *Physics Letters A* **104**, 207–211.

Orszag, S. A. and C.-M. Tang: 1979, 'Small-scale structure of two-dimensional magnetohydrodynamic turbulence'. *J. Fluid Mech.* **90**, 129–143.

Oswald, L. H.: 1963, 'Why I shot JFK'. *J. Consp. Theor.* **666**, 1–17.

Ott, F. and E. Schnetter: 2003, 'A modified SPH approach for fluids with large density differences'.

physics/0303112.

Ouyed, R. and R. E. Pudritz: 1997, 'Numerical Simulations of Astrophysical Jets from Keplerian Disks. I. Stationary Models'. *ApJ* **482**, 712.

Ouyed, R. and R. E. Pudritz: 1999, 'Numerical simulations of astrophysical jets from Keplerian discs - III. The effects of mass loading'. *MNRAS* **309**, 233–244.

Ouyed, R., R. E. Pudritz, and J. M. Stone: 1997, 'Episodic jets from black holes and protostars'. *Nature* **385**, 409–414.

Parker, E. N.: 1958, 'Dynamics of the Interplanetary Gas and Magnetic Fields.'. *ApJ* **128**, 664.

Parshikov, A. N. and S. A. Medin: 2002, 'Smoothed Particle Hydrodynamics Using Interparticle Contact Algorithms'. *J. Comp. Phys.* **180**, 358–382.

Pelupessy, F. I., W. E. Schaap, and R. van de Weygaert: 2003, 'Density estimators in particle hydrodynamics. DTFE versus regular SPH'. *A&A* **403**, 389–398.

Phillips, G. J.: 1982, 'Numerical simulations of collapsing, isothermal, magnetic clouds'. *Proceedings of the Astronomical Society of Australia* **4**, 371–373.

Phillips, G. J.: 1983a, 'An investigation of fragmentation in collapsing magnetic gas clouds'. *Proceedings of the Astronomical Society of Australia* **5**, 180–182.

Phillips, G. J.: 1983b, 'Three dimensional numerical simulations of collapsing, isothermal, magnetic gas clouds'. Ph.D. thesis, Monash University, Melbourne, Australia.

Phillips, G. J.: 1985, 'Fragmentation in collapsing magnetic gas clouds - Non-uniform initial fields'. *Proceedings of the Astronomical Society of Australia* **6**, 205–207.

Phillips, G. J.: 1986a, 'Three-dimensional numerical simulations of collapsing, isothermal magnetic gas clouds'. *MNRAS* **221**, 571–587.

Phillips, G. J.: 1986b, 'Three-dimensional numerical simulations of collapsing isothermal magnetic gas clouds - Non-uniform initial fields'. *MNRAS* **222**, 111–119.

Phillips, G. J. and J. J. Monaghan: 1985, 'A numerical method for three-dimensional simulations of collapsing, isothermal, magnetic gas clouds'. *MNRAS* **216**, 883–895.

Picone, J. M. and R. B. Dahlburg: 1991, 'Evolution of the Orszag-Tang vortex system in a compressible medium. II - Supersonic flow'. *Physics of Fluids B* **3**, 29–44.

Powell, K. G.: 1994, 'An approximate Riemann solver for magnetohydrodynamics (that works in more than one dimension)'. Technical Report ICASE 94-24, NASA Langley Research center (available from http://techreports.larc.nasa.gov/ltrs/dublincore/1994/icase-1994-24.html).

Powell, K. G., P. L. Roe, T. J. Linde, T. I. Gombosi, and D. L. de Zeeuw: 1999, 'A Solution-Adaptive Upwind Scheme for Ideal Magnetohydrodynamics'. *J. Comp. Phys.* **154**, 284–309.

Press, W. H., S. A. Teukolsky, W. T. Vetterling, and B. P. Flannery: 1992, *Numerical recipes in FORTRAN. The art of scientific computing*. Cambridge: University Press, —c1992, 2nd ed.

Pringle, J. E.: 1981, 'Accretion discs in astrophysics'. *Ann. Rev. Astron. Astrophys.* **19**, 137–162.

Pringle, J. E.: 1989, 'A boundary layer origin for bipolar flows'. *MNRAS* **236**, 107–115.

Pruet, J., G. M. Fuller, and C. Y. Cardall: 2001, 'On Steady State Neutrino-heated Ultrarelativistic Winds from Compact Objects'. *ApJ* **561**, 957–963.

Pudritz, R. E. and C. A. Norman: 1986, 'Bipolar hydromagnetic winds from disks around protostellar objects'. *ApJ* **301**, 571–586.

Pyo, T., M. Hayashi, N. Kobayashi, H. Terada, M. Goto, T. Yamashita, A. T. Tokunaga, and Y. Itoh:

2002, ‘Velocity-resolved [Fe II] Line Spectroscopy of L1551 IRS 5: A Partially Ionized Wind under Collimation around an Ionized Fast Jet’. *ApJ* **570**, 724–733.

Rees, M. J.: 1984, ‘Black Hole Models for Active Galactic Nuclei’. *Ann. Rev. Astron. Astroph.* **22**, 471–506.

Reipurth, B. and J. Bally: 2001, ‘Herbig-Haro Flows: Probes of Early Stellar Evolution’. *Ann. Rev. Astron. Astroph.* **39**, 403–455.

Reipurth, B., S. Heathcote, J. Morse, P. Hartigan, and J. Bally: 2002, ‘Hubble Space Telescope Images of the HH 34 Jet and Bow Shock: Structure and Proper Motions’. *AJ* **123**, 362–381.

Richtmyer, R. D. and K. W. Morton: 1967, *Difference methods for initial-value problems*. Wiley, New York.

Ritchie, B. W. and P. A. Thomas: 2001, ‘Multiphase smoothed-particle hydrodynamics’. *MNRAS* **323**, 743–756.

Rosswog, S. and M. B. Davies: 2002, ‘High-resolution calculations of merging neutron stars - I. Model description and hydrodynamic evolution’. *MNRAS* **334**, 481–497.

Rosswog, S., M. B. Davies, F.-K. Thielemann, and T. Piran: 2000, ‘Merging neutron stars: asymmetric systems’. *A&A* **360**, 171–184.

Rosswog, S., E. Ramirez-Ruiz, and M. B. Davies: 2003, ‘High-resolution calculations of merging neutron stars - III. Gamma-ray bursts’. *MNRAS* **345**, 1077–1090.

Ruffert, M. and H.-T. Janka: 2001, ‘Coalescing neutron stars - A step towards physical models. III. Improved numerics and different neutron star masses and spins’. *A&A* **380**, 544–577.

Ryu, D. and T. W. Jones: 1995, ‘Numerical magetohydrodynamics in astrophysics: Algorithm and tests for one-dimensional flow‘’. *ApJ* **442**, 228–258.

Ryu, D., T. W. Jones, and A. Frank: 1995, ‘Numerical Magnetohydrodynamics in Astrophysics: Algorithm and Tests for Multidimensional Flow’. *ApJ* **452**, 785.

Salmon, R.: 1988, ‘Hamiltonian fluid mechanics’. *Annual Review of Fluid Mechanics* **20**, 225–256.

Schäfer, C., R. Speith, M. Hipp, and W. Kley: 2004, ‘Simulations of planet-disc interactions using Smoothed Particle Hydrodynamics’. *A&A* **418**, 325–335.

Schutz, B. F.: 1985, *A first course in general relativity*. Cambridge: University Press, 1985.

Serna, A., J.-M. Alimi, and J.-P. Chieze: 1996, ‘Adaptive Smooth Particle Hydrodynamics and Particle-Particle Coupled Codes: Energy and Entropy Conservation’. *ApJ* **461**, 884.

Shakura, N. I. and R. A. Sunyaev: 1973, ‘Black holes in binary systems. Observational appearance.’. *A&A* **24**, 337–355.

Shapiro, S. L. and S. A. Teukolsky: 1983, *Black holes, white dwarfs, and neutron stars: The physics of compact objects*. New York, Wiley-Interscience.

Shibata, M. and K. Ōo. Uryū: 2000, ‘Simulation of merging binary neutron stars in full general relativity: Γ=2 case’. *Phys. Rev. D* **61**(6), 064001.

Shu, F. H., F. C. Adams, and S. Lizano: 1987, ‘Star formation in molecular clouds - Observation and theory’. *Ann. Rev. Astron. Astroph.* **25**, 23–81.

Shu, F. H., S. Lizano, S. P. Ruden, and J. Najita: 1988, ‘Mass loss from rapidly rotating magnetic protostars’. *ApJL* **328**, L19–L23.

Sod, G. A.: 1978, ‘A Survey of Several Finite Difference Methods for Systems of Nonlinear Hyperbolic Conservation Laws’. *J. Comp. Phys.* **27**, 1–31.

Springel, V. and L. Hernquist: 2002, 'Cosmological smoothed particle hydrodynamics simulations: the entropy equation'. *MNRAS* **333**, 649–664.

Spruit, H. C., T. Foglizzo, and R. Stehle: 1997, 'Collimation of magnetically driven jets from accretion discs'. *MNRAS* **288**, 333–342.

Stellingwerf, R. F. and R. E. Peterkin: 1990, 'Smooth Particle Magnetohydrodynamics'. Technical Report MRC/ABQ-R-1248, Mission Research Corporation, Albuquerque,NM.

Stellingwerf, R. F. and R. E. Peterkin: 1994, 'Smooth Particle Magnetohydrodynamics (Invited review)'. *Memorie della Societa Astronomica Italiana* **65**, 991.

Stoffer, D.: 1995, 'Variable steps for reversible integration methods'. *Computing* **55**(1), 1–22.

Stone, J. M., J. F. Hawley, C. R. Evans, and M. L. Norman: 1992, 'A test suite for magnetohydrodynamical simulations'. *ApJ* **388**, 415–437.

Stone, J. M. and M. L. Norman: 1992, 'ZEUS-2D: A Radiation Magnetohydrodynamics Code for Astrophysical Flows in Two Space Dimensions. II. The Magnetohydrodynamic Algorithms and Tests'. *ApJS* **80**, 791.

Stone, J. M., E. C. Ostriker, and C. F. Gammie: 1998, 'Dissipation in Compressible Magnetohydrodynamic Turbulence'. *ApJL* **508**, L99–L102.

Tóth, G.: 2000, 'The ∇.B=0 Constraint in Shock-Capturing Magnetohydrodynamics Codes'. *J. Comp. Phys.* **161**, 605–652.

Tóth, G.: 2002, 'Conservative and Orthogonal Discretization for the Lorentz Force'. *J. Comp. Phys.* **182**, 346–354.

Thompson, T. A., A. Burrows, and B. S. Meyer: 2001, 'The Physics of Proto-Neutron Star Winds: Implications for r-Process Nucleosynthesis'. *ApJ* **562**, 887–908.

Toro, E. F.: 1992, 'The Weighted Average Flux Method Applied to the Euler Equations'. *Philosophical Transactions: Physical Sciences and Engineering* **341**, 499–530.

Tout, C. A., M. Livio, and I. A. Bonnell: 1999, 'The ages of pre-main-sequence stars'. *MNRAS* **310**, 360–376.

Tout, C. A. and J. E. Pringle: 1992, 'Accretion disc viscosity - A simple model for a magnetic dynamo'. *MNRAS* **259**, 604–612.

Tout, C. A. and J. E. Pringle: 1996, 'Can a disc dynamo generate large-scale magnetic fields?'. *MNRAS* **281**, 219–225.

Urry, C. M. and P. Padovani: 1995, 'Unified Schemes for Radio-Loud Active Galactic Nuclei'. *PASP* **107**, 803.

von Neumann, J. and R. D. Richtmyer: 1950, 'A method for the numerical calculation of hydrodynamic shocks'. *J. Appl. Phys.* **21**, 232.

Whitehouse, S. C. and M. R. Bate: 2004, 'Smoothed particle hydrodynamics with radiative transfer in the flux-limited diffusion approximation'. *astro-ph/0406392*.